LA-UR-98- 3043
April 1998

RECEIVED
FEB 23 1999
OSTI

REFLOOD COMPLETION REPORT

VOLUME I

A PHENOMENOLOGICAL THERMAL-HYDRAULIC MODEL OF HOT ROD BUNDLES EXPERIENCING SIMULTANEOUS BOTTOM AND TOP QUENCHING AND AN OPTIMIZATION METHODOLOGY FOR CLOSURE DEVELOPMENT

by

R. A. Nelson, Jr., D. A. Pimentel,
S. J. Jolly-Woodruff, and J. W. Spore

MASTER

DISTRIBUTION OF THIS DOCUMENT IS UNLIMITED

Photograph: by Chris J. Lindberg

DISCLAIMER

REFLOOD COMPLETION REPORT

VOLUME I

A PHENOMENOLOGICAL THERMAL-HYDRAULIC MODEL OF HOT ROD BUNDLES EXPERIENCING SIMULTANEOUS BOTTOM AND TOP QUENCHING AND AN OPTIMIZATION METHODOLOGY FOR CLOSURE DEVELOPMENT

by

Ralph A. Nelson Jr., David A. Pimentel, Susan Jolly-Woodruff, and Jay Spore
Nuclear Systems Design and Analysis
Los Alamos National Laboratory
Los Alamos, New Mexico

CONTENTS

PAGE

1. INTRODUCTION 1
   - 1.1. Development of Complex Closure Models in Two-fluid Thermal-Hydraulic Codes 3
   - 1.2. Conceptualization of Unidirectional Flow Bottom-up Quenching 5
   - 1.3. Conceptualization of Unidirectional Flow Top-down Quenching 6
   - 1.4. Conceptualization of Bidirectional Flow Quenching 7
2. DESCRIPTION OF THE THERMAL HYDRAULIC MODEL 8
   - 2.1. Bottom-Up and Top-Down Reflood Modeling 8
   - 2.2. Post-CHF Flow Regimes 11
   - 2.3. Partitioning of the Constitutive Relations for Wall-to-Fluid and Interfacial Heat Transfer 11
   - 2.4. Correlation Selection and Modification 12
   - 2.5. Wall Heat Transfer 12
     - 2.5.1. Primary Quench Front and Transition Boiling 12
     - 2.5.2. Secondary (Downstream) Quenches 15
     - 2.5.3. Hot Patches 15
     - 2.5.4. Modeling Constant Wall Temperatures 16
     - 2.5.5. Film Boiling 16
   - 2.6. Interfacial Heat Transfer 19
   - 2.7. Interfacial-Drag Coefficients 21
     - 2.7.1. Interfacial-Drag Model for Subcooled Nucleate Boiling, Saturated Nucleate Boiling, and Transition Boiling 22
     - 2.7.2. Smooth IAF Interfacial-Drag Model 23
     - 2.7.3. Rough/wavy IAF Interfacial-Drag Model 24
     - 2.7.4. Agitated IAF Interfacial-Drag Model 24
     - 2.7.5. Highly Dispersed Flow Interfacial-Drag Model 24
     - 2.7.6. Dispersed (Postagitated) Flow Interfacial-Drag Model 26
     - 2.7.7. Combinations of the Individual Drag Models for a Control Volume 26
   - 2.8. Grid Spacer Model 27
3. METHODOLOGY—OPTIMIZATION AND CLOSURE DEVELOPMENT 27
4. SOFTWARE AND COMPUTATION ORGANIZATION 27
   - 4.1. Closure Model Coding Structure 27
     - 4.1.1. Code Structure for the Wall Heat-Transfer Model 27
     - 4.1.2. Code Structure for the Interfacial Heat-Transfer and Drag Models 30
   - 4.2. Optimization Coding Structure 30
     - 4.2.1. Adding or Deleting the Tunable Factors 32
   - 4.3. Input Changes 34

CONTENTS (cont)

PAGE

5. RESULTS......34
- 5.1. Winfrith Database......35
  - 5.1.1. Up-Flow Experiments......35
    - 5.1.1.1. Absolute Pedigree......35
    - 5.1.1.2. Conditional Pedigree......36
  - 5.1.2. Down-Flow Experiments......37
    - 5.1.2.1. Absolute Pedigree......38
    - 5.1.2.2. Conditional Pedigree......38
- 5.2. INEL Database......38
  - 5.2.1. Absolute Pedigree......38
  - 5.2.2. Conditional Pedigree......39
- 5.3. Berkley Tube-Quenching Experiments......39
  - 5.3.1. Absolute Pedigree......40
  - 5.3.2. Conditional Pedigree......41
- 5.4. FLECHT-SEASET Run 31504......42
  - 5.4.1. Absolute Pedigree......42
  - 5.4.2. Conditional Pedigree......45

6. SUMMARY......46

7. CONCLUSIONS......49

REFERENCES......51

APPENDIX A AVERAGING AND THE LIMITATIONS IT GENERATES......71
- A.1. Local-Instantaneous Formulation......71
- A.2. Time Averaging......72
- A.3. Classes of Transient Problems......72
- A.4. Steady or Quasi-Steady Models......74
- A.5. Averagers and Limiters Arising From Small Timestep Sizes and Temporal-Averaging Considerations......75
  - A.5.1. Instantaneous Closure......75
  - A.5.2. Arithmetic-Averaging of Closure......75
  - A.5.3. Limiters of Closure Change......76
  - A.5.4. Transport Equations......76
- A.6. Considerations Associated with Large Timestep Sizes or Rapid Transients......77
- A.7. Spatial Averaging......77

CONTENTS (cont)

PAGE

APPENDIX B THE METHODOLOGY OF OPTIMIZATION AND CLOSURE DEVELOPMENT 78

B.1. The TRAC Problem....79
B.2. General Two-fluid Closure Optimization....79
REFERENCES 77

B.3 Optimization Techniques 81
B.4. Technical Issues Associated with Closure Optimization....83
B.5. Optimization Methodology....84
B.5.1. Original TRAC MOD2 Reflood Model....84
B.5.2. Original NRC SET and Code Development Philosophy....86
B.5.3. Closure Development Using Nonlinear Optimization....87
B.5.4. Generalized Penalty Function....87
REFERENCES 88

APPENDIX C OPTIMIZATION IMPLEMENTATION 89

C.1. Optimization Convergence Criteria....89
C.2. Optimization Algorithm....90
C.3. Interfacial Heat-Transfer Optimization....92
C.4. Interfacial-drag Optimization....92
C.5. Wall Heat-Transfer Optimization....93
REFERENCES 93

APPENDIX D RESULTS OF OPTIMIZATION STUDIES 94

D.1. Interfacial Drag. 94
D.2. Wall Heat Transfer....95
D.3. Interfacial Heat Transfer and Interfacial Drag. 95

APPENDIX E DESCRIPTION OF I/O FILES AND EXAMPLES....97

APPENDIX F TRACIN INPUT CHANGES....104

F.1. Changes to Standard TRAC Input....104
F.2. New TRAC Input....105

FIGURES

PAGE

Fig. 1. Sketch of possible classical flow regimes that may be experienced during reflood of a tube....107

Fig. 2. Sketch of possible flow regimes that may be experienced during reflood within a rod bundle (only two rods shown)....108

Fig. 3. Sketch of correlation and new closure development methodologies....109

Fig. 4. Sketch of possible flow regimes that may be experienced during reflood within a rod bundle experiencing bottom-up flow and multiple quenches (only two rods shown)....110

Fig. 5. Sketch of possible flow regimes that may be experienced during reflood within a rod bundle experiencing top-down flow and multiple quenches (only two rods shown)....111

Fig. 6. Typical axial wall heat flux profile for IAF. Axial distance is based on the relative coordinate system determined by liquid velocities at the bottom and top of the core....112

Fig. 7. Illustration of HTC selection logic. Axial distance is based on the relative coordinate system determined by liquid velocities at the bottom and top of the core....113

Fig. 8. The interfacial-drag coefficient model selection logic in the IAF regime-void fraction plane. Axial distance is based on the relative coordinate system determined by liquid velocities at the bottom and top of the core...114

Fig. 9. Bubble attached to wall in subcooled boiling....115

Fig. 10. Proposed scheme for the dispersed region in reactor geometry....115

Fig. 11. Basic coding structure of Subroutine HTSTR1....116

Fig. 12. Basic coding structure of Subroutine CORE1....117

Fig. 13. Basic coding structure of Subroutine CORE1N....118

Fig. 14. Basic coding structure of Subroutine ZLOOP....119

Fig. 15. Subroutine calling sequence diagram of wall heat transfer....120

Fig. 16. Subroutine calling sequence diagram of interfacial heat transfer....121

Fig. 17. Subroutine calling sequence diagram of 3D interfacial drag....121

Fig. 18. Structure diagram of the optimization, TRAC code and necessary files.....122

Fig. 19. Time-averaged wall heat flux calculated using the Absolute Pedigree coefficients vs Winfrith steady-state and quasi-steady-state post-CHF-up-flow data....123

Fig. 20. Time-averaged wall heat flux calculated using the Absolute Pedigree coefficients vs Winfrith steady-state and quasi-steady-state post-CHF-up-flow data — same as Fig. 19 with adjusted ordinate scale....124

Fig. 21. Time-averaged vapor void fraction calculated using the Absolute Pedigree coefficients vs Winfrith steady-state and quasi-steady-state post-CHF-up-flow data....125

FIGURES (cont)

PAGE
Fig. 21a. Time averaged vapor void fraction calculated using the Absolute Pedigree coefficients vs winfrith steady-state and quasi-steady-state post-CHF-up-flow data (modified range on axes) 126
Fig. 21b. Time averaged vapor void fraction calculated using the Absolute Pedigree coefficients vs winfrith steady-state and quasi-steadt state post-CHF-up-flow data (modified range on axes) 127
Fig. 22. Time-averaged vapor temperature calculated using the Absolute Pedigree coefficients vs Winfrith steady-state and quasi-steady-state post-CHF-up-flow data 128
Fig. 23. Time-averaged wall heat flux calculated using the Conditional Pedigree coefficients vs Winfrith steady-state and quasi-steady-state post-CHF-up-flow data. 129
Fig. 23a. Time-averaged wall heat flux calculated using the Conditional Pedigree coefficients vs Winfrith steady-state and quasi-steady-state post-CHF-up-flow data (modified vertical axis range) 130
Fig. 24. Time-averaged vapor void fraction calculated using the Conditional Pedigree coefficients vs Winfrith steady-state and quasi-steady-state post-CHF-up-flow data 131
Fig. 24a. Time-averaged vapor void fraction calculated using the Conditional Pedigree coefficients vs Winfrith steady-state and quasi-steady-state post-CHF-up-flow data (modified ranges on axes). ..132
Fig. 24b. Time-averaged vapor void fraction calculated using the Conditional Pedigree coefficients vs Winfrith steady-state and quasi-steady-state post-CHF-up-flow data (modified ranges on axes). ..133
Fig. 25. Time-averaged vapor temperature calculated using the Conditional Pedigree coefficients vs Winfrith steady-state and quasi-steady-state post-CHF-up-flow data 134
Fig. 26. Time-averaged wall heat flux calculated using the Absolute Pedigree coefficients vs Winfrith steady-state and quasi-steady-state post-CHF-down-flow data. 135
Fig. 27. Time-averaged vapor void fraction calculated using the Absolute Pedigree coefficients vs Winfrith steady-state and quasi-steady-state post-CHF down-flow data. 136
Fig. 28. Time-averaged vapor temperature calculated using the Absolute Pedigree coefficients vs Winfrith steady-state and quasi-steady-state post-CHF down-flow data. 137
Fig. 29. Time-averaged wall heat flux calculated using the Conditional Pedigree coefficients vs Winfrith steady-state and quasi-steady-state post-CHF down-flow data. 138
Fig. 30. Time-averaged vapor void fraction calculated using the Conditional Pedigree coefficients vs Winfrith steady-state and quasi-steady-state post-CHF-up-flow data. 139

Fig. 31. Time-averaged vapor temperature calculated using the Conditional Pedigree coefficients vs Winfrith steady-state and quasi-steady-state post-CHF-up-flow data. 140
Fig. 32. Time-averaged wall heat flux calculated using the Absolute Pedigree coefficients vs INEL steady-state and quasi-steady-state post-CHF-up-flow data....141
Fig. 33. Time-averaged wall heat flux calculated using the Absolute Pedigree coefficients vs INEL steady-state and quasi-steady-state post-CHF-up-flow data—same as Fig. 32 with adjusted ordinate scale. 142
Fig. 34. Time-averaged vapor temperature calculated using the Absolute Pedigree coefficients vs INEL steady-state and quasi-steady-state post-CHF-up-flow data. 143
Fig. 35. Time-averaged wall heat flux calculated using the Conditional Pedigree coefficients vs INEL steady-state and quasi-steady-state post-CHF-up-flow data. 144
Fig. 36. Time-averaged wall heat flux calculated using the Conditional Pedigree coefficients vs INEL steady-state and quasi-steady-state post-CHF-up-flow data—same as Fig. 35 with adjusted ordinate scale. 145
Fig. 37. Time-averaged vapor temperature calculated using the Conditional Pedigree coefficients vs INEL steady-state and quasi-steady-state post-CHF-up-flow data....146
Fig. 38. Time-dependent cladding temperature calculated using the Absolute Pedigree coefficients vs experimental data for Berkeley Run 166 147
Fig. 39. Time-dependent cladding temperature calculated using the Absolute Pedigree coefficients vs experimental data for Berkeley Run 167 147
Fig. 40. Time-dependent cladding temperature calculated using the Absolute Pedigree coefficients vs experimental data for Berkeley Run 186 148
Fig. 41. Time-dependent cladding temperature calculated using the Conditional Pedigree coefficients vs experimental data for Berkeley Run 166 148
Fig. 42. Time-dependent cladding temperature calculated using the Conditional Pedigree coefficients vs experimental data for Berkeley Run 167 149
Fig. 43. Time-dependent cladding temperature calculated using the Conditional Pedigree coefficients vs experimental data for Berkeley Run 186 149
Fig. 44. Cross-sestion diagram of the FLECHT-SEASET heater-rod bundle....150
Fig. 45. TRAC model of the FLECHT-SEASET facility....151
Fig. 45a. Initial axially dependent cladding temperature calculated using the Absolute Pedigree coefficients vs the FLECHT-SEASET Run 31504 experimental data 152

Fig. 46. Time-dependent cladding temperature at 0.305 m (12 in.) calculated using the Absolute Pedigree coefficients vs the FLECHT-SEASET Run 31504 experimental data 152
Fig. 47. Time-dependent cladding temperature at 0.991 m (39 in.) calculated using the Absolute Pedigree coefficients vs the FLECHT-SEASET Run 31504 experimental data 153
Fig. 48. Time-dependent cladding temperature at 9.981 m (78 in.) calculated using the Absolute Pedigree coefficients vs the FLECHT-SEASET Run 31504 experimental data 153
Fig. 49. Time-dependent cladding temperature at 2.819 m (111 in.) calculated using the Absolute Pedigree coefficients vs the FLECHT-SEASET Run 31504 experimental data 154
Fig. 50. Time-dependent cladding temperature at 3.048 m (120 in.) calculated using the Absolute Pedigree coefficients vs the FLECHT-SEASET Run 31504 experimental data 154
Fig. 51. Time-dependent cladding temperature at 3.353 m (132 in.) calculated using the Absolute Pedigree coefficients vs the FLECHT-SEASET Run 31504 experimental data 155
Fig. 52. Time-dependent cladding temperature at 3.505 m (138 in.) calculated using the Absolute Pedigree coefficients vs the FLECHT-SEASET Run 31504 experimental data 155
Fig. 53. Initial axially dependent vapor temperature calculated using the Absolute Pedigree coefficients vs the FLECHT-SEASET Run 31504 experimental data 156
Fig. 54. Time-dependent vapor temperature at 0.991 m (39 in.) calculated using the Absolute Pedigree coefficients vs the FLECHT-SEASET Run 31504 experimental data 156
Fig. 55. Time-dependent vapor temperature at 1.219 m (48 in.) calculated using the Absolute Pedigree coefficients vs the FLECHT-SEASET Run 31504 experimental data 157
Fig. 56. Time-dependent vapor temperature at 1.524 m (60 in.) calculated using the Absolute Pedigree coefficients vs the FLECHT-SEASET Run 31504 experimental data 157
Fig. 57. Time-dependent vapor temperature at 1.702 m (67 in.) calculated using the Absolute Pedigree coefficients vs the FLECHT-SEASET Run 31504 experimental data 158
Fig. 58. Time-dependent vapor temperature at 2.134 m (84 in.) calculated using the Absolute Pedigree coefficients vs the FLECHT-SEASET Run 31504 experimental data 158
Fig. 59. Time-dependent vapor temperature at 2.286 m (90 in.) calculated using the Absolute Pedigree coefficients vs the FLECHT-SEASET Run 31504 experimental data 159
Fig. 60. Time-dependent vapor temperature at 2.438 m (96 in.) calculated using the Absolute Pedigree coefficients vs the FLECHT-SEASET Run 31504 experimental data 159

Fig. 61. Time-dependent vapor temperature at 2.819 m (111 in.) calculated using the Absolute Pedigree coefficients vs the FLECHT-SEASET Run 31504 experimental data........160
Fig. 62. Time-dependent vapor temperature at 3.048 m (120 in.) calculated using the Absolute Pedigree coefficients vs the FLECHT-SEASET Run 31504 experimental data........160
Fig. 63. Time-dependent vapor temperature at 3.353 m (132 in.) calculated using the Absolute Pedigree coefficients vs the FLECHT-SEASET Run 31504 experimental data........161
Fig. 64. Time-dependent differential pressure from 0 to 0.3048 m (0 to 12 in.) calculated using the Absolute Pedigree coefficients vs the FLECHT-SEASET Run 31504 experimental data........161
Fig. 65. Time-dependent differential pressure from 0.3048 to 0.6096 m (12 to 24 in.) calculated using the Absolute Pedigree coefficients vs the FLECHT-SEASET Run 31504 experimental data........162
Fig. 66. Time-dependent differential pressure from 0.6096 to 0.9144 m (24 to 36 in.) calculated using the Absolute Pedigree coefficients vs the FLECHT-SEASET Run 31504 experimental data........162
Fig. 67. Time-dependent differential pressure from 0.9144 to 1.2192 m (36 to 48 in.) calculated using the Absolute Pedigree coefficients vs the FLECHT-SEASET Run 31504 experimental data........163
Fig. 68. Time-dependent differential pressure from 1.2192 to 1.524 m (48 to 60 in.) calculated using the Absolute Pedigree coefficients vs the FLECHT-SEASET Run 31504 experimental data........163
Fig. 69. Time-dependent differential pressure from 1.524 to 1.8288 m (60 to 72 in.) calculated using the Absolute Pedigree coefficients vs the FLECHT-SEASET Run 31504 experimental data........164
Fig. 70. Time-dependent differential pressure from 1.8288 to 2.1336 m (72 to 84 in.) calculated using the Absolute Pedigree coefficients vs the FLECHT-SEASET Run 31504 experimental data........164
Fig. 71. Time-dependent differential pressure from 2.1336 to 2.4384 m (84 to 96 in.) calculated using the Absolute Pedigree coefficients vs the FLECHT-SEASET Run 31504 experimental data........165
Fig. 72. Time-dependent differential pressure from 2.4384 to2.7432 m (96 to 108 in.) calculated using the Absolute Pedigree coefficients vs the FLECHT-SEASET Run 31504 experimental data........165
Fig. 73. Time-dependent differential pressure from 2.7432 to 3.048 m (108 to 120 in.) calculated using the Absolute Pedigree coefficients vs the FLECHT-SEASET Run 31504 experimental data........166
Fig. 74. Time-dependent differential pressure from 3.048 to 3.3528 m (120 to 132 in.) calculated using the Absolute Pedigree coefficients vs the FLECHT-SEASET Run 31504 experimental data........166
Fig. 75. Time-dependent differential pressure from 3.3528 to 3.6576 m (132 to 144 in.) calculated using the Absolute Pedigree coefficients vs the FLECHT-SEASET Run 31504 experimental data........167

Fig. 76. Time-dependent differential pressure from 0 to 3.3528 m (0 to 144 in.) calculated using the Absolute Pedigree coefficients vs the FLECHT-SEASET Run 31504 experimental data 167
Fig. 77. Initial axially dependent cladding temperature calculated using the Conditional Pedigree coefficients vs the FLECHT-SEASET Run 31504 experimental data 168
Fig. 78. Time-dependent cladding temperature at 0.305 m (12 in.) calculated using the Conditional Pedigree coefficients vs the FLECHT-SEASET Run 31504 experimental data 168
Fig. 79. Time-dependent cladding temperature at 0.991 m (39 in.) calculated using the Conditional Pedigree coefficients vs the FLECHT-SEASET Run 31504 experimental data 169
Fig. 80. Time-dependent cladding temperature at 1.981 m (78 in.) calculated using the Conditional Pedigree coefficients vs the FLECHT-SEASET Run 31504 experimental data 169
Fig. 81. Time-dependent cladding temperature at 2.819 m (111 in.) calculated using the Conditional Pedigree coefficients vs the FLECHT-SEASET Run 31504 experimental data 170
Fig. 82. Time-dependent cladding temperature at 3.048 m (120 in.) calculated using the Conditional Pedigree coefficients vs the FLECHT-SEASET Run 31504 experimental data 170
Fig. 83. Time-dependent cladding temperature at 3.353 m (132 in.) calculated using the Conditional Pedigree coefficients vs the FLECHT-SEASET Run 31504 experimental data 171
Fig. 84. Time-dependent cladding temperature at 3.505 m (138 in.) calculated using the Conditional Pedigree coefficients vs the FLECHT-SEASET Run 31504 experimental data 171
Fig. 85. Initial axially-dependent vapor temperature calculated using the Conditional Pedigree coefficients vs the FLECHT-SEASET Run 31504 experimental data 172
Fig. 86. Time-dependent vapor temperature at 0.991 m (39 in.) calculated using the Conditional Pedigree coefficients vs the FLECHT-SEASET Run 31504 experimental data 172
Fig. 87. Time-dependent vapor temperature at 1.219 m (48 in.) calculated using the Conditional Pedigree coefficients vs the FLECHT-SEASET Run 31504 experimental data 173
Fig. 88. Time-dependent vapor temperature at 1.524 m (60 in.) calculated using the Conditional Pedigree coefficients vs the FLECHT-SEASET Run 31504 experimental data 173
Fig. 89. Time-dependent vapor temperature at 1.702 m (67 in.) calculated using the Conditional Pedigree coefficients vs the FLECHT-SEASET Run 31504 experimental data 174
Fig. 90. Time-dependent vapor temperature at 2.134 m (84 in.) calculated using the Conditional Pedigree coefficients vs the FLECHT-SEASET Run 31504 experimental data 174

Fig. 91. Time-dependent vapor temperature at 2.286 m (90 in.) calculated using the Conditional Pedigree coefficients vs the FLECHT-SEASET Run 31504 experimental data 175
Fig. 92. Time-dependent vapor temperature at 2.438 m (96 in.) calculated using the Conditional Pedigree coefficients vs the FLECHT-SEASET Run 31504 experimental data 175
Fig. 93. Time-dependent vapor temperature at 2.819 m (111 in.) calculated using the Conditional Pedigree coefficients vs the FLECHT-SEASET Run 31504 experimental data 176
Fig. 94. Time-dependent vapor temperature at 3.048 m (120 in.) calculated using the Conditional Pedigree coefficients vs the FLECHT-SEASET Run 31504 experimental data 176
Fig. 95. Time-dependent vapor temperature at 3.353 m (132 in.) calculated using the Conditional Pedigree coefficients vs the FLECHT-SEASET Run 31504 experimental data 177
Fig. 96. Time-dependent differential pressure from 0 to 0.3048 m (0 to 12 in.) calculated using the Conditional Pedigree coefficients vs the FLECHT-SEASET Run 31504 experimental data 177
Fig. 97. Time-dependent differential pressure from 0.3048 to 0.6096 m (12 to 24 in.) calculated using the Conditional Pedigree coefficients vs the FLECHT-SEASET Run 31504 experimental data 178
Fig. 98. Time-dependent differential pressure from 0.6096 to 0.9144 (24 to 36 in.) calculated using the Conditional Pedigree coefficients vs the FLECHT-SEASET Run 31504 experimental data 178
Fig. 99. Time-dependent differential pressure from 0.9144 to 1.2192 m (36 to 48 in.) calculated using the Conditional Pedigree coefficients vs the FLECHT-SEASET Run 31504 experimental data 179
Fig. 100. Time-dependent differential pressure from 1.2192 to 1.524 m (48 to 60 in.) calculated using the Conditional Pedigree coefficients vs the FLECHT-SEASET Run 31504 experimental data 179
Fig. 101. Time-dependent differential pressure from 1.524 to 1.8288 m (60 to 72 in.) calculated using the Conditional Pedigree coefficients vs the FLECHT-SEASET Run 31504 experimental data 180
Fig. 102. Time-dependent differential pressure from 1.8288 to 2.1336 m (72 to 84 in.) calculated using the Conditional Pedigree coefficients vs the FLECHT-SEASET Run 31504 experimental data 180
Fig. 103. Time-dependent differential pressure from 2.1336 to 2.4384 m (84 to 96 in.) calculated using the Conditional Pedigree coefficients vs the FLECHT-SEASET Run 31504 experimental data 181
Fig. 104. Time-dependent differential pressure from 2.4384 to 2.7482 m (96 to 108 in.) calculated using the Conditional Pedigree coefficients vs the FLECHT-SEASET Run 31504 experimental data 181
Fig. 105. Time-dependent differential pressure from 2.7432 to 3.048 m (108 to 120 in.) calculated using the Conditional Pedigree coefficients vs the FLECHT-SEASET Run 31504 experimental data 182

Fig. 106. Time-dependent differential pressure from 3.048 to 3.3528 m (120 to 132 in.) calculated using the Conditional Pedigree coefficients vs the FLECHT-SEASET Run 31504 experimental data....182
Fig. 107. Time-dependent differential pressure from 3.3528 to 3.6576 m (132 to 144 in.) calculated using the Conditional Pedigree coefficients vs the FLECHT-SEASET Run 31504 experimental data....183
Fig. 108. Time-dependent differential pressure from 0 to 3.3528 m (0 to 144 in.) calculated using the Conditional Pedigree coefficients vs the FLECHT-SEASET Run 31504 experimental data....183
Fig. 109. The "Optimation Tree" showing various optimation techniques and their interrelationships....184
Fig. 110. The penalty function (PF) and coefficient **frw** (Section 4) are shown as functions of each iteration of TRAC using the post-CHF-up-flow data and TRAC input deck for Winfrith Experiment 405 and beginning with the Conditional Pedigree values....185
Fig. 111. The partial derivative (gradPF) of the penalty function (PF) with respect to the coefficient **frw** (Section 4) is shown as a function of each iteration of TRAC using the post-CHF-up-flow data and TRAC input deck for Winfrith Experiment 405 and beginning with the Conditional Pedigree values....186
Fig. 112. The penalty function (PF) and coefficient **fsm** (Section 4) are shown as functions of each iteration of TRAC using the post-CHF-up-flow data and TRAC input deck for Winfrith Experiment 405 and beginning with the Conditional Pedigree values....187
Fig. 113. The partial derivative (gradPF) of the penalty function (PF) with respect to the coefficient **fsm** (Section 4) is shown as a function of each iteration of TRAC using the post-CHF-up-flow data and TRAC input deck for Winfrith Experiment 405 and beginning with the Conditional Pedigree values....188
Fig. 114. The void fraction corresponding to the experimental measurement elevation(s) is shown as a function of each iteration of TRAC as the coefficients **frw** and **fsm** (Section 4) are tuned using the post-CHF-up-flow data and TRAC input deck for Winfrith Experiment 405 and beginning with the Conditional Pedigree values....189
Fig. 115. The penalty function (PF) and coefficient **fdham** (Section 4) are shown as functions of each iteration of TRAC using the post-CHF-up-flow data and TRAC input deck for Winfrith Experiment 405 and beginning with the Conditional Pedigree values....190

FIGURES (cont)

PAGE

Fig. 116. The partial derivative (gradPF) of the penalty function (PF) with respect to the coefficient **fdham** (Section 4) is shown as a function of each iteration of TRAC using the post-CHF-up-flow data and TRAC input deck for Winfrith Experiment 405 and beginning with the Conditional Pedigree values. 191

Fig. 117. The wall heat transfer corresponding to the experimental measurement elevation(s) is shown as a function of each iteration of TRAC as the coefficient **fdham** (Section 4) is tuned using the post-CHF-up-flow data and TRAC input deck for Winfrith Experiment 405 and beginning with the Conditional Pedigree values (plot 1 of 4). 192

Fig. 118. The wall heat transfer corresponding to the experimental measurement elevation(s) is shown as a function of each iteration of TRAC as the coefficient **fdham** (Section 4) is tuned using the post-CHF-up-flow data and TRAC input deck for Winfrith Experiment 405 and beginning with the Conditional Pedigree values (plot 2 of 4). 193

Fig. 119. The wall heat transfer corresponding to the experimental measurement elevation(s) is shown as a function of each iteration of TRAC as the coefficient **fdham** (Section 4) is tuned using the post-CHF-up-flow data and TRAC input deck for Winfrith Experiment 405 and beginning with the Conditional Pedigree values (plot 3 of 4). 194

Fig. 120. The wall heat transfer corresponding to the experimental measurement elevation(s) is shown as a function of each iteration of TRAC as the coefficient **fdham** (Section 4) is tuned using the post-CHF-up-flow data and TRAC input deck for Winfrith Experiment 405 and beginning with the Conditional Pedigree values (plot 4 of 4). 195

Fig. 121. The penalty function (PF) and coefficient **fwebb** (Section 4) are shown as functions of each iteration of TRAC using the post-CHF-up-flow data and TRAC input deck for Winfrith Experiment 405 and beginning with the Conditional Pedigree values. 196

Fig. 122. The partial derivative (gradPF) of the penalty function (PF) with respect to the coefficient **fwebb** (Section 4) is shown as a function of each iteration of TRAC using the post-CHF-up-flow data and TRAC input deck for Winfrith Experiment 405 and beginning with the Conditional Pedigree values. 197

FIGURES (cont)

PAGE

Fig. 123. The wall heat transfer corresponding to the experimental measurement elevation(s) is shown as a function of each iteration of TRAC as the coefficient **fwebb** (Section 4) is tuned using the post-CHF-up-flow data and TRAC input deck for Winfrith Experiment 405 and beginning with the Conditional Pedigree values (plot 1 of 4)....198

Fig. 124. The wall heat transfer corresponding to the experimental measurement elevation(s) is shown as a function of each iteration of TRAC as the coefficient **fwebb** (Section 4) is tuned using the post-CHF-up-flow data and TRAC input deck for Winfrith Experiment 405 and beginning with the Conditional Pedigree values (plot 2 of 4)....199

Fig. 125. The wall heat transfer corresponding to the experimental measurement elevation(s) is shown as a function of each iteration of TRAC as the coefficient **fwebb** (Section 4) is tuned using the post-CHF-up-flow data and TRAC input deck for Winfrith Experiment 405 and beginning with the Conditional Pedigree values (plot 3 of 4)....200

Fig. 126. The wall heat transfer corresponding to the experimental measurement elevation(s) is shown as a function of each iteration of TRAC as the coefficient **fwebb** (Section 4) is tuned using the post-CHF-up-flow data and TRAC input deck for Winfrith Experiment 405 and beginning with the Conditional Pedigree values (plot 4 of 4)....201

Fig. 127. The penalty function (PF) and coefficient **fgam2** (Section 4) are shown as functions of each iteration of TRAC using the post-CHF-up-flow data and TRAC input deck for Winfrith Experiment 448 and beginning with the Conditional Pedigree values....202

Fig. 128. The partial derivative (gradPF) of the penalty function (PF) with respect to the coefficient **fgam2** (Section 4) is shown as a function of each iteration of TRAC using the post-CHF-up-flow data and TRAC input deck for Winfrith Experiment 448 and beginning with the Conditional Pedigree values....203

Fig. 129. The penalty function (PF) and coefficient **ffd** (Section 4) are shown as functions of each iteration of TRAC using the post-CHF-up-flow data and TRAC input deck for Winfrith Experiment 448 and beginning with the Conditional Pedigree values....204

Fig. 130. The partial derivative (gradPF) of the penalty function (PF) with respect to the coefficient **ffd** (Section 4) is shown as a function of each iteration of TRAC using the post-CHF-up-flow data and TRAC input deck for Winfrith Experiment 448 and beginning with the Conditional Pedigree values....205

FIGURES (cont)

PAGE

Fig. 131. The vapor temperature corresponding to the experimental measurement elevation(s) is shown as a function of each iteration of TRAC as the coefficients **fgam2** and **ffd** (Section 4) are tuned using the post-CHF-up-flow data and TRAC input deck for Winfrith Experiment 448 and beginning with the Conditional Pedigree values. 206

Fig. 132. The void fraction corresponding to the experimental measurement elevation(s) is shown as a function of each iteration of TRAC as the coefficients **fgam2** and **ffd** (Section 4) are tuned using the post-CHF-up-flow data and TRAC input deck for Winfrith Experiment 448 and beginning with the Conditional Pedigree values. 207

TABLES

PAGE

TABLE 1: POST-CHF FLOW-REGIME TRANSITION CRITERIA 55

TABLE 2: COEFFICIENT B AS A FUNCTION OF REYNOLDS NUMBER AND VOID FRACTION 56

TABLE 3: WALL-TO-FLUID HEAT-TRANSFER CORRELATIONS IN FILM BOILING 57

TABLE 4: INTERFACIAL-DRAG MODELS 58

TABLE 5: INTERFACIAL HEAT TRANSFER TUNABLE PARAMETER DESCRIPTIONS 60

TABLE 6: INTERFACIAL DRAG TUNABLE PARAMETER DESCRIPTIONS 61

TABLE 7: WALL HEAT TRANSFER TUNABLE PARAMETER DESCRIPTIONS..62

TABLE 8: NEW REFLOOD WALL HEAT TRANSFER SUBROUTINES AND THEIR FUNCTION 63

TABLE 9. FILES CONTAINING SUBROUTINES AND NAMED COMMON BLOCKS USED IN THE OPTIMIZATION PROCESS 64

TABLE 10: FUNCTION OF THE INPUT/OUTPUT FILES IN OPTIMIZATION......65

TABLE 11: SUMMARY OF WINFRITH POST-CHF UP-FLOW EXPERIMENTS USED WITH TRAC 66

TABLE 12: SUMMARY OF WINFRITH POST-CHF DOWN-FLOW EXPERIMENTS USED WITH TRAC 67

TABLE 13: LEGEND KEY TO VOID FRACTION FLOW REGIME PREDICTIONS.....68

TABLE 14: SUMMARY OF INEL POST-CHF UP-FLOW EXPERIMENTS USED WITH TRAC 69

TABLE 15: SUMMARY OF BERKELEY REFLOOD EXPERIMENTS USED WITH TRAC 70

NOMENCLATURE

A	surface area
A_f	flow area
B	transition boiling exponent coefficient (units of 1/m)
Ca	Capillary number
C_i	interfacial-drag coefficient
d	bubble or droplet diameter
D	diameter
f	friction factor
f_l	wall area fraction in contact with liquid (dimensionless)
F_s	sink function used in Webb-Chen correlation
F_u	fraction of unheated surface area in the core
g	gravitational acceleration
G	mass flux
h	heat-transfer coefficient
h'	phasic wall-to-fluid heat-transfer coefficient
h_{fg}	latent heat of evaporation
h'_{fg}	modified latent heat of evaporation
k	thermal conductivity
m	viscosity
P	pressure
Pe	perimeter
Pr	Prandtl number,
q	heat flux
q'	phasic heat flux
Re	Reynolds number
t	time
T	temperature
V	velocity

NOMENCLATURE (cont)

Vol	cell volume
W	weighting factor
X	quality
Y_b	bubble height
Z	axial elevation
α	void fraction
α_l	thermal diffusivity
Γ	vapor generation rate
δ	film thickness
$\Delta\rho = \rho_l - \rho_v$	density difference
ε	roughness
ε_r	emissivity
λ	Taylor wavelength
ρ	density
σ	surface tension
σ_r	Stefan-Boltzmann constant
τ	shear stress

Subscripts

ac	actual
ag	agitated
b	bubble
Brom	Bromley correlation
CHF	critical heat flux
c	core
cr	critical

NOMENCLATURE (cont)

dd	single droplet
d	droplets
Den	Denham correlation
df	highly dispersed flow
fr	free stream
fls	flashing
fo	single phase
lf	liquid film
film	film boiling
g	gas
gap	gap between wall and liquid core
hom	homogeneous
h	hydraulic
i,inv	interfacial, inverted annular flow
i,lf	interfacial, liquid film
i,d	interfacial, droplet
i,df	interfacial, highly dispersed flow
i,sb	interfacial, subcooled boiling
i,fr	interfacial, free stream
i,sm	interfacial, smooth IAF
i,rw	interfacial, rough/wavy IAF
i,dd	interfacial, droplets
i,pa	interfacial, postagitated IAF
i,cell	interfacial, finite-difference cell
inv	inverted annular flow
il	interface-to-liquid
ig	interface-to-gas
lc	liquid core
l	liquid

NOMENCLATURE (cont)

min	minimum film boiling
nuc	nucleate boiling
pa	postagitated
r	relative
ra	radiation
rw	rough/wavy IAF
sat	saturation
sv	saturation temperature of vapor
sb	subcooled boiling
sm	smooth IAF
slab	heat structure
total	total
top	top of the finite-difference cell
tb	transition boiling
teo	theoretical
u	unheated
v	vapor
w	wall
wg	wall-to-gas
wl	wall-to-liquid
wi	wall-to-vapor/liquid interface
W-C	Webb-Chen Correlation

REFLOOD COMPLETION REPORT

VOLUME I

A PHENOMENOLOGICAL THERMAL-HYDRAULIC MODEL OF HOT ROD BUNDLES EXPERIENCING SIMULTANEOUS BOTTOM AND TOP QUENCHING AND AN OPTIMIZATION METHODOLOGY FOR CLOSURE DEVELOPMENT

by

Ralph A. Nelson Jr., David A. Pimentel, Susan Jolly-Woodruff, and Jay Spore

ABSTRACT

In this report, a phenomenological model of simultaneous bottom-up and top-down quenching is developed and discussed. The model was implemented in the TRAC-PF1/MOD2 computer code. Two sets of closure relationships were compared within the study, the Absolute set and the Conditional set. The Absolute set of correlations is frequently viewed as the "pure" set because the correlations utilize their original coefficients as suggested by the developer. The Conditional set is a modified set of correlations with changes to the correlation coefficient only. Results for these two sets indicate quite similar results.

This report also summarizes initial results of an effort to investigate nonlinear optimization techniques applied to the closure model development. Results suggest that such techniques can provide advantages for future model development work, but that extensive expertise is required to utilize such techniques (i.e., the model developer must fully understand both the physics of the process being represented and the computational techniques being employed). The computer may then be used to improve the correlation of computational results with experiments.

1. INTRODUCTION

Boiling systems normally operate in the nucleate boiling regime. However, as the heat flux from the heated wall increases or the cooling capability of the fluid decreases, a point is reached where the heated wall can no longer sustain liquid contact. Such a situation is called the Critical Heat Flux (CHF), burnout, or the dryout condition. Prediction of the wall heat transfer beyond the CHF condition (post-CHF) is an important aspect of nuclear reactor safety and the safety of other boiling systems, such as cryogenic systems, metallurgical processing, and steam generators. In these post-CHF regimes, the two-phase fluid may exist in a nonequilibrium state, both mechanical and thermal. Ishii and his coworkers[1-3] observed mechanical nonequilibrium between the phases: Nijhawan et al.,[4] Evans et al.,[5] and Gottula et al.[6] for single tubes; and Unal et al.[7] and Loftus et al.[8] for rod-bundles confirmed thermodynamic nonequilibrium. These citations of nonequilibrium are not comprehensive.

The classical perspective of boiling beyond the CHF location views the flow pattern as two different flow configurations depending upon the flow quality and mass flux at the CHF point (Fig. 1). Ishii and his coworkers[1-3] reported a detailed study of the inverted annular flow (IAF) regime. Figure 1a shows the classical sketch of the IAF regime in a tube. If CHF occurs at very low or negative (subcooled liquid) flow qualities, the flow pattern can be expected to be an inverted annular flow. In inverted-annular flow, an annular vapor film surrounds a liquid core. Further downstream, the liquid core may break up into an agitated region of slugs or large droplets, and may later be followed by a small-droplet dispersed flow or postagitated region. At high qualities, the flow pattern may be thought of as dryout of a liquid film from the wall, which creates a small droplet-dispersed flow regime downstream of the dryout location (Fig. 1b). Within these sketches, spatial lengths for the various regimes are implied; the lengths shown are arbitrary and do not represent the relative lengths of the regimes.

For a nuclear reactor, the flow regimes within the rod bundles are pictured using sketches similar to those shown in Fig. 1. The channels within the bundle may have various configurations depending on whether the rod configuration is square and triangular. Figure 2 includes sketches that replace the tube wall with a side view of two rods. This difference in perspective (compared with Fig. 1) is important because it allows flow between the channels, i.e., multidimensional effects. Figure 2 includes 3 sketches, Fig. 2a represents the inverted-annular regime, Fig. 2b the slug-churn regime, and Fig. 2c the annular regime. Once subcooling is eliminated, the slug-churn regime replaces the inverted-annular regime. Liquid subcooling during typical reflooding is of short duration, whereas during the blowdown period the liquid is most likely saturated as the system pressure drops below ~7 MPa for pressurized water reactors (PWRs).

In the last three decades, a significant number of experimental and analytical studies have been published that report on post-CHF boiling in the flow regimes depicted in Fig. 2. Chen[9] summarized the latest information in the study of convective post-CHF heat transfer. He classified the studies into two major groups: local and history-dependent models. Unal et al.[10] assessed some of the recommended local and history-dependent models against rod-bundle data obtained at Lehigh University and showed that a large amount of scatter exists between the predictions from published correlations and measured data. Yadigaroglu et al.[11] summarized the state-of-the-art in modeling reflood, or quenching of the core from a post-CHF condition.

When published correlations are used in computer codes such as TRAC[12] and RELAP,[13] the disagreement between data and predictions frequently becomes profound because the codes are transient codes, whereas most of the available models and correlations were developed from steady-state experiments. Another reason for the disagreement is that the majority of the models were developed from data where information regarding companion phenomena was missing. For example, heat-transfer correlations are developed without information on the hydraulic aspects of the experiments, e.g., phasic velocities. Similarly, hydraulic correlations are frequently derived from adiabatic experiments. Therefore, the majority of these models, both heat-transfer and hydrodynamic, report correlations and data that cannot be separated into the phasic components. The data obtained by Unal et al.[7] and Evans et al.[5] are examples of this situation. These data include only the heat-transfer information, wall and vapor temperatures, and heat flux, whereas information on void fraction and phasic velocities is not available. Naturally, most of the heat-transfer models developed from such databases used the homogeneous flow assumption. Other researchers put emphasis on the measurement of hydrodynamic parameters, such as velocity and void fraction, and performed their tests on adiabatic test rigs. Models developed from this kind of data must use other models for heat transfer or assume no influence because of their omission from the experimental results.

Thermal-hydraulic computer codes such as TRAC solve the mass, momentum, and energy equations for each phase. They require constitutive relations to determine mass, momentum, and heat-transfer interchange between the phases and between either heated or unheated structures and the phases. Because phasic constitutive relations are generally not available except under certain special conditions, code developers are forced to infer these phasic relationships based on limited information available from the data they are analyzing. Modifying existing models and combining these models to represent the different phasic phenomena for the required contributions is the standard approach.

To develop more accurate models, information on heat transfer must be used with the best available hydrodynamic data. If such a model is used in the large computer codes, the prediction of post-CHF heat transfer can be improved. In this report, a previously developed post-CHF model[14-16] for large-scale computer codes is extended to model both bottom-up and top-down quenching as might occur for the AP600 advanced PWR. The formulation of the thermal-hydraulic heat-transfer model is explained in the next section entitled "Description of the thermal-hydraulic model."

1.1. Development of Complex Closure Models in Two-fluid Thermal-Hydraulic Codes

Simulation involving nonequilibrium two-phase flow can involve the interaction of a significant number of relationships (closure correlations). This is particularly true of reflood modeling. As discussed by Nelson and Unal[14] and noted above, these correlations are most often developed independent of one another based upon simple assumptions regarding the "other's" behavior. For that reason, this work undertook an investigation of a new approach, i.e., the use of optimization to refine the development of the closure relationships by allowing the relationships to be considered within the same framework (the TRAC code). This method allows the reengineering of the original correlations within a framework allowing their interactions.

The correlation-development methodology for various closure models is an established practice (Fig. 3a). Such correlation development usually takes one of two forms: (1) development of statistical correlations based upon parameters or variables that are known to influence the process, or (2) development of phenomenological correlations based upon some physical process model (occasionally called "first-principle" models), where unknown coefficients or exponents within the physical model are adjusted using the data. Either of these approaches can be used to define the function, f, in Fig. 3a where some optimization process is used to refine the function to minimize the difference between data and the prediction from the function.

The work by Nelson and Unal[14] made an effort to integrate the process of correlation refinement further by taking into account the interactions between the correlations, (e.g., the interfacial drag affects the void fraction, that affects the interfacial heat transfer, that in turn affects the wall heat transfer). Unfortunately, Nelson and Unal's approach used rudimentary methods of running short windows of selected experiments and adjusting the correlation packages by hand.

Figure 3b represents the methodology undertaken in the current work. It is conceptually the same methodology used by Nelson and Unal[14] and is quite similar to that used in correlation development. However, this methodology replaces the function, f, with TRAC itself. The refinement work by Nelson and Unal is automated using the computer.

Within the context of model development for a system code, it is possible to define several variations of the correlation packages that are of interest. One variation is termed the Absolute case and represents the correlations in the original form that the correlation developer suggested. The second is termed the Conditional case and is the modified set of correlations as determined by Nelson and Unal.[14] And finally, we can define a set that is being optimized that will be termed the Optimized case.

The Absolute set of correlations is frequently viewed as the "pure" set. The exponents and coefficients of each correlation are those determined by the original developer. As noted earlier, these variables were often determined using simple models for other phenomena that the correlator neither represented nor measured. For example, the Webb-Chen correlation, used for vapor film boiling heat transfer in this study, was developed using the no-slip condition between the vapor and liquid drops when it is known that this regime can and does experience significant slip. Also, another issue associated with the purity of the Absolute case is that frequently numerous splines are required to bridge from one regime (correlation) to another. In some situations, these splines span a significant portion of the physical parameter space and thus either dominate or significantly affect the values produced by the pure correlation set.

The Conditional set developed by Nelson and Unal,[14] argued that at least the coefficients of the correlation package sets could be reengineered within the framework of the code to better represent the physics by allowing for the interactions of various closure packages. The Conditional set accepted the functional form of the original correlation and did not change the exponents. Within the work done here, the coefficients reengineered by Nelson and Unal are used for this set.

The Optimized case uses optimization to reengineer the coefficient set within the framework of the same closure packages. Of course, this is very similar to the same process suggested by Nelson and Unal;[14] however, the computer is used instead to reengineer the coefficients.

Whereas it is not investigated here, it should be realized that once the coefficients are reengineered, the exponents as adjusted by the correlator could, and maybe should, be reengineered also. If the exponents were originally uncertain within the theory that produced them, they remain uncertain and should be part of the process when the simple assumptions are eliminated. For some correlations, their functional form might also require rederivation as the simple assumptions are replaced with enhanced representation.

1.2. Conceptualization of Unidirectional Flow Bottom-up Quenching

When reflood or blowdown quenches occur in experiments simulating the possible behavior of reactor systems, the nonuniform axial power distribution frequently produces multiple quench fronts. Figure 4 represents a sketch of this behavior with quenches shown at both the bottom and top of the rods and where flow within the core is assumed to be from the bottom and exiting the top, i.e., unidirectional. We will characterize this condition using the liquid velocities at the core's bottom and top such that

$$v_{l,\,\mathrm{bottom}} > 0,$$

and

$$v_{l,\,\mathrm{top}} > 0.$$

The flow regimes at the core bottom will be one of those shown in Fig. 2 plus typically an annular regime at the top. Figure 4a shows the case of inverted-annular and annular quenches. Figure 4b represents the case of slug-churn and annular quenches, and Fig. 4c shows the case of annular quenches at both the bottom and top.

Conceptually, it is possible for the annular regime at the top to be replaced by a liquid-dominated regime. This configuration would be possible if either very high liquid flow rates push a significant amount of liquid "through" the core, or two quench fronts are physically very near allowing the bottom inverted-annular or slug regimes to bridge to the upper quench front. The model discussed within this report encompasses those cases because of its ability to determine the lower and upper quench-front locations, the ability to differentiate between the two, and the coupling that results because the closure relationships use the same flow map. This combination results in the correct selection of a bubbly nucleate boiling case above the upper quench front for these particular cases.

The implication thus far is that steady flow is typical. This flow behavior is called forced flow or forced reflood. Numerous experiments have been performed where this inlet assumption is true. However, the geometry of a reactor with a typical downcomer does allow oscillating flows between the core and downcomer to occur. Numerous prototypical experiments have been performed also that allow this behavior. Such experiments are often characterized as gravity reflood. All three cases shown in Fig. 4 would be realized early in the reflooding process. One could envision the reflooding process being captured within a series of strobe-flash pictures as a sequence of the following figures: 4b, 4a, 4b, 4c, 4b, 4a, 4b, etc. A higher strobe rate requires the reader to envision a more continuous transition from one frame to the next.

The modeling to be undertaken in this study will represent the various phenomena that can occur in these various flow regimes and the dynamic behavior they may exhibit. Representation of this dynamic behavior requires that the process be quasi-steady state. This requirement is common to all transients represented by codes such as TRAC and RELAP and is not particular to reflood or the model. Whereas this assumption is commonly understood by most, Appendix A includes a more detailed discussion of this assumption and its implications as they may apply to reflood.

1.3. Conceptualization of Unidirectional Flow Top-down Quenching

In the case of flow into the top of the core and exiting the bottom, we restrict the liquid velocities such that

$$v_{l,\,top} < 0,$$

and

$$v_{l,\,bottom} < 0.$$

One might conceptually envision just inverting the Fig. 4 sketches. However, the physics are different in that gravity is aiding the movement of the liquid down the core as opposed to impeding it in the bottom upflow case. Thus, this gravity assist will affect the regime for the case when low void liquid enters the top at slow speeds (i.e., it will naturally fall through the core). Figure 5 represents the behavior at both the bottom and top of the rods when flow is assumed to be entering the core from the top and exiting the bottom. Figure 5a shows the case of an "inverted-annular-like" regime at the top and an annular quench at the bottom. As the liquid velocity increases for the low void case, forced flow conditions will exist in the limit, and gravity effects can be ignored. Figure 5b shows the case of annular quenches at both the bottom and top, which may result when high void liquid enters the top.

These cases imply that the lower plenum has not filled. If this were not the case, a pooling of the liquid would occur in the bottom of the core that would replace the annular flow region in the Fig. 5 sketches.

The modeling to be undertaken for the top-down quenching case will represent the various phenomena that can occur in the various flow regimes and the dynamic behavior they may exhibit.

1.4. Conceptualization of Bidirectional Flow Quenching

The preceding two cases are simple flow configurations that can occur as part of a blowdown or reflood situation. However, there are at least two additional cases that are of importance to this model. One is the case of liquid entering both the top and bottom of the core denoted as

$$v_{l,\,top} < 0,$$

and

$$v_{l,\,bottom} > 0.$$

The other is the case of liquid exiting both the top and bottom of the core as denoted by

$$v_{l,\,top} > 0,$$

and

$$v_{l,\,bottom} < 0.$$

These cases occur as part of the transient behavior that can occur in various scenarios.

It is believed that such configurations are generally short lived, typically ending in one of the simple configurations noted above. Thus, position-dependent information downstream of the CHF point (to be discussed later) retains the last "simple" configuration results until a new simple flow configuration reestablishes itself. The use of this "old" information does not prevent the CHF location from moving; whereas, it was unclear initially if this representation would perform well. Initial results indicate that it is adequate.

2. DESCRIPTION OF THE THERMAL-HYDRAULIC MODEL

The model discussed below has been developed for the TRAC-PF1/MOD2 computer code to model the thermal hydraulics in a reactor core undergoing simultaneous bottom-up and top-down quenching. The TRAC program is a best-estimate computer program for analyzing light-water reactor (LWR) accidents. The TRAC series of codes formulate the fluid dynamics using the six-equation, two-fluid, nonequilibrium model with a staggered-difference scheme. The mass, momentum, and energy equations are available in three-dimensional form in the vessel component and in one-dimensional form in other available components. A detailed description of the capabilities of the code and the numerical solution method are available in Ref. 17.

The field equations used in the TRAC-PF1/MOD2 code require closure relationships to represent the wall heat transfer (wall-to-liquid and wall-to-vapor), the interfacial heat transfer, the wall shear (wall-to-liquid and wall-to-vapor), interfacial drag or shear, the net vaporization rate, and state equations. The TRAC-PF1/MOD2 code, as well as other TRAC series codes, invokes a quasi-steady approach to the closure relations for interfacial heat transfer, interfacial drag, and wall-to-fluid drag. This quasi-steady approach assumes detailed knowledge of the local fluid parameters and ignores time dependencies of the closure quantities themselves. This implies the time rate of change in the closure relationships become infinite (the time constants are zero). (See Appendix A for additional information related to the quasi-steady assumption.) The quasi-steady approach has the advantages of being reasonably simple and applicable to a wide range of problems.

2.1. Bottom-Up and Top-Down Reflood Modeling

The original version of the TRAC-PF1/MOD2 reflood model (Nelson and Unal,[14] Unal and Nelson,[15] and Unal et al.,[16]) was developed to represent bottom-up reflood behavior. The model developed for the AP600 and discussed here is built around that earlier model but has been generalized to address simultaneous or separate bottom-up and top-down quenching dominated by convective considerations. Changes were needed because of the position-dependent nature of the post-CHF portion of the earlier model. These changes allowed the switch from an absolute coordinate system located at the bottom quench front and positive in the vertical direction to a relative coordinate system located at a quench front with the positive direction either up or down depending on the flow through the core (see Sections 1.2 and 1.3). Changes were required also to provide (1) the ability to track the positions of both quench fronts (bottom and top), (2) decision-making logic to determine the direction of quench, and (3) the ability to model the physics of the two quenches differently if needed.

It is well recognized that the physical behavior related to bottom-up and top-down reflood behavior may or may not be different. At low flooding rates, gravity effects dominate either flooding direction. While at very high flooding rates, the results are independent of direction because of the dominance of liquid momentum. Thus, one would expect some revisions would be needed at the lower flooding rates. For this reason, data storage was developed that retained information associated with the two quench fronts. These data included different correlation coefficients or flow regime information, should their revision be needed.

The change in the coordinate system from an absolute to a relative one is a simple conceptual adjustment to make, but it required a rather significant change to the original coding itself. Early in the project it was determined that at least two software approaches were possible.

1. Because the original coding was written based on a logical computational flow from the bottom to the top, one could add if-then-else tests to check for the quench direction and then "invert the calculations being made."

2. Rewrite the coding to reflect the calculations in a relative sense so that the quench direction was determined at a higher logical level and the model computations were therefore modular. Quench direction might then be reflected by the flow regime map or the correlation coefficient.

After some initial investigation employing the first approach, it was determined that the approach would approximately double the coding needing to represent the AP600 model. It was found also that the coding was very difficult to understand with this if-then-else structure and that debugging of test problems was extremely difficult. This latter issue becomes extremely important when debugging model refinements during the developmental assessment. For these reasons, the second approach was undertaken.

The model to determine quench direction was developed using a heuristic approach. The data structure developed for the AP600 model retains the information associated with two quench fronts. This retention allows proper calculation of the model hydrodynamics and heat transfer using the proper definition of pre-CHF or post-CHF flow independent of the flow direction. The direction of the marching solution from the bottom or top of the heat structure is determined from the core inlet and outlet liquid velocities. If they are both in the same direction, the quench front is assumed to propagate downstream in the flow direction. If the two flows do not agree in direction, the last direction used is retained. For the cases studied to date, this contradiction in flow direction has occurred only over short periods of time before deciding in one direction or the other. Thus, the choice of direction when contradictions occur is not critical to the outcome of the prediction.

2.2. Post-CHF Flow Regimes

The flow regimes downstream of a quench front can be determined from the map suggested by Ishii and DeJarlais,[1,2] and Obot and Ishii.[3] Ishii and DeJarlais[1,2] performed visualization experiments of IAF in the central channel of a heated double-quartz tube. The flow direction of these experiments was bottom-up. A summary of their qualitative results is depicted in Fig. 1a. The inverted annular region was initiated using concentric injection nozzles with liquid injected from an inner nozzle surrounded by a vapor annulus. Both motion and still pictures were taken to identify the flow-regime characteristics. In the region directly downstream of the nozzles, a smooth liquid core was observed. This was followed by wave development on the liquid-core's surface. The wavelengths were on the order of 10 mm, with droplets being sheared from the wave crests. Also observed (although not shown in the figure) was a thin, highly agitated annular sheet of liquid near the heated wall. Above this region, an agitated slug/churn region was observed. Droplets (<3-mm diam) swept past the slugs. The slugs were deformed into multiple ligaments and were eventually broken up. In the dispersed region, the droplets evaporated and unsuperheated the steam. Several droplet sizes were observed from the agitated liquid annulus (0.05 mm), from the wave crests (0.2 mm), and from the slug breakup (0.6 to 3 mm).

Obot and Ishii[3] extended the work of Ishii and DeJarlais[1,2] and developed the flow-regime transition criteria. The final results were developed in terms of the capillary number and the length above the quench front (indicated in Fig. 1 and listed in). The relatively large droplets observed downstream of the agitated region become smaller as the void fraction increases further downstream. We have further refined the dispersed flow to consist of two regions. First, a dispersed-flow regime with large droplets, and second, a highly dispersed flow regime with fine droplets. The highly dispersed flow regime was assumed to occur when the cell void fraction was >98%. Additional constraints based on the void fraction were also introduced to force the IAF regimes to occur within certain void fraction ranges (see Table 1). This was required because transient calculations realize situations not present in the steady-state experiments used in Ishii's model development. For example, the early part of a prediction with liquid flowing into an empty tube may, based upon the capillary number for the liquid velocity alone, indicate flow-regime lengths downstream at locations where the liquid has not yet had time to move.

Table 1 shows Ishii's original post-CHF flow-regime correlations and the modifications made for application to the TRAC model. The application in TRAC adds a void-fraction criteria to Ishii's original model.

Because of the change to a relative position coordinate system dependent upon the flow configuration (discussed in the Introduction), the capillary number was determined based on the absolute value (computational safety) of the liquid velocity at the "inlet" CHF location. For those cases where bidirectional flow into or out of the core were occurring, the CHF position was allowed to move based on local CHF calculations, and the relative position of the remaining downstream post-CHF positions was retained.

2.3. Partitioning of the Constitutive Relations for Wall-to-Fluid and Interfacial Heat Transfer

The TRAC code partitions the total energy transferred from the wall to a nonequilibrium (both mechanical and thermal) two-phase mixture into the components going into the respective phases. This division is required by the two-fluid model to determine the sensible heat present in each phase. The solution of the conduction problem associated with each structure present in the fluid, however, uses the total energy transferred to the phases. Thus, the total wall heat flux consists of the two phasic components (wall-to-vapor and wall-to-liquid) and is given by

$$q_{total} = q'_{wl} + q'_{wg} = f_l h'_{wl}\left(T_w - T_l\right) + \left(1 - f_l\right) h'_{wg}\left(T_w - T_g\right), \tag{1}$$

where h'_{wl} and h'_{wg} are the separate phasic heat-transfer coefficients (HTCs) not yet defined by experiments. The measurement and modeling of the liquid/solid contact fraction of the total area, f_l, are very limited for forced convection. Therefore, the effect of the phasic wall/liquid contact area is assumed to be included within both phasic models and the weighting factors used to combine the separate correlations.

The interfacial heat-transfer rate is calculated by combining the volume-averaged liquid-side and vapor-side heat-transfer rates. The interface is always assumed to be at the saturation temperature corresponding to the partial steam pressure. The rate of mass transfer between phases is determined from a simple thermal-energy jump relationship given by

$$\Gamma = -\frac{\left(q_{il} + q_{ig}\right)}{h_{fg}\,\mathrm{Vol}} = -\frac{\left[h_{il}A_{il}\left(T_{sv} - T_l\right) + h_{ig}A_{ig}\left(T_{sv} - T_g\right)\right]}{h_{fg}\,\mathrm{Vol}}. \tag{2}$$

2.4. Correlation Selection and Modification

As in Nelson and Unal,[14] correlations known to apply to a given regime for a particular closure quantity were used wherever possible. Frequently, however, the original correlation could not be applied directly but required modification. For those cases, we tried to use the "kernel" or "functional" dependence of the original correlation and modify only its magnitude by use of a multiplier. When no correlations were available for given regimes, we tried to define known bounding regimes and to use a weighting function between the known regimes.

2.5. Wall Heat Transfer

The wall-to-fluid HTCs in the nucleate boiling region are calculated using the Chen correlation, as discussed in Spore et al.[17] While interfacial heat transfer and drag for nucleate boiling will be discussed in greater detail, nucleate boiling wall heat transfer will not be discussed in detail because of its straightforward nature. The following subsections describe the HTC correlations used in the wall-to-fluid heat-transfer model in the post-CHF region.

2.5.1. Primary Quench Front and Transition Boiling

The primary quench front is defined to be the one located nearest the core inlet based on the relative coordinate system. The core inlet may be either the bottom or top, depending upon the flow direction as discussed earlier.

The transition-boiling regime spans the boiling surface between CHF and minimum film boiling. In earlier TRAC codes (TRAC-PF1/MOD1[12]), transition boiling was thought to be a combination of both nucleate boiling (wet-wall) and film boiling (dry-wall) heat transfer. A weighting factor representing the fraction of wet vs dry surface that was dependent upon wall temperature was applied to both the CHF and minimum film boiling heat flux. Transition boiling was assumed to occur if the wall temperature was between T_{chf} and T_{min} where T_{min} was determined from a correlation.

This earlier modeling approach does not depend upon axial position. Instead, it depends upon the local wall temperature at any position downstream of the CHF point. It has been observed that very different results for wall temperature history and precursory cooling can be obtained if the axial heat-structure node size was changed from large to small, or vice versa.[18] We determined that this node size sensitivity arose because the only limiting criteria within the code in such a local-temperature formulation are those inherent within the numerics associated with axial conduction solution. In particular, for the earlier model, no spatial requirement was placed on the spatial dimension over which a given convective heat-transfer process, such as transition boiling, must apply.

Thus, a local-temperature transition-boiling formulation will allow the axial temperature distribution to grow sharper as the node size is decreased until a size smaller than that required to properly model the axial conduction effect is reached.

The formulation, and therefore the code, has no way of knowing the proper spatial temperature distribution. The local-wall temperature formulation of transition boiling contains no provision to prevent the "axial collapse" of the convective transition boiling process to that imposed by the axial conduction limit for the wall. In general, this collapse is not correct; however, some flow states exist where this collapse of transition boiling to the axial conduction limit is the correct representation of the convective process.

As seen in many experimental studies,[5-7] the extension of the transition boiling downstream of a CHF point in forced convective flow depends upon the thermal-hydraulic conditions at the CHF point. Thus, to eliminate difficulties associated with nodalization, an axial-dependent transition-boiling model was developed. The concept of axial-dependent transition boiling was initially proposed by Yu[19] and Yadigaroglu[20] and further developed by Nelson and Unal.[14]

Typical conditions for a post-CHF convective flow are illustrated in Fig. 6. Figure 6 shows the inverted annular flow-regime map with a representative axial wall heat-flux profile. Flow is assumed unidirectional from left to right in the figure, and the primary quench front is that located in the left part of the figure. The wall heat flux at the CHF point is significantly higher than the heat flux of the film-boiling regime. The transition boiling heat flux is limited by a maximum of q_{chf} and a minimum of q_{min} that occurs from the correlation package, i.e., not an explicit q_{min} correlation. It was assumed, in the current model, that the total transition boiling heat flux exponentially decreased with the axial distance from the CHF location. An exponential decrease for heat flux is the most common representation for transition boiling correlations that are position dependent. The total transition boiling heat flux is given by

$$q_{tb} = q_{chf} e^{-B\left(z - z_{chf}\right)} \quad . \tag{3}$$

In this case, z is measured related to the relative coordinate system.

The determination of the coefficient B (units of 1/m) is not straightforward and should ultimately consider all possible post-CHF flow conditions and wall material and thickness combinations that are of interest. As originally discussed by Nelson and Unal,[14] we propose that three hydrodynamic flow parameters—the capillary number, the vapor Reynolds number, and the void fraction at the CHF point—should be considered in determining B (Table 2).

The flow-regime map of Fig. 1 indicates that the length of each IAF regime is proportional with the square root of the capillary number defined at the "inlet" CHF point. Thus, the IAF flow regimes extend further when the liquid velocity increases at the CHF point for a given pressure. We assume that the length of transition boiling should exhibit the same trend; higher liquid velocities at the CHF point should extend the transition-boiling region further downstream. Therefore, the first dimensionless parameter in determining B is the capillary number at CHF. B is assumed to be proportional to the inverse square root of the capillary number ($B = \text{Constant} \times Ca^{-1/2}$). The proportionality constant was found to vary with vapor Reynolds number (defined at the CHF point) from 16 to 10 when the vapor flow changed from laminar to turbulent (Table 2).

For higher void fractions, the flow regimes downstream of the CHF point are expected be annular transition and dispersed flow, respectively. We believe that the transition-boiling region should occur in a relatively short region for these high-void flow conditions and should diminish when the void fraction goes to unity. Thus, the transition-boiling region is forced to decrease with increasing void fraction if the void fraction at CHF is between 0.8 to 0.995. This choice is somewhat arbitrary and determined in developmental testing by Unal, Haytcher and Nelson.[16]

To better understand this formulation, we can first note that the length of the transition-boiling region can be determined from Eq. (3) to be

$$z_{tb} - z_{chf} = \frac{-\ln\left(\frac{q_{tb}}{q_{chf}}\right)}{\text{Constant } Ca^{-0.5}}, \tag{4}$$

for the case where $\alpha < 0.8$. Dividing Eq. (4) by the diameter yields

$$\frac{z_{tb} - z_{chf}}{D} = \text{Constant } Ca^{1/2}, \tag{5}$$

which is the same type of formulation developed by Obot and Ishii[3] for his flow-regime map.

In the current formulation, the coding is generalized to use different dependencies based on either the up-flow or down-flow cases. Based on initial results, those two cases remain the same. If additional data become available to better characterize the thermal-hydraulic behavior in downflows, the coefficient B can be defined separately from the up-flow case.

To partition the total transition boiling heat flux into its phasic components, the gas phase HTC, h_{wg}, was evaluated by the Webb-Chen.[21] This correlation is explained in Section 3.2. Once h_{wg} is evaluated, the wall-to-vapor heat flux, q_{wv}, can be calculated. Then h_{wl} is found by dividing the difference between the total transition boiling heat flux, q_{tb}, and the heat flux from wall to vapor, q_{wv}, by the driving force of (T_w-T_l).

Several tests were made to determine if the transition-boiling regime exists. These tests are defined by three basic considerations as follows:

1. Has CHF occurred?

2. Are we far enough downstream that film boiling must exist?

3. Is the void fraction too high?

The first consideration was relatively simple and determined that CHF had been exceeded if $T_w > T_{CHF}$, using temperature, or if $q_{\text{nucleate boiling}} > q_{CHF}$, using heat flux.

The second consideration was made to save computational time and involved several steps. In the first step, the distance past the CHF point was considered, with transition boiling being possible if $Z_{tb} - Z_{CHF} < Z_{tb,\ max}$ where $Z_{tb,\ max}$ is a practical numeric value beyond which transition boiling is not expected. Then, if transition boiling was possible based on this distance criterion, both the transition boiling and film boiling heat fluxes were evaluated. Finally, if q_{tb} was greater than q_{film}, transition boiling was determined to have occurred at that particular Z. This heat flux comparison leads to the definition/determination of Z_{tb}.

The third consideration involved a test on void fraction ($\alpha > 0.995$) to ensure continuity in the high-void region as the flow becomes single-phase vapor.[14]

2.5.2. Secondary (Downstream) Quenches

The secondary quench front is located downstream of the primary quench front and is situated nearer the core outlet based on the relative coordinate system. In Fig. 6, the secondary quench is the one on the right side of the figure. The core outlet may be either the bottom or top, depending upon the flow direction as discussed earlier.

No transition boiling model is employed at the secondary quench front. For the unidirectional flows where dispersed flow exists prior to the secondary quench, the model will naturally change from the dispersed flow regime to the nucleate boiling regime downstream of the secondary quench. Axial conduction within the code's rezoning fine mesh model will properly represent the conduction process for this situation. For the cases where significant liquid is present before the secondary quench front, additional convective effects will result from the film-boiling portion of the model. The current representation will not be sufficient for those cases where transition boiling might contribute. Preliminary results do not show a sensitivity to this potential situation, but it is most likely that representative low-void experimental information is not available.

2.5.3. Hot Patches

In steady-state post-CHF tests using hot patches,[5-7] the wall temperature profile showed a sharp increase following the CHF point. We believe that the transition-boiling regime for such tests should be limited to a very short region. Thus, the coefficient B (see **Table 2**) was multiplied by a constant to ensure that the length of the transition region was very small in calculations including hot patches.

2.5.4. Modeling Constant Wall Temperatures

Hot patch experiments also give rise to test sections continually under constant flow and heater conditions, i.e., the quench fronts are prevented from entering either end of the test section. Thus the test section experiences constant wall temperatures denoted by

$$\frac{d\overline{T}_w}{dt} = 0 .$$

See Appendix A for further discussion of this property.

In the past, to simulate these experiments an analyst would specify the geometry, flow conditions, power input to the test section, and heat losses. Comparison would then be made to measured wall temperatures. This comparison is possible when the power input is sufficient to prevent the code from predicting a quench. However at lower powers, the energy balance at the heater test section entrance is delicate. If the code overpredicts the convective wall heat transfer even slightly, an inlet quench will occur and propagate up the test section. The only way the analyst might determine how bad the prediction would be a trial-and-error approach of continually raising the input power to determine at what heat flux the initiation of the quenching is prevented.

For this reason and the fact that heat losses are sometimes difficult to specify for these delicate situations, a constant wall temperature option was added to the reflood model. For those experiments where the data were reduced to provide both the wall temperature distribution plus the convective wall heat transfer, this option may be used for model validation. The wall temperature distribution is specified and comparison is made to the total convective heat flux.

The constant temperature wall model bypasses the conduction solution using the input temperatures within the heat structure (i.e., new time temperatures are set equal to old time temperatures). The convective heat-transfer boundary condition can, and should, be used for the heat structure so that the convective wall heat-transfer coefficients are evaluated based upon the fixed wall temperatures and the hydraulic state determined by the flow equations. This model also bypasses the need for heat losses from the wall but requires that the experimentalist must have eliminated it within the data-reduction process.

2.5.5. Film Boiling

The film-boiling heat-transfer regime incorporated several different correlations to describe the HTCs in each of the IAF regimes. The film-boiling regime was assumed to occur when $T_w > T_{CHF}$ and $Z - Z_{CHF} > Z_{tb}$. The wall-to-liquid and wall-to-vapor HTCs, h_{wl} and h_{wv}, were treated separately for each of the individual IAF regimes. Figure 7 shows the selection logic for the HTCs in the film-boiling regimes. In this case, for simplicity, only one quench front is shown. In this figure, the trend of each correlation in each IAF regime is shown. Whereas the weighting functions are shown as linear in Fig. 7, this is only a conceptual representation, with the true weighting frequently being nonlinear. The following paragraphs discuss the selected HTC correlations in each of the IAF regimes. Table 3 provides the details related to the correlations used in film-boiling regime.

In the smooth IAF regime, the total heat generated by the wall was assumed to be transferred directly to the liquid interface across the vapor film surrounding the liquid core. Denham[22] recently developed an expression for heat transfer in the IAF. The derivation of that correlation was similar to that of the Bromley correlation except that the vapor film thickness was obtained from a force balance on vapor film. The wall-to-liquid HTC is determined by dividing the thermal conductivity of vapor by the vapor film thickness. Because the total heat generated by the wall was assumed to be transferred directly to the liquid, no heat transfer to the vapor phase was assumed to occur. The heat transfer by radiation from wall-to-liquid HTC was also considered and added to the wall-to-liquid HTC for all film-boiling regimes.

In the flow regimes downstream of smooth IAF, the wall was assumed to be cooled by a combination of vapor and liquid. The Webb-Chen[21] correlation was used to obtain the wall-to-vapor HTC in the remainder of the flow regimes downstream of smooth IAF. The Webb-Chen correlation was developed from a nonequilibrium database for single tubes. It was based upon the momentum-transfer analogy and considered possible entrance-region effects and the effect of entrained liquid droplets.

The Webb-Chen[21] correlation alone cannot result in the correct prediction of the heat transfer in the IAF regimes downstream of the smooth IAF. As noted earlier, Ishii[1-3] experimentally observed the existence of a fine sheet of liquid drops/ligaments between the liquid core of the IAF regime and the wall. It is clear from these studies that the hydrodynamic behavior in the rough/wavy and agitated IAFs shows a unique characteristic. Interfacial surface area is increased significantly, and liquid exists near the wall, possibly in momentary contact with the wall. As a result, the heat-transfer mechanism in these flow regimes is significantly enhanced. Whereas the heat-transfer aspects of the flows were not measured by Ishii[1-3] and coworkers, the existence of a post-transition boiling region (near region) immediately downstream of the CHF point was found by Unal et al.[23] Unal et al. indicate that the evaporation of liquid is very efficient in the post-transition boiling region and therefore the measured vapor temperature is close to the saturation temperature of the fluid. They hypothesize that the heat-transfer enhancement could be due to liquid/wall direct contact heat transfer. Another mechanism that might explain this efficient process is the increase in local turbulence near the wall due to the existence of liquid droplets.[24,25]

Although either of these theories can predict heat-transfer enhancement in the IAF regimes downstream of smooth IAF, it is not clear that only one of two is the responsible mechanism for the overall heat-transfer enhancement. It is more likely that both heat-transfer mechanisms can exist. In our model, we name this heat-transfer mechanism the "near-wall liquid" effect. We assumed that it starts at the beginning of the rough/wavy IAF and gradually increases with increasing axial distance until the agitated IAF region. In agitated flow, we postulate that the near-wall liquid effect is at a maximum because of high turbulence and some possible liquid/ wall contact. Downstream of the agitated region, this effect gradually decreases and finally becomes negligible in highly dispersed flow.[23]

We induce this near-wall liquid effect through the wall-to-liquid HTC, h_{wl}. One can argue that this effect is due to either liquid/wall contact or turbulence enhancement where, much like Denham's model, the transport of wall energy into the vapor and then into the liquid is short-circuited because of the extremely fast and efficient transport process. There is no mechanistic model to predict this contribution. Therefore, we selected the modified Bromley correlation[26] as the "kernel" for the model while extending the model to include the affect of increasing with increased mass flux for a given heat flux and inlet subcooling. This is consistent with the experimental findings reported by Unal et al.[23] (see Fig. 9) who indicated that their transition region extended further downstream with an increase in vapor flux.

Thus, for the Bromley correlation,[26] we introduce a multiplier that depends on the vapor Reynolds number. Although we arrived at the idea of introducing a Reynolds number-dependent enhancement factor to the Bromley correlation, we have since found that Mosaad and Johannsen[27] used the same idea except that their correlation was based upon the liquid Reynolds number while ours was based upon the vapor Reynolds number. The simple functional form of F listed in Table 3 is very similar to that suggested by Mosaad and Johannsen and was obtained from a limited steady-state post-CHF database representing the typical operating range of the Winfrith post-CHF data. The functional form of the multiplier was found by matching the calculated wall and vapor temperatures to measurements for five of the Winfrith steady-state post-CHF tests. The functional form was found to be a linear function of vapor Reynolds number defined at the agitated IAF.

The functional form listed in Table 3 gives a multiplication factor varying between 0.2 and 1.0 for Reynolds number varying between 900 and 2300. With this modification, low-pressure data were predicted reasonably well, whereas higher-pressure data showed an underprediction of the measured wall temperatures. This underprediction arises because the Reynolds number becomes much higher than 2300 because of the increase in vapor density with pressure. The multiplication factor always becomes 1, resulting in high wall-to-liquid HTCs at higher pressures. Therefore, a pressure-dependent exponent was introduced and applied to the Reynolds number, as summarized in Table 3. This correction was made to use the same functional form of F allowing enhancement factor being <1 for higher Reynolds numbers.

The overall formulation of the enhancement factor emphasizes an important point: the heat-transfer enhancement in the agitated inverted-annular flow is a function of vapor Reynolds number. The determination of a more adequate functional form considering the pressure and other effects can be obtained if a mechanistic model is considered with a large number of data from several different databases. In this paper, we made an effort to give priority to the evaluation of key dimensionless numbers that control the enhancement of heat transfer due to the near-wall liquid effect.

The model, as coded in TRAC, allows extension of the model to the postagitated region or to a point defined by void fraction α_2 to match the experimental wall temperature in this region. The current value of α_2 is limited to values between 0.45 and 0.75. These limiters were applied for much the same reasons as those noted for the application of Ishii's model shown in Table 1. This is obviously an area where phenomenological modeling is needed in the feature.

As noted earlier, we forced the near-wall liquid effects to be diminished gradually with increasing axial distance downstream of the agitated IAF. This effect was accomplished by introducing the weighting function listed in Table 3. The exponent of the weighting function was also found to be a function of vapor Reynolds number at the beginning of the agitated IAF. Although the form of exponent, F_1, looks complicated, it only changes the shape of the weighting function varying with void fraction.

If the liquid is subcooled in the film-boiling regime, an additional HTC, h_{gam}, is calculated and used to separate the latent heat of evaporation effect from the sensible heat effect. As Denham[22] indicated, the interface of the subcooled liquid becomes saturated because of condensation. Thus, the heat transfer from saturated interface to subcooled liquid core, q_{il}, was expressed as the conduction solution of a cylinder with a change in the surface temperature. The time required by his expression can be calculated as the ratio of node size to liquid velocity. The q_{il} becomes

$$q_{il} = k_l \sqrt{\frac{V_l}{\pi \alpha_l (Z_{top} - Z_{tb})}} \frac{V_l D_h^2}{V_l D_h^2 + 15 \alpha_l (Z_{top} - Z_{tb})} (T_{sat} - T_l) \ . \tag{6}$$

Finally, h_{gam} can be calculated as the total wall-to-liquid heat transfer, less q_{il} divided by the driving force of $(T_w - T_l)$. This h_{gam} is calculated in all IAF regimes except highly dispersed flow.

2.6. Interfacial Heat Transfer

To estimate the heat- and mass-transfer rates between phases, the interfacial surface areas and the vapor-to-interface and liquid-to-interface HTCs are required [see Eq. (2)]. The term q_{il} in Eq. (2) accounts for the sensible heat transferred to or from the interface where the thermal energy is converted to or released as latent heat. The interfacial heat-transfer model treats evaporation and flashing separately.

Consequently, two different liquid-side heat-transfer factors exist in the current model: one for flashing and another for evaporation. Evaporation occurs if $T_{sv} < T_l < T_{sat}$, and flashing occurs if $T_l > T_{sat}$. The interfacial surface area and heat-transfer coefficients for evaporation, condensation, and flashing are defined for each of the IAF regimes and other flow regimes. In addition to the post-CHF regimes, we will limit ourselves to consideration of the nucleate boiling region. The selected correlations for determining liquid- and vapor-side HTCs and interfacial areas are summarized below.

In the nucleate boiling region, the liquid-side HTC is calculated by using either the Chen-Mayinger or Wittaker correlations.[17] The vapor-side HTC was assumed to be constant, 1000 W/m^2 °C, which was chosen to be large enough to keep the vapor near saturation. The interfacial surface area in the nucleate-boiling regime is calculated depending upon the flow regime. For bubbly flow, a simple expression was used for the bubble diameter as suggested by Ishii.[28] In annular-mist flow, the interfacial surface areas due to liquid film on the wall and liquid droplets are calculated separately and then combined. The droplet diameter, the entrainment fraction, and other parameters are calculated using models developed by Ishii and his coworkers.[17]

In the nucleate boiling regime, if the liquid temperature is higher than the saturation temperature, $T_l > T_{sat}$, flashing of the liquid is allowed. To determine the liquid-side HTC, a simple flashing model is used, and the interfacial surface areas are determined as discussed above. The heat-transfer coefficient due to flashing was calculated using the kinetic theory of evaporation from a liquid surface.[29] This theoretical maximum evaporation rate was converted to an equivalent HTC. The coefficient of 0.04 suggested by Hsu and Graham to predict the evaporation rate in experimental studies was modified for each of the individual flow regimes in nucleate and film boiling. A modified coefficient of 0.002 was used for the possible nucleate-boiling regimes. The HTC for nucleate boiling is given by

$$h_{fls,nuc} = 0.002\, h_{fls,teo} = 0.002 \times 0.01857 \frac{\rho_v h_{fg}^2}{T_{sat}^{1.5}} \quad . \tag{7}$$

In the smooth, rough/wavy, agitated, and postagitated IAFs, the interfacial area was calculated by adding the surface area of the liquid core and the surface area of the bubbles in the liquid core if they exist. In post-CHF experiments),[30,23] the measured vapor superheat was not significantly high in the region near the CHF location. The axial vapor temperature profile showed an S-shaped profile low in the region near to CHF and high in the far region. This S-shaped vapor temperature profile was encountered in relatively high-void-fraction dispersed-flow conditions,[23] as compared with IAF. Thus, we would expect very little vapor superheat in the smooth, rough/wavy, and agitated IAFs. For this reason, the vapor-to-interface HTC in these flow regimes, h_{ig}, was assumed to be relatively high. A constant value of 3000 W/m^2°C was used to ensure that the vapor was not superheated significantly. If the liquid is subcooled, the rate of heat transfer is represented by h_{gam} as discussed in the previous section. When the liquid is superheated, the flashing HTC in the inverted annular flows (the smooth, rough/wavy, agitated, and postagitated flows), $h_{fls,inv}$, is obtained by multiplying $h_{fls,teo}$ with a constant of 0.02 ($h_{fls,inv} = 0.02\ h_{fls,teo}$).

For highly dispersed flow, the interfacial area consists of two components: liquid film on cold walls and liquid droplets. The vapor-to-interface HTC, h_{ig}, was obtained from the correlation for the rate of vapor generation in dispersed flow suggested by Unal et al.[10] This correlation was modified and converted to a heat-transfer coefficient. For subcooled liquid conditions, the rate of heat transfer is considered to be h_{gam} as discussed above. The flashing HTC in highly dispersed IAF, $h_{fls,dfs}$, is obtained by multiplying $h_{fls,teo}$ with a constant of 0.02 ($h_{fls,dfs} = 0.0002\ h_{fls,teo}$).

Depending upon the location of a given cell with respect to the IAF elevations, the appropriate HTCs are determined using weighting factors (W_{sb}, W_{df}, W_{inv}). These weighting factors are based upon cell-length averaging. The logic of the weighting factors is summarized by Nelson and Unal.[14] The final HTCs were obtained by the following equation:

$$h = h_{sb}\, W_{sb} + h_{df}\, W_{df} + h_{inv}\, W_{inv}\ , \qquad (8)$$

where h represents either h_{ig} or h_{il}/h_{fls}.

2.7. Interfacial-Drag Coefficients

Models for the interfacial-drag coefficients in a reflooding core were developed based on the inverted annular flow map shown in Fig. 1a. For each flow regime, a separate interfacial-drag model was developed. Because Ishii's flow map (Fig. 1) does not consider transient effects and the resulting availability of liquid, void fraction was used to limit the potential IAF regimes. This void effect is also present in lower-liquid flow-rate situations, where the liquid flow is insufficient to produce the IAF configuration. Thus, models for each of the flow regimes were defined in the flow-regime void fraction plane, as shown in Fig. 8 and summarized in Table 4. Three void fraction regions were identified: (1) the low void fraction region, which spans smooth, rough/wavy, and agitated IAF regimes, characterized by void fractions <0.75; (2) the high void fraction region, corresponding to the highly dispersed region, and characterized by void fractions higher than 0.98; and (3) the intermediate void fraction region, or the dispersed regime, between the high- and low-void regions. In the following subsections, the interfacial-drag models for each IAF regime are presented from the bottom to the top of the channel in the following order: subcooled and saturated nucleate boiling, smooth inverted annular, rough/wavy inverted annular, agitated, highly dispersed, and dispersed (or postagitated) flow.

2.7.1. Interfacial-Drag Model for Subcooled Nucleate Boiling, Saturated Nucleate Boiling, and Transition Boiling

Two regions characterize subcooled nucleate boiling: (1) the partial-boiling region in which the bubbles remain attached to the wall, and (2) the fully developed boiling region where bubbles enter the free stream.[31] In the partial-boiling region, the wall is sufficiently hot to cause a layer of superheated liquid to exist near the heated surface and cause bubble formation. The bulk fluid remains subcooled, hence the term "subcooled boiling." As shown in Fig. 9, the dominant forces on a bubble are buoyancy, drag, and surface tension. For our purposes, the film of bubbles attached to the wall in subcooled boiling can be considered to be a film of vapor instead of individual bubbles. At the interface the surface is rough, or dimpled. The vapor is moving relative to the liquid and is considered to be a continuous phase. Thus, the vapor can be pictured as flowing around a roughened liquid core with a diameter very similar to the diameter of the channel. By performing a steady-state force balance on the channel and using the vapor momentum equation and the definition of the shear stress, the interfacial-drag coefficient for partial-subcooled boiling, $C_{i,sb}$ can be expressed as

$$C_{i,sb} = \frac{2\rho_g f_{sm}}{D_h} . \tag{9}$$

The Colebrook friction factor for turbulent flow and a completely rough zone is used as f_{sm} in Eq. (9). The roughness parameter required by the Colebrook friction factor is estimated to be the time-average height of the growing bubbles.[31] We assumed that the roughness, ε, is 1% of the bubble height, Y_b. As given by Collier,[31] the bubble height can be found by assuming that it is proportional to the bubble radius and can be obtained from a force balance equation between the buoyancy, drag, and surface tension forces.[31]

When the liquid is saturated, superheated, or when fully developed, subcooled nucleate boiling occurs; bubbles also exist in the free stream. The interfacial-drag coefficient is needed because of bubbles in the free stream. To obtain this quantity, the portion of the bubbles on the wall and those in the free stream must be defined (see Table 3). Assuming that the bubbles attached to the wall are packed in a square grid, Collier[31] indicated that the void fraction at the wall, α_w, can be expressed in terms of the bubble height and the hydraulic diameter. Once α_w is known, the void fraction of the bubbles traveling in the free stream, α_{fr}, can be found by subtracting α_{fr} from the total void fraction, α_g.

The free-stream drag coefficient is obtained from the drag force expression given for bubble flows by Ishii[2] as

$$C_{i,fr} = \frac{\alpha_{fr}}{2\left[\frac{\sigma}{g\Delta\rho}\right]^{\frac{1}{2}}} \left[\frac{1 + 17.67\left(1 - \alpha_{fr}\right)^{1.3}}{18.76\left(1 - \alpha_{fr}\right)^{1.5}}\right]^2 \rho_l \frac{\left(C_1 V_v - C_0 V_l\right)^2}{\left(V_v - V_l\right)^2} . \tag{10}$$

The total interfacial-drag coefficient for fully developed nucleate boiling regime is obtained by a momentum-weighted equation given by

$$C_{i,sb} = \frac{C_{i,sb} V_l^2 + 0.00175\, C_{i,fr} V_r^2}{\left(\alpha_w + \alpha_{fr}\right) V_r^2} . \tag{11}$$

This interfacial-drag model is used when the cell void fraction is <0.5.

For void fractions >0.98, the interfacial-drag coefficient is calculated by the interfacial-drag model for the annular-mist flow regime as given in Spore et al.[17] For void fractions >0.5 but <0.98, a liquid-void-cubic weighting is used and is given by

$$C_{i,sb} = C_{i,sb}\, 0.125\, (1 - \alpha)^3 . \tag{12}$$

Ishii[2] suggests this type of liquid-void dependence for the slug regime. We apply it to the total drag coefficient as given in Eq. (11) to maintain continuity. If $C_{i,sb}$ calculated by Eq. (11) is less than the value of the drag coefficient in annular-mist flow, the annular-mist flow interfacial-drag coefficient is used.

2.7.2. Smooth IAF Interfacial-Drag Model

Using a steady-state force balance, the vapor momentum equation, and the definition of the shear stress, the interfacial-drag coefficient for smooth IAF is found to be (see O'Mahoney[18] for details)

$$C_{i,sm} = 2\rho_g f_{i,sm} \frac{\left(1 - \alpha_g\right)^{1/2}}{D_h} . \tag{13}$$

In this region, the interface is assumed to be smooth. Therefore, a simple smooth-tube correlation for the interfacial friction factor[31] is used for both laminar and turbulent flows.

The interfacial-drag coefficient is further redefined based upon the cell void fraction, as illustrated in Fig. 8. If the cell resides in the low void fraction region, no adjustment is made. If the cell is located in the high void fraction region, the interfacial-drag coefficient is assumed to be equal to that of the highly dispersed flow. In the transition between the high and low void fraction regions, the following weighting is used based upon the void fraction:

$$C_{i,sm} = C_{i,sm} + \left(C_{i,df} - C_{i,sm}\right) (4.348\,\alpha - 3.261)^{0.7} \tag{14}$$

2.7.3. Rough/Wavy IAF Interfacial-Drag Model

This regime is similar to the smooth IAF case. However, the interfacial friction is now increased because of the presence of waves and the shearing of droplets from the wave crests. The formulation of the interfacial-drag coefficient for rough/wavy IAF is similar to that of smooth IAF. To express the friction factor, $f_{i,rw}$, the turbulent rough-pipe correlation suggested by Colebrook[32] is used. The wavy vapor-liquid interface is considered to represent the pipe roughness. The roughness in Colebrook's friction factor is assumed to be proportional to the diameter of liquid droplets entrained from the wavy interface. The diameter of the liquid droplets is calculated using Ishii's equation for small droplets[2] with a proportionality constant of 80. If $\varepsilon/D_h > 1$, then a constant of 0.77 is used for $f_{i,rw}$. The interfacial-drag coefficient is further weighted based upon the cell void fraction as done before for the smooth IAF regime [replacing $C_{i,sm}$ with $C_{i,rw}$ in Eq. (14)].

2.7.4. Agitated IAF Interfacial-Drag Model

Large liquid slugs of a diameter sometimes approaching the liquid core diameter characterize the agitated IAF region. The breakup of the slugs into smaller pieces and droplets eventually occurs. The region is quite chaotic. The mechanism of droplet entrainment and breakup of the inverted annular liquid core should again dominate the interfacial drag. For this region, the same correlation as applied to the rough/wavy region is used.

2.7.5. Highly Dispersed Flow Interfacial-Drag Model

The dispersed region is composed of droplets flowing up the channel. The droplet diameter is calculated using Ishii's dispersed flow droplet diameter correlation[2] given in terms of the Laplace and viscosity numbers. Ishii and Chawla[33] also gave the interfacial-drag coefficient obtained by performing a separate force balance on the droplet that is in highly dispersed flow. Their expression requires the droplet velocity. An estimate of the droplet velocity, obtained from a separate momentum balance, is given by

$$V_d = V_v - 2.462 \left[\frac{(\rho_l - \rho_v)\, g\, d_d}{2\,\rho_v}\right]^{1/2} , \tag{15}$$

assuming that the droplet drag coefficient is 0.44 (Ref. 33).

In numerous experimental studies and in all power reactor geometries, some of the structural surfaces are unheated because of the presence of control rods and structures at the periphery of the core. Thus, a liquid film may establish itself on these cold surfaces, adding significantly to the overall liquid fraction at the top of the core. A typical PWR core contains 45 548 heated rods of 10.73-mm diameter and 3860 control rods of 13.8-mm diameter. Thus, the unheated surface of the control rods alone accounts for ~10% of the total rod heat-transfer surface area. From geometric considerations for typical reactor hardware, one can calculate the local volumetric liquid fraction to vary from 0.6 to 9% for liquid film thickness varying from 0.2 to 3.0 mm. Thus, the liquid contained in this film cannot be neglected because it can represent a significant portion of the total liquid fraction in the high-void region.

Williams[34] has shown that the vapor velocities generated in the core during reflood are at about the correct value to cause countercurrent flow limitation. Thus, the drag and gravity forces balance, creating a "hanging" film condition. Figure 10 depicts this condition in a top view. The overall drag coefficient must consider both the droplets and the film. It is not possible to do this directly with the two-fluid approximation because only one liquid field is assumed.

Pasamehmetoglu[17] derived the amount of liquid that can hang on the wall using a force balance on a differential liquid element that includes the forces caused by gravity and interfacial shear. The film liquid fraction can then be obtained from geometrical consideration and is given by $\alpha_{lf} = Pe\delta_{lf}F_u/A$. The film liquid fraction, α_{lf}, can also be limited by the total liquid fraction, α_l, available to be deposited on the unheated surface area. If the liquid and the unheated surface area are homogeneously distributed within a control volume, the amount of liquid on the unheated surfaces might be considered to be $F_u(1-\alpha_g)$. However, with cross flow between subchannels and the ability of unheated surfaces to collect liquid and hold it, the amount of liquid "hanging" on an unheated wall may become greater than $F_u(1-\alpha_g)$. This effect is included in the following relationship, which has been developed using results from CCTF run 14:[35]

$$\alpha_{lf} = 5\left(\frac{\alpha_g - \alpha_{ag}}{\alpha_{df} - \alpha_{ag}}\right)^{0.5} F_u\left(1 - \alpha_g\right) \ . \qquad (16)$$

The first part of Eq. (16) is a weighting factor that allows the limiting amount of liquid deposited on the cold wall to be an amount greater than the homogeneous fraction of the unheated surface area. We assumed that the weighting becomes unimportant when the void fraction is less than α_{ag}. The weighting also allows the maximum fraction of the liquid to be accumulated in the dispersed flow regime.

The droplet fraction becomes $\alpha_{dd} = 1 - \alpha_{lf} - \alpha_g$. Using the modified Wallis relation[36] for the interfacial friction between the liquid film and the vapor, the interfacial drag on the film can be estimated by

$$C_{i,lf} = \frac{2\,\alpha_g\,[0.005\,(1 + 75\,\alpha_{lf})]}{D_h} \ . \tag{17}$$

$C_{i,lf}$ and $C_{i,dd}$ were multiplied by 0.5 and 0.15, respectively, to predict available pressure-drop data.

The total weighted, averaged interfacial-drag coefficient for this regime is expressed by an average momentum balance equation between the liquid and gas. Assuming that the film velocity is small compared with the vapor velocity and that the total liquid velocity can be expressed in terms of weighted droplet velocity, the interfacial-drag coefficient becomes

$$C_{i,df} = \frac{C_{i,dd}\,V_r^2 + C_{i,lf}\,V_v^2}{\left[V_v - \dfrac{\alpha_{dd}\,V_d}{(1-\alpha_g)}\right]^2} \ . \tag{18}$$

2.7.6. Dispersed (postagitated) Flow Interfacial-Drag Model

This region is located downstream of the agitated IAF and extends until the highly dispersed flow regime, where the droplets become smaller. In this region, the interfacial-drag coefficient is obtained by performing a void fraction weighting using the interfacial-drag coefficients in the rough/wavy and highly dispersed flow regimes. The interfacial-drag coefficient is calculated as

$$C_{i,pa} = 1.5\,C_{i,rw} + \left[C_{i,df} - 1.5\,C_{i,rw}\right]\left[\frac{\alpha - \alpha_{ag}}{\alpha_{df} - \alpha_{ag}}\right]^{0.5} , \qquad \text{if } C_{i,df} < 1.5 C_{i,rw} \tag{19}$$

or

$$C_{i,pa} = 1.5\,C_{i,rw} , \qquad \text{if } C_{i,df} = 1.5\ C_{i,rw} \ . \tag{20}$$

In Eqs. (19) and (20), α_{ag} is selected to be the minimum of calculated α_{ag} and the upper limit imposed on the agitated regime as noted in Table 1.

2.7.7. Combinations of the Individual Drag Models for a Control Volume

When multiple regimes occur in a given hydro cell, the interfacial-drag models developed for each region of the core during reflood are length averaged to determine the cell-average drag. The overall interfacial-drag coefficient for such a situation is given by

$$C_{i,cell} = W_{sb}\, C_{i,sb} + 2.5W_{sm}\, C_{i,sm} + 1.5W_{rw}\, C_{i,rw} + W_{pa}\, C_{i,pa} + W_{df}\, C_{i,df} \ . \tag{21}$$

For each IAF regime, a linear weighting is used in the above equation (W_{sb}, W_{sm}, W_{rw}, W_{pa}, W_{df}), which is based upon axial distance. The transition boiling length is included in the W_{sb} term. Details of this weighting are available by Nelson and Unal.[14]

2.8. Grid Spacer Model

The grid spacer model remains the same simple models as that of Nelson and Unal.[14] This model uses a fixed interfacial heat-transfer term to enhance vapor desuperheating. In both highly dispersed flow and other IAF flows, if there is a spacer located in a finite-difference cell, h_{ig} is assumed to be 10^6 W/m^2°C to simulate the enhanced interfacial heat transfer.

3. METHODOLOGY—OPTIMIZATION AND CLOSURE DEVELOPMENT

Appendix B contains details related to the methodology and theory behind the development of closure relationships using optimization methods. Appendix C contains a summary of the implementation of these methods. Appendix D contains a discussion of the optimization study results. Appendix E compiles detailed descriptions of a subset of the input/output files of Table 9.

4. SOFTWARE AND COMPUTATION ORGANIZATION

Development of the new AP600 reflood model required both revision of "old" coding and development of new coding. As indicated in the section on description of the Thermal-hydraulic Model, it was determined that a rewrite of the original MOD2 reflood model was the best avenue for further development of the model. This section will discuss the new structure of the coding and relate it to the previous implementation. It will also indicate the structure of the coding needed for the optimization effort.

4.1. Closure Model Coding Structure

This section will briefly discuss the changes made to the structure of the convective wall heat transfer and to both interfacial heat transfer and drag.

4.1.1. Code Structure for the Wall Heat-Transfer Model

In the computational logic of TRAC's prepass, HTSTR1 is the subroutine that controls the calculation of the power to be removed from the Heat Structures, via convection and radiation, if the radiation model is active. Figure 11 shows the basic logic within HTSTR1. Two namelist flags are used to control the calculational logic of the code, NENCL and NEWRFD, as well as a reflood trip and fine-mesh rezoning trip (these two trips are not shown in Fig. 11). The reflood and the fine mesh rezoning trips must be "on" to allow the reflood model to be used. NENCL is a namelist variable that indicates the number of radiation enclosure present in the model. NEWRFD is a namelist variable that was in the original MOD2, which has been extended to control the closure models and data structure as follows:

NEWRFD	Wall Heat-Transfer Model	Data Structure	Radiation Possible
0	MOD1	old	yes
1	Original MOD2 reflood	old	no
2	MOD1	new	yes
3	New reflood model	new	no

The radiation and reflood models cannot be applied in the same model. Input checking (not shown) is used to detect this case, and the computation is aborted after input checking is completed.

In terms of determining convective wall heat transfer, CORE1 and CORE1N are the two subroutines controlling the calculation of the wall heat-transfer coefficients. CORE1 is the "old" or original subroutine and contains the logic to use either the original MOD1 heat-transfer logic contained in subroutine HTCOR or the MOD2 reflood model contained in subroutine HTVSSL. As shown in Fig. 12, CORE1N is a new routine that is used instead of CORE1 when NEWRFD is neither zero nor one.

Figure 12 shows the basic logic of CORE1 dealing with the calculation of the heat-transfer coefficients for a particular rod of a Heat Structure and its surface(s) exposed to convection and for each axial level of that surface. The axial levels may experience axial mesh rezoning each timestep.

Figure 13 shows the basic logic of CORE1N, which is similar to CORE1 except the coding for the inner do-loop on axial level is replaced by a new subroutine ZLOOP. The basic logic structure of ZLOOP is shown in Fig. 14. This revision was made for two reasons. First, the old subroutine CORE1 was over 2000 lines long and was extremely difficult to understand and debug. Second, the MOD2 reflood model solution, coded within CORE1, marched up the rod to evaluate the convective heat transfer in a sequential manner. Again, this was a very complex procedure requiring several flags to coordinate the computation. We found the restructuring in CORE1N, ZLOOP, and the other new subroutines to be a significant improvement to readability and maintainability of the new model during its development.

The separation of the calculational process using the new heat-transfer logic was ultimately designed to delete the old CORE1. However, this action was not taken in this phase of model development to allow complete null testing between the new and old versions during developmental assessment, if desired. It appears that nonreflood heat transfer is present by monitoring the tests within the code that evaluates whether the model is turned on. If we first consider that case without the reflood model within Fig. 14, it is instructive to define the function of the ZDRIVE_X subroutines where X is either A, D, or F as defined below.

ZDRIVE_A — calculates an interpolated void fraction based on conduction node elevation for use in the heat transfer. Normal hydrodynamic cell-center quantities result if the fine mesh is off.

ZDRIVE_D — calculates the wall heat-transfer coefficients. This makes the appropriate call to HTCOR.

ZDRIVE_F — calculates the length averaged heat transfer for the hydro cells.

We could have chosen to bypass the call to ZDRIVE_A, but it does not affect standard problems without the rezoning fine mesh.

In case the reflood model is turned-on, the following sequence of operations occurs:

ZDRIVE_A — calculates an interpolated void fraction based on conduction node elevation for use in the heat transfer. The fine mesh must be turned on, or the calculation would not be at this location in the logic.

ZDRIVE_B — calculates the critical heat flux, finds up to two CHF points, and locates the elevations and other needed information associated with the quench front.

ZDRIVE_C — calculates all other flow-regime locations with the exception of transition boiling. The transition boiling location is estimated at this point.

ZDRIVE_D — calculates the wall heat-transfer coefficients. This makes the appropriate call to HTVSSLN (the newer version of HTVSSL).

ZDRIVE_E — calculates the true location of transition boiling.

ZDRIVE_F — calculates the length-averaged heat transfer for the hydro cells.

It should be apparent from Fig. 14 that each of these ZDRIVE_X subroutines and those under them function on the individual axial cell, or local, level.

The calling hierarchy of the new subroutines below the ZDRIVE_X subroutine is shown in Fig. 15. The function of each of these subroutines is defined in Table 3.

4.1.2. Code Structure for the Interfacial Heat-Transfer and Drag Models

Restructuring of the interfacial heat transfer and drag models was required to use the automatic differentiation tool ADIFOR to provide derivatives for the optimization. Both subroutines HTIF and CIF3, which were the MOD2 subroutines for interfacial heat transfer and drag respectively, were very long and old subroutines. As was the case for CORE1, these subroutines had both the standard and MOD2 reflood packages intertwined. Thus the arguments for coding readability and maintainability apply to these subroutines as well as CORE1; however, this restructuring was not nearly as extensive.

The result of the restructuring of HTIF and CIF3 is summarized in Fig. 16 for the interfacial heat transfer and in Fig. 17 for the interfacial drag. The reflood packages were separated out for the newer versions, denoted as HTIFN and CIF3N. The subroutine CORIFHT contains the new interfacial heat-transfer package, whereas RBSHRZ contains the new reflood interfacial-drag package. The correlations and modeling within both these packages have been discussed previously. The original versions of the complete subroutines are retained within the code also. The ADIFOR-generated versions of these two subroutines are G_CORIFHT and G_RBSHRZ and contain the coding that generates the desired partial derivatives.

4.2. Optimization Coding Structure

A global perspective of the software structure and input/output files associated with the optimization process is shown in Fig. 18. Optimization requires that an optimization code be interfaced with the TRAC code. Optimization executes the TRAC code in an iterative manner. This iteration can occur at two levels, simulation of multiple experiments and interaction for the optimized coefficients.

Multiple decks and data may be available for the optimization; see the left most box in Fig. 18 where ### indicates the run number of an experiment. The optimizer is shown as the next major box. Necessary information for the communication between the optimizer and TRAC is captured within boxes A and B with A containing vital TRAC-related information and B containing time-averaged information used by the optimizer. Box C contains the summary files written to aid analysis. For each experiment simulated, TRAC is run for a period of time to establish the average behavior. The optimizer adjusts the coefficients that are under study, TRAC executes to determine the effect of these changes, the coefficients are readjusted, and TRAC executes. This iteration on the coefficient set continues until convergence after which the procedure is repeated for the next experiment.

Table 10 includes brief descriptions of the subroutines and named common blocks used for the optimization of the reflood closure packages. The following logic exists within the subroutine htifn:

```
 if (ad4code) then
   call g_corifht(alp,alpo,rov,rol,visv,visl,p,arv,arl,chti,alv,dr,
&                 wa,tln,tvn,dx,vol,jcell,hla,cl,rova,cv,tssn,
&                 sidx,favol,sigma,vvvol,vlvol,dalva,hgam,hfg,
&                 gravol,alpmn,alpmx,vlvc,fasmlt,vlalp,finan,
&                 bitn,bit,vrv,wfsv,gavv,hdv,hlatw,hdva,chtia,
&                 alve,tsat,spifz,xfunh,
&                 xzchf,xztb,xzsm,xzag,xalpsm,xalpag,
&                 icrl,icru,icrr,nsgrid,zsgrid,irefld,njflip,
&                 lcore,l1d,lcond,flip)
 else
   call corifht(alp,alpo,rov,rol,visv,visl,p,arv,arl,chti,alv,dr,
&               wa,tln,tvn,dx,vol,jcell,hla,cl,rova,cv,tssn,
&               sidx,favol,sigma,vvvol,vlvol,dalva,hgam,hfg,
&               gravol,alpmn,alpmx,vlvc,fasmlt,vlalp,finan,
&               bitn,bit,vrv,wfsv,gavv,hdv,hlatw,hdva,chtia,
&               alve,tsat,spifz,xfunh,
&               xzchf,xztb,xzsm,xzag,xalpsm,xalpag,
&               icrl,icru,icrr,nsgrid,zsgrid,irefld,njflip,
&               lcore,l1d,lcond,flip)
 endif
```

Figure 16 shows the calling structure.

Within the subroutine **cif3n**, the following logic exists:

```
if (ad4code) then
  call g_rbshrz
else
  call rbshrz
endif
```

Figure 17 shows the calling structure.

Within the subroutine **htc**, the following logic exists:

```
 if (ad4code) then
   call g_htvssln(j,tave, roave, cpave, cnave,
&        emave, a(lhdr+k5), a(lpr+k5), a(ltsatr+k5), a(lhfgr+k5),
&        a(lclr+k5), a(lcvr+k5), a(lcplr+k5), a(lcpvr+k5),
&        a(lrolr+k5),
&        a(lrovr+k5), a(lromr+k5), a(lvislr+k5), a(lvisvr+k5),
&        alpha, a(lsigr+k5), odum, vlin, vlzp, zdum1,
&        vvin, a(lvvcr+kx), zdum2, a(lvmzr+kx),
&        zdum3, zdum4,
&        a(ltlr+k5), a(ltvr+k5), zslab, pdratr, idum1,
&        a(lelr+k5), a(levr+k5), a(ldrvdt+k5), a(ldrldt+k5),
&        a(lear+k5), a(lroar+k5), a(lpar+k5), a(ltssnr+k5),
&        a(lhlsr+k5), a(lhvsr+k5), hrg,
&        hl,          hv,           qchf,         tchf,
&        a(lihtf+k7), a(lstnu+k7), a(ltld+k7), dtstepr,frsttime)
 else
   call htvssln(j,tave, roave, cpave, cnave,
```

```
     &         emave, a(lhdr+k5), a(lpr+k5), a(ltsatr+k5), a(lhfgr+k5),
     &         a(lclr+k5), a(lcvr+k5), a(lcplr+k5), a(lcpvr+k5),
     &         a(lrolr+k5),
     &         a(lrovr+k5), a(lromr+k5), a(lvislr+k5), a(lvisvr+k5),
     &         alpha, a(lsigr+k5), odum, vlin, vlzp, zdum1,
     &         vvin, a(lvvcr+kx), zdum2, a(lvmzr+kx),
     &         zdum3, zdum4,
     &         a(ltlr+k5), a(ltvr+k5), zslab, pdratr, idum1,
     &         a(lelr+k5), a(levr+k5), a(ldrvdt+k5), a(ldrldt+k5),
     &         a(lear+k5), a(lroar+k5), a(lpar+k5), a(ltssnr+k5),
     &         a(lhlsr+k5), a(lhvsr+k5), hrg,
     &         hl,          hv,           qchf,         tchf,
     &         a(lihtf+k7), a(lstnu+k7), a(ltld+k7), dtstepr,frsttime)
      endif
```

Figure 15 shows the calling structure.

4.2.1. Adding or Deleting the Tunable Factors

To add a new tunable factor, the following must be done:

Assume its factor is called XXX, its ID is KXXX, and its absolute pedigree value is #.

Step 1. Determine whether the factor is currently in COMMON, initialized by a local DATA statement, or hardwired and go to Step 1A, Step 1B, or Step 1C respectively.

Step 1A. (Tunable factor in COMMON.)

-Ensure that factor is data-initialized in BLKDAT.

-Ensure that required common is *CAlled in INITCLO and CLOSET

Step 1B. (Tunable factor in local data statement.)

-Move local data statement to appropriate Block Data routine:

cif3blkd for CIF3

htifblkd for HTIF

htvblkd for HTVSSL

-Add variable to appropriate comdeck/common:

rafcif3 for CIF3

rafhtif for HTIF

rafhtv for HTVSSL

Step 1C. (Tunable factor in local data statement.)

-Update coding to use a scalar variable rather than a hard-wired constant. Either pick a mnemonic name or use the next one in the FACnnn series.

-Add data statement to appropriate Block Data routine:

cif3blkd for CIF3
htifblkd for HTIF
htvblkd for HTVSSL

-Add variable to appropriate comdeck/common:

rafcif3 for CIF3
rafhtif for HTIF
rafhtv for HTVSSSL

Step 2. Modify comdeck RAFDATA to include the declaration and parameter value for KXXX and change the definition of NFAC.

SAMPLE ORIGINAL CODING.

```
      parameter (kfac019 =   53)

C     Maintenance point.
C     (1) Add declaration and parameter statement for new factor.
C     (2) Redefine NFAC.
      integer nfac
      parameter (nfac = kfac019)
```

SAMPLE NEW CODING.

NFAC

```
      parameter (kfac019 =   53)
      parameter (kxxx    =   54)

C     Maintenance point.
C     (1) Add declaration and parameter statement for new factor.
C     (2) Redefine NFAC.
```

```
integer nfac
parameter (nfac = kxxx)
```

Step 3. Initialize label, copy of conditional pedigree value, and absolute pedigree value in INITCLO.

```
clolab(kxxx ) = 'xxx '
...
clofac(iset,kxxx ) = xxx
...
clofac(iset,kxxx) = #
```

Step 4. Add assignment statement to CLOSET.

```
xxx  = clofac(iset,kxxx )
```

4.3. Input Changes

Input changes that are required by the new reflood model are summarized in Appendix E.

5. RESULTS

Four data sets are discussed within this document, one from Winfrith Laboratory in England, another from the Idaho National Engineering Laboratory (INEL), one from the University of California at Berkeley, and one for the Nuclear Regulatory Commission- (NRC-) sponsored FLECHT test series. The first three experiments were done using internal flow in heated tubes. Steady-state post-CHF conditions were achieved by the use of hot patches for the Winfrith experiments. Whereas the INEL experiment did have hot patches, their effectiveness was limited to low flow rates so that most of the INEL data were obtained from slow quasi-steady quenching experiments. The Winfrith and INEL experiments were efforts to measure both the mechanical and thermal nonequilibrium present under post-CHF conditions. The Berkeley experiments were also done with a tube but without the same nonequilibrium instrumentation as those of Winfrith and INEL. However, the Berkeley experiments do provide a good database with which to investigate the quenching process. The FLECHT test uses a rod bundle to investigate reflood behavior under forced flow conditions. Comparison of these data sets is made to the Absolute and Conditional coefficient sets.

5.1. Winfrith Database

A summary of the Winfrith tests under consideration is contained in Table 11 and Table 12. Twenty-seven up-flow tests and eight down-flow tests are considered spanning a variety of test conditions.

5.1.1. Up-flow Experiments

A summary of the Winfrith upflow tests[39,40] under consideration is contained in Table . The number of up-flow tests available for consideration greatly exceeded those available for down-flow study. Those selected represent a reasonable spectrum of the parameters covered within the tests.

5.1.1.1. Absolute Pedigree. Figures 19 through 22 provide a comparison of the code simulations with up-flow data. Data for the Winfrith tests were measured or calculated based upon measurement for the total wall heat flux, void fraction, and vapor superheat. The experimental heat flux was a computed quantity based upon an energy balance at each of the test section's thermocouples. The void fraction was measured at three different elevations based upon a traversing gamma densitometer, and the vapor superheat was measured at the exit of test section using a thermocouple in the flow channel.

Figures 19 and 20 are plots of the total wall heat flux compared with the data. The code-calculated quantity is the sum of the time-averaged phasic wall heat fluxes. Figure 19 shows all the computed points and indicates that outliers do exist. These two points for Run 367 represent locations that were computed as nucleate boiling and therefore significantly overpredict the wall heat flux. The fact that nucleate boiling was predicted indicates that most likely a problem exists in the prediction of CHF. This suggestion was not investigated further because of the time restrictions.

Figure 20 shows the same comparison with the high-heat-flux outliers eliminated. The comparison shows broad scatter of the prediction with a number of the points exceeding the ±30% bounds. In general the observation can be made that the predictions for most runs show a greater total wall heat-flux sensitivity than the experiments. Also with the reduced scale in the figure, we can observe that Run 434 exhibited significant underprediction.

Figure 21 shows the predicted time-average void fractions vs those measured. For $\alpha_{avg}>80\%$ (see Fig. 21b), the code slightly underpredicts the experiments. Runs 434 and 451, indicated that single phase vapor was predicted. For $50\% \leq \alpha_{avg} \leq 80\%$ (see Fig. 21b), the code prediction is within the data scatter. The scatter also increases below 75% with more underprediction of voids as the void decreases. For $\alpha_{avg} <50\%$ (see Fig. 21a), the code systematically underpredicts the data. The capability to determine what portion of the drag model is being used is also contained in Fig. 21 by the letters within the symbols. Table 13 provides the letter/symbol key used inside each run-number legend of Fig. 22 for the different flow regions. Thus a triangle with vertex right and an N inside indicates Run 373 with a low-void dispersed region. The configuration of Table 13 is the same as shown in Fig. 8.

From Figs. 8 and 21, one can conclude that the rough/wavy model is underpredicting the drag, see points labeled H and K. The postagitated region, denoted as N, is showing some scatter with the lower α_{data} overpredicted and the higher voids underpredicted. This suggests that the pure rough/wavy prediction used for this region is unable to capture the needed variation where the prediction is too high at the lower voids (α_{cal}~50%) but too low as the void increases to 75%.

Figure 22 shows the time-average vapor temperatures computed vs those measured. Only a few data points are available for comparison because the lower void fraction experiments tend to quench the measurement thermocouple. The vapor temperature is systematically overpredicted by 50–100K.

5.1.1.2. Conditional Pedigree. A data comparison was done for the Conditional set that was similar to those done for the Absolute set of coefficients.

Figures 23 to 25 provide the comparisons of code simulation with data. Figure 23 compares the total wall heat flux, and as with the Absolute results, several outliers exist and are associated with Run 367 because of a prediction of nucleate boiling. Figure 23a eliminates the high-heat-flux outliers so that two groups are observed, one that principally lies above the +30% bound and one that lies below the –30% bound. An underprediction of Run 434 is again observed. On the basis of a global overview, it can be suggested that the Conditional case does no better than the absolute case. In case of the overall scatter, the Conditional set may not provide as good a prediction as does the Absolute set.

This similar result for the Absolute and Conditional predictions might initially be thought of as a validation of the Absolute case. This view may be desirable but is not the case. The problem lies in the definition of the Absolute case. This topic was discussed in a more limited sense in the Introduction. For the code to execute, it was necessary to retain the numerous splines developed within the Conditional code. The splines smooth the discontinuities that do exist between the various closure relationships. These splines dominate evaluation of the closure quantities in many of the calculations. Also, length averaging of the interfacial drag and heat transfer contributes to this problem. Both these effects were developed within the framework of the Conditional case and could not be separated from the Absolute definition without a significant amount of work that was not the thrust of this effort.

However, the Conditional set may provide an advantage if the reason for the two observed groups in Fig. 23a can be determined to represent a particular parameter. In that case, the two groups might be adjusted to compare better with data and produce a significant reduction in the scatter. A detailed study of Fig. 23 and Table 11 reveals that for heat fluxes <130 kW/m^2, the two groups are primarily dependent on flow rate (see right-most column of Table 11). The upper group corresponds to low flow rates and the lower group corresponds to high flow rates. Scatter within each run is generally less than that exhibited by the corresponding

Absolute Run. Above 130 kW/m^2, each run experiences a larger variation in the predicted heat flux compared with the data. This same characteristic of increased scatter can be observed again in the Absolute set and suggests an additional sensitivity that is not identified currently.

Figure 24 shows the time-average predicted void fractions vs those measured. As noted, Table provides the letter keys to the flow regions shown between Fig. 8 and Fig. 24. In a global sense, this comparison is somewhat similar to that of the Absolute set shown in Fig. 21a. The prediction is good for $\alpha \geq 75\%$ (see Fig. 24b). From Fig. 24a, we can conclude that the rough/wavy model underpredicts the drag (see points labeled H and K) and that the dispersed (postagitated) region, denoted as N, is overpredicted.

Figure 25 shows the time-average vapor temperatures computed vs those measured. The vapor temperature is generally underpredicted by ~20–80K. This is better than that of the Absolute set.

To better understand the effect of flowrate exhibited by Fig. 23, consider the flow regions for the various experimental runs. From Table 11 and Fig. 24, we can conclude that the low-flow-rate experiments produce the higher-void-fraction tests with the majority of the measurements occurring in the intermediate void range of dispersed flow (denoted as O). From Fig. 24 and Table 11, this means the wall heat transfer uses those models denoted as agitated and postagitated. For the wall-to-liquid heat transfer, the factors F and F_1 reflect the effect of vapor velocity at the location where agitated flow is defined to begin. The wall-to-vapor heat transfer is influenced by the vapor Reynolds number as shown. Because the vapor temperature prediction is quite reasonable, it can be concluded that these two flow effects combine to overpredict the wall heat transfer at low flows.

It should be noted that Runs 367 and 434 experienced problems within the flow-regime identification logic and produced single-phase vapor. This overpredicted the void fraction and vapor superheat while underpredicting the wall heat transfer. This problem was not typical of the vast majority of the simulations.

Similarly for the high flow cases and consideration of Table 11, Fig. 23, and Fig. 24, we can conclude that the principle flow region is rough/wavy and agitated (denoted as H and K in Fig. 24). Again the factors F and F_1 reflect the effect of flow rate for the wall-to-liquid heat transfer, whereas the vapor Reynolds number affects the wall-to-vapor heat transfer. In the case of high flow rates, the vapor superheat cannot be measured but is likely to be near saturation because of the low void fractions. Thus, factors F and F_1 underpredict the wall heat transfer.

5.1.2. Down-Flow Experiments

A summary of the Winfrith down-flow tests under consideration is contained in Table 12. The number of down-flow experiments available for study were limited.

5.1.2.1. Absolute Pedigree. Figures 26 through 28 show the results of the comparison of the Winfrith post-CHF database using the Absolute set of coefficients. Figure 26 shows the results of the total wall heat-flux comparison. Generally the Absolute set overpredicts a large number of points, but its general trends are good. Whereas it could be improved, the span of heat fluxes is in reasonable agreement with the calculation and data. Run 485 and a few other points exhibit an underprediction. Figure 28 shows the comparison for the predicted and measured-vapor void fraction. Unfortunately, as can be seen, the void measurements for the down-flow cases were not useful and do not help identify how well the hydraulics are predicted and thus do not help resolve some of the issues within Fig. 26. On the basis of the typical error within a gamma densitometer (a few percent), we might suggest that the code slightly underpredicts the void. Figure 28 shows the comparison for the predicted and measured vapor temperatures. Generally the vapor temperature is overpredicted with a few significant overpredictions.

5.1.2.2. Conditional Pedigree. Figures 29 through 31 show the results of the comparison of the Winfrith post-CHF database using the Conditional set of coefficients. Figure 29 shows the result of the total wall heat-flux comparison. These results are clearly not as good as the Absolute case. Also there is much more variation in the prediction than exhibited by the data so that significantly more variation is being expressed along the flow channel than really exists. Figure 31 shows the comparison for the predicted and measured vapor void fraction. The same problems exist as noted above in the Absolute case. Figure 31 shows the comparison for the predicted and measured vapor temperatures. A reasonable scatter about the measured vapor temperature is observed, and this prediction is better than the Absolute case.

5.2. INEL Database

A summary of the INEL tests under consideration in this study is presented in Table 14. Twenty-one up-flow tests are considered spanning a variety of test conditions. The INEL data set is one of few experiments, with measurement of the vapor superheat that include high pressures up to 7 MPa. Whereas the experiment did include the use of a gamma densitometer, the instrument proved faulty and no void fraction data were obtained. Thus, the data only include wall superheat, computed wall heat flux, and vapor superheat.

5.2.1. Absolute Pedigree

Figures 32 through 34 show the results of the comparison of the INEL post-CHF database using the Absolute set of coefficients. Figure 32 shows the results in the total wall heat-flux comparison establishing that outliers do exist. Again, these points represent ones that were computed as nucleate boiling (most likely implying a CHF prediction problem) and therefore significantly overpredict the wall heat flux. Figure 33 shows the same comparison with the high heat flux outliers eliminated. Significant scatter is seen with a large number of points outside the ±30% bounds. Also, some predicted points are negative. These negative predictions (as well as the smaller positive predictions) result from an overprediction of the vapor temperature at the upper elevations of the test tube where the wall temperature decreases (or does not increase as rapidly) so that the thermal driving potential becomes small or negative. A study of Figs. 32 and 33 and Table 14 shows that the majority of the overprediction occurs with the intermediate pressure simulations, i.e., 3.6 MPa.

Figure 34 shows the comparison for the predicted and measured vapor temperatures. An underprediction of the measured vapor temperature is observed. This is the opposite trend observed within the Winfrith data set.

5.2.2. Conditional Pedigree

Figures 35 and 37 show the results of the comparison of the INEL post-CHF database using the Conditional coefficients. As with the Absolute set, Fig. 35 shows that outliers again exist. Figure 36 shows the same comparison with the outliers eliminated. Significant scatter is observed with a large number of points outside the ±30% bounds. Whereas the overpredictions are not quite as high, they are globally very similar to the Absolute case. The intermediate pressure range is again the main source of trouble. Figure 37 shows the comparison between the predicted and measured vapor temperatures. The vapor temperatures are underpredicted and are very similar to the Absolute results.

Overall, as in the case of the Winfrith upflow results, the Absolute and Conditional results are quite similar. As noted above in the discussion of the Winfrith results, this similarity occurs because of the use of the splines needed to smooth the discontinuities between correlations and spatial averaging within the interfacial drag and heat transfer.

5.3. Berkeley Tube-Quenching Experiments

Three Berkeley Tube experiments[37] were considered for this report, and the experimental test conditions are summarized in Table 15. The experimental data consist of tube wall temperatures at various elevations within the heated section.

The Berkeley reflood test facility consisted of a 3.6576-m Inconel 600 alloy tube with an inside diameter of 14.4 mm and a wall thickness of 0.76 mm. The reflood tests were performed at atmospheric pressures, and the data from reflood tests include the temporal variation of wall temperature at various axial locations, quality of steam at the tube exit, input power to tube, inlet and outlet fluid temperatures, and heat losses. A detailed description of the test facility and the tabulated data can be found in Ref. 37. The test tube was heated to a stable initial temperature. Then the subcooled liquid was introduced to the test section, and the data acquisition system was started to record the data.

Three Berkeley reflood tests were chosen for this assessment work: test numbers 166, 167, and 186. The operating parameters of these tests are given in Table 15. The mass fluxes have been corrected since the 1993 version of this assessment to reflect the reported data of Ref. 37. These tests were selected to investigate the effect of the mass flow rate on the thermal-hydraulic characteristics of the test tube undergoing reflood. Note that the electrical power listed in Table 15 does not include the heat losses.

The TRAC model of this facility was simple, consisting of the following components: a Vessel, two Pipes, a Break, and a Fill. The Vessel component was one-dimensional, consisting of 24 axial levels. The Fill component simulated the constant water injection to the test tube, whereas the Break component simulated the outlet boundary conditions. The heat losses from the test tube to the surroundings were given with a temperature-dependent, heat-transfer coefficient in Ref. 37. A special update considering this temperature-dependent heat-transfer coefficient was used in the TRAC code for the heat losses.

5.3.1. Absolute Pedigree

Figure 38 shows the calculated and measured wall-temperature histories for Run 166 at 5 different thermocouple locations (0.61, 1.372, 1.83, 2.44, and 3.05 m from the inlet of the test section); unless otherwise mentioned in the following paragraphs, the thermocouple locations refer to these axial locations). The predicted wall temperatures follow the measured data poorly because of significantly overpredicted peak wall temperatures, indicating that the precursory cooling rates are not reasonably predicted for low flow rates. As a result, a qualitative assessment of Fig. 38 demonstrates the predicted quench times increasingly disagree with the measured quench times with respect to elevation. At higher elevations, 1.37 m and 1.83 m, the decrease in wall temperatures in the prediction starts a few seconds later than data. The predicted quench time delay is more profound at the 2.44-m axial elevation, and the predicted quench time is not readily apparent from Fig. 38 for the 3.05 m elevation.

When the mass flux is increased, whereas the other variables (electrical power, inlet fluid temperature and initial wall temperature) are kept constant, one could expect the time required to quench a particular axial location to decrease. This trend is shown in Fig. 39, which shows the predicted and measured wall temperature histories of the aforementioned axial locations for Run 167. In Run 167, the mass flux is increased to 74 kg/m^2s. The overprediction of the peak wall temperatures has been greatly reduced from that of Run 166. A comparison of the predicted temperatures in Figs. 38 and 39 clearly shows that an increase in the mass flow rate causes an increased magnitude of $\frac{dT}{dt}$ for quench times of elevations near or above 1.37 m, indicating that the precursory cooling rate has increased. As expected, a mass flux increase corresponds to a decrease in both predicted and measured quench times, which can be seen from a qualitative comparison of Figs. 38–39.

The effect of mass flux was further investigated in Run 186, as shown in Fig. 40. Run 186 was performed with the same power, inlet temperature, and initial wall temperature as those used in Runs 166 and 167; however, the mass flux was increased to 123.4 kg/m^2s. The precursory cooling rates and the temperature histories at each thermocouple elevation agree reasonably with the measured data. The quench times, however, are typically overpredicted.

5.3.2. Conditional Pedigree

Figure 41 shows the calculated and measured wall-temperature histories for Run 166 at the aforementioned thermocouple locations. The predicted wall temperatures follow the measured data poorly because of significantly overpredicted peak wall temperatures, indicating the precursory cooling rates are not reasonably predicted for low flow rates. As a result, a qualitative assessment of Fig. 41 demonstrates the predicted quench times increasingly disagree with the measured quench times with respect to elevation. Therefore, one can see that at higher elevations, 1.37 and 1.83 m, the decrease in wall temperatures in the prediction starts a few seconds later than data, and the quench time delay is more profound at axial elevations of 2.44 and 3.05 m.

When the mass flux is increased, whereas the other variables (electrical power, inlet fluid temperature and initial wall temperature) are kept constant, one could expect that the time required to quench a particular axial location to decrease. This trend is shown in Fig. 42, which shows the predicted and measured wall-temperature histories of five different axial locations for Run 167. In Run 167 the mass flux is increased to 74 kg/m^2s. The overprediction of the peak wall temperatures has been greatly reduced from that of Run 166. A comparison of the predicted temperatures in Fig. 41 and Fig. 42 clearly shows that an increase in the mass flow rate causes an increased magnitude of $\frac{dT}{dt}$ for quench times of elevations near or above 1.37 m, indicating the precursory cooling rate has increased. As expected, a mass flux increase corresponds to a decrease in both predicted and measured quench times, which can be seen from a qualitative comparison of Figs. 41–42.

The effect of mass flux was further investigated in Run 186, as shown in Fig. 43. Run 186 was performed with the same power, inlet temperature, and initial wall temperature as those used in Runs 166 and 167, but the mass flux was increased to 123.4 kg/m^2s. The precursory cooling rates and the temperature histories at each thermocouple elevation agree very well with the measured data. The quench times, however, are slightly overpredicted in the lower regions of the test section.

In spite of continuing deficiencies for lower mass fluxes, the Conditional-Pedigree-Predicted wall temperatures are nearer the measured temperatures than those of the Absolute Pedigree case discussed previously. Also, the peak wall temperatures for the lower mass flux have been significantly reduced from those predicted using the Absolute Pedigree, which allows quenching, albeit late, at the uppermost tube elevations.

5.4. FLECHT-SEASET Run 31504

One FLECHT-SEASET forced-reflood bundle experiment[38] was considered for this report. The chosen experiment (Run 31504) used a core simulator consisting of 161 electrically heated rods—two of which were unpowered—within a 17 x 17 square matrix (i.e., duplicates a Westinghouse 17 x 17 bundle) with a uniform radial power distribution and a cosine-shaped axial power distribution. No flow blockages due to cladding swelling and rupture were modeled. A nominal reflood rate of 2.46 cm/s and an injected-fluid temperature of 51°C were used. The available experimental data reported within this document consisted of heater-rod-cladding and steam-probe-vapor temperatures at various radial and axial positions, and differential pressures for various axial ranges. All measurements reported here were made within the heated region of the rod bundle.

The data labels use a general naming convention based upon their position within the bundle. Figure 44 shows the general cross section of the heater rod bundle and a rod-labeling grid. The rod-cladding temperatures are labeled as cc_z, where "cc" refers to a heater rod ID and "z" refers to an elevation of z in. referenced to the bottom of heated region (i.e., 9G_012 is located at rod 9G at 12 in.). The steam probe-vapor temperatures are labeled as SPcc_y_z, where "cc" refers to a heater rod ID, and "y_z" refers to an elevation of y ft and z in. (not always shown) referenced to the bottom of heated region (i.e., SP7F_7_6 is located at rod 7F at 7 ft 6 in.). Finally, the differential pressures are labeled as BU_x_y where "x" and "y" refer to the elevations (ft) of the lower and upper-pressure taps respectively relative to the bottom of the heated region (i.e., BU_2_3 refers to the differential pressure from 2 to 3 ft). All calculated values are labeled similarly to those of the experimental data with "TRAC" as a prefix. It is important to note that the calculated differential pressures are computed based upon collapsed liquid levels.

Calculations were performed with TRAC-M/F77 version 1.10R+; the "R" indicates that the new reflood model was included, and the "+" indicates that this version contained all known error corrections and updates existing at the time the computation was performed (February 1998). These results are for newrfd=3, which activates the reflood model with explicit top-down reflood modeling.

5.4.1. Absolute Pedigree

Figures 45a through 76 contain the results of the FLECHT-SEASET Reflood experimental data compared with the TRAC output using the Absolute Pedigree Coefficients. In general, the calculated cladding (wall) temperature profile is shown to be in minimal-to-reasonable agreement with the experimental data, in reasonable agreement with the measured values in the bottom one-half of the core, and in minimal agreement with the measured values above the core midplane. The predicted and measured quench times are in reasonable agreement to an elevation of 1.5 m (59.1 in.). Between 1.5 and 2.75 m (59.1 and 108.2 in.), the predicted quench times are earlier than measured by as much as ~130 s. For elevations higher than 2.75 m (108.2 in.), the predicted quench time is later than measured. Overall, the agreement between predicted and measured quench times is judged to range between minimal and reasonable.

The predicted and measured cladding thermal responses at 7 axial locations are compared in Figs. 46 through 52. At the 0.3048-m level above the bottom of the heated core (Fig. 46), the predicted quench time is slightly late, as is the peak temperature turnaround time. The predicted peak cladding temperature is in reasonable agreement with that measured. The predicted and measured thermal performances are also in agreement at the 0.9906-m level (Fig. 47), although the predicted cooling rate following the peak temperature turnaround is too high. The cooling rate slightly above the core midplane at the 1.9813-m level (Fig. 48) is too large following the turnaround in cladding temperature. The peak cladding temperature is in reasonable agreement with that measured. At the 2.8194-m level (Fig. 49), the predicted peak cladding temperature exceeds the measured peak temperature by 85 K. The quench time is 125 s later than measured. In the upper elevations of the core (3.3048, 3.353, and 3.505 m as shown in Figs. 50 through 52, respectively), too little cooling is predicted resulting in significantly higher peak cladding temperatures and delayed quench times. The predicted cladding temperatures are higher than measured by 60 K at the 3.048-m (120-in.) level and by 225 K at the 3.505-m (138-in.) level.

The FLECHT SEASET test bundle contained eight grid spacers. These were not included in the TRAC model of FLECHT SEASET Test 31504 because we have determined that the present TRAC grid-spacer model is seriously flawed. Our studies of the impact of grid spacers and the deficiencies of the TRAC grid-spacer model have been reported elsewhere.[41] These studies form the basis for our conclusion that the grid spacers in the FLECHT SEASET facility played a significant role in enhancing bundle cooling in the upper portions of the test bundle. We have concluded that some, but certainly not all, of the overprediction of wall temperature in the upper portion of the core for FLECHT SEASET Test 31504 is caused by the absence of an adequate grid-spacer modeling capability.

The predicted and measured vapor temperatures at several elevations in the core are presented in Figs. 53 through 63. The initial vapor temperature axial distribution provided as input to the code is provided in Fig. 53. The agreement between predicted and measured vapor temperatures are in reasonable agreement to a height of 2.438 m (Figs. 54–60). Dimensional effects are observed in the test; a 1D representation of the core is used in the TRAC model. The multidimensional behavior in the test is particularly evident at the 2.438-m (8-ft) level as shown in Fig. 60. By referring to Fig. 44, it can be seen that at the steam probes at locations 10L and 4F are separated by a distance equivalent to slightly more than 55% of the inner diameter of the shroud. With the exception of the first 100 s of the transient, the TRAC-calculated vapor temperature lies between the two measured values. A similar relationship between multiple measured vapor temperatures and the TRAC-calculated vapor temperature occurs at the 1.702-m level (Fig. 57). At the

2.819-m and higher levels of the core, the predicted vapor temperature is significantly higher than measured (Figs. 61–63).

The predicted and measured differential pressures across 12, 1-ft segments through the core are presented in Figs. 64 through 75. The pressure differentials are interpreted as a direct measurement of liquid present between each set of pressure taps. The predicted and measured differential pressure results are consistent with the cladding thermal discussions presented above. With the exception of the bottom four 1-ft segments (Figs. 64–67), the calculated pressure differentials are in minimal agreement with the data.

The differential pressure trace corresponding to the heater-rod cladding temperature history at the 0.305-m level (Fig. 46) is shown in Fig. 64. A slightly slower initial accumulation of liquid at this level results in the slightly delayed peak cladding turnaround time. The predicted post-turnaround cooling mirrors the measured rate until the predicted accumulation of liquid stalls at 15 s and the cooling rate is slowed until ~35 s when the coolant again begins to increase to fill this level with liquid.

The differential pressure trace corresponding to the heater-rod cladding temperature history at the 0.991-m level (Fig. 47) is shown in Fig. 67. The peak cladding temperature and quench time are in reasonable agreement with the data. At this level, the code predicts a too-rapid filling with liquid, and the predicted cooling rate immediately after the cladding temperature begins to decrease is too high.

The differential pressure trace corresponding to the heater-rod cladding temperature history at the 1.981-m level (Fig. 48) is shown in Fig. 70. At this level, the code predicts a too-rapid filling with liquid, and the predicted cooling rate is too high, resulting in an early quench. In addition, sloshing oscillations beginning at ~150 s cause the corresponding small reheat and cooling cycle observed in the cladding response. The cause of these oscillations has not been thoroughly investigated, but they are clearly nonphysical.

The differential pressure trace corresponding to the heater-rod cladding temperature histories at the 2.819 and 3.048-m levels (Figs. 49 and 50) is shown in Fig. 73. At this level, the code again underpredicts the liquid inventory until 200 s with the resultant overprediction of cladding temperature. Beginning at 200 s, the code predicts extensive sloshing, which cools the heater rods at these elevations. At the 2.819-m level, quenching is predicted to occur 120 s early. At the 3.048-m level, the predicted temperature trace mirrors that measured until 550 s, at which time quenching is observed in the test but not predicted by the code, which shows the heat supplied to the rod and the cooling to be in balance.

The differential pressure trace corresponding to the heater-rod cladding temperature histories at the 3.353 and 3.505-m levels (Figs. 51 and 52) is shown in Fig. 75. At this level, the code underpredicts the liquid inventory. Therefore, too little cooling is predicted and the peak cladding temperatures are higher than measured, and the quench times are late.

The total core predicted and measured ΔPs are shown in Fig. 76. TRAC overpredicts the core liquid content and distribution in that too much liquid resides in the core except at the highest elevations where there is too little liquid. The refill-dump cycles beginning at 200 s are nonphysical, and the source of these must be traced and understood. This has not yet been done.

5.4.2. Conditional Pedigree

Figures 77 through 108 contain the results of the FLECHT-SEASET Reflood experimental data compared with the TRAC output using the Conditional Pedigree Coefficients. Although there are detectable differences between the two calculations, they are, in all major respects, similar. Specifically, the cladding temperature is overpredicted at the higher core elevations, and this overprediction is related to an underprediction of liquid later in the test above the quench front.

Several of the differences are described to illustrate the similarities. After the cladding temperature peaks at the 0.991-m level, the cladding temperature decreases more rapidly for the conditional pedigree case (Fig. 79) than for the absolute pedigree case (Fig. 47). The differences are attributed to the additional coolant present in the conditional pedigree prediction (Fig. 99) compared with the absolute pedigree prediction (Fig. 67). The peak cladding temperatures, turnaround times, and quench times are similar.

At the 2.819-m level, the predicted cladding-temperature response for the conditional pedigree case (Fig. 81) is in closer agreement with the data than the absolute pedigree case (Fig. 49). The differences are once again attributed to differences in the coolant present at this elevation for the conditional pedigree case (Fig. 105) and absolute pedigree case (Fig. 73). For the conditional pedigree case, the sloshing oscillations begin at 150 s, 50 s earlier than for the absolute pedigree case. As a consequence, enhanced cooling is predicted, and the overprediction of cladding temperature is reduced relative to the absolute pedigree case. In addition, the intensity of the sloshing oscillations appear to be less than for the absolute pedigree case, and thus the overcooling is limited and the quench time is much closer to that observed in the test. The sloshing is not observed in the data.

At the 3.505-m level, the predicted cladding thermal response for the conditional pedigree (Fig. 84) and the absolute pedigree (Fig. 52) cases are very similar. Extensive overheating is predicted in both cases. Again, we speculate that the grid spacers in the test appear to have the greatest cooling effect in the upper regions of the core. The grid spacers are not modeled in this calculation but are modeled in other calculations with the TRAC code; the grid spacer model, although seriously flawed, did provide a strong indication of the influence of the grid spacer.[41]

Although the conditional pedigree prediction of cladding thermal performance at the 2.819-m level is better than the absolute pedigree prediction, we must emphasize that the phenomena that resulted in the improvement do not appear to have a physical counterpart in the test. Thus, two sources of inquiry regarding code deficiencies should be pursued. The first is the source of the nonphysical sloshing or oscillatory behavior. The second is the source of the underprediction of liquid in the various levels above the quench front.

Comparisons of the predicted and measured differential pressures across the entire core for the conditional pedigree (Fig. 108) and absolute pedigree (Fig. 76) cases show that both overpredict the total amount of liquid in the core throughout most of the transient. Both predictions show a sawtooth behavior that is clearly nonphysical.

6.0. SUMMARY

A quenching model has been developed and implemented into the modernized TRAC computer code (TRAC-M) to improve the ability to predict simultaneous bottom and top quenches during either blowdown or reflooding of a PWR reactor simulation. Following the philosophy of Nelson and Unal,[14] correlations known to apply to the defined flow regimes were used. The closure set is called the "Absolute set" where the correlation set uses the correlation as originally proposed by its developer. We must realize that even though these correlations were in their original form, all interpolating functions were retained to produce continuity between their defined ranges of applicability. Also, new models required and developed by Nelson and Unal (e.g., transition boiling) were retained within the Absolute set. These additional models have a significant impact on some simulations, and the interpolating functions can also dominate closure evaluation. This leads to similar results in the majority of comparisons.

The fundamental issue lies in the definition of an Absolute set that is defensible based on physics yet also allows the code to execute. A study of how one minimizes the regions covered by the interpolating functions has not been undertaken. Such a study might appear straightforward in terms of just adjusting the end points and functional form, even if it is potentially time consuming. Unfortunately this process would involve all the issues of time and spatial averaging and phenomenological coupling discussed earlier and in Appendix A. Within the framework of a finite-difference quasi-steady code such as TRAC, these issues manifest themselves as follows: time averaging is reflected by the "limitations" placed on closure changes, and spatial averaging is reflected within the nodalization and the flow maps used to determine closure correlation selection.

The "Conditional set" of correlations was defined to be that set developed by Nelson and Unal.[14] These correlations used the "kernel" or "functional" dependence of the original correlation and modified only its magnitude by use of a multiplier. (The same set of multipliers as defined by Nelson and Unal were used.) When no correlations were available for given regions, the Nelson and Unal weighting functions between the known regimes were used to represent the unknown quantities. These weighting functions were the same as the "interpolating functions" used within the "Absolute Set" noted above. As noted by Nelson and Unal, the need to develop weighting functions to bridge various flow regimes is one measure of the current state of the art. The development of the kernels, new correlations, and interpolating functions was undertaken within the framework of time and spatial averaging and phenomenological coupling (and the limits imposed within that framework) for the Conditional set.

Within a nonlinear optimization effort, it is possible to develop an "Optimized Set" of closure models. Whereas an optimization process was used to optimize a number of coefficients for various correlations in separate test cases, no complete overall optimization was completed because of early termination of that portion of the project.

Realizing the difficulty of coupling interrelated closure relationships and the requirements imposed by temporal and spatial averaging, we believe that model development in the future using optimization is required to properly simulate multidimensional, multiple-fields, nonlinear phenomena. However in such cases, the model developer must realize that the technique does not replace his or her expertise. The developer must be cautious not to become preoccupied with the optimization process. Most importantly, the model-developer must work with the physics of the phenomena present. Is an improved model needed for a particular phenomenon alone? What time scale should the code represent? Is the regime map valid or does it need additional consideration or refinement? Do shortcomings exist within a current correlation that the comparisons and optimization process are indicating? The optimization process cannot provide the model developer with these answers or perspectives. Just for the original correlation, the form of the correlation, denoted as f(x,y,z, ...), must be the correct representation (see Fig. 3a) for the optimizer to produce a valid model.

A methodology for model development or refinement using optimization was developed and presented. A process was defined that allows the model developer to utilize the power of computing to enhance modeling efforts and a number of examples were presented within Appendix D that did individually improve the results.

Perhaps more important than the definition of the process were the tools developed for optimization. These tools allow a better understanding of the simulation characteristics. These tools may be applied independent of optimization and were in fact used to generate the majority of the results presented within this study. These tools include time averaging of various thermal and hydrodynamic properties to allow better comparison to data, scripts to run multiple runs and handle the data output, and scripts or tools to automate the multiple run comparisons. These capabilities were used to generate many of the plots in this report that are able to provide the broader understanding for the various data sets.

A number of shortcomings with this model development can be identified as follows:

- Ishii's work on modeling interfacial drag coefficients remains the best-understood set of closure relationships; however, it lacks much in terms of specifying how to model the oscillating flows that frequently occur, even under simple forced reflooding conditions.

- The flow-regime map still employs the heuristic approximations developed by Nelson and Unal,[14] which deal with transient effects. Solution of this issue suggests different methods other that the local-instantaneous methodology employed in the majority of current United States codes. The most obvious is the use of transport equations to conserve properties of particular importance. This concept is not new and was at one time implemented in a research version of the TRAC code.

- The current formulation of the axial-distance-dependent transition-boiling model remains quite empirical. No attempt has been made to develop a detailed mechanistic model due to the lack of the necessary experimental data. The determination of the coefficient *B* in the transition boiling model developed by Nelson and Unal[14] still needs improvement. In particular, downflow post-CHF and quenching data that span the pressure and flow variation believed to occur during blowdown are needed. Very low flow rates within the Berkeley quenching experiments also show a need for additional information and refinement.

- The original estimation of heat-transfer enhancement due to near-wall liquid effects also remains the same as that of Nelson and Unal,[14] i.e., empirical. Again, we did not attempt to develop a detailed mechanistic model because of a lack of necessary experimental data. Our ability to separate the phasic components remains an issue here. It is clear from the Winfrith comparisons that improvement is needed to represent the broad spectrum of flow rates; from the INEL comparisons it is clear that improvement is needed to represent the pressure effects, in particular around 3.6 MPa.

- Large uncertainties exist in the interfacial heat transfer resulting in phase change. Not only are applicable HTCs limited, but models and data for the interfacial area are also minimal.

- Wet-unheated walls need additional work. While a model is present that makes an effort to address this issue, two-field codes can never allow the proper representation of the liquid films that occur in systems with wet-walls present. Similarly, the downstream quenched region of a fuel rod experience the same needs.

Three-field codes are required to address fully this issue. However, the introduction of the third field requires the definition of closure packages that represent the closure phenomena for the third field. These closure packages may be the same as those already within the code, or they may require new models. Thus, the model developer may be forced to deal with multidimensional and multifield issues as well as thermal and mechanical nonequilibrium. Again, we believe optimization gives the model developer a method to develop and study these packages better.

- The grid spacer model remains that originally implemented by Nelson and Unal.[14] It is a very simple model that needs improvement[41]. This might be undertaken in the current two-field configuration; however, three fields are needed, and the problem is similar to the wet-wall issue noted above.

7.0. CONCLUSIONS

A quenching model has been developed and implemented into the TRAC-M computer code to improve our ability to predict simultaneous bottom and top quenches during either blowdown or reflooding of a PWR reactor simulation. The model was adapted from earlier work by Nelson and Unal,[14] Unal and Nelson,[15] and Unal et al.[16] This work also investigates the potential use of nonlinear optimization techniques within the development process of complex interrelated closure models. Because the optimization work was terminated before its completed application to model development, a summary of the optimization work is included within the Appendices.

The quenching model is built around the flow-regime map of Ishii and his coworkers. The modifications of Nelson and Unal,[14] are retained to account for transient situations. Because the post-CHF model is position-dependent, an implementation using a relative coordinate system was required to allow both bottom-up and top-down situations. The necessary closure relations, which include interfacial heat transfer, interfacial drag, and wall heat transfer, were discussed relative to the flow map. The new model in the code allows for different models for the bottom-up and top-down quenching processes. However, currently the two closure models are the same for both directions.

The selection of one of three closure sets is possible via the input. One set, the Absolute set, used the correlations as originally proposed by the developer. A second set, the Conditional set, used the same correlations but as modified by Nelson and Una.[14] The third set, called the Optimized Set, can be adjusted via the code within the framework of nonlinear optimization or can be defined to be a third set of correlations that are not optimized.

Results for the Absolute and Conditional sets were found to be quite similar. This similarity resulted from the use of the transition and near-wall heat-transfer models developed by Nelson and Unal[14] and the interpolating functions required for continuity between correlations dominate closure evaluation. The fundamental issue lies in the definition of an Absolute set that allows the code to execute satisfactorily.

We believe that future model development using optimization is required to simulate properly multidimensional, multifield nonlinear phenomena. However in such cases, the model developer must realize that the technique does not replace his or her expertise. Most importantly, the model-developer must work with the physics of the phenomena present. A methodology for model development or refinement using optimization was developed and presented. A process was defined that allows the model developer to utilize the power of computing to enhance modeling efforts, and a number of examples were presented.

Tools were developed that allow a better understanding of the simulation characteristics. These tools generated the majority of the results presented within this study. These tools include the time averaging of various thermal and hydrodynamic properties to allow (1) better comparison with data, (2) scripts to run multiple runs and handle the data output, and (3) scripts or tools to automate the multiple run comparisons.

In terms of this model development effort, several shortcomings were identified. Overall, the results are similar to those obtained by Unal et al.[16] for the tube experiments. The results for FLECHT-SEASET, the only bundle data used for the model development, are in minimal to reasonable agreement with the data. During a related study, we determined that the TRAC-M grid-spacer model is serious flawed.[41] The calculated results in this study, therefore, did not include a grid-spacer model. We do believe, however, that a complete assessment of the code adequacy for FLECHT SEASET reflood tests cannot be completed unless the code contains a physically-based grid-spacer model.

REFERENCES

1. M. Ishii and G. DeJarlais, "Flow Regime Transition and Interfacial Characteristics of Inverted Annular Flow," *Nuclear Engineering and Design* **95**, 171–184 (1986).

2. M. Ishii and G. DeJarlais, "Flow Visualization Study of Inverted Annular Flow of Post Dryout Heat-Transfer Region," *Nuclear Engineering and Design* **99**, 187–199 (1987).

3. N. T. Obot and M. Ishii, "Two-Phase Flow Regime Transition Criteria in Post-Dryout Region Based on Flow Visualization Experiments," *Int. J. Heat Mass Transfer* **31**(12), 2559–2570 (1988).

4. S. Nijhawan, J. C. Chen, R. K. Sundaram, and E. J. London, "Measurement of Vapor Superheat in Post-CHF Boiling," *Trans. ASME J. of Heat Transfer* **102**(3), 465–470 (1980).

5. D. G. Evans, S. W. Webb, and J. C. Chen, "Axially Varying Vapor Superheats in Convective Boiling," *ASME J. of Heat Transfer* **107**, 663–669 (1985).

6. R. C. Gottula, K. G. Condie, R. K. Sundaram, S. Neti, J. C. Chen, J and R. A. Nelson, "Forced Convection, Nonequilibrium, Post-CHF Heat Transfer," *Trans. of Twelfth Water Reactor Safety Research Int. Meet.* (Gaithersburg, Maryland, 1985).

7. C. Unal, K. Tuzla, O. Badr, S. Neti, and J. Chen, "Experimental Study of Nonequilibrium Post-CHF Heat Transfer in Rod Bundles," *Proceedings of The Eight International Heat Transfer Conference*, 2417 (1986).

8. M. J. Loftus, L. E. Hochreither, C. E. Convay, E. R. Rosal, and A. H. Wenzel, "Non-Equilibrium Vapor Temperature Measurements in Rod Bundles and Steam Generator Two-Phase Flow," in Proceedings of the OECD(NEA) CSNI 3rd Specialist Meeting on Trans. Two-Phase Flow, CSNI Report No. 61. (1981).

9. J. C. Chen, "A Short Review of Dispersed Flow Heat Transfer in Post-Dryout Boiling," *Nuclear Engineering and Design* **95**, 375–383 (1986).

10. C. Unal, K. Tuzla, C. A. Tuzla, and J. C. Chen, "Vapor Generation Model for Dispersed Drop Flow," *ANS Proceedings of the 1989 National Heat Transfer Conference* Vol. 4. (1989).

11. G. Yadigaroglu, R. A. Nelson, V. Teschendorff, Y. Murao, J. Kelly, and D. Bestion, "Modeling of reflooding," *Nuclear Eng. & Design* **145**, 1–35 (1993).

12. D. Liles, et al., "TRAC-PF1/MOD1: An Advanced Best-Estimate Computer Program for Pressurized Water Reactor Thermal-Hydraulic Analysis," Los Alamos National Laboratory report LA-10157-MS, NUREG/CR-3858 (1986).

13. R. A. Dimenna, et al., "RELAP5/MOD2 Models and Correlations," Nuclear Regulatory Commission report NUREG/CR-5194, EGG-2531 (1988).

14. R. A. Nelson and C. Unal, "A Phenomenological Model of the Thermal Hydraulics of Convective Boiling During the Quenching of Hot Rod Bundles Part I: Thermal Hydraulic Model," *Nuclear Eng. & Design* **136**, 277–298 (1992).

15. C. Unal and R. A. Nelson, "A Phenomenological Model of the Thermal Hydraulics of Convective Boiling During the Quenching of Hot Rod Bundles Part II: Assessment of the model with steady-state and transient post-CHF data," *Nuclear Eng. & Design* **136**, 299–318 (1992).

16. C. Unal, E. Haytcher, and R. A. Nelson, "A Phenomenological Model of the Thermal Hydraulics of Convective Boiling During the Quenching of Hot Rod Bundles Part III: Model Assessment Using Winfrith Steady-State, Post-CHF, Void-Fraction and Heat-Transfer Measurements and Berkeley Transient-Reflood Test Data," *Nuclear Eng. & Design* **140**, 211–227 (1993).

17. J. Spore, et al., "TRAC-PF1/MOD2: An Advanced Best-Estimate Computer Program for Pressurized Water Reactor Thermal-Hydraulic Analysis," LA-12031-M, NUREG/CR-5673 (1993).

18. R. O'Mahoney, "Time Step and Mesh Size Dependence in the Heat Conduction Solution of a Semi Implicit, Finite Difference Scheme for Transient Two-Phase Flow," Winfrith United Kingdom Atomic Energy Authority report AEEW-M-2590 (1989).

19. K. P. Yu and G. Yadigaroglu, "Heat Transfer Immediately Downstream of the Quench Front During Reflooding," ASME 79-HT-48, 18th National Heat Transfer Conference, San Diego, CA (1979).

20. G. Yadigaroglu and K. P. Yu, "Heat Transfer at and Near the Quench Front During Reflooding," Trans. ANS 31, 385–387 (1979).

21. S. W. Webb and J. C. Chen, "A Two-Region Vapor Generation Rate Model for Convective Film Boiling," Int. Post-Dryout Heat Transfer Workshop, Salt Lake City (1984).

22. M. K. Denham, "Inverted Annular Film Boiling and The Bromley Model," Winfrith United Kingdom Atomic Energy Authority report AEEW-R 1590 (1983).

23. C. Unal, K. Tuzla, O. Badr, S. Neti, and J. Chen, "Convective Boiling In a Rod Bundle: Axial Variation of Nonequilibrium Evaporation Rates," *Int. J. Heat Mass Transfer* **31**(10), 2091–2100 (1988).

24. A. F. Varone, Jr. and W. M. Rohsenow, "Post-Dryout Heat Transfer Predictions," *Nucl. Eng. and Design* **95**, 315–327 (1986).

25. K. Kiangah and V. K. Dhir, "An Experimental and Analytical Study of Dispersed Flow Heat Transfer," *Int. J. of Experimental Thermal and Fluid Science* **2**, 410–424 (1989).

26. L. A. Bromley, "Heat Transfer in Stable Film Boiling," Chem. Eng. Prog. **46**(5), 221–227 (1950).

27. M. Mosaad and K. Johannsen, "Experimental Study of Steady-State Film boiling Heat Transfer of Subcooled Water Flowing Upwards in a Vertical Tube," *International Journal of Experimental Thermal and Fluid Science*, No. 2, 477–493 (1989).

28. M. Ishii, Personal Communication with R. Nelson (July 1987).

29. Y. Y. Hsu and R. W. Graham, *Transport Processes in Boiling and Two-Phase Systems* (Hemisphere Publishing Corporation, Washington, 1976).

30. K. Tuzla, C. Unal, O. Badr, S. Neti, and J. C. Chen, "Thermodynamic Nonequilibrium in Post-Critical-Heat-Flux Boiling in a Rod Bundle," Nuclear Regulatory Commission report NUREG/CR-5095, Vols. 1–4 (1987).

31. J. G. Collier, *Convective Boiling and Condensation* (McGraw-Hill Book Company, New York, 1972).

32. H. Schlichting, *Boundary-layer Theory* (McGraw-Hill Book Company, New York, 1979).

33. M. Ishii and T. C. Chawla, "Local Drag Laws in Dispersed Two-Phase Flow," Nuclear Regulatory Commission report NUREG/CR 1230 (1979).

34. K. A. Williams, "On the Explanation and Calculation of Anomalous Reflood Hydrodynamics in Large PWR Cores," Winter ASME Meeting, Miami, Florida, WA/HT-30 (1985).

35. K. Hirano, et al., "Data Report on Large Scale Reflood Test-14, CCTF Test CI-5 (Run 014)," JAERI memo 57-214 (1982).

36. G. B. Wallis, *One- Dimensional Two-Phase Flow* (McGraw-Hill Book Company, New York, 1969).

37. R. Seban, et al., "UC-B Reflood Program: Experimental Data Report," NP-743, Research Project 248-1 (1978).

38. "PWR FLECHT SEASET Unblocked Bundle, Forced and Gravity Reflood Task Data Report," Vol. 2, Westinghouse Electric Corporation, NUREG/CR-1532-V2.

39. D. Swinnerton, R. A. Savage, and K. G. Pearson, "Heat Transfer Measurements in Steady-State Post-Dryout at Low Quality and Medium Pressure," AEA

Thermal Reactor Services, Physics and Thermal Hydraulic Division Report AEA-TRS-1045, Winfrith, United Kingdom Atomic Energy Report AEEW-R 2503 (1990).

40. D. Swinnerton, M. L. Hood, and K. G. Pearson, "Steady State Post-Dryout at Low Quality and Medium Pressure Data Report," Winfrith United Kingdom Atomic Energy Authority report AEEW-R 2267 (1988).

41. B. E. Boyack, J. F. Lime, D. A. Pimentel, J. W. Spore, and J. L. Steiner, "TRAC-M/F77, Version 5.5, Developmental Assessment Manual," Los Alamos National Laboratory draft document (March 1998).

TABLE 1
POST-CHF FLOW-REGIME TRANSITION CRITERIA

Regime	Ishii's Corr.	Implementation in TRAC	TRAC Implemented void limits
Smooth Inverted Annular Flow (IAF)	$\frac{Z}{D} = 60\ Ca^{1/2}$	$\frac{Z}{D} = 60\ Ca^{1/2}$	$0.05 < \alpha < .3$
Rough/wavy IAF	$\frac{Z}{D} = 295\ Ca^{1/2}$	$\frac{Z}{D} = 295\ Ca^{1/2}$	$0.3 < \alpha < 0.4$
Agitated IAF	$\frac{Z}{D} = 595\ Ca^{1/2}$	$\frac{Z}{D} = 595\ Ca^{1/2}$	$0.4 < \alpha < 0.75$
Dispersed (postagitated IAF)			$0.75 < \alpha < 0.98$
Highly dispersed			$\alpha > 0.98$

TABLE 2
COEFFICIENT B FOR DETERMINING TRANSITION BOILING

$$B = \text{Cons.Ca}_l^{-0.5} \qquad \text{if } \alpha \le \alpha_{\text{low}},$$

$$B = e^{\left(\ln\left(\text{Cons.Ca}_l^{-0.5}\right)+\left(\frac{\alpha-\alpha_{\text{low}}}{\alpha_{\text{high}}-\alpha_{\text{low}}}\right)^{\psi}\left(7.601-\ln(\text{Cons.})\text{Ca}_l^{-0.5}\right)\right)} \qquad \text{if } \alpha_{\text{low}} < \alpha < \alpha_{\text{high}},$$

$$B = 2000 \qquad \text{if } \alpha_{high} \le \alpha,$$

where

$$\psi = 1.5$$

$$\alpha_{\text{low}} = 0.8$$

$$\alpha_{\text{high}} = 0.995$$

$$\text{Cons.} = C_0 + C_1\,\text{Re}_v + C_2\,\text{Re}_v{}^2 \begin{cases} C_0 = 18.75 \\ C_1 = 10^{-4} \\ C_2 = -3\times10^{-6} \end{cases} \qquad \text{if } \text{Re}_v \le 2000,$$

$$\text{Cons.} = D_0 + D_1\,\text{Re}_v + D_2\,\text{Re}_v{}^2 \begin{cases} D_0 = 10.425 \\ D_1 = -1.925\times10^{-3} \\ D_2 = 1.25\times10^{-7} \end{cases} \qquad \text{if } \text{Re}_v > 2000,$$

$$\text{Ca}_l = \left(\frac{V_l\mu_l}{\sigma}\right)_{\text{CHF}}$$

$$\text{Re}_v = \left(\frac{\alpha\rho_v D_h V_v}{\mu_v}\right)_{\text{CHF}}$$

TABLE 3
WALL-TO-FLUID HEAT-TRANSFER CORRELATIONS IN FILM BOILING

Regime	**Wall-to-Liquid**	**Wall-to-Vapor**
Smooth IAF	$h_{Den} + h_{ra}$, where $h_{Den} = 0.4472\, k_v \left[\frac{g\,(\rho_l - \rho_v)}{\mu_v V_v}\right]^{\frac{1}{2}}$ and $h_{ra} = (0.9999-\alpha)\,\sigma_r\,\varepsilon_r \frac{(T_w^4 - T_{sat}^4)}{(T_w - T_l)}$	not used
Rough/wavy IAF	$h_{Den}\left(\frac{Z_{slab} - Z_{sm}}{Z_{rw} - Z_{sm}}\right)^{0.5} +$ $h_{mod-Brom}\left(\frac{Z_{slab} - Z_{sm}}{Z_{rw} - Z_{sm}}\right)^{0.9} + h_{ra}$ where $h_{mod-Brom} = h_{Brom} F\left(Re_{v,ag}\right)$ $h_{Brom} = 0.62 \left(\frac{\rho_g k_g^3 (\rho_l - \rho_g)\, g\, h'_{fg}}{\mu_g (T_w - T_{sat})\lambda}\right)^{0.25}$ $F\left(Re_{v,ag}\right) = -0.51498 + 6.4895\left(10^{-4}\right) Re_{v,ag}$ where $0.2 \le F\left(Re_{v,ag}\right) \le 1$ $Re_{v,ag} = \left(\frac{\alpha \rho_v D_h V_v}{\mu_v}\right)_{ag}^{\left(1 + (1-0.95)\frac{P - 2(10^5)}{10^6 - 2(10^5)}\right)}$ where $900 \le Re_{v,ag} \le 2300$	$1.2\, h_{W-C}$ where $h_{w-c} = \frac{f}{2} G X_a C_{p,vf} Pr_{vf}^{-2/3}\left(1 + F_s\right)$ $F_s = 250\left(\frac{P}{P_{cr}}\right)^{0.69}\left(\frac{1 - X_{ac}}{X_{ac}}\right)^{0.49} Re_v^{-0.55}$ $Re_v = \frac{\rho_v D_h V_v}{\mu_v}$
Agitated and Postagitated IAF	$h_{Brom}\ (F(Re_{v,ag})(\frac{0.75-\alpha}{0.75-\alpha_2})^{F_1(Re_{v,ag})}$ $+ h_{ra}$ where $F_1\left(Re_{v,ag}\right) = 14.61 - 2.442\left(10^{-2}\right) Re_{v,ag}$ $+1.4313\left(10^{-5}\right) Re_{v,ag}^2 - 2.7797\left(10^{-9}\right) Re_{v,ag}^3$ where $0.7 \le F_1\left(Re_{v,ag}\right) \le 2.0$	$1.2\, h_{W-C}$
Highly Dispersed	not used	$1.2\, h_{W-C}$

TABLE 4
INTERFACIAL-DRAG MODELS

Flow Regime	Characteristic Dimensions or Number	Void Fraction	Drag Coefficient or Friction Factor
Subcooled Nucleate Boiling	$Y_b = C\left[\frac{\sigma D_h}{\frac{0.01197\ G^2}{2\rho_l}}\right]^{\frac{1}{2}}$	$\alpha_{fr} = \alpha_g - \alpha_w$ where	$C_{i,fr} = \alpha\frac{\alpha_{fr}}{d_b} f(\alpha)\,\zeta_\rho \frac{(C_1 V_v - C_0 V_l)^2}{(V_v - V_l)^2}$ where
	$d_b = 2\left[\frac{\sigma}{g\Delta\rho}\right]^{\frac{1}{2}}$	if $T_l \le T_{sat} + 5K$, $\alpha_w = \frac{\Pi}{6}\frac{Y_b}{D_h}$	$f(\alpha) = \left[\frac{1+17.67\ (1-\alpha_{fr})^{1.3}}{18.76\ (1-\alpha_{fr})^{1.5}}\right]^2$
	$\varepsilon = 0.01 Y_b$	if $T_{sat} - 5K \le T_l < T_{sat}$ $\alpha_w = \frac{\Pi}{6}\frac{Y_b}{D_h}\left[0.2\left(T_{sat} - T_l\right)\right]$ if $T_{sat} \le T_l$, $\alpha_w = 0$	$C_{i,sb} = \frac{2\rho_g}{D_h}\left[1.14 - 2.0\log_{10}\left(\frac{\varepsilon}{D_h}\right)\right]^{-2}$
	The momentum-weighted final $C_{i,sb}$ is given by		
		if $\alpha_w = 0$	$C_{i,sb} = \frac{0.00175 C_{i,fr}}{\alpha_{fr}}$
		if $\alpha_w < 0$	$C_{i,sb} = \frac{C_{i,w} V_l^2 + 0.00175 C_{i,fr} V_r^2}{\left(\alpha_{fr} + \alpha_w\right) V_r^2}$
Smooth IAF	$Re_g = \frac{(D_h - D_c)\alpha_g \rho_v V_v}{2\mu_v}$		$C_{i,sm} = 2\zeta_g f_{i,sm} \frac{(1-\alpha_g)^{1/2}}{D_h}$ $f_{i,sm} = \frac{16}{Re_g}$ $f_{i,sm} = 0.079 Re_g^{-0.25}$
Rough/wavy IAF	$\varepsilon = 80 \times 0.613\left[\frac{\sigma}{g(\rho_l - \rho_v)}\right]^{1/2} N_{\mu g}^{1/3}$		$C_{i,rw} = 2\rho_g f_{i,rw} \frac{(1-\alpha_g)^{1/2}}{D_h}$
	if $\varepsilon/D_h < 1$		$f_{rw} = \left[1.14 - 2.0\log_{10}\left(\frac{\varepsilon}{D_h}\right)\right]^{-2}$
	if $\varepsilon/D_h > 1$		$f_{rw} = 0.76946753$

TABLE 4 (cont)
INTERFACIAL-DRAG MODELS

Flow Regime	Characteristic Dimensions or Number	Void Fraction	Drag Coefficient or Friction Factor
Highly Dispersed IAF	$d_d=1.838\left[\frac{\sigma}{g\,(\rho_l-\rho_v)}\right]^{1/2} N_{\mu g}^{1/3}$	$\alpha_{dd}=1-\alpha_{lf}-\alpha_g$	$C_{i,dd}=\frac{0.75\,\alpha_{dd}\,\rho_g C_d}{d_d}$
	$N_{\mu g}=\frac{\mu_g}{\sqrt{\rho_g\sigma\sqrt{\frac{\sigma}{g(\rho_l-\rho_g)}}}}$	$\alpha_f=\frac{Pe\,\delta_f\,F_u}{A}$	$C_d=\frac{24(1+0.1\ Re_d^{0.75})}{Re_d}$
	$Re_d=\frac{\rho_d d_d(V_v-V_d)(1-\alpha_{dd})^{2.5}}{\mu_v}$	$\alpha_{lf}=5\left[\frac{\alpha_{df}-\alpha_g}{\alpha_{df}-\alpha_{ag}}\right]^{0.5} F_u(1-\alpha_g)$	$C_{i,f}=\frac{2\,\rho_g f_{i,f}}{D_h}$
	$V_d=V_v-2.462\left[\frac{(\rho_l-\rho_v)\,g\,d_d}{2\,\rho_v}\right]^{1/2}$		$f_{i,f}=0.005\,(1+75\,\alpha_f)$
	$\delta_f=\frac{0.0025\ \rho_l\,V_g^2}{g\,\rho_l-\frac{0.75\ \rho_g V_g^2}{Dh}}$		$C_{i,df}=\frac{C_{i,dd}V_r^2+C_{i,f}V_v^2}{\left[V_v-\frac{\alpha_{dd}V_d}{(1-\alpha_g)}\right]^2}$

TABLE 5
INTERFACIAL HEAT TRANSFER TUNABLE PARAMETER DESCRIPTIONS

TRAC Variable Name	Description
fgam1	multiplier on the heat-transfer coefficient (hA) calculated using the Unal-Chen model for vapor to interface heat transfer
fgam2	multiplier on the heat-transfer coefficient (hA) calculated using the Unal-Chen model for vapor to interface heat transfer
fgam3	exponent on the heat-transfer coefficient (hA) calculated using the Unal-Chen model for vapor to interface heat transfer
fgamw	multiplier on the heat-transfer coefficient (hA) calculated using the Unal-Chen model for vapor to interface heat transfer
qvapor	heat-transfer rate from vapor to the phase interface, $\dot{q}_{vap,calc}$
spacer	multiplier on the heat-transfer coefficient (hA) for grid spacer effects
tvn	vapor temperature, $T_{vap,calc}$ (tvnj in modernized TRAC code)

TABLE 6
INTERFACIAL-DRAG TUNABLE PARAMETER DESCRIPTIONS

TRAC Variable Name	Description
cfzi	length-weighted drag coefficient, C_i
fac008	multiplier on the subcooled-nucleate-boiling-regime drag coefficient
fac009	multiplier on the subcooled-nucleate-boiling-regime void fraction
fac010	multiplier on the momentum-weighted drag coefficient in the annular-mist flow regime
fac011	multiplier on the regime drag-coefficient upper limit in the annular-mist flow regime
fac012	multiplier on the regime drag-coefficient lower limit in the annular-mist flow regime
fcdrop	multiplier on the regime drag coefficient in the lightly dispersed annular-mist flow regime
fc1	multiplier on the subcooled-nucleate-boiling-regime interfacial shear
fc2	multiplier on the subcooled-nucleate-boiling-regime void fraction
fc3	multiplier on the subcooled-nucleate-boiling-regime drag coefficient
fc4	multiplier on the roughness coefficient in the rough/wavy-flow regime
fdis	multiplier on the highly dispersed flow regime drag coefficient
ffd	multiplier on the regime drag coefficient in the highly-dispersed annular-mist flow regime
ffs	multiplier on the free-stream nucleate boiling for subcooled or superheated liquid drag coefficient
fmdis	multiplier on the moderately dispersed flow regime drag coefficient
frw	multiplier on the rough/wavy-flow-regime drag coefficient
fsb	multiplier on the subcooled-boiling-flow-regime drag coefficient
fsm	multiplier on the smooth-flow-regime drag coefficient
xhvdis	exponent on smooth and rough/wavy-flow-regime drag-coefficient multipliers for high-void condition
xmdis	exponent on postagitated and large-drop-flow-regime drag-coefficient multipliers for high-void condition
xnbs	exponent on churn/turbulent-transition-flow-regime drag coefficient

TABLE 7
WALL HEAT TRANSFER TUNABLE PARAMETER DESCRIPTIONS

TRAC Variable Name	Description
adqdz	void-fraction lower bound (α_{low}) for the CHF transition-boiling heat-flux parameter, B, correlation (Table 2)
alpctr	void-fraction upper bound (α_{high}) for the CHF transition-boiling heat-flux parameter, B, correlation (Table 2)
dqcmax	maximum value of Constant (Cons. in Table 2)
dqcmim	minimum value of Constant (Cons. Table 2)
dqdzmx	maximum value of the CHF transition boiling heat flux parameter, B (Table 2)
fac013	multiplier on the condensation heat-transfer coefficient
fac014	multiplier on the condensation heat-transfer coefficient
fac015	multiplier on the natural-convection heat-transfer coefficient
fac016	multiplier on the laminar-flow heat-transfer coefficient
fac017	multiplier on the turbulent-flow heat-transfer coefficient
fac019	multiplier on the natural-convection heat-transfer coefficient in turbulent flow
facthl1	exponent on the Denham liquid heat-transfer coefficient
facthl2	exponent on the Bromley liquid heat-transfer coefficient
facthv	exponent on the vapor heat-transfer coefficient weighting factor within the film boiling regime
fdham	multiplier on the Denham inverted annular liquid film boiling
fwebb	multiplier on the vapor heat-transfer coefficient with in the film boiling regime
qtot	total heat flux from the heated surface(s) to the fluid, $q''_{wall,calc}$
rel1	zero-order coefficient (C_0) for the quadratic model of Cons. where $\mathrm{Re}_v \leq 2000$ (Table 2)
rel2	first-order coefficient (C_1) for the quadratic model of Cons. where $\mathrm{Re}_v \leq 2000$ (Table 2)
rel3	second-order coefficient (C_2) for the quadratic model of Cons. where $\mathrm{Re}_v \leq 2000$ (Table 2)
ret1	zero-order coefficient (D_0) for the quadratic model of Cons. where $\mathrm{Re}_v > 2000$ (Table 2)
ret2	first-order coefficient (D_1) for the quadratic model of Cons. where $\mathrm{Re}_v > 2000$ (Table 2)
ret3	second-order coefficient (D_2) for the quadratic model of Cons. where $\mathrm{Re}_v > 2000$ (Table 2)
tw	wall temperature, $T_{wall,calc}$
xdqdz	exponent (ψ) on the void ratio within the B parameter correlation where $\alpha_{low} < \alpha < \alpha_{high}$ (Table 2)

TABLE 8
NEW REFLOOD WALL HEAT-TRANSFER SUBROUTINES AND THEIR FUNCTION

Subroutine Name	Function
ALPINT	calculates an interpolated void fraction based on conduction cell elevation with the hydro-cell center void fractions serving as the two end points. The end points are set up by SALPBD.
DEFPNT	defines the proper pointer increments for K3, K4, K5, K5IN, and K5OUT. Also sets VSIGN to 1.0 or -1.0 for use with the velocities depending upon up flow or down flow.
DEFVELS	define the flow velocities to be used in the heat transfer. These depend on bottom-up versus top-down logic and also utilize VSIGN defined in subroutine DEFPNT.
FINDCHF	finds the CHF locations on the rod. This logic was separated from the heat-transfer coefficient subroutine (HTVSSLN) where it has historically been located.
G_HTVSSLN	ADIFOR generated version of HTVSSLN that contains the desired partial derivatives. Not part of standard TRAC code.
HTC	makes proper call to either HTCOR or HTVSSLN to determine the wall heat-transfer coefficients.
HTVSSLN	determines the phasic wall heat-transfer coefficients.
SALPBD	Sets up the end points defined by the two bounding hydro-cell centers over which the void fraction will be interpolated.
SETLOG	sets logical variables (INIT, FINISH, FIXED, BOTHALF, and TOPHALF) and case integer (ICASE) to specify cell type. These are necessary for the proper functioning of the ZDRIVE_X subroutines.
SUMIT	length averages the wall heat transfer for use by the hydraulic nodes.
TBZFCN	determines transition boiling's distance from quench front functional relationship. The first call to TBZFCN from ZDRIVE_B provides an estimate. The second call from HTC via ZDRIVE_D provides a refined calculation after the proper position of CHF is defined.
ZCORE_A	determines axial levels of CHF where two CHF levels are allowed. Initialize the remaining regime levels to CHF level.
ZCORE_B	determines remaining post-CHF regime axial positions for primary (average) rod. The "average" rod is used to control the wall heat-transfer calculation.
ZCORE_C	determines remaining post-CHF regime axial positions for secondary rods. For example, a cooler or hotter rod will have experienced a different location and this must be taken into account with defining the convective energy to be removed from the rod.
ZCORE_D	determines post-CHF regime void fractions based on their axial position. Void limits for the various post-CHF regimes are applied here to refine the axial regime levels if needed.
ZCORE_E	determines the axial position for transition boiling.

TABLE 9
FUNCTION OF THE INPUT/OUTPUT FILES IN OPTIMIZATION

File Name	Description
tracin	standard TRAC input deck
DATA	experimental data corresponding tracin
trcrst	standard TRAC restart deck
rvalue	initial r value [see Eq. (36)or Eq. (38)]
rafin	alternate tunable coefficient values input by TRAC
inclvect	flag values corresponding to tunable coefficients to determine which coefficients to include in the optimization process
gamma	flag values corresponding to the three general parts of the Penalty Function (i.e., Interfacial Heat Transfer, Interfacial Drag, and Wall Heat Transfer) that are used to exclude/include said parts
PFtmp.out	Penalty Function value and its partial derivative vector for the current TRAC run
PFtmavg1.out	time-averaged information corresponding to the Interfacial Heat-Transfer component of the Penalty Function (i.e., vapor temperature)
PFtmavg2.out	time-averaged information corresponding to the Interfacial-drag component of the Penalty Function (i.e., void fraction)
PFtmavg3.out	time-averaged information corresponding to the Wall-Heat-Transfer component of the Penalty Function (i.e., wall temperature/heat flux)
PFcrrnt_g.out	contains a list of all available non-zero partial derivatives—values in 'gamma' and 'DATA' are considered, but values in 'inclvect' are ignored
n_cntarry.out	number of axial cells contributing to each value in PF_arrytmp.out
PF_arrytmp.out	Penalty Function values corresponding to the tunable parameters (i.e., correlation contributions)
tune.out	tunable coefficient values used for current TRAC run
task.out	optimizer task information for each TRAC run iteration (traciter)
PFcoef.out	summary of the Penalty Function and the tunable coefficient values for each Minimizer iteration (mnmzriter)
PFgrad.out	summary of the Penalty Function and its gradient values for each Minimizer iteration (mnmzriter)
PFtvapinst.out	information for each TRAC run iteration (traciter)—vapor temperature
PFvoidinst.out	information for each TRAC run iteration (traciter)—void fraction
PFqinst.out	information for each TRAC run iteration (traciter)—wall heat transfer
PFgradinst.out	Penalty Function and its gradient information for each TRAC run iteration (traciter)
PFarrayinst.out	Penalty Function information with respect to each tunable coefficient for each TRAC run iteration (traciter)
PFcntrsinst.out	number of axial cells that contributed to each Penalty Function partial derivative value for each TRAC run iteration (traciter)
PFparts1.out	information used within TRAC to calculate the Penalty Function and its gradient with respect to the vapor temperature (interfacial heat transfer)
PFparts2.out	information used within TRAC to calculate the Penalty Function and its gradient with respect to the void fraction (interfacial drag)
PFparts3.out	information used within TRAC to calculate the Penalty Function and its gradient with respect to the wall temperature or heat flux (wall heat transfer)
trac.scrndmp	redirected screen dump information for the latest TRAC run

TABLE 10
FILES CONTAINING SUBROUTINES AND NAMED COMMON BLOCKS USED IN THE OPTIMIZATION PROCESS

SUBROUTINE/COMMON NAME (FILE)	PARENT ROUTINE (FILE)	DESCRIPTION
g_chen (g_chen.f)	g_htvssln (g_htvssln.f)	converted from chen (chen.f) by ADIFOR 2.0
g_corifht (g_corifht.f)	htifn (htifn.f)	performs interfacial heat-transfer calculations; converted from corifht (corifht.f) by ADIFOR 2.0
g_cpvv1 (g_cpvv1.f)	g_htvssln (g_htvssln.f)	converted from cpvv1 (cpvv1.f) by ADIFOR 2.0
g_cpvv1d (g_cpvv1d.f)	g_htvssln (g_htvssln.f)	converted from cpvv1d (cpvv1d.f) by ADIFOR 2.0
g_cpvv1h (g_cpvv1h.f)	g_htvssln (g_htvssln.f)	converted from cpvv1h (cpvv1h.f) by ADIFOR 2.0
g_hlflmr (g_hlflmr.f)	g_htvssln (g_htvssln.f)	converted from hlflmr (hlflmr.f) by ADIFOR 2.0
g_htvssln (g_htvssln.f)	htc (htc.f)	performs wall-to-fluid heat-transfer calculations; converted from rbshrz (rbshrz.f) by ADIFOR 2.0
g_hvnb (g_hvnb.f)	g_htvssln (g_htvssln.f)	converted from hvnb (hvnb.f) by ADIFOR 2.0
g_hvwebb (g_hvwebb.f)	g_htvssln (g_htvssln.f)	converted from hvwebb (hvwebb.f) by ADIFOR 2.0
g_rbshrz (g_rbshrz.f)	cif3n (cif3n.f)	performs interfacial-drag calculations; converted from htvssln (htvssln.f) by ADIFOR 2.0
g_satprd (g_satprd.f)	g_htvssln (g_htvssln.f)	converted from satprd (satprd.f) by ADIFOR 2.0
g_satprh (g_satprh.f)	g_htvssln (g_htvssln.f)	converted from satprh (satprh.f) by ADIFOR 2.0
g_satprs (g_satprs.f)	g_htvssln (g_htvssln.f)	converted from satprs (satprs.f) by ADIFOR 2.0
g_tbzfcn (g_tbzfcn.f)	g_htvssln (g_htvssln.f)	converted from tbzfcn (tbzfcn.f) by ADIFOR 2.0
g_thcv (g_thcv.f)	g_htvssln (g_htvssln.f)	converted from thcv (thcv.f) by ADIFOR 2.0
g_viscv (g_viscv.f)	g_htvssln (g_htvssln.f)	converted from viscv (viscv.f) by ADIFOR 2.0
g_viscvd (g_viscvd.f)	g_htvssln (g_htvssln.f)	converted from viscvd (viscvd.f) by ADIFOR 2.0
g_viscvh (g_viscvh.f)	g_htvssln (g_htvssln.f)	converted from viscvh (viscvh.f) by ADIFOR 2.0

TABLE 11
SUMMARY OF WINFRITH POST-CHF UP-FLOW EXPERIMENTS USED WITH TRAC

Run #	Inlet Pressure		Inlet Temperature		Total Power		Inlet Mass Flowrate		'X' denotes Existing Data			Grouping in Inlet Mass Flowrate
	MPa	psi	°K	°F	W	Btu/hr	kg/m^2 s	kg/s	α	T_v	q_{fluid}	
363	0.499	72.37	419.95	296.24	3498	11936	203	0.015156	X	X	X	upper
364	0.502	72.81	420.15	296.6	2804	9568	202	0.015082	X	X	X	upper
365	0.496	71.94	419.95	296.24	2190	7473	207	0.015455	X		X	upper
366	0.5	72.52	420.25	296.78	1682	5739	201	0.015007	X		X	upper
367	0.502	72.81	419.95	296.24	1388	4736	205	0.015306	X		X	
373	0.203	29.44	388.55	239.72	1400	4777	508	0.037928	X		X	
375	0.205	29.73	388.55	239.72	1419	4842	505	0.037704	X		X	
378	0.495	71.79	419.45	295.34	4451	15187	495	0.036958	X		X	
379	0.509	73.82	419.65	295.7	2824	9636	505	0.037704	X		X	upper
380	0.503	72.95	420.25	296.78	1430	4879	505	0.037704	X		X	upper
398	0.501	72.66	421.45	298.94	2236	7630	997	0.074438	X		X	lower
399	0.263	38.14	387.25	237.38	6771	23104	2007	0.149846	X		X	
400	0.254	36.84	387.35	237.56	5829	19889	2010	0.15007	X		X	
401	0.245	35.53	392.55	246.92	4490	15321	2007	0.149846	X		X	
402	0.234	33.94	387.65	238.1	3503	11953	2014	0.150369	X		X	lower
403	0.232	33.65	388.55	239.72	2816	9609	1986	0.148279	X		X	lower
404	0.235	34.08	389.55	241.52	2528	8626	2006	0.149772	X		X	lower
405	0.222	32.2	387.75	238.28	2218	7568	1996	0.149025	X		X	lower
412	0.508	73.68	419.45	295.34	2812	9595	1999	0.149249	X		X	
413	0.51	73.97	420.25	296.78	2537	8657	1992	0.148727	X		X	lower
414	0.5	72.52	419.85	296.06	2221	7578	1986	0.148279	X		X	lower
434	0.199	28.86	387.45	237.74	2804	9568	99	0.007392	X	X	X	very low
441	0.498	72.23	418.75	294.08	1697	5790	51	0.003808	X	X	X	upper
446	0.506	73.39	420.95	298.04	2541	8670	98	0.007317	X	X	X	upper
448	0.501	72.66	420.75	297.68	1683	5743	99	0.007392	X	X	X	upper
451	0.501	72.66	420.85	297.86	1096	3740	99	0.007392	X		X	upper
456	1.009	146.34	447.65	346.1	1680	5732	99	0.007392	X		X	

TABLE 12
SUMMARY OF WINFRITH POST-CHF DOWN-FLOW EXPERIMENTS USED WITH TRAC

Run #	Inlet Pressure		Inlet Temperature		Total Power		Inlet Mass Flowrate		'X' denotes Existing Data		
	MPa	psi	°K	°F	W	Btu/hr	kg/m^2s	kg/s	α	T_v	q_{fluid}
213	0.493	71.5	419.15	294.8	2230	7609	200	0.014932		X	X
216	0.505	73.24	419.75	295.88	1096	3740	200	0.014932		X	X
219	0.508	73.68	420.35	296.96	434	1481	198	0.014783			X
230	0.493	71.5	418.35	293.36	1421	4849	101	0.007541		X	X
233	0.498	72.23	418.05	292.82	612	2088	102	0.007616		X	X
235	0.507	73.53	417.25	291.38	229	781	102	0.007616			X
484	0.202	29.3	385.95	235.04	1101	3757	51	0.003808	X	X	X
485	0.203	29.44	392.15	246.2	2462	8401	52	0.003882	X	X	X

TABLE 13
LEGEND KEY TO VOID-FRACTION FLOW-REGIME PREDICTIONS

	Low Void	Intermediate Void	High Void
Highly Dispersed	Q	R	S
Dispersed	N	O	P
Agitated	K	L	M
Rough-Wave	H	I	J
Smooth	E	F	G
Transition Boiling	B	C	D
Nucleate Boiling	A	A	A

TABLE 14
SUMMARY OF INEL POST-CHF UP-FLOW EXPERIMENTS USED WITH TRAC

Run #	Inlet Pressure		Inlet Saturation Temperature		Total Power		Inlet Mass Flowrate		'X' denotes Existing Data			Quench-Front Status
	MPa	psi	°K	°F	W	Btu/hr	kg/m^{2}s	kg/s	α	T_v	q_{fluid}	
2	0.49	71.07	424.22	303.93	1607	5484	13.9	0.001035		X	X	steady
3	0.48	69.62	423.82	303.21	1607	5484	18.1	0.001351		X	X	steady
4	0.49	71.07	423.93	303.4	1153	3934	12.1	0.000902		X	X	steady
45	0.46	66.72	421.88	299.71	14448	49298	17	0.001266		X	X	steady
49	0.45	65.27	421.44	298.92	1871	6382	14.2	0.001061		X	X	steady
50	0.48	69.62	423.44	302.52	5159	17605	18.5	0.001383		X	X	quasi-steady
66	0.49	71.07	424.49	304.41	8111	27677	42.1	0.003145		X	X	quasi-steady
68	0.48	69.62	423.82	303.21	2159	7365	17.9	0.001339		X	X	quasi-steady
89	3.57	517.78	516.77	470.52	3760	12831	46.6	0.003476		X	X	quasi-steady
90	3.57	517.78	516.81	470.59	6665	22743	66.9	0.004993		X	X	quasi-steady
91	3.56	516.33	516.74	470.46	2898	9888	16.8	0.001254		X	X	quasi-steady
92	3.57	517.78	516.89	470.73	2079	7093	30.2	0.002251		X	X	quasi-steady
93	3.58	519.24	516.96	470.86	5033	17174	70.7	0.005276		X	X	quasi-steady
95	3.58	519.24	517.01	470.95	7130	24329	61	0.004553		X	X	quasi-steady
96	3.58	519.24	517.04	471	2767	9442	48.7	0.003638		X	X	quasi-steady
119	3.59	520.69	517.09	471.09	4005	13665	19.9	0.001489		X	X	quasi-steady
121	7.06	1023.97	559.53	547.48	3287	11216	20.8	0.001551		X	X	quasi-steady
125	7.07	1025.42	559.58	547.57	7526	25681	30.8	0.0023		X	X	quasi-steady
138	7.01	1016.71	559.02	546.57	7734	26388	43.2	0.003228		X	X	quasi-steady
140	7	1015.26	558.98	546.49	3504	11955	24.8	0.001852		X	X	quasi-steady
144	7.01	1016.71	559.05	546.62	3487	11898	26.2	0.001957		X	X	quasi-steady

TABLE 15
SUMMARY OF BERKELEY REFLOOD EXPERIMENTS USED WITH TRAC

Run #	G (kg/m^{2}s)	$Q_{electric}$ (W)	P (bar)	T_{in} (°C)
166	23.6	1172	1.0	25.0
167	71.0	1172	1.0	23.3
186	117.5	1145	1.0	23.3

APPENDIX A
AVERAGING AND THE LIMITATIONS IT GENERATES

The coupled-equation set that combines the single-phase fluid field equations for mass, momentum, and energy with the equation for heat diffusion within a bounding wall is called the conjugate problem. In the case of transient two-phase flow, the problem becomes even more difficult because an additional set of field equations for the second fluid phase must be solved simultaneously together with the necessary closure relations to couple the two fluid phases.

The TRAC code, as well as other similar codes, invokes a quasi-steady approach to the heat-transfer coupling between the wall and the fluid, as well as the closure relations for interfacial heat transfer and drag and wall-to-fluid drag. This quasi-steady approach assumes detailed knowledge of the local fluid parameters and ignores time dependencies. The quasi-steady approach has the advantages of being reasonably simple and generally applicable to a wide range of problems and of not requiring previous knowledge of the given transient.

An alternative to the quasi-steady approach does exist on a case-by-case basis. If the necessary initial and boundary conditions are known, the solution of the conjugate problem requires no a priori knowledge of the wall-to-fluid convective heat transfer. Studies such as those of Sucec[A-1,A-2] have used this latter approach to obtain both analytical and numerical solutions for many single-phase transients. These results, when compared with those using the quasi-steady approach, have led to an understanding of the conditions under which the quasi-steady approach produces valid results.

For the heat-transfer coupling between the wall and the fluid, the quasi-steady approach works well provided that the fluid responds more rapidly than the wall. For example, the fluid boundary layer responds so quickly that the surface temperature of a thick, high-conductivity wall does not have time to change. However, when the wall changes faster than the fluid, one must use transient closure relations to solve the problem accurately.

Despite the difficulties and limitations of the quasi-steady approach for solution of the two-phase flow conjugate problem, this approach is the only method available to simulate transient conditions in large, complex, two-phase systems such as a nuclear power plant. This Appendix will investigate those limitations relative to the wall-to-fluid heat-transfer process.

A.1. Local-Instantaneous Formulation

To investigate the limitations imposed by averaging inherent within the quasi-steady assumption, write a general expression for the transient heat flux in local condition functional form. This general quantity will be represented as

$$q = \vec{q} \bullet \vec{n} = q\left(t,\ T_W,\ \alpha,\ T_f,\ p,\ v_l,\ v_V,\ \ldots\right)\ , \tag{A1}$$

where $\vec{q}$ denotes the vector heat flux at a local point on the surface, $\vec{n}$ is the normal to the local surface position, q is the normal heat flux to the local surface position, t denotes time, T_W is the local surface temperature, α denotes the local vapor void fraction, T_f represent a local phasic fluid temperature, p denotes the pressure, v_l is the liquid phasic velocity, v_V is the vapor phasic velocity, and "..." denotes that additional parameters may be of importance. Equation (A1) is typically called a local-instantaneous representation.

The commonly used steady-state representation of Eq. (A1) is denoted by

$$q = \vec{q} \bullet \vec{n} = q\left(T_W,\ \alpha,\ T_f,\ p,\ v_l,\ v_V,\ \ldots\right)\ . \tag{A2}$$

In the vast majority of cases, Eq. (A2) represents the closure relationships used in two-phase modeling.

A.2. Time Averaging

Because of the many interfaces in two-phase flow and our inability to track them, averaging is a common practice. Averaging can include both temporal and spatial averaging. For this discussion, we will emphasis the effects of temporal averaging. The standard time average of a quantity, in this case the heat flux, is typically written as

$$\overline{q} = \frac{1}{\Delta t} \int_{\Delta t} q\, du\ ,$$

where Δt is the time increment over which the heat flux will be averaged and u is the dummy variable of integration. Applying this average to Eqs. (A1) and (A2) produces

$$\overline{q} = \overline{\vec{q}} \bullet \vec{n} = q\left(\overline{t},\ \overline{T}_W,\ \overline{\alpha},\ \overline{T}_f,\ \overline{p},\ \overline{v}_l,\ \overline{v}_V,\ \ldots\right)\ , \tag{A3}$$

where time averaged parameters are used within the representation.

A.3. Classes of Transient Problems

To investigate transient conditions, differentiate Eq. (A3) with respect to time

$$\frac{d\overline{q}}{dt} = \frac{\partial\overline{q}}{\partial t} + \frac{\partial\overline{q}}{\partial\overline{T}_W}\frac{d\overline{T}_W}{dt} + \frac{\partial\overline{q}}{\partial\overline{\alpha}}\frac{d\overline{\alpha}}{dt} + \frac{\partial\overline{q}}{\partial\overline{T}_f}\frac{d\overline{T}_f}{dt} + \ldots \tag{A4}$$

One should note here that t is not the averaging time, $\bar{t}$.

Three classes of transient conditions may be considered with respect to Eq. (A4) as follows:

Class 1: Results when

$$\frac{\partial\overline{q}}{\partial t} = 0, \tag{A5}$$

and is the quasi-steady-state convection case denoted as Eq. (A2) after averaging. In this case, Eq. (A4) yields

$$\frac{d\overline{q}}{dt} = \frac{\partial\overline{q}}{\partial\overline{T}_W}\frac{d\overline{T}_W}{dt} + \frac{\partial\overline{q}}{\partial\overline{\alpha}}\frac{d\overline{\alpha}}{dt} + \frac{\partial\overline{q}}{\partial\overline{T}_f}\frac{d\overline{T}_f}{dt} + \ldots. \tag{A6}$$

This transient behavior can be determined using steady-state characteristics represented by the terms $\left(\frac{\partial\overline{q}}{\partial\overline{T}_W}, \frac{\partial\overline{q}}{\partial\overline{\alpha}}, \frac{\partial\overline{q}}{\partial\overline{T}_f}, \ldots\right)$, and the transient wall and hydraulic conditions represented by the terms $\left(\frac{d\overline{T}_W}{dt}, \frac{d\overline{\alpha}}{dt}, \frac{d\overline{T}_f}{dt}, \ldots\right)$.

Class 2: Results when

$$\frac{d\overline{T}_W}{dt} = \frac{d\overline{\alpha}}{dt} = \frac{d\overline{T}_f}{dt} = \ldots = 0 \tag{A7}$$

so that Eq. (A4) reduces to

$$\frac{dq}{dt} = \frac{\partial q}{\partial t}. \tag{A8}$$

Two further subclasses exist, where Eq. (A6) is satisfied and where it is not. When Eq. (A5) is satisfied, one has the classically steady-state case where

$$\frac{d\overline{q}}{dt} = \frac{\partial\overline{q}}{\partial t} = \frac{d\overline{T}_w}{dt} = \frac{d\overline{\alpha}}{dt} = \frac{d\overline{T}_f}{dt} = \ldots = 0. \tag{A9}$$

We will discuss the situation where this is not the case below in the Steady or Quasi-steady Model section.

Class 3: Results when

$$\frac{\partial\overline{q}}{\partial t} \neq 0. \tag{A10}$$

This represents the truly transient situation and is particularly difficult to represent within the framework of the heuristic models implied by Eq. (A1). Physically this means the averaged heat flux is changing as one moves the averaging window even slightly. Also, each of the partial derivatives is time dependent. Practically the best solution to this class of problems is to develop a detail transient model that captures the basic physics of the process.

A.4. Steady or Quasi-steady Models

Steady-state information is obtained by analyzing data in which Eq. (A5) is valid. Such information is time or ensemble averaged to minimize the effects of random variations or to capture the "average" behavior. By collecting data for a number of different parametric states, the time averaged relationship similar to Eq. (A2) may be obtained represented as

$$\overline{q} = \overline{\vec{q}} \bullet \vec{n} = q\left(\overline{T}_w, \overline{\alpha}, \overline{T}_f, \overline{p}, \overline{v}_l, \overline{v}_v, \ldots\right). \tag{A11}$$

The requirement placed on this time average is that the interval Δt must be chosen long enough so that minor changes in the length of this time interval do not change the average. If Δt_p represents the controlling period of the physical process and n_o the minimal number of occurrences (cycles) required to produce an average insensitive to time, the minimum time for a statistically sufficient sample can be written as $\Delta t_{min} = n_0 \Delta t_p$. If the time resolution of interest in the simulation is greater than this minimum time, the local time-averaged heat flux is independent of time. This insensitivity can be observed from the fact that if the time interval over which averaging is done were increased by some arbitrary amount of time δt, no change should be observed in the average value so that

$$\int_{\Delta t_{min}+\delta t} q\, du = \int_{\Delta t_{min}} q\, du \quad . \tag{A12}$$

Hence, it can be concluded that

$$\frac{\partial \bar{q}}{\partial t} = \lim_{\delta t \to 0} \frac{1}{\delta t} \left\{ \int_{\Delta t_{min} + \delta t} q \, du - \int_{\Delta t_{min}} q \, du \right\} = 0 \quad . \tag{A13}$$

This property is one of the characteristics of a stationary process. In effect, this implies that Eq. (A3) should have been written as

$$\bar{q} = \bar{\bar{q}} \bullet \bar{n} = q\left(\bar{T}_w, \bar{\alpha}, \bar{T}_f, \bar{p}, \bar{v}_l, \bar{v}_v, \ldots\right)$$

so that the quasi-steady condition represented by Eq. (A5) or the steady-state case as represented by Eq. (A9) are satisfied.

If the solution time frame desired is $< \Delta t_{min}$, $\bar{q}$ will reflect a sensitivity to time resulting from the averaging process. To analyze times shorter than Δt_{min}, an instantaneous representation must be known with respect to its individual controlling phenomenon and on a time scale $< \Delta t_p$.

A.5. Averagers and Limiters Arising from Small Timestep Sizes and Temporal-Averaging Considerations

System codes have used various techniques to control how the closure quantities are allowed to change with time, i.e., what happens if $\delta t_{code} \leq \Delta t_{min}$ where δt_{code} represents the code timestep size.

A.5.1. Instantaneous Closure

In some transient analysis codes, the closure relations are free to respond instantaneously (within a single timestep) to any changes occurring within the flow field. Typically, as long as the timestep size desired by the code is $> \Delta t_{min}$ ($\delta t_{code} \geq \Delta t_{min}$), standards correlations should provide a reasonable representation. However when this condition is not met, the resulting quantities have no physical basis for their value.

A.5.2. Arithmetic-averaging of Closure

Arithmetic-averaging has been a method used to "relax" the change in closure quantities with time. This technique can be represented by the following relationship:

$$Y^n_{used} = \Psi Y^{n-1} + (1-\Psi)Y^n, \qquad \text{(A14)}$$

where Y represents some closure quantity, Ψ is a fraction between zero and one, and the superscripts n-l and n indicate old- and new-time values of Y, respectively. The Y^n_{used} is the closure-relationship value used in the current timestep and becomes Y^{n-1} for the next timestep. Thus, as Ψ approaches one, Y_{used} would change very slowly, and for Ψ equal to zero, Y_{used} would change instantly.

The problem with arithmetic-averaging as given by Eq. (A14) is that it produces a time-averaging scheme that is timestep-size dependent. For example, if we were to run a transient calculation with a fixed timestep size of 100 ms and then repeat the calculation with a timestep size of 10 ms, we would obtain a change in the answer because of this type of averager. Fortunately, this sensitivity has been found to be limited to those flow regimes where either large interfacial heat-transfer or interfacial area changes may take place.

Also as noted above for the instantaneous case when $\delta t_{code} \le \Delta t_{min}$, the resulting value has no physical meaning.

A.5.3. Limiters of Closure Change

To eliminate the problems associated with arithmetic averaging, limiters were implemented in the MOD2 TRAC code. These can be denoted as

$$Y_{min} \le Y^n_{used} \le Y_{max} ,$$

where Y_{min} and Y_{max} are reasonable bounds for Y and depend on the phenomenon addressed by the closure relationship.

A.5.4. Transport Equations

An alternative method to these averagers and/or limiters is the use of additional transport equations within the code to convect such quantities as interfacial area or drop/bubble diameter. However, while these transport equations do “stabilize” the potential "instantaneous response" problem, they do not directly address the problem that still exists, namely that the closure relationships are quasi-steady at best. Currently, we have not implemented the alternative approach, and TRAC relies on averagers and limiters.

A.6. Considerations Associated with Large Timestep Sizes or Rapid Transients

Just as problems can occur when $\delta t_{code} \leq \Delta t_{min}$, problems can occur also when

1. the transient under consideration is too rapid, or
2. δt_{code} is too related to the system parameters.

The first case can be represented by $\tau < \Delta t_{min}$ where τ represents the system's time constant. To represent this case, transient closure relationships are once again required. The second case can be denoted by $\delta t_{code} \geq \tau$. In the past, numerical requirements associated with the material Courant limit have frequently prevented this problem from occurring. However as improved numerics methods continue to be developed, this case may become an issue at some time in the future.

A.7. Spatial Averaging

Spatial averaging requirements similar to those for temporal issues discussed above can be obtained. Spatial averaging relaxes the local characterization represented in Eqs. (A1) and (A2). For brevity, those will not be presented here. The influence of the spatial-averaging operator is realized principally through its influence in data reduction and is therefore inherent within the closure relationships. The code makes no checks to investigate the influence of the spatial-averaging.

REFERENCES

A-1. J. Sucec, "Unsteady Heat Transfer Between a Fluid, With a Time Varying Temperature and a Plate: An Exact Solution," *Int. J. Heat Mass Transfer* **18**, 25–36 (1975).

A-2. J. Sucec, "Analytical solution for Unsteady Heat Transfer in a Pipe," presented at the ASME Winter Annual Meeting (Anaheim, California, December 7–12, 1986) ASME paper 86-WA/HT-75.

APPENDIX B
THE METHODOLOGY OF OPTIMIZATION AND CLOSURE DEVELOPMENT

Optimization* problems have three basic elements:

1. A penalty function (also often called an objective function) that one wishes to minimize or maximize. For instance, in a manufacturing process, one might want to *maximize the profit* or *minimize the cost.* In fitting experimental data to a user-defined model, one might *minimize the total deviation* of observed data from predictions based on the model.

   Often the user would actually like to optimize several different objectives at once. For instance, in a panel design problem, it would be nice to *minimize weight* and *maximize strength* simultaneously. Usually, the different objectives are not compatible; the variables that optimize one objective may be far from optimal for the others. In practice, problems with multiple objectives are reformulated as single-objective problems by either forming a weighted combination of the different objectives or by replacing some of the objectives by constraints.

2. A set of unknowns, or variables, that affect the value of the penalty function. In the manufacturing problem, the variables might include the *amounts of different resources used* or the *time spent on each activity.* In the fitting-the-model-to-data problem, the unknowns are the *parameters* that define the model.

   Variables are essential. If there are no variables, we cannot define the objective function and the problem constraints.

3. A set of constraints that allow the unknowns to take on certain values but exclude others. For the manufacturing problem, it does not make sense to spend a negative amount of time on any activity, so we constrain all the "time" variables to be non-negative.

Constraints are not essential. In fact, the field of unconstrained optimization is a large and important one for which many algorithms and software are available. It has been argued that almost all problems *really do* have constraints. For example, any variable denoting the "number of objects" in a system can only be useful if it is less than the number of elementary particles in the known universe! In practice though, answers that make good sense in terms of the underlying physical or economic problem can often be obtained without putting constraints on the variables.

---

* Much of the discussion of optimization is taken from documentation of the Optimization Technology Center at Argonne National Laboratory and Northwestern University.

B.1. The TRAC Problem

TRAC solves the two-field fluid conservation equations and the required closure relationships to find

$$\left\{\begin{array}{l} P(x,y,z,t) \\ \alpha(x,y,z,t) \\ T_l(x,y,z,t) \\ T_v(x,y,z,t) \\ v_l(x,y,z,t) \\ v_v(x,y,z,t) \end{array}\right\} \text{ or } \left\{\begin{array}{l} P(\vec{z},t) \\ \alpha(\vec{z},t) \\ T_l(\vec{z},t) \\ T_v(\vec{z},t) \\ v_l(\vec{z},t) \\ v_v(\vec{z},t) \end{array}\right\} . \tag{B1}$$

Structures (both heated and unheated) can be added to the system along with the heat diffusion conservation equation to produce a further coupled system yielding a solution represented by:

$$\left\{\begin{array}{l} P(\vec{z},t) \\ \alpha(\vec{z},t) \\ T_l(\vec{z},t) \\ T_v(\vec{z},t) \\ v_l(\vec{z},t) \\ v_v(\vec{z},t) \\ T_w(\vec{z},t) \end{array}\right\} . \tag{B2}$$

Equation (B2) represents the variables for which the conservation equations are solved and that vary in both space and time.

B.2. General Two-fluid Closure Optimization

The general optimization problem regarding the development of closure relationships for a two-fluid code like TRAC becomes

$$\left\{\begin{matrix} P\left(\vec{z},t,\left\{c_{tp}\right\}\right) \\ \alpha\left(\vec{z},t,\left\{c_{tp}\right\}\right) \\ T_l\left(\vec{z},t,\left\{c_{tp}\right\}\right) \\ T_v\left(\vec{z},t,\left\{c_{tp}\right\}\right) \\ v_l\left(\vec{z},t,\left\{c_{tp}\right\}\right) \\ v_v\left(\vec{z},t,\left\{c_{tp}\right\}\right) \\ T_w\left(\vec{z},t,\left\{c_{tp}\right\}\right) \end{matrix}\right\} , \tag{B3}$$

where the equation set is that required to yield Eq. (B3) plus a penalty function, ϕ. The thermal-hydraulic system variables are $\left\{P,\ \alpha,\ T_l,\ T_v,\ v_l,\ v_v,\ \text{and}\ T_w\right\}$, and $\left\{c_{tp}\right\}$ represents the set of closure coefficients. The penalty function is arbitrary depending upon the end result desired; however, for the sake of discussion, we will define it initially to be

$$\phi = \sum_{j=1}^{J} \sum_{k=1}^{K_j} \gamma_j (\beta - 1)_{jk}^2 , \tag{B4}$$

where β represents the ratio of a code-calculated quantity to its measurement, K_j is defined as the number of data points available from an experiment that correspond to the chosen calculated quantity, and J is the number of calculated quantities to be optimized (i.e., T_w, α, q'', ...). Also, γ_j is a weighting factor that is defined by the analyst, and it is to be used to emphasize or de-emphasize a specific quantity. As an example, one might choose T_w as the only variable to optimize, which would yield

$$\phi = \sum_{k=1}^{K} \left(\frac{T_{w,calc}}{T_{w,data}} - 1 \right)_k^2 \tag{B5}$$

as the penalty function where K is defined as the number of thermocouples used in an experiment. This would be the only possible comparison to be made for an old postcritical-heat-flux tube experiment.

For a single closure coefficient, $\{c_{tp}\} = c_1$, one can argue the solution might be unique because one equation has been added to the original equation set; however, for $tp \geq 2$, the system must be underspecified or underdetermined. This implies the solution isn't unique, and the determination of c_n would depend upon $\{c_{tp}\}$ where $tp \leq n-1$.

B.3. Optimization Techniques

A number of different techniques are available to optimize different problems. Figure 109 is a visual summary of these techniques and should imply the massive size of this field of study. It is not our purpose here to review this technology, just to note it. For a better understanding, the reader is referred to the Optimization Technology Center,* and for information related to available software.[B-1]

The basic structure of the problem we wish to optimize has been discussed in the section above, and details are discussed further below. For our solution method, we chose a gradient-based one because we felt that our initial estimates, as represented by either the Absolute set of coefficients or the Conditional set, might be near enough to the final solution to allow a gradient based method to quickly find "a" solution. This solution will represent a local minimum, and care must be exercised to limit or bound our solution to what we believe is a reasonable solution space, thus the problem is a constrained one. Also, because of various data comparisons to be made, the problem has multiobjective functions. These can be included within the single function, as represented by Eq. (B4). The reader should realize that this choice of optimization method is not a absolute one and that there are advantages to nonderivative based methods that might be considered in the future.

---

* A joint enterprise of Argonne National Laboratory and Northwestern University founded in 1994 with support from the U.S. Department of Energy and Northwestern University.

The use of a gradient-based optimizer to determine $\{c_{tp}\}$ in the general formulation, as noted by Eq. (B3), requires the generation of

$$\frac{\partial \beta}{\partial c_{tp}} = \left\{ \begin{matrix} \frac{\partial P}{\partial c_{tp}} \\ \frac{\partial \alpha}{\partial c_{tp}} \\ \frac{\partial T_l}{\partial c_{tp}} \\ \frac{\partial T_v}{\partial c_{tp}} \\ \frac{\partial v_l}{\partial c_{tp}} \\ \frac{\partial v_v}{\partial c_{tp}} \\ \frac{\partial T_w}{\partial c_{tp}} \end{matrix} \right\} (\tilde{z}, t) \tag{B6}$$

for all *tp*. Determination of these partial derivatives has historically been done either analytically by hand and then programmed, or by finite-difference approximations obtained by numerical evaluation of the particular quantity by variation of the variable of interest. Both of these methods provide their own problems and are particularly difficult within the framework of a complex code such as TRAC.

Fortunately, software has been developed that allows automatic generation of these derivatives. Some of this software is in its second generation and thus provides a validated configuration. The software selected for use within our work was ADIFOR (Automatic Differentiation of Fortran Code). ADIFOR* is a tool for the automatic differentiation of Fortran 77 programs. Given Fortran 77 source code and a user's specification of dependent and independent variables, ADIFOR will generate an augmented derivative code that computes the original result(s) plus the partial derivatives of all specified dependent variables with respect to all of the specified independent variables.

---

* ADIFOR is a collaborative project between the Mathematics and Computer Science Division at Argonne National Laboratory and the Center for Research on Parallel Computation at Rice University.

B.4. Technical Issues Associated with Closure Optimization

There are several issues faced in the optimization of closure relationships that are not encountered in typical optimization problems. First, most systems that are optimized are not transient in nature. Their behavior is steady-state. Second, the finite-difference formulation used in TRAC removes the implicit dependence of measurements at a particular location on upstream phenomena.

Even during "steady-state" experiments, two-phase systems often experience pulsating or oscillatory behavior. Thus, in this context, the term steady-state is that within the Class 2 transient problem, as discussed in Appendix A and denoted by

$$\frac{d\overline{q}}{dt} = \frac{\partial \overline{q}}{\partial t} = \frac{d\overline{T}_W}{dt} = \frac{d\overline{\alpha}}{dt} = \frac{d\overline{T}_f}{dt} = \ldots = 0, \qquad \text{(B7)}$$

where $\overline{q}$ represents the time-averaged heat flux, $\overline{T}_w$ the time-averaged wall temperature, etc. As discussed in Appendix A to satisfy this condition requires that the time averaging window be sufficiently long so that the average is independent of the length of the window or the point at which the window is started.

In running "steady-state" experiments, data are commonly time-averaged before being reported. In simulation of these experiments, it is common for the code to oscillate or pulsate. If the code is simulating true physical behavior, time averaging of the code results should be performed to compare with the experimental data. Time averaging has been developed as part of the optimization process because optimization techniques cannot be expected to optimize a continually changing (oscillating) system.[*] Optimization should be undertaken to obtain the average behavior. An additional desirable comparison is the frequency content of the averaged information, both experimental and simulated. While it is possible to generate this information within the simulation, its value is limited because of the general lack of experimental information in this regard. It would be useful in the future from a code development standpoint if this experimental information were gathered whenever possible.

When the experiments are transient, their data are still most often time-averaged. For codes such as TRAC to provide valid predictions of these "transient" experiments, the transient must be slow enough that the quasi-steady condition is satisfied. Appendix A discusses the requirements on this assumption,

---

[*] What limits our ability to potentially optimize this situation is the transport time of the flow and the possible time constant of the walls and phases. If these were small enough so that coefficient changes would be reflected correctly each timestep, an optimizer might be able to optimize the coefficients. However because this is not the case and several seconds of transient simulation are required to reflect a new coefficient, one must provide average behavior to the optimizer.

$$\frac{\partial \bar{q}}{\partial t} = 0 \ . \qquad \text{(B8)}$$

To utilize this type of experiment, short time windows where Eq. (B8) is satisfied must be considered and the optimizer reruns this window repeatedly using the "restart" capability of the code where the coefficients are adjusted in each restart. The length of each restart run must be sufficient to allow the new coefficients to propagate within the system and then produce a meaningful time average at the end of the run.

The finite-difference formulation used in TRAC removes the implicit dependence of measurements at a particular location on upstream phenomena. For example, the vapor superheat downstream of the critical heat flux point is an integral property involving phasic wall heat transfer, interfacial phasic heat transfer, and interfacial phasic drag along the channel. The measurement of the vapor temperature at a particular point within the flow stream indicates the result of this integration process prior to that point. And whereas the finite-difference method is solving this problem, one cannot determine the derivative of the vapor temperature with respect to one of the coefficients of an upstream processes. This limits our ability to investigate some sensitivities and to optimize some behavior within the closure relationships.

B.5. Optimization Methodology

Whereas Eqs. (B3) (B4), and (B6) represent the general optimization problem for closure development, it is a problem that we cannot solve. The difficulty lies in the fact that β does not exist for all the independent parameters reflected in Eq. (B2). Typically, because of the lack of hydrodynamic data, the penalty function cannot be constrained to assure that the proper hydrodynamic state exits. For example, using an old post-CHF tube experiment, one would know the pressure, mass flux, heat flux, and a set of tube wall temperatures. This knowledge would allow a TRAC input model to be built and a penalty function like Eq. (B5) to be defined. However, this system is underspecified, and hydrodynamic information is not part of the penalty function, so determination of the "proper hydro-state" cannot be assured.

B.5.1. Original TRAC MOD2 Reflood Model

For a moment, consider the recorrelation of the original MOD2 reflood models to those used in the code. It was a four-step process described as follows:

1. Recorrelate interfacial drag to predict the CCTF Run 14 void profiles using fixed heat-transfer (both wall and interfacial) coefficients.

2. Recorrelate wall post-CHF heat transfer to predict a set of tube experiments assuming the drag from step 1 is correct and retaining a fixed set of interfacial heat-transfer coefficients.

3. Recorrelate the interfacial heat transfer to predict vapor superheat measured in selected post-CHF tube experiments assuming the drag and wall heat transfer determined in steps 1 and 2 are correct.

4. Repeat step 1 using new heat-transfer coefficients. Continue repeating this process until satisfied.

Effectively, the eyeball evaluated the "individual penalty function" associated with each step, whereas "brain power" served as an extremely-limited optimizer. Thus, one could say (regarding only step 1 for example) that the eyeball evaluated

$$\phi = \sum_{j=1}^{J} \sum_{k=1}^{K_j} \gamma_j \left(\frac{\alpha_{calc}}{\alpha_{data}} - 1 \right)_{jk}^{2} \quad . \tag{B9}$$

Unfortunately, recorrelating all the interfacial-drag coefficients at one time was too complex for the optimizer so that each step was further separated into subregions. For example, first the nucleate boiling coefficients were recorrelated by considering the end of the transient when everything was quenched. Then, post-CHF boiling regions were added trying to limit the addition to one new region at a time by selecting other time frames from the experiment to analyze.

This process can be represented by defining a limited subset of the $\{c_{tp}\}$ in Eq. (B2) to be "optimized in each subregion." For the first substep of nucleate boiling, one would have a small number of coefficients (maybe 2 or 3) to recorrelate, i.e., $\{c_{tp}\}$ where $tp = \left\{ \begin{array}{l} \text{nucleate boiling} \\ \text{interfacial drag} \\ \text{coefficients} \end{array} \right\}$ or $\{c_{tp}\}_{NB,drag}$. After completing this task, assume the next state to be added is the highly-dispersed film boiling region, and denote this set as $\{c_{tp}\}_{HD,drag}$. Realize that this second recorrelation substep depends upon the assumption that the $\{c_{tp}\}_{\mathrm{NB,drag}}$ is correct and remains untouched. One may write this new limited set as

$$\{c_{tp}\}_{\mathrm{set,drag}} = \left\{ \{c_{tp}\}_{\mathrm{NB,drag}}, \{c_{tp}\}_{\mathrm{HD,drag}} \right\} \quad . \tag{B10}$$

Remember the system is underdetermined. Effectively, this process is like building up the underdetermined states (regions) one at a time. In the end, it should lead to a valid solution, but not necessarily the only valid solution.

One continues this process until the entire set of interfacial-drag coefficients is defined for step 1 and can be written as

$$\left\{c_{tp}\right\}_{\text{drag}}=\left\{\left\{c_{tp}\right\}_{\text{NB}},\left\{c_{tp}\right\}_{\text{HD}},\left\{c_{tp}\right\}_{\text{dispersed}},\left\{c_{tp}\right\}_{\text{RW}},\ldots\right\}_{\text{drag}}\ , \tag{B11}$$

where the subscripts dispersed and RW represent the dispersed and rough/wavy post-CHF regions, respectively.

Having completed step 1 for the interfacial drag as represented by Eq. (11), one progresses to step 2, continuing the subregion process as often as possible. For example if we pick an experiment with only highly-dispersed post-CHF heat transfer (HDHT), then

$$\left\{c_{tp}\right\}_{\text{set}}=\left\{\left\{c_{tp}\right\}_{\text{drag}},\left\{c_{tp}\right\}_{\text{HDHT}}\right\}\ , \tag{B12}$$

where $\left\{c_{tp}\right\}_{drag}$ is the set represented by Eq. (11).

The process continues until at the end of step 3 one produces the complete set $\left\{c_{tp}\right\}$ represented by

$$\left\{c_{tp}\right\}=\left\{\left\{c_{tp}\right\}_{\text{drag}},\left\{c_{tp}\right\}_{\text{wall heat transfer}},\left\{c_{tp}\right\}_{\text{interface heat transfer}}\right\}\ , \tag{B13}$$

and the sequence of operation has been to define the various subsets of coefficients on the right-hand side of Eq. (B13) from left to right assuming all other sets are constant. Having reached this point in the process, one can now return to step 1 using the new $\left\{c_{tp}\right\}_{\text{wall heat transfer}}$ and $\left\{c_{tp}\right\}_{\text{interface heat transfer}}$ to further refine $\left\{c_{tp}\right\}_{\text{drag}}$. This iteration can be repeated as many times as needed; however, during the development of MOD2 it was found that two iterations produced reasonable results.

B.5.2. Original NRC SET and Code Development Philosophy

To represent the original NRC philosophy, we will write

$$\left\{c_{tp}\right\}=\left\{\left\{c_{tp}\right\}_{\text{SET1}},\left\{c_{tp}\right\}_{\text{SET2}},\left\{c_{tp}\right\}_{\text{SET3}},\ldots\right\}\ , \tag{B14}$$

where the subscript SET1 represents one Separate Effects Test (SET) defined to produce a measure of a particular closure phenomena, etc. One could use the data from this experiment to define $\{c_{tp}\}_{\mathrm{SET1}}$.[*] Through a process of running a number of SETs, one could then arrive at a complete set of closure relationships. Whereas not as clean as the original NRC code development SET philosophy, the development of the TRAC MOD2 reflood was meant to be an approximate application of it. The general philosophy represented within Eq. (B14) can also be more flexible than that just noted. Some of the SET experiments may be designed to produce specific coefficient sets alone,[*] and one might denote these to be $\{c_{tp}\}_{\mathrm{SET1}}$ and $\{c_{tp}\}_{\mathrm{SET3}}$ for the sake of discussion. Others may then be built off these initial sets. For example, $\{c_{tp}\}_{\mathrm{SET2}}$ might be developed based upon $\{c_{tp}\}_{\mathrm{SET1}}$. An experiment where the walls are adiabatic followed by one where they are heated would be an example of this sequence. The initial adiabatic experiment might be used to develop the drag coefficients whereas the heated experiment might provide the wall heat-transfer coefficients assuming the drag coefficients are correct, etc.

B.5.3. Closure Development Using Nonlinear Optimization

What we would like to do within the current closure development is remain as true to the process implied by Eq. (B14) as possible realizing that there are significant constraints upon the data available for phenomena that we need to model.

Optimization may also allow greater flexibility in the development of $\{c_{tp}\}_{\mathrm{SET1}}$ and $\{c_{tp}\}_{\mathrm{SET2}}$ than that just noted above. One can develop the initial sets of quantities as just discussed. These sets can then be used as a starting point for a solution of the combined sets of coefficients and data, i.e., $\{c_{tp}\}_{\mathrm{SET1}}$ is not constant during final development. This may produce a better set of coefficients than can be obtained otherwise; however, this point requires further investigation.

B.5.4. Generalized Penalty Function

The optimization process described above requires a set of automated tools for recorrelation of the TRAC closure coefficients. The method selected involves an iterative implementation of the penalty function defined by Eq. (B4). The penalty function is nondimensionalized and is normalized to produce,

$$\phi = \sum_{e=1}^{E}\sum_{j=1}^{J}\sum_{k=1}^{K_{ej}} \frac{r\gamma_j}{K_{ej}}\left(\hat{\beta}-1\right)_{ejk}^{\xi}, \qquad \text{(B15)}$$

where E is the number of TRAC input decks to be used for each determination of a penalty function value, and its gradient, r, is a dynamically determined

---

[*] One can read $\{c_{tp}\}_{\mathrm{SET1}}$ as correlation or closure relationship in this case.

[*] Independent of the other sets.

convergence acceleration parameter that was patterned from reference B-2, $\xi = 2$, and

$$\hat{\beta} = \frac{x_{calc}}{x_{data}}, \tag{B16}$$

where x is some quantity that is either calculated or measured. It follows that the gradient of the penalty function in Eq. (B16) is defined as

$$\frac{\partial \phi}{\partial c_{tp}} = \sum_{e=1}^{E} \sum_{j=1}^{J} \sum_{k=1}^{K_{ej}} \left\{ \frac{r \gamma_j \xi}{K_{ej}} \left(\hat{\beta} - 1 \right)_{ejk}^{\xi - 1} \left(\frac{\partial \hat{\beta}}{\partial c_{tp}} \right)_{ejk} \right\}, \tag{B17}$$

where $\hat{\beta}$ is averaged over a specified region of time. These partial derivatives can be calculated within TRAC by implementing subroutines generated by ADIFOR.

It is important to check that the averaged quantity $\hat{\beta}$ is stationary to reflect behavior around a limit attractor or strange attractor. If this is not the case, the characteristics of the behavior must be investigated.

REFERENCES

B-1 J. J. Moré and Wright, Stephen J., *Optimization Software Guide* (SIAM Publications, 1993).

B-2 R. L. Fox, *Optimization Methods for Engineering Design*. (Addison-Wesley Publishing Company, Massachusetts, 1971).

APPENDIX C
OPTIMIZATION IMPLEMENTATION

The implementation of the preceding optimization discussion required a software package to perform the minimization of Eq. (B15). The selected Minimizer* is a Limited Memory Quasi-Newton Solver using a line search method that implements a direct primal method to determine a search direction.[C-1,C-2] The Optimizer** is a stand-alone program that performs the optimization of the TRAC code.

C.1. Optimization Convergence Criteria

The Optimizer has been equipped with a convergence criteria based upon the tunable parameter values (i.e., independent variables of the penalty function), and the Minimizer has intrinsic convergence criteria based upon both user specified values and machine precision. First, the Optimizer considers the relative change of the tunable parameters with a stopping criterion of

$$\left|\frac{c_{tp,n} - c_{tp,n+1}}{c_{tp,n+1}}\right| \le 10^{-14}, \qquad \text{(C1)}$$

which, when active, will preempt a restart in the steepest direction for a failed line search.[C-2] Second, the Minimizer considers the relative change of the penalty function value

$$\frac{(f_n - f_{n+1})}{\max(|f_n|,|f_{n+1}|,1)} \le \vartheta M_p \quad \begin{cases} \vartheta = user-defined\,factor \\ M_p = machine\,precision \end{cases}, \qquad \text{(C2)}$$

where the machine precision is typically on the order of 10^{-16} for double precision accuracy. For the TRAC optimization process, $\vartheta \equiv 10^{12}$. Finally, the Minimizer considers the projected gradient $(\text{proj}\, g)$, which is the projection of the penalty function's gradient vector onto the space tangent to the active bounds. When the infinity norm of this projection meets the criterion

$$\|\text{proj}\, g\|_\infty \le \varepsilon_{grad}, \qquad \text{(C3)}$$

the optimization process is terminated. The test of Eq. (C3) will be very difficult to satisfy if ε_{grad} is set to anything smaller than $\sqrt{M_p}$. For the purposes of the TRAC

---

* LBFGS-B version 2.3 written in F77.

** F77 driver to run Minimizer and TRAC.

optimization, ε_{grad} is set to 10^{-5}. The subscript n in Eq. (C1) through Eq. (C3) refers to a specific Minimizer iteration.

C.2. Optimization Algorithm

The following algorithm outlines the method of optimizing TRAC with respect to specified closure parameters:

1. Start: choose initial values for r and $\{c_{tp}\}$ (realize that $\{c_{tp}\}$ will be divided into two subsets, one set that remains constant and a much smaller set to be recorrelated). Also, the Optimizer requires knowledge of the type of independent variables' bounds and the test numbers corresponding to the desired TRAC input decks.

2. If the convergence criterion of Eqs. (Cl) through (C3) is true, then quit the algorithm.

3. Run TRAC using the input specified within *decklist* (described below) to calculate the penalty function and its gradient with respect to $\{c_{tp}\}_{recorrelate}$.

4. If TRAC fails to generate ϕ and $\dfrac{\partial\phi}{\partial c_{tp}}$, then the current values of $\{c_{tp}\}_{recorrelate}$ are inappropriate for the current TRAC input. Reset $\{c_{tp}\}_{recorrelate} = \dfrac{\{c_{tp}\}_{recorrelate,current} + \{c_{tp}\}_{recorrelate,previous}}{2}$ and get the first input specified within *decklist*. Return to step 3.

5. If another set of input is specified for TRAC within *decklist*, get it and return to step 3.

6. Generate new $\{c_{tp}\}_{recorrelate}$ values* based upon the current values of ϕ and $\dfrac{\partial\phi}{\partial c_{tp}}$.

7. If the norm of the gradient, $\left\|\dfrac{\partial\phi}{\partial c_{tp}}\right\| \le \zeta$, then $r \Leftarrow \Omega r$ where Ω and ζ are user-defined parameters with typical values of 10 and 10^{-2} respectively. This step was deactivated with $\Omega < 0$, and r had a constant value of one for the optimization of TRAC documented here.

8. Return to step 2.

---

* Performed by the Minimizer.

The current value of the convergence parameter, r, is stored in a file called *rvalue* (Appendix E) within the current working directory, which is read by TRAC and is both read and written by the Optimizer. If *rvalue* does not exist, then r has a default value of 1.

TRAC writes the current tunable parameter values to a file called *tune.out* (Appendix E). The Optimizer reads from *tune.out* and writes new values to a file called *rafin* (Appendix E), which must exist in the current working directory before running the Optimizer because it is required by TRAC during the optimization process.

A file called *gamma* (Appendix E) within the current working directory will contain the value and a string of characters corresponding to the parameter γ_j. The strings of characters are IFHT, VOID, and QWAL (all caps) corresponding to the interfacial heat transfer, void fraction, and wall heat-transfer components of the penalty function respectively. If the file *gamma* doesn't exist or it doesn't contain a value for a specific penalty function component, the default value is zero.

A file called *bounds* (Appendix E) within the current working directory can contain one of the words BOUNDED,[*] LOBOUNDED,[**] or HIBOUNDED[†] (all caps). If one of these options is selected, then the second line of *bounds* will contain a number (η) by which the initial independent variable values[††] ($\{c_{ip}\}_{initial}$) will be multiplied to obtain upper bounds. For all bounded options, the lower bounds are preset to 10^{-10}. If *bounds* doesn't exist in the current working directory, then no bounds are placed upon the independent variables, and the optimizer considers the problem to be unconstrained.

A file called *decklist* (Appendix E) within the current working directory must contain a list of the test numbers the analyst wishes to be used in the optimization process. The Optimizer will not operate without this file in the current working directory.

A file called *inclvect* (Appendix E) within the current working directory may contain the integer values to activate or deactivate the tunable parameters.

The TRAC input decks must be stored in a subdirectory of the current working directory called *DECKS*. Within *DECKS* the files named *xxx.dmp*, *tracin.xxx.rst*, and *data.xxx* (*xxx* refers to a test number). The files are the TRAC binary dump file, the TRAC restart input deck, and the experimental data file respectively.

---

[*] Indicates upper and lower bounds put onto the independent variables.

[**] Indicates only lower bounds put onto the independent variables.

[†] Indicates only upper bounds put onto the independent variables.

[††] Found in *rafin*.

C.3. Interfacial Heat-Transfer Optimization

Using ADIFOR, the product of the interfacial heat-transfer coefficient and the interfacial area was differentiated with respect to several closure parameters and the vapor temperature. The said product and independent variables are in Table 5.

Within the subroutine generated by ADIFOR, the dependence of vapor temperature upon the tunable parameters was not visible, so the partial derivative in Eq. (C1), $\left.\frac{\partial \hat{\beta}}{\partial c_{tp}}\right|_{j=1} = \frac{1}{T_{vap,data}} \frac{\partial T_{vap,calc}}{\partial c_{tp}}$, was determined using

$$\frac{\partial T_{vap,calc}}{\partial c_{tp}} = \frac{\partial \dot{q}_{vap,calc}}{\partial c_{tp}} \left(\frac{\partial \dot{q}_{vap,calc}}{\partial T_{vap,calc}} \right)^{-1} \qquad \text{(C4)}$$

where c_i is an arbitrary closure parameter and

$$\dot{q}_{vap,calc} = (hA)_{vap,calc} \left(T_{vap,calc} - T_{sat} \right) \ . \qquad \text{(C5)}$$

The ADIFOR generated routine was used to calculate all of the derivatives on the right-hand side of Eq. (C4).

C.4. Interfacial-drag Optimization

Once again, using ADIFOR, the interfacial-drag coefficient was differentiated with respect to several closure parameters within TRAC. The said interfacial-drag coefficient and closure variables are described in Table 6.

Within the subroutine generated by ADIFOR, the dependence of the drag coefficient upon the void fraction was not visible, so the partial derivative $\frac{\partial \alpha_{calc}}{\partial C_i}$ was determined from second-order polynomial regressions of the time-averaged values of α_{calc} and C_i at each hydro-cell-centered elevation. These polynomials were calculated using α_{calc} and C_i at five axial positions with the current cell as a center. Using the ADIFOR generated gradient vector in conjunction with the regressions' derivatives allowed the partial derivative in Eq. (B17) $\left.\frac{\partial \hat{\beta}}{\partial c_{tp}}\right|_{j=2} = \frac{1}{\alpha_{data}} \frac{\partial \alpha_{calc}}{\partial c_{tp}}$ to be determined using

$$\frac{\partial \alpha_{calc}}{\partial c_{tp}} = \frac{\partial \alpha_{calc}}{\partial C_i}\frac{\partial C_i}{\partial c_{tp}}. \qquad \text{(C6)}$$

C.5. Wall Heat-Transfer Optimization

Using ADIFOR, the total wall heat flux was differentiated with respect to several closure parameters and the heated wall temperature. The said heat flux, closure variables, and temperature are described in Table 7.

The objective of this component of the overall penalty function was to allow the user to select the system variable to optimize (q''_{wall} or T_{wall}) depending upon the available experimental data. For the q''_{wall} option, the ADIFOR routine was capable of calculating the partial derivative in Eq. (C1), $\left.\frac{\partial \hat{\beta}}{\partial c_{tp}}\right|_{j=3} = \frac{1}{q''_{wall,data}}\frac{\partial q''_{wall,calc}}{\partial c_{tp}}$, directly; however, the chain rule had to be implemented for the T_{wall} option,

$$\left.\frac{\partial \hat{\beta}}{\partial c_{tp}}\right|_{j=3} = \frac{1}{T_{wall,data}}\frac{\partial T_{wall,calc}}{\partial c_{tp}} = \frac{1}{T_{wall,data}}\frac{\partial T_{wall,calc}}{\partial q''_{wall,calc}}\frac{\partial q''_{wall,calc}}{\partial c_{tp}}. \qquad \text{(C7)}$$

REFERENCES

C-1. R. H. Byrd, J. Nocedal, and R. G. Schnabel, *A Limited Memory Algorithm for Bound Constrained Optimization*. SIAM Journal on Scientific Computing **16**:5 1190–1208 (1994).

C-1 C. Zhu, R. H. Byrd, P. Lu, and J. Nocedal, *"L-BFGS-B: FORTRAN Subroutines for Large Scale Bound Constrained Optimization,"* Northwestern University document NAM-11 (1994).

APPENDIX D
RESULTS OF OPTIMIZATION STUDIES

The optimization task associated with development of an AP600 quenching model was incomplete because of migration problems of the workstation-developed code to the archival storage media on the Los Alamos National Laboratory (LANL) mainframe systems. Code development had been specified as taking place on workstations to minimize any costs that might be experienced on the mainframe systems maintained by LANL. However at that time, code storage was on those mainframe systems using an "update-like" archival storage process. For the TRAC code, these two systems used different processes to make, store, and build codes. Simply stated, the workstation code-development environment employed the standard Unix "makefile" setup that was not compatible with archival storage process.

Figures 110 through 114 show various optimization studies that were undertaken with Winfrith experiment 405. The methodology shows potential, but its evaluation is incomplete.

D.1. Interfacial Drag

Figures 112 and 113 show the results of optimization work done on the interfacial drag. As indicated by the previous section, the rough/wavy interfacial-drag model produced too little drag. Figures 110 and 111 show the results of optimization applied to this model for Winfrith experiment 405. Figure 110 indicates the behavior of TRAC for the repeated runs (a TRAC Iteration) where the optimizer adjusted the multiplier, f_{rw}, on the rough/wavy drag. As f_{rw} is raised, the penalty function decreases as expected. Figure 111 shows the behavior of the gradient of the penalty function.

Figures 112 and 113 show the behavior when f_{sm} is considered. Early in the computation, a smooth regime drag point existed; however, after the first few iterations, the regime was changed to rough/wavy because of the initial increase in smooth drag.

Figure 114 shows the result of a run that combines the optimization of both f_{sm} and f_{rw}. Initially, the void fractions for all three levels are underpredicted. The void fraction at the highest two levels are raised to significantly improve the comparison, but the multipliers cannot be raised further as the penalty function balances the slight void fraction overpredictions against the underprediction at the lowest level.

The results shown in Fig. 114 raise important issues associated with potential strategies that might be employed by a model-developer using optimization. The balancing of under- and overpredictions by the penalty function might be eliminated if one considers initially only the lowest elevation. This might allow the optimizer to further increase f_{rw} so that the higher elevations are no longer in the rough/wavy or agitated regions. This is a step that would most likely follow.

However, the model-developer must also be cautious not to become preoccupied with the optimization process. All the results for the Absolute and Conditional sets indicate an underprediction by the current rough/wavy correlation. Most importantly, the model-developer must work with the physics of the phenomena present. Is the regime map valid or does it need additional consideration or refinement? Is an improved model for the drag in the rough/wavy and agitated regions alone needed? Are there shortcomings within the current model that the comparisons and optimization process are indicating? The optimization process cannot provide the model-developer with these answers or perspectives. As was the case for the original correlation developer if f(x,y,z, ...) is not the correct representation (see Fig. 3a), the optimizer will not produce a valid model.

D.2. Wall Heat Transfer

Figures 115 through 126 summarize studies dealing with the wall heat transfer. Figures 115 through 120 show the influence of the multiplier, fdham, on the Denham inverted-annular flow model; only two iterations were required for convergence. Figures 115 and 116 show the penalty function, the multiplier, and the gradient of the penalty function. The multiplier is increased from its initial of about one to six. Figures 117 through 120 show the effect of the multiplier change on all levels of the model using the Denham correlation. Once again, the balancing effect that occurs with multiple levels in the penalty function can be seen.

Figures 121 through 126 show the influence of the multiplier, fwebb, on the Webb-Chen vapor heat-transfer model with 22 iterations shown. Figures 121 and 122 show the penalty function, the multiplier, and the gradient of the penalty function. The multiplier is increased from its initial ~0.5 to 4. One can see the optimizer trying to significantly increase the value of the multiplier several times, (e.g., the second, fourth, and eighth) but the changes are too great as the penalty function overshoots. This overshoot is reflected by the sign change in the penalty function shown in Fig. 122. Figures 123 through 126 show the effect of the multiplier change on all levels of the model using the Webb-Chen correlation, with balancing again apparent.

D.3. Interfacial Heat Transfer and Interfacial Drag

Figures 127 through 132 show the results of an initial multiple closure package investigation involving both the interfacial heat transfer and drag with fgam2 and ffd being the two respective multipliers. Winfrith experiment 448 was used for this investigation. Figures 127 and 128 show the penalty function, the multiplier, and the gradient of the penalty function for fgam2. The multiplier fgam2 is increased from its initial of ~30 to ~59, and the gradient of the penalty function hovers around zero. Figures 129 and 130 show the penalty function, the multiplier, and the gradient of the penalty function for ffd. The multiplier ffd is decreased from its initial of ~0.5 to ~0.25, and again the gradient of the penalty function hovers around zero. The results of this combined optimization can be seen in Figs. 131 and 132.

Figure 131 shows the improved prediction of the vapor superheat, whereas Fig. 132 shows the effect on void fraction. A minimal change is seen in the void fraction because its original prediction was reasonable.

APPENDIX E
DESCRIPTION OF I/O FILES AND EXAMPLES

The following is an example of the file called *rvalue* that is read by TRAC. The first 20 columns are reserved for the value of r in double precision scientific notation as shown below.

```
1.0000000000000E+00
```

The following is an example of the file called *tune.out* that is written by TRAC and read by the Optimizer. The format of the file is only limited to three things:

1. The first row is reserved for the value of the variable storing the number of tunable parameters (ntune).
2. The first 13 columns are reserved for the variable label.
3. Columns 14 through 33 contain the number of tunable parameters (ntune) in integer format or the current tunable parameter value in double precision scientific notation as shown.

```
ntune        25
fgam2        3.0000000000000E+01
frw          1.2500000000000E+00
rel1         1.8750000000000E+01
rel2         1.0000000000000E-04
rel3        -3.0000000000000E-06
ret1         1.0425000000000E+01
ret2        -1.9250000000000E-03
ret3         1.2500000000000E-07
dqcmax       2.0000000000000E+01
dqcmim       2.0000000000000E+00
dqdzmx       2.0000000000000E+03
adqdz        8.0000000000000E-01
xdqdz        1.5000000000000E+00
fac013       9.4280000000000E-01
fac014       3.0000000000000E-03
fac015       1.3000000000000E-01
fac016       5.9000000000000E-01
fac017       1.0000000000000E-01
fac018       1.5000000000000E+01
fwebb        1.2000000000000E+00
```

facthv	1.0000000000000E-02
fac019	2.3000000000000E-02
facthl1	5.0000000000000E-01
facthl2	9.0000000000000E-01
fdham	1.0000000000000E+00

The following is an example of the file called *rafin* that is read by TRAC and written by the Optimizer. The format of the file is only limited to three things:

1. Columns 1 through 5 are ignored
2. Columns 6 through 13 are reserved for the variable label.
3. Columns 14 through 33 are reserved for the tunable parameter value in double precision scientific notation as shown.

```
fgam2    3.0000000000000E+01    used in    CORIFHT    (RAFHTIF)
frw      1.2500000000000E+00    used in    RBSHRZ     (IFCRS)
rel1     1.8750000000000E+01    used in    HTVSSLN    (RAFHTIF)
rel2     1.0000000000000E-04    used in    HTVSSLN    (RAFHTIF)
rel3    -3.0000000000000E-06    used in    HTVSSLN    (RAFHTIF)
ret1     1.0425000000000E+01    used in    HTVSSLN    (RAFHTIF)
ret2    -1.9250000000000E-03    used in    HTVSSLN    (RAFHTIF)
ret3     1.2500000000000E-07    used in    HTVSSLN    (RAFHTIF)
dqcmax   2.0000000000000E+01    used in    HTVSSLN    (RAFHTIF)
dqcmim   2.0000000000000E+00    used in    HTVSSLN    (RAFHTIF)
dqdzmx   2.0000000000000E+03    used in    HTVSSLN    (RAFHTIF)
adqdz    8.0000000000000E-01    used in    HTVSSLN    (RAFHTIF)
xdqdz    1.5000000000000E+00    used in    HTVSSLN    (RAFHTIF)
fac013   9.4280000000000E-01    used in    HTVSSLN    (RAFHTIF)
fac014   3.0000000000000E-03    used in    HTVSSLN    (RAFHTIF)
fac015   1.3000000000000E-01    used in    HTVSSLN    (RAFHTIF)
fac016   5.9000000000000E-01    used in    HTVSSLN    (RAFHTIF)
fac017   1.0000000000000E-01    used in    HTVSSLN    (RAFHTIF)
fwebb    1.2000000000000E+00    used in    HTVSSLN    (RAFHTIF)
facthv   1.0000000000000E-02    used in    HTVSSLN    (RAFHTIF)
fac019   2.3000000000000E-02    used in    HTVSSLN    (RAFHTIF)
facthl1  5.0000000000000E-01    used in    HTVSSLN    (RAFHTIF)
facthl2  9.0000000000000E-01    used in    HTVSSLN    (RAFHTIF)
fdham    1.0000000000000E+00    used in    HTVSSLN    (RAFHTIF)
```

The following is an example of the file called *gamma* that is read by TRAC and the Optimizer. The format of the file is only limited to three things:

1. The first 20 columns are reserved for the value of γ_j in double precision scientific notation as shown below.
2. Columns 21 and 22 must be blank.
3. Then one of the labels shown below must be placed starting in column 33.

```
0.0000000000000E+00    IFHT
0.0000000000000E+00    VOID
1.0000000000000E+00    QWAL
```

The following is an example of the file called *bounds* that is read/written by the Optimizer. The format of the file is only limited to two things:

1. The first line is reserved for the label indicating desired bounds.
2. The second line is reserved for the factor by which bounds are calculated based upon the initial tunable parameter values found in *rafin*.

```
LOBOUNDED
1.0E+02
```

The following is an example of the file called *decklist* that is read by the Optimizer. The format of the file is only limited to the following:

1. Each test number must exist on a line by itself.

```
363
364
365
366
367
373
375
378
379
380
398
399
400
401
402
403
404
405
412
413
414
434
441
446
448
451
456
```

The following is an example of the file called *inclvect* that is read by TRAC and read/written by the Optimizer. The format of the file is only limited to three things:

1. The first 5 columns are reserved for the integer value (0 or 1) that activates or deactivates a desired tunable parameter.
2. Columns 6 through 10 are ignored.
3. Columns 11 through 18 are reserved for the tunable parameter label.

```
0    fgam2     corifht
0    frw       rbshrz
0    adqdz     htvssl
0    alpctr    htvssl
0    dqcmax    htvssl
0    dqcmim    htvssl
0    dqdzmx    htvssl
0    fac013    htvssl
0    fac014    htvssl
0    fac015    htvssl
0    fac016    htvssl
0    fac017    htvssl
0    fac018    htvssl
0    fac019    htvssl
0    facthl1   htvssl
0    facthl2   htvssl
0    facthv    htvssl
1    fdham     htvssl
0    fwebb     htvssl
0    rel1      htvssl
0    rel2      htvssl
0    rel3      htvssl
0    ret1      htvssl
0    ret2      htvssl
0    ret3      htvssl
0    xdqdz     htvssl
```

APPENDIX F
TRACIN INPUT CHANGES

A few input changes and additions are required for the new AP600 reflood model. These changes can be divided into those that affect the standard TRAC input and those that are new.

F.1. Changes to Standard TRAC Input

INOPTS on card 2 must be set to 2 to activate the RAFOPTS namelist variables (see next section for description). These have been added for optimization.

The INOPTS namelist variable NEWRFD has had its range extended to represent the following:

Variable	Value Range	Description	Default Value
newrfd	0	MOD 1 closure and original data storage	0
	1	original MOD2 reflood model and original data storage	
	2	MOD 1 closure and new data storage with multiple quench fronts	
	3	new reflood closure and new data storage with multiple quench fronts	

A new INOPTS namelist variable, IPATCH, has been added.

Variable	Value Range	Description	Default Value
ipatch	>largest hydro #,<1000	Heat Structure component having hot patches. Only one such Heat Structure is allowed. The user is also required to set idbco=1.	0

A new variable has been added to the Heat Structure data card 4. The variable, ICWTMP, is flag that keeps the heat structure's temperature constant with time.

Card Number 4. (Format 2I14,2E14.6,I14) IDBCI,IDBCO,HDRI,HDRO,ICWTMP

Columns	Variable	Description
1-56	unchanged	unchanged
57-70	ICWTMP	Controller flag to keep constant temperatures over time. Default is off. Turned on by inputting integer 1.

The variable IPATCH was originally input on Heat Structure card 5. This card is changed to eliminate this input.

Card Number 5. (Format E14.6) WIDTH

Columns	**Variable**	**Description**
1-14	WIDTH	unchanged

The variables ZLOBOT, ZLPTOP, ZUPBOT, and ZUPTOP for the hot patches' axial locations were originally input as card 6, this changes that to two cards, one for the lower patch and one for the upper. In addition, the hot patch temperatures are added to each respective card.

Card Number 6a. (Format 3E14.6) ZLPBOT,ZLPTOP,TLP

Columns	**Variable**	**Description**
1-14	ZLPBOT	Elevation of the lower hot patches' bottom
14-28	ZLPTOP	Elevation of the lower hot patches' top.
29-42	TLP	Temperature of the lower hot patches

Card Number 6b. (Format 3E14.6) ZUPBOT,ZUPTOP,TUP

Columns	**Variable**	**Description**
1-14	ZUPBOT	Elevation of the upper hot patches' bottom.
14-28	ZUPTOP	Elevation of the upper hot patches' top
29-42	TUP	Temperature of the upper hot patches

F.2. New TRAC Input

In addition to the standard TRAC input changes, new input variables are required for optimization. These are input within the RAFOPTS namelist option. They are as follows:

ntune—number of parameter values to read from *rafin* by TRAC.

irafset—indicates closure coefficient set to use;

1 = Conditional (default)

2 = Absolute.

raftime—zero or greater value indicates TRAC to read *rafin* values; negative value indicates TRAC to ignore values in *rafin.*

rafopt—value of 1 indicates TRAC to activate closure parameter logic.

An example of this type input for a Winfrith optimization run is as follows:

```
free format
*
*************
* main data *
*************
*
*       numtcr          ieos         inopt          nmat
            16             0             2             1
*
****************************************************************
****************************************************************
****************************************************************
*****                                                      *****
*                                                              *
*     winfrith-upflow post-CHF heat transfer experiment        *
*     test 405 : xeo = subcooled (xeo=-0.0167 at dryout point) *
*                p   = 2.2200E+05 Pa                           *
*                g   = 1.9960E+03 kg/m**2-s                    *
*                P   = 2.2180E+03 watts                        *
*                                                              *
*****                                                      *****
****************************************************************
****************************************************************
*
*
*****************
* namelist data *
*****************
*
 &rafopts  ntune=48,    irafset=1,    raftime=0.0,    rafopt=1.0 &
 &inopts  icflow=0, nhtstr=1, nrslv=1, ipatch=999, newrfd=1,
  ipowr=-1, tpowr=0.0, idiag=1, iadded=10 &
*
*        dstep         timet
          etc.
etc.
```

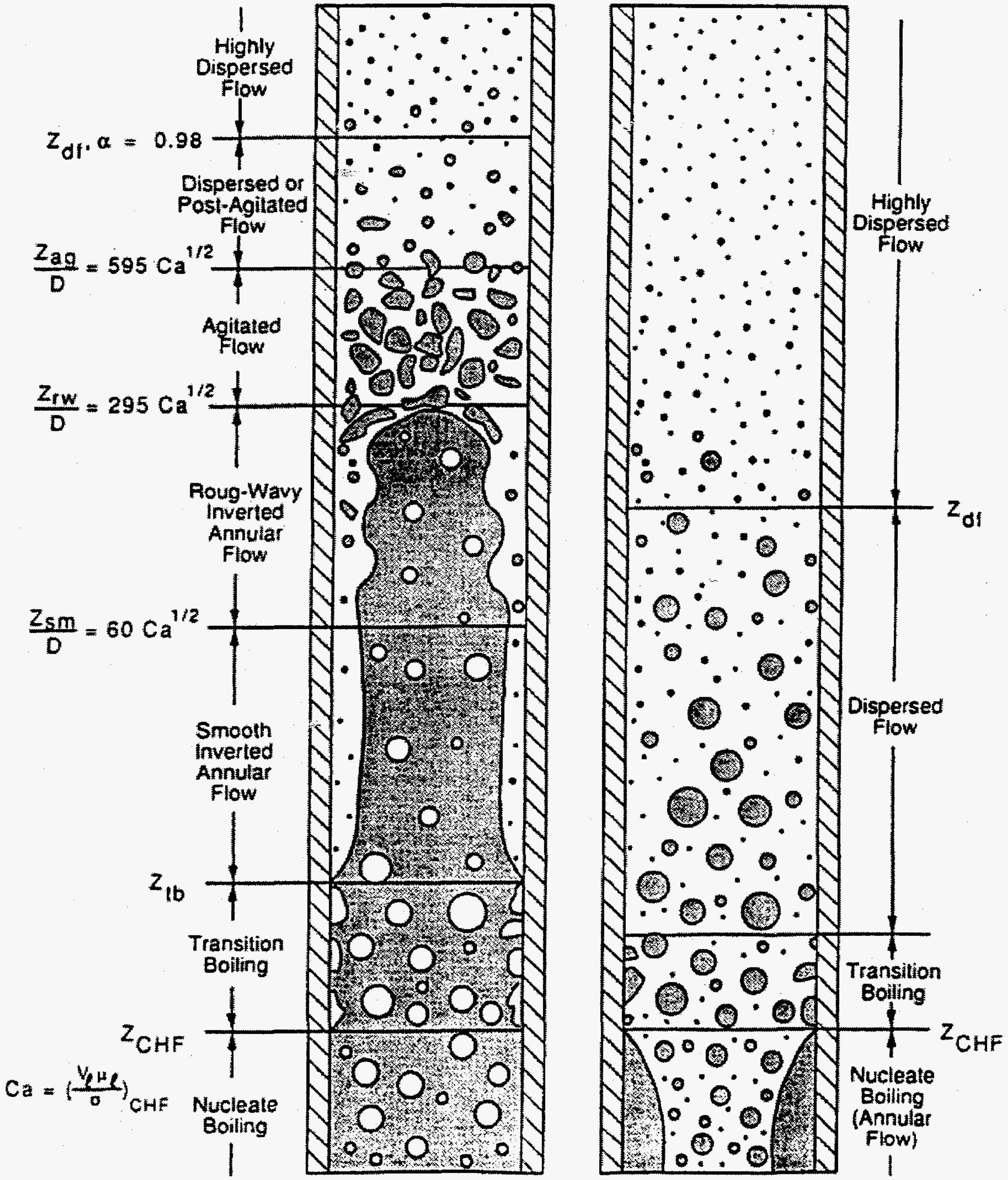

(a) Low Quality Inverted Annular CHF

(b) High Quality Annular CHF

Fig. 1. Sketch of possible classical flow regimes that may be experienced during reflood of a tube.

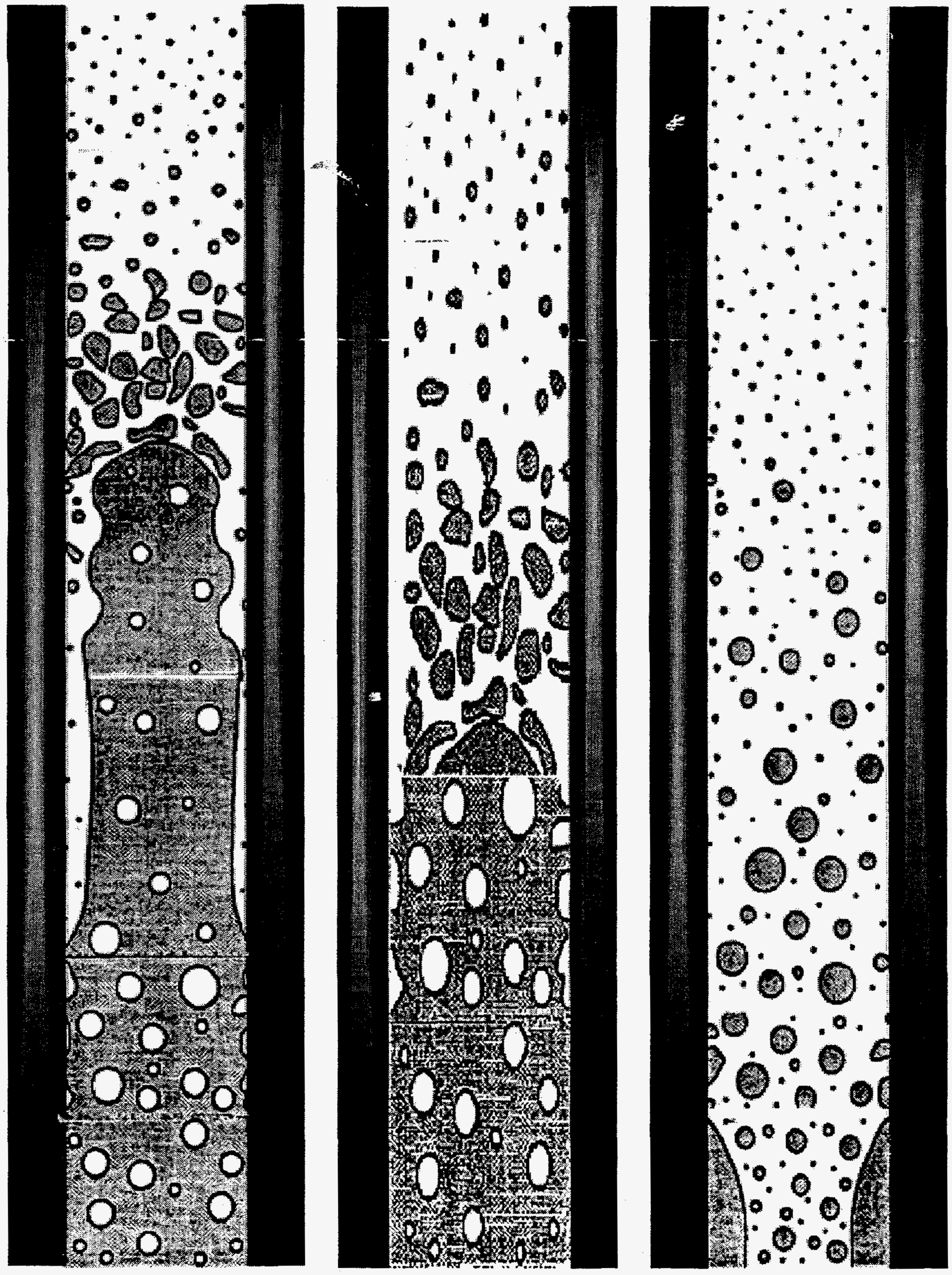

(a) Inverted Annular CHF (b) Slug-Churn CHF (c) Annular CHF

Fig. 2. Sketch of possible flow regimes that may be experienced during reflood within a rod bundle (only 2 rods shown).

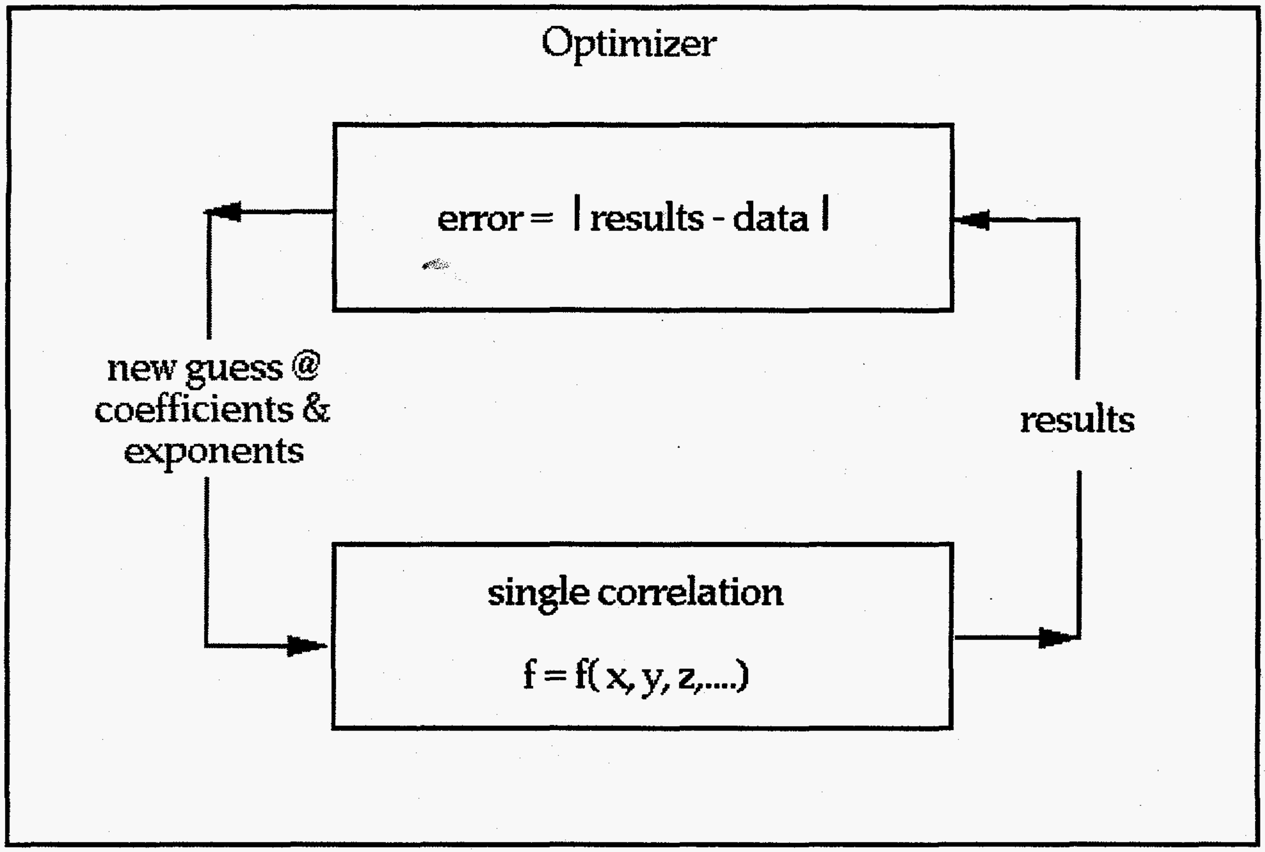

(a) Typical correlation development methodology

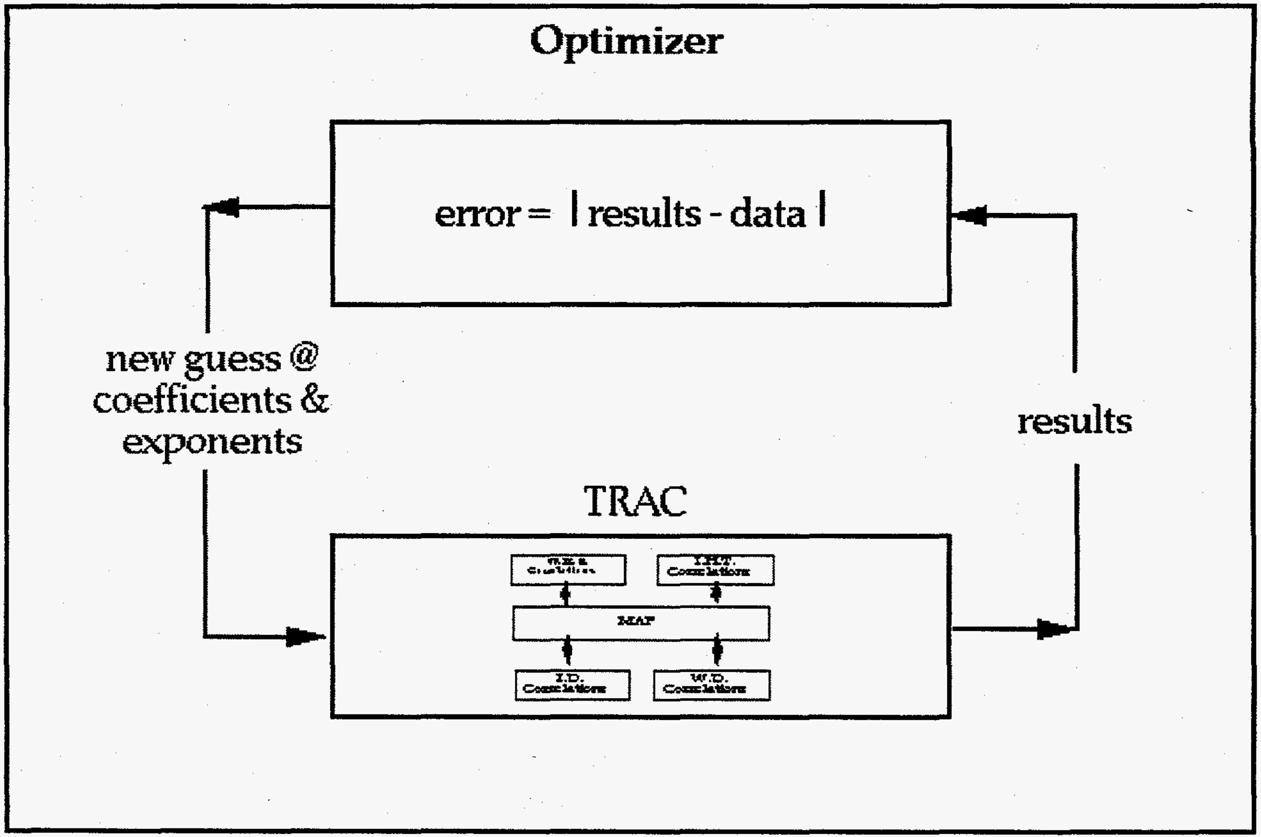

(b) Closure development based on optimization methodology

Fig. 3. Sketch of correlation and new closure development methodologies.

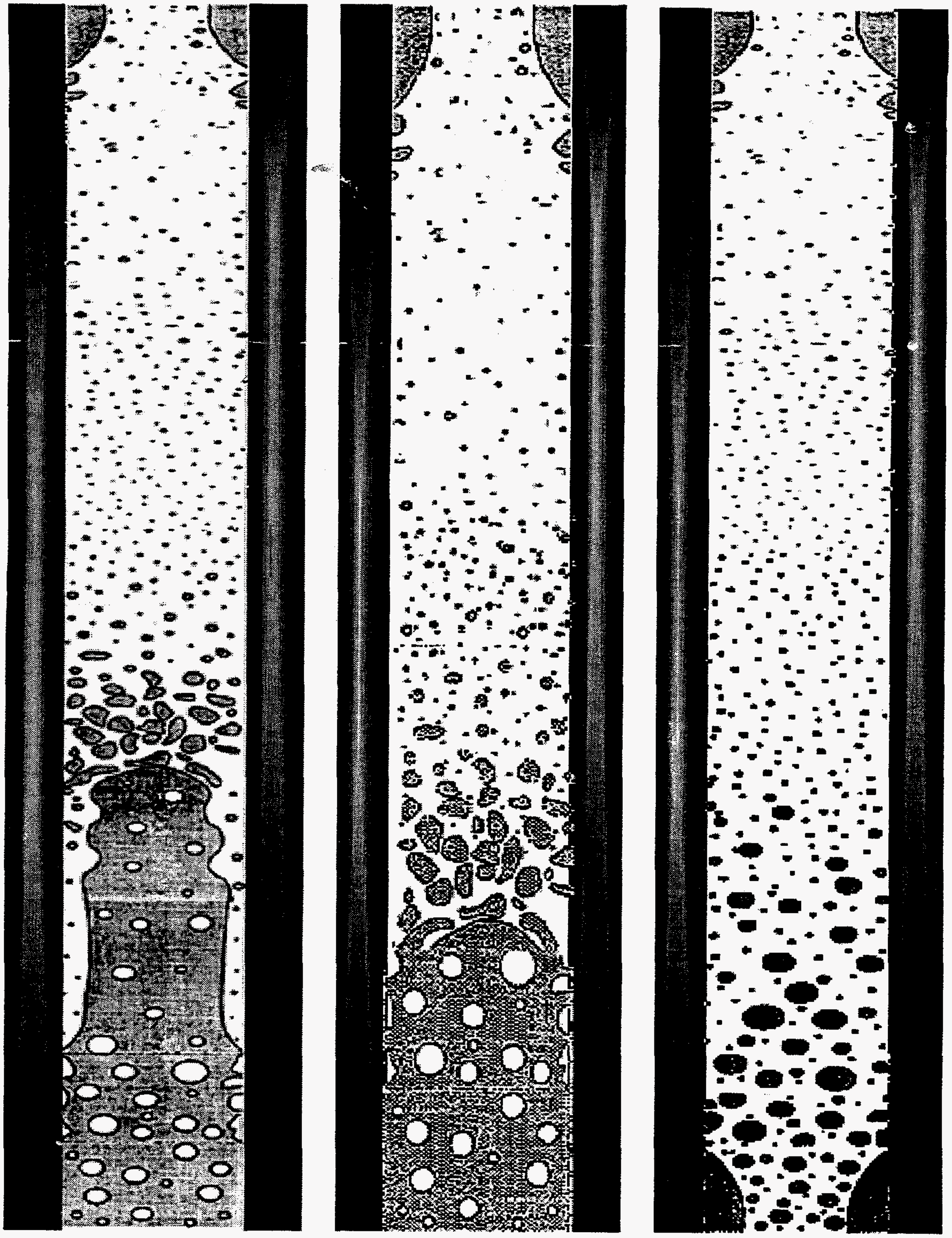

(a) Inverted Annular and Annular Quenches

(b) Slug-Churn and Annular Quenches

(c) Annular and Annular Quenches

Fig. 4. Sketch of possible flow regimes that may be experienced during reflood within a rod bundle experiencing bottom-up flow and multiple quenches (only 2 rods shown).

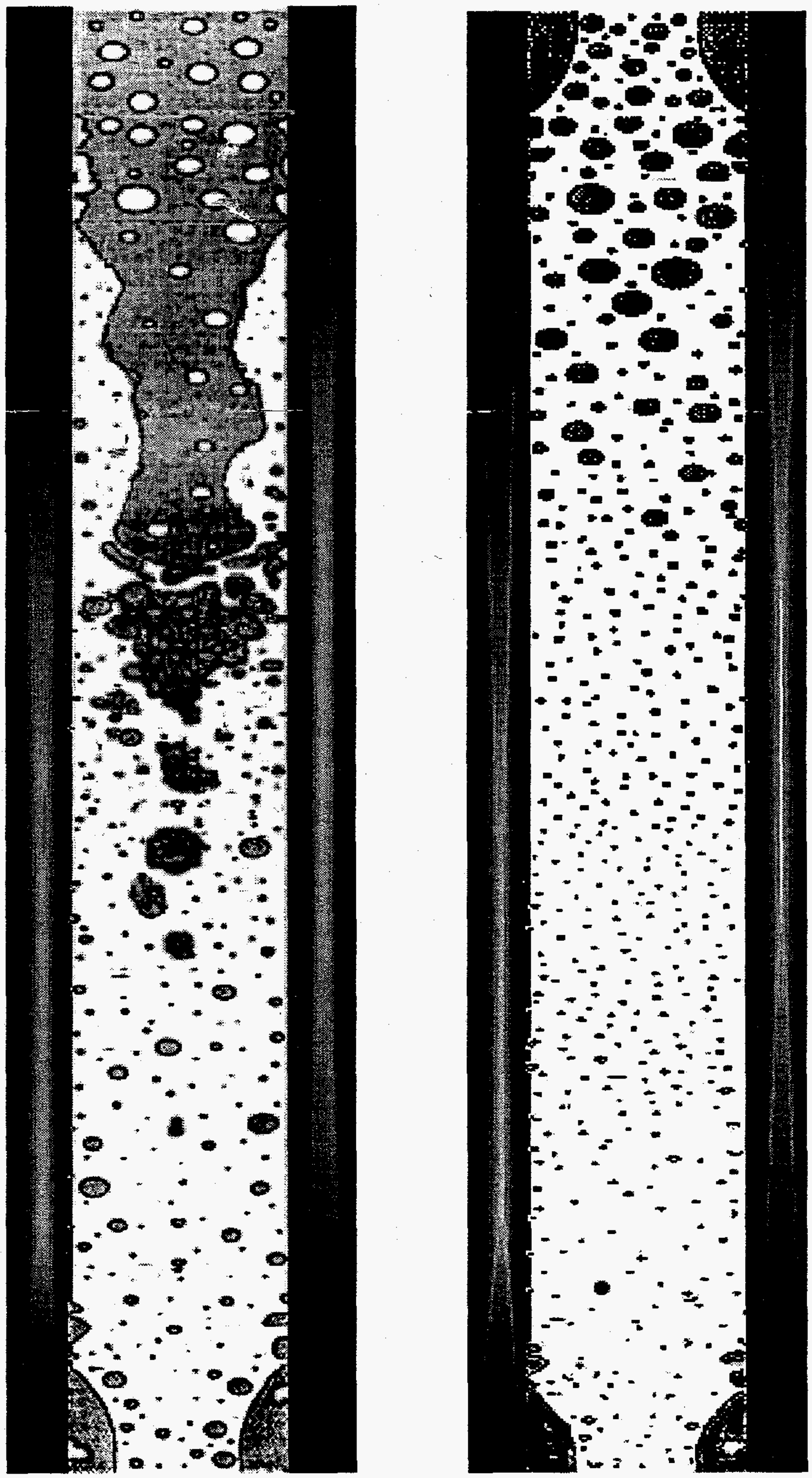

(a) Inverted Annular and Annular Quenches

(b) Slug-Churn and Annular Quenches

Fig. 5. Sketch of possible flow regimes that may be experienced during reflood within a rod bundle experiencing top-down flow and multiple quenches (only 2 rods shown).

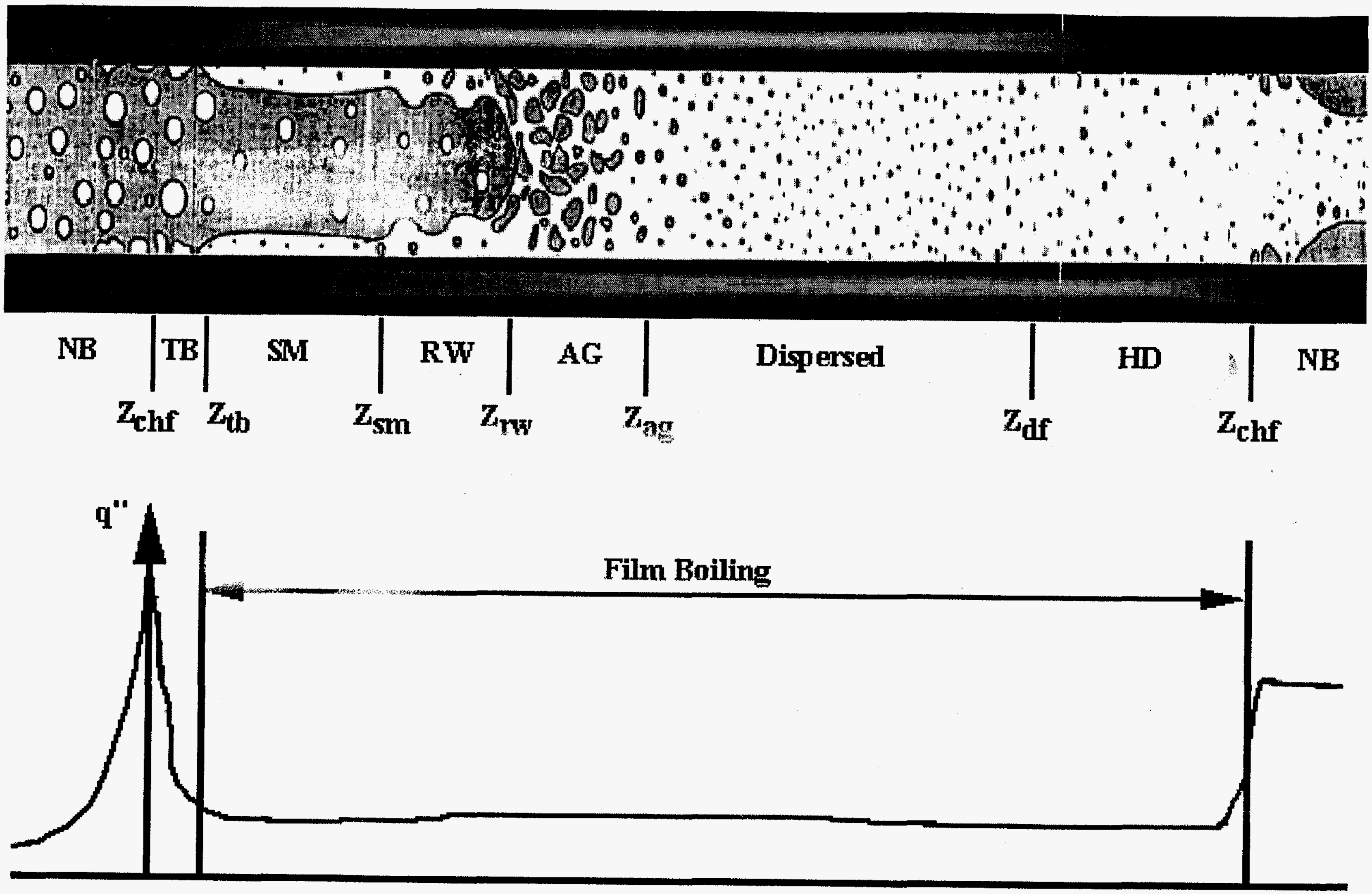

Fig. 6. Typical axial wall heat flux profile for IAF. Axial distance is based on the relative coordinate system determined by liquid velocities at the bottom and top of the core.

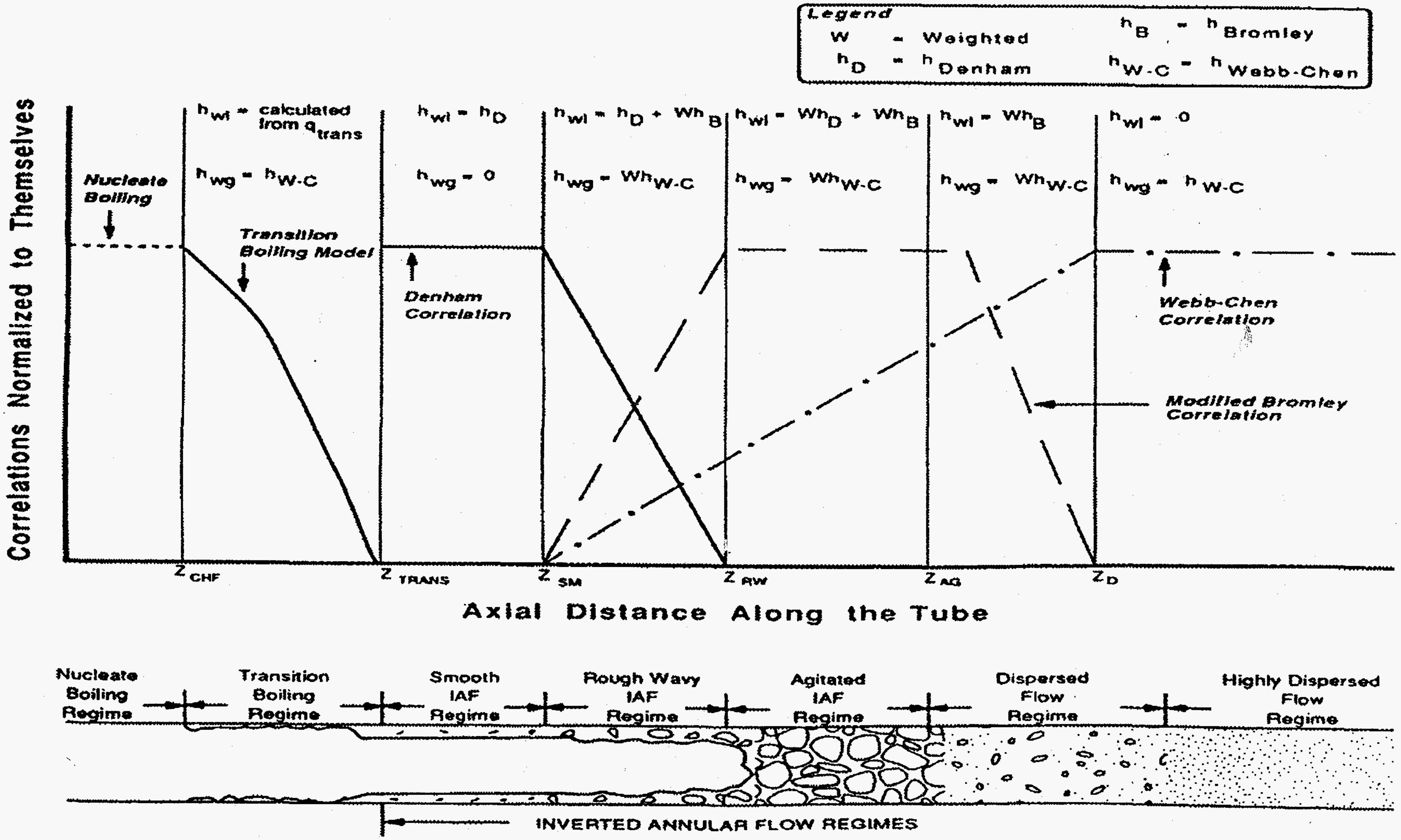

Fig. 7. Illustration of HTC selection logic. Axial distance is based on the relative coordinate system determined by liquid velocities at the bottom and top of the core.

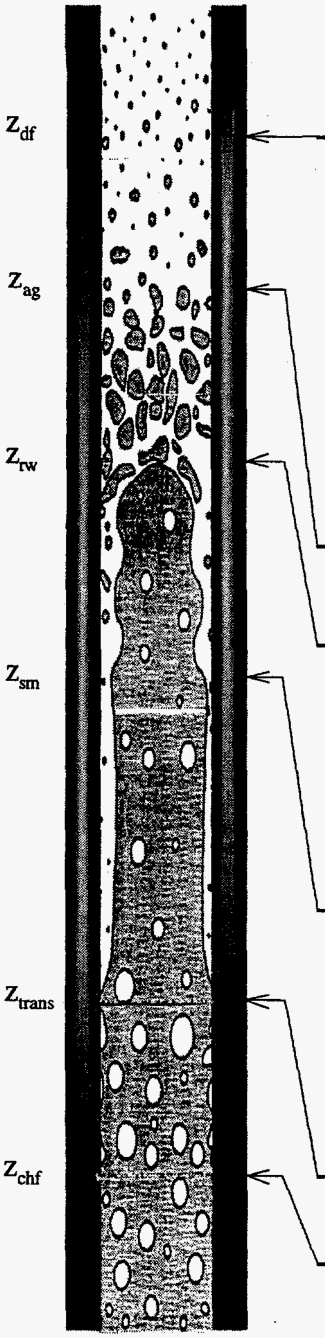

Highly Dispersed Flow Regime	$C_{i,df}$			
Dispersed Flow Regime (Post-Agitated)	if $f_{dis}C_{i,df} < f_{rw}C_{i,rw}$ $C_{i,pa} = C_{i,rw}\frac{f_{rw}}{f_{mdis}} + \left(C_{i,df}\frac{f_{dis}}{f_{mdis}} - C_{i,rw}\frac{f_{rw}}{f_{mdis}}\right)\left(\frac{\alpha-\alpha_{ag}}{\alpha_3-\alpha_{ag}}\right)^{m_3}$ where $\begin{cases} 0 \le \left(\frac{\alpha-\alpha_{ag}}{\alpha_3-\alpha_{ag}}\right)^{m_3} \le 1 \\ \alpha_{ag} = \min(\alpha_{ag}, 0.7) \end{cases}$ else $C_{i,pa} = C_{i,rw}\frac{f_{rw}}{f_{mdis}}$			$C_{i,pa} = C_{i,df}$
Agitated IAF Regime	Same as Rough Wavy		Same as Rough Wavy	Same as Rough Wavy

Rough Wavy IAF Regime	$C_{i,rw}$		if $C_{i,rw} > C_{i,df}$ then
			$C_{i,rw} = C_{i,rw} + (C_{i,df} - C_{i,rw})\left(\frac{\alpha-\alpha_2}{\alpha_3-\alpha_2}\right)^{m_2}$
			where $0 \le \frac{\alpha-\alpha_2}{\alpha_3-\alpha_2} \le 1$
			else
			$C_{i,rw} = C_{i,df}$
				$C_{i,rw} = C_{i,df}$

Smooth IAF Regime	$C_{i,sm}$		if $C_{i,sm} > C_{i,df}$ then
			$C_{i,sm} = C_{i,sm} + (C_{i,df} - C_{i,sm})\left(\frac{\alpha-\alpha_2}{\alpha_3-\alpha_2}\right)^{m_2}$
			where $0 \le \frac{\alpha-\alpha_2}{\alpha_3-\alpha_2} \le 1$
			else
			$C_{i,sm} = C_{i,df}$
				$C_{i,sm} = C_{i,df}$

Transition Boiling Regime	$C_{i,sb}$		$C_{i,sb} = \max\left(C_{i,iam}, C_{i,sb}\left(\frac{1-\alpha}{1-\alpha_1}\right)^{m_1}\right)$	$C_{i,sb} = C_{i,iam}$
Nucleate Boiling Regime	$C_{i,sb}$			

$\alpha_1 = 0.5$ $\alpha_2 = 0.75$ $\alpha_3 = 0.98$

Void Fraction

NOTES: $m_1 = 3$, $m_2 = m_3 = 0.5$, $\frac{f_{dis}}{f_{mdis}} = 1$ and $\frac{f_{rw}}{f_{mdis}} = 1.25$

Fig. 8. The interfacial drag coefficient model selection logic in the IAF regime-void fraction plane. Axial distance is based on the relative coordinate system determined by liquid velocities at the bottom and top of the core.

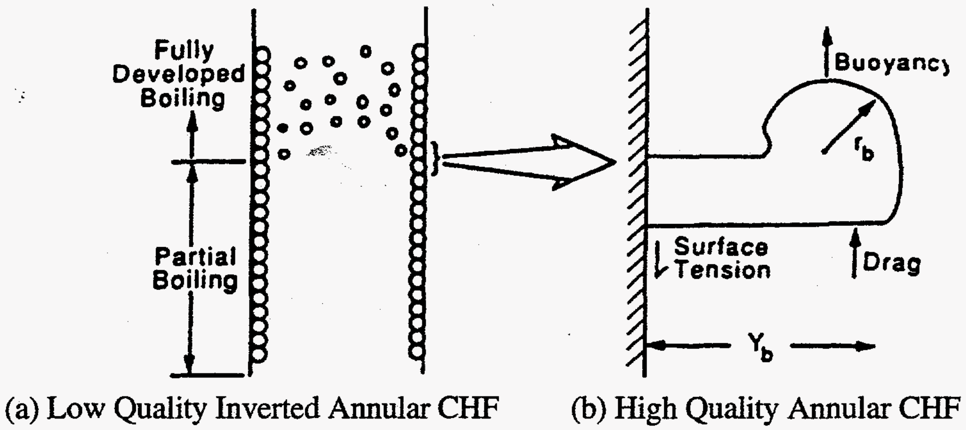

(a) Low Quality Inverted Annular CHF (b) High Quality Annular CHF

Fig. 9. Bubble attached to wall in subcooled boiling.

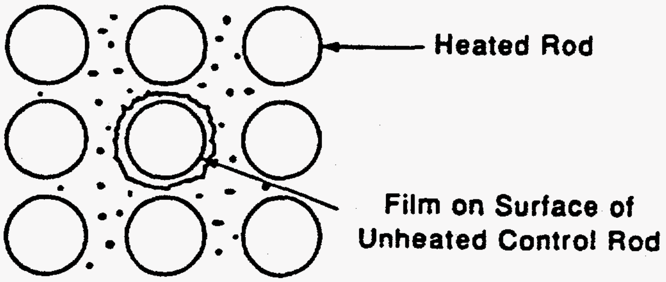

Fig. 10. Proposed scheme for the dispersed region in reactor geometry.

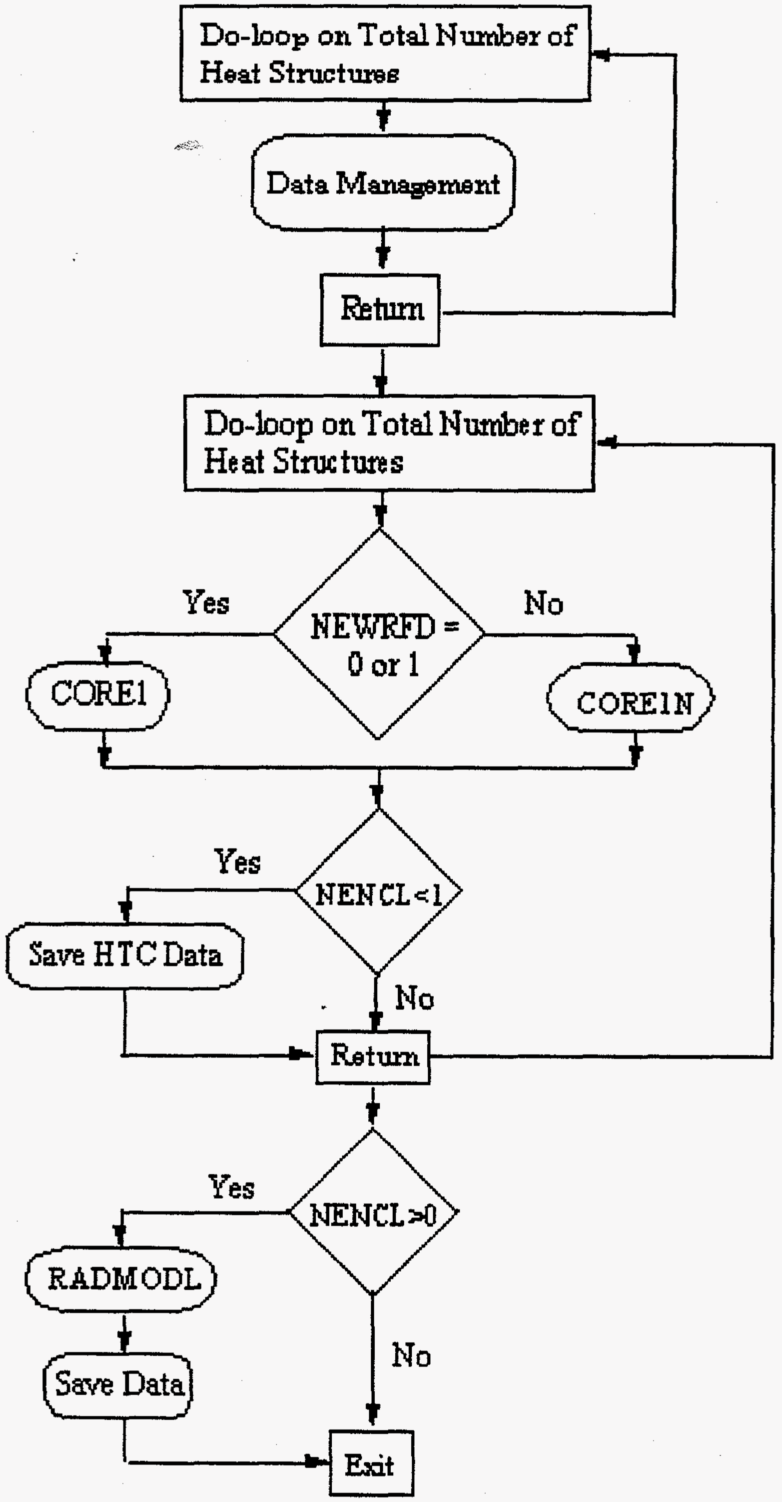

Fig. 11. Basic coding structure of subroutine HTSTR1.

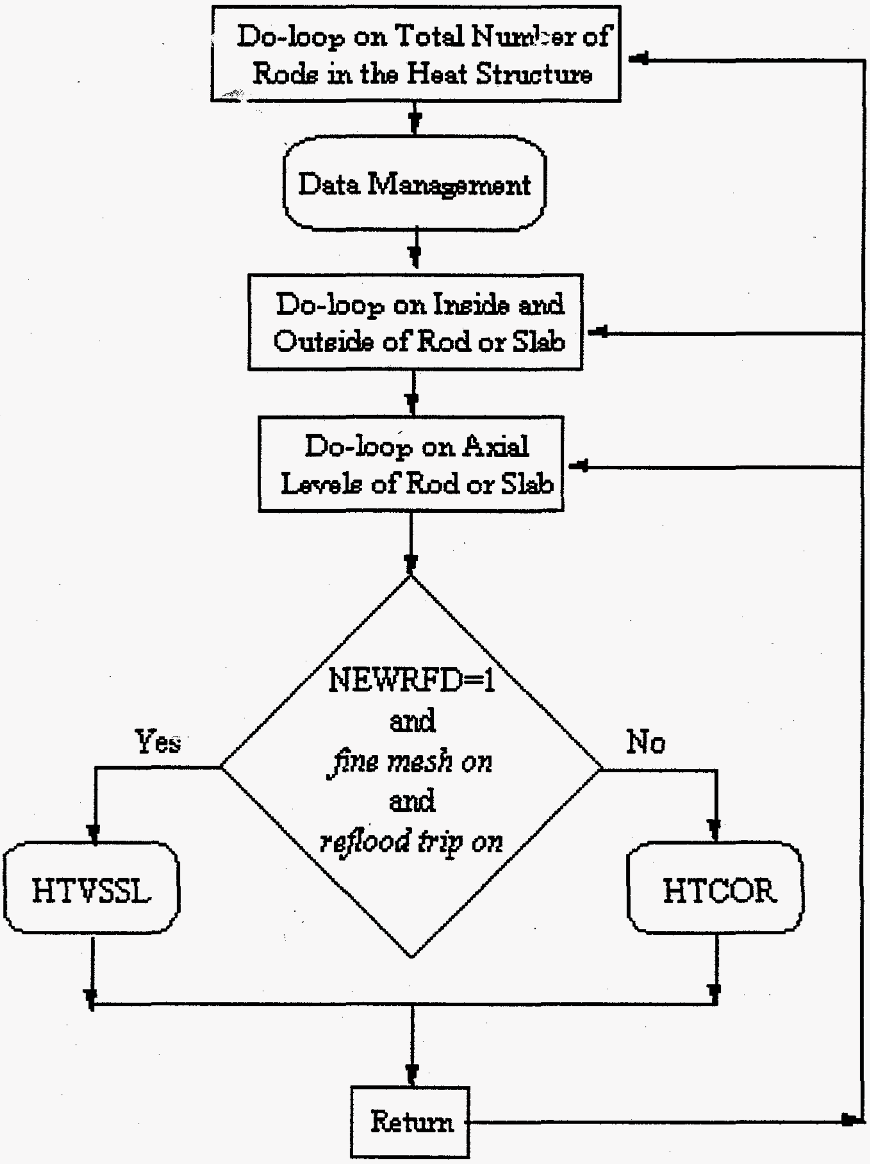

Fig. 12. Basic coding structure of subroutine CORE1.

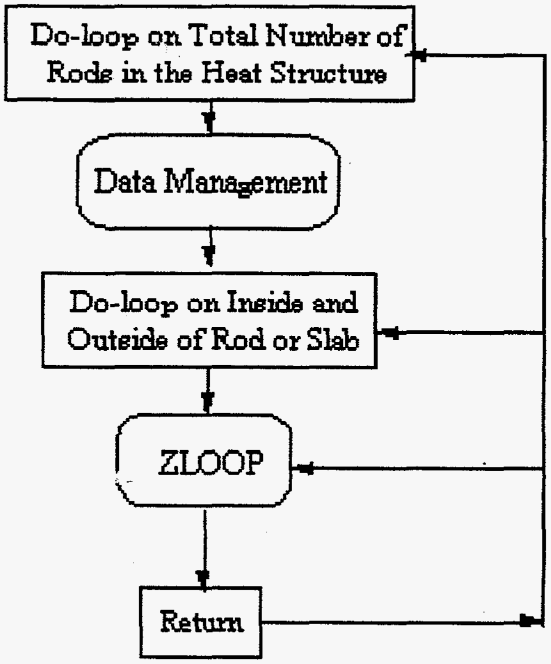

Fig. 13. Basic coding structure of subroutine CORE1N.

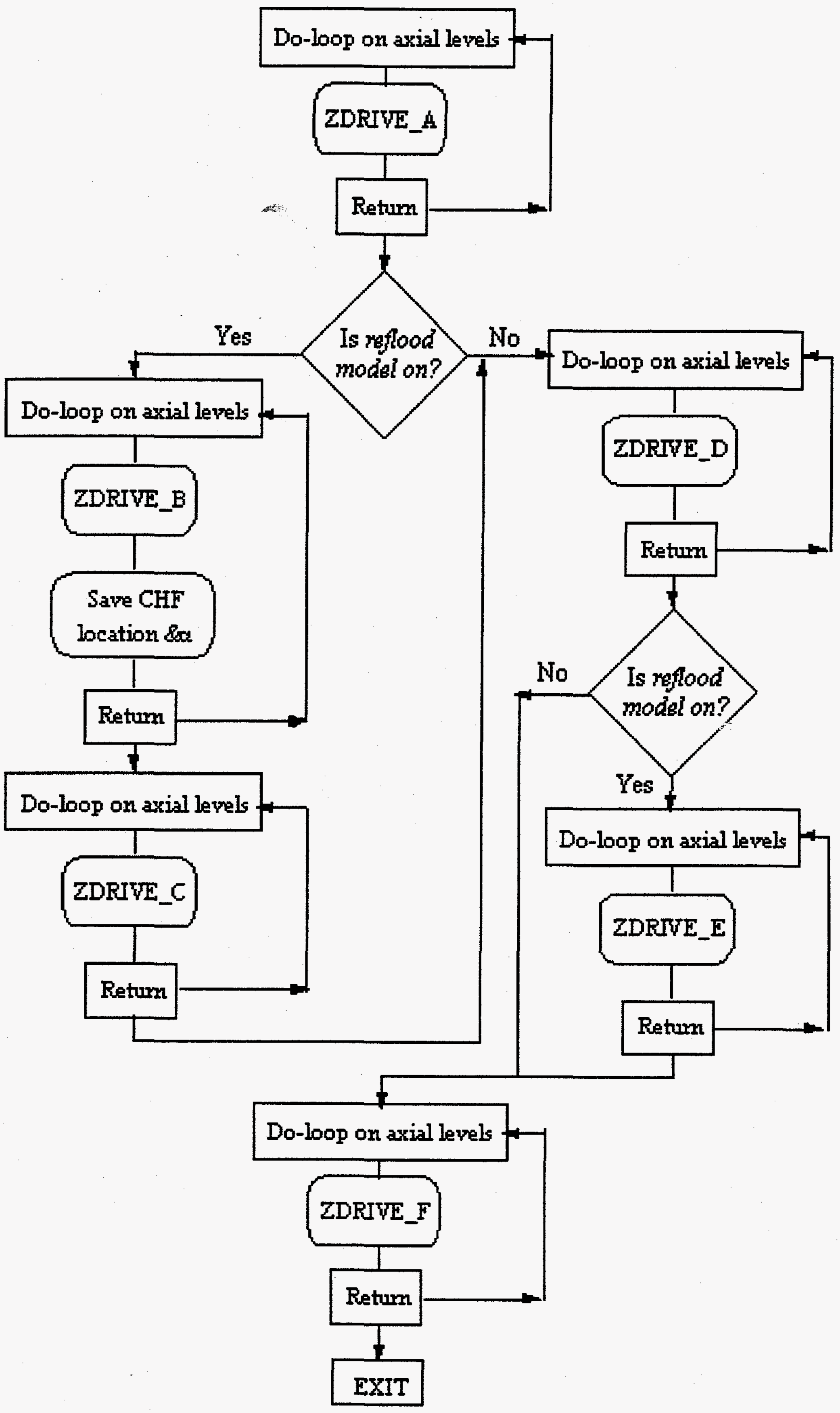

Fig. 14. Basic coding structure of subroutine ZLOOP.

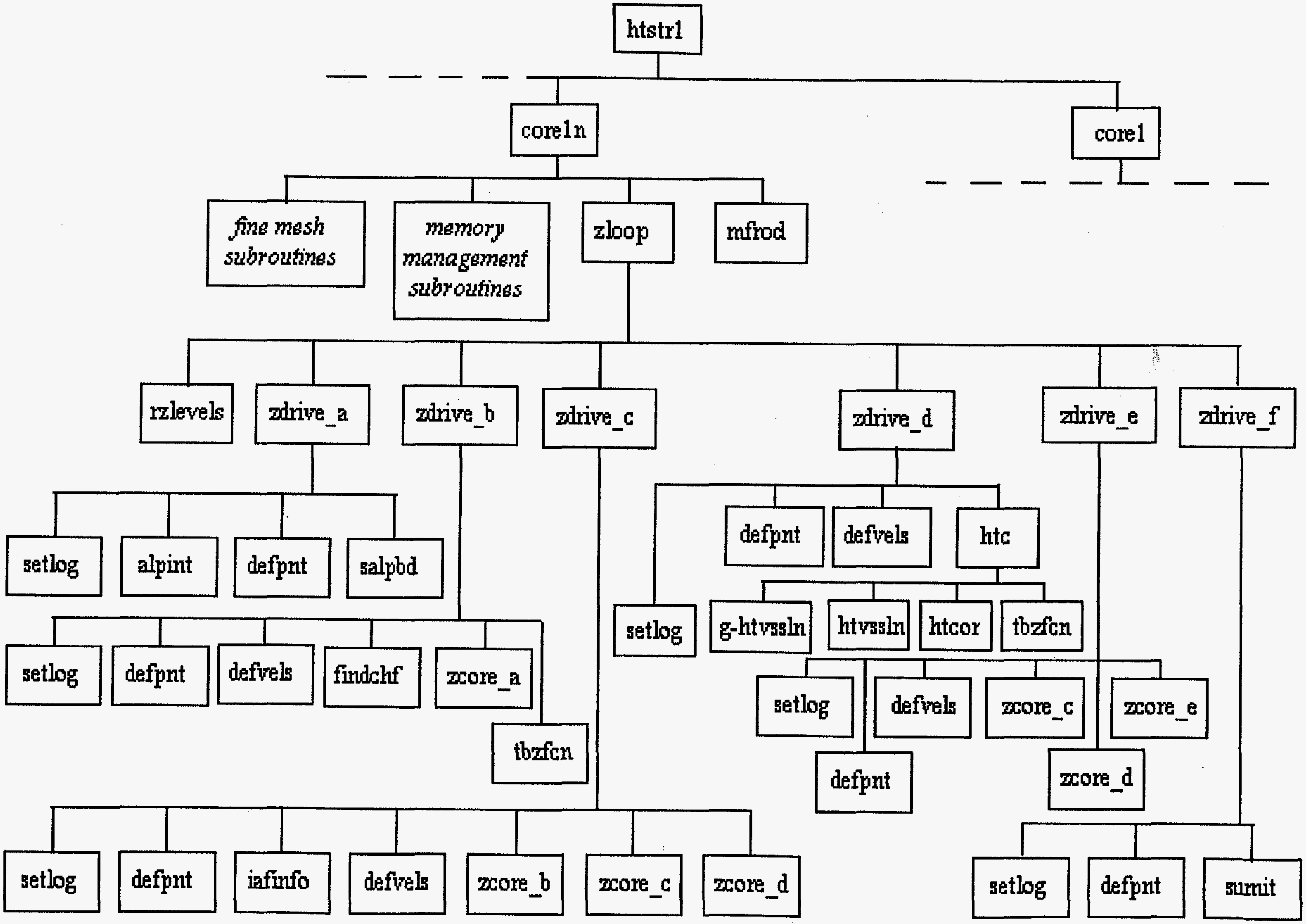

Fig. 15. Subroutine calling sequence diagram of wall heat transfer.

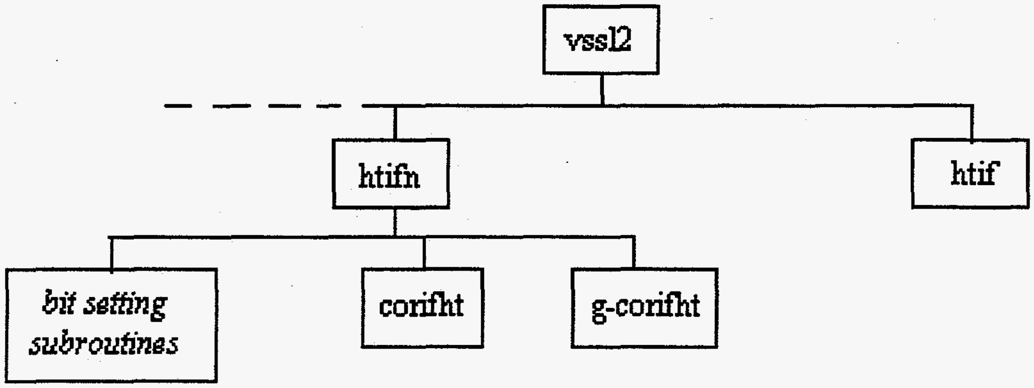

Fig. 16. Subroutine calling sequence diagram of interfacial heat transfer.

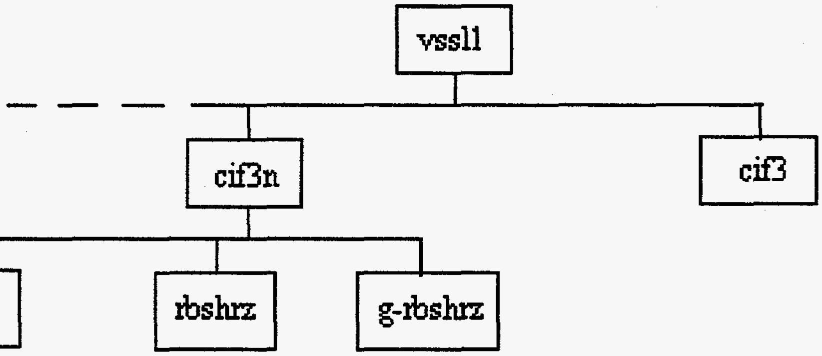

Fig. 17. Subroutine calling sequence diagram of 3D interfacial drag.

Optimization Information Flow Diagram.
A: Vital TRAC information
B: Time-averaged and Penalty Function information used for optimization and summarization
C: General summary information

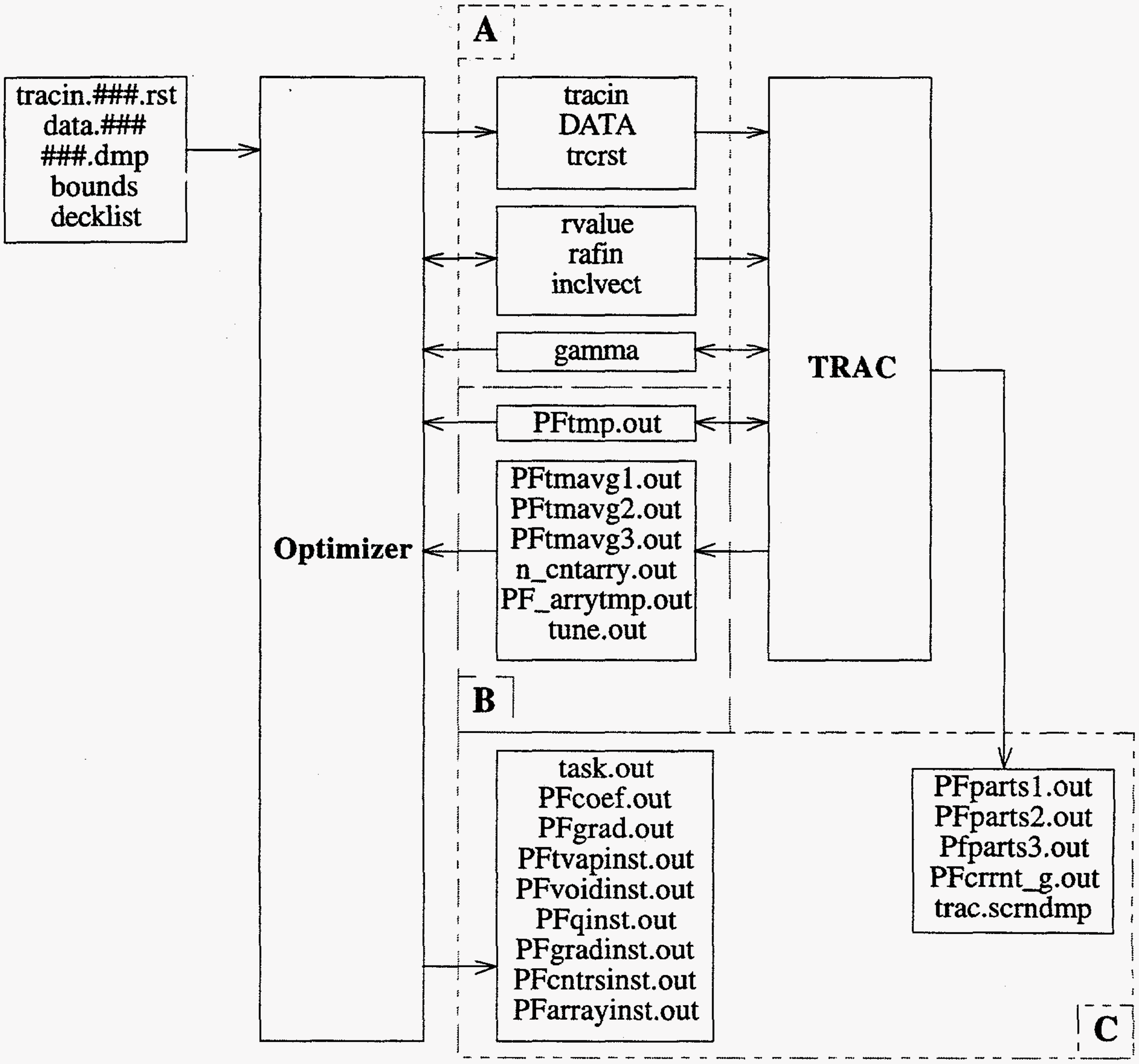

Fig. 18. Structure diagram of the optimization, TRAC code and necessary files.

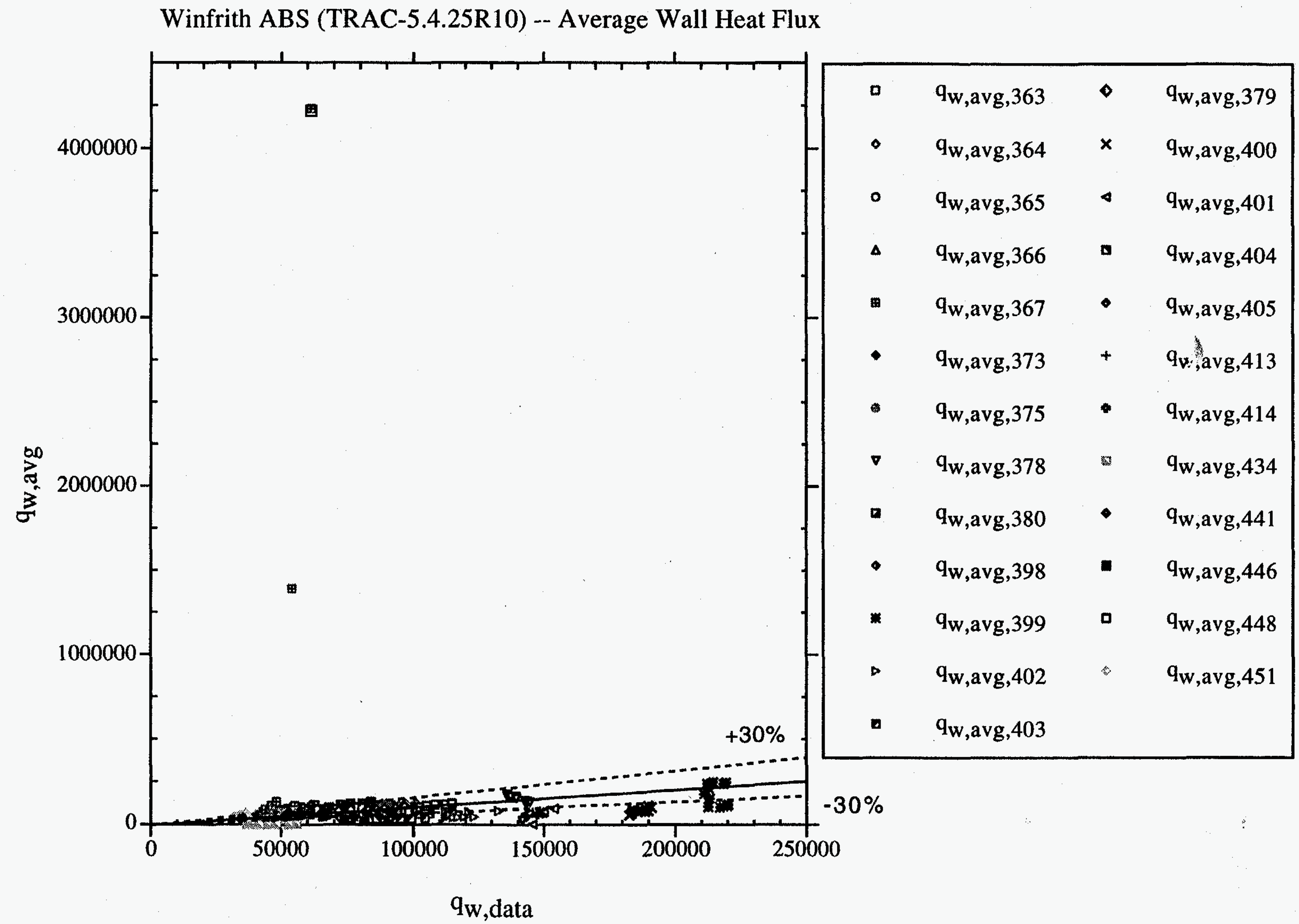

Fig. 19. Time-averaged wall heat flux calculated using the Absolute Pedigree coefficients vs Winfrith steady-state and quasi-steady-state post-CHF-up-flow data.

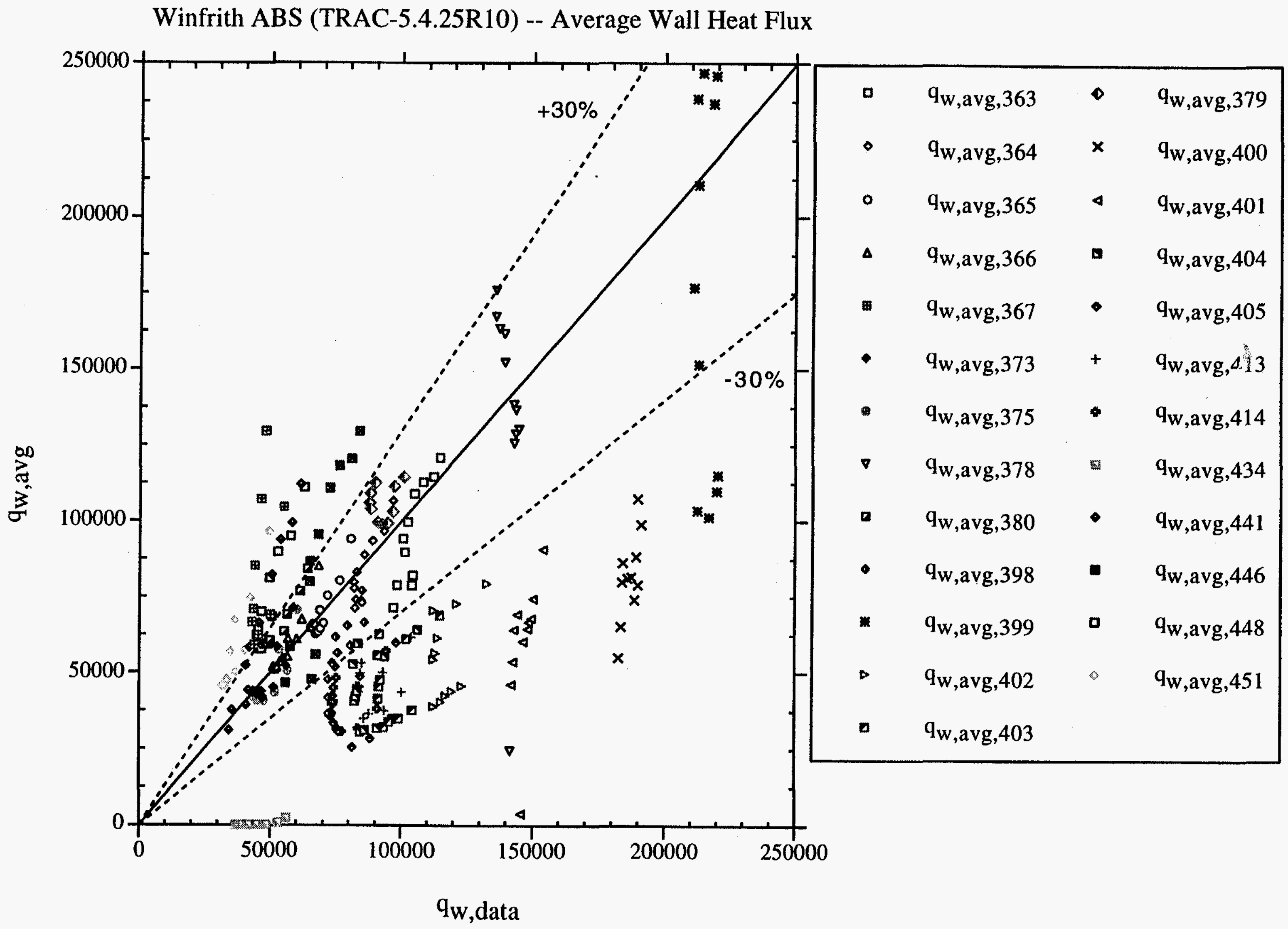

Fig. 20. Time-averaged wall heat flux calculated using the Absolute Pedigree coefficients vs Winfrith steady-state and quasi-steady-state post-CHF-up-flow data—same as Fig. 19 with adjusted ordinate scale.

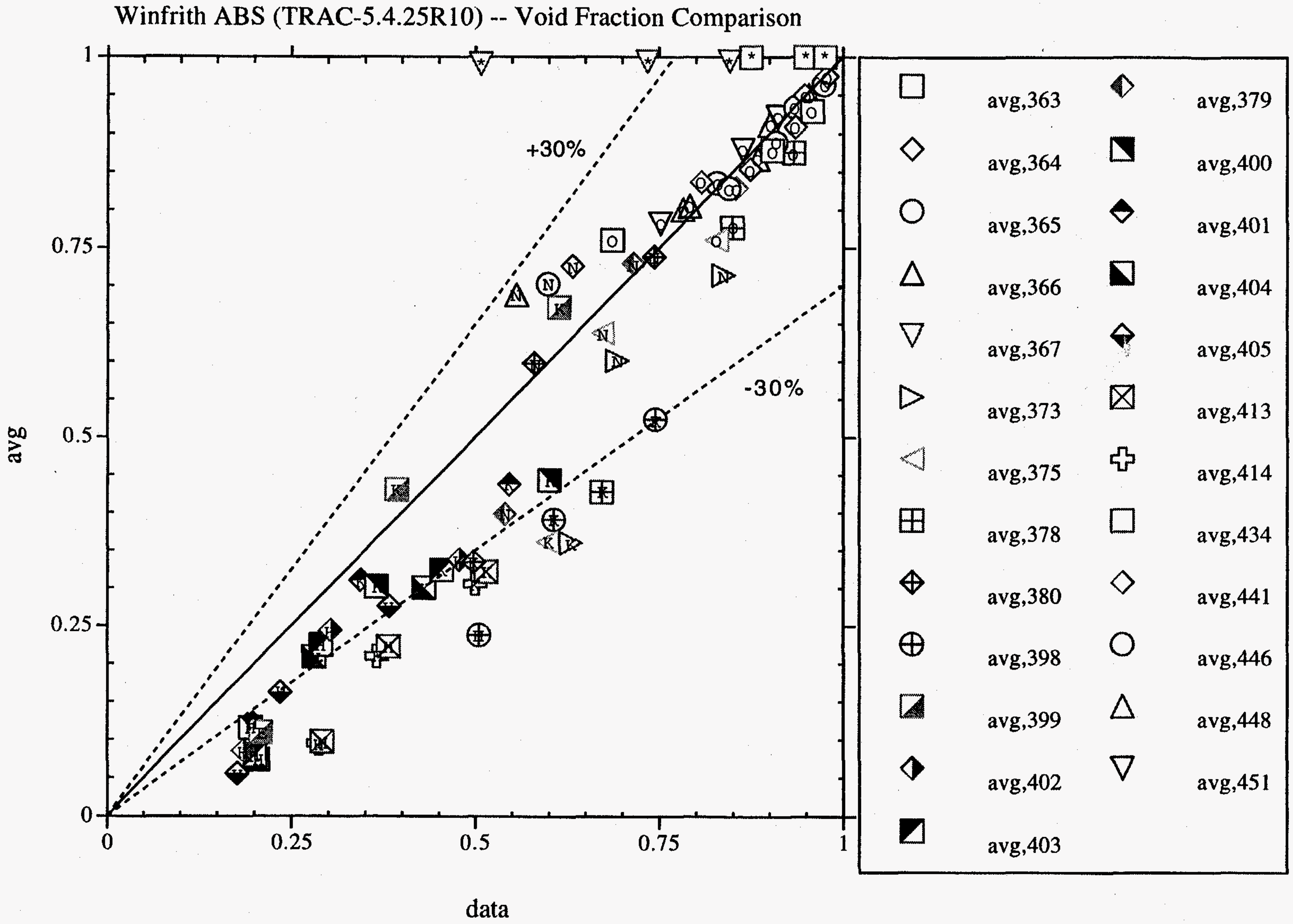

Fig. 21. Time-averaged vapor void fraction calculated using the Absolute Pedigree coefficients vs Winfrith steady-state and quasi-steady-state post-CHF-up-flow data.

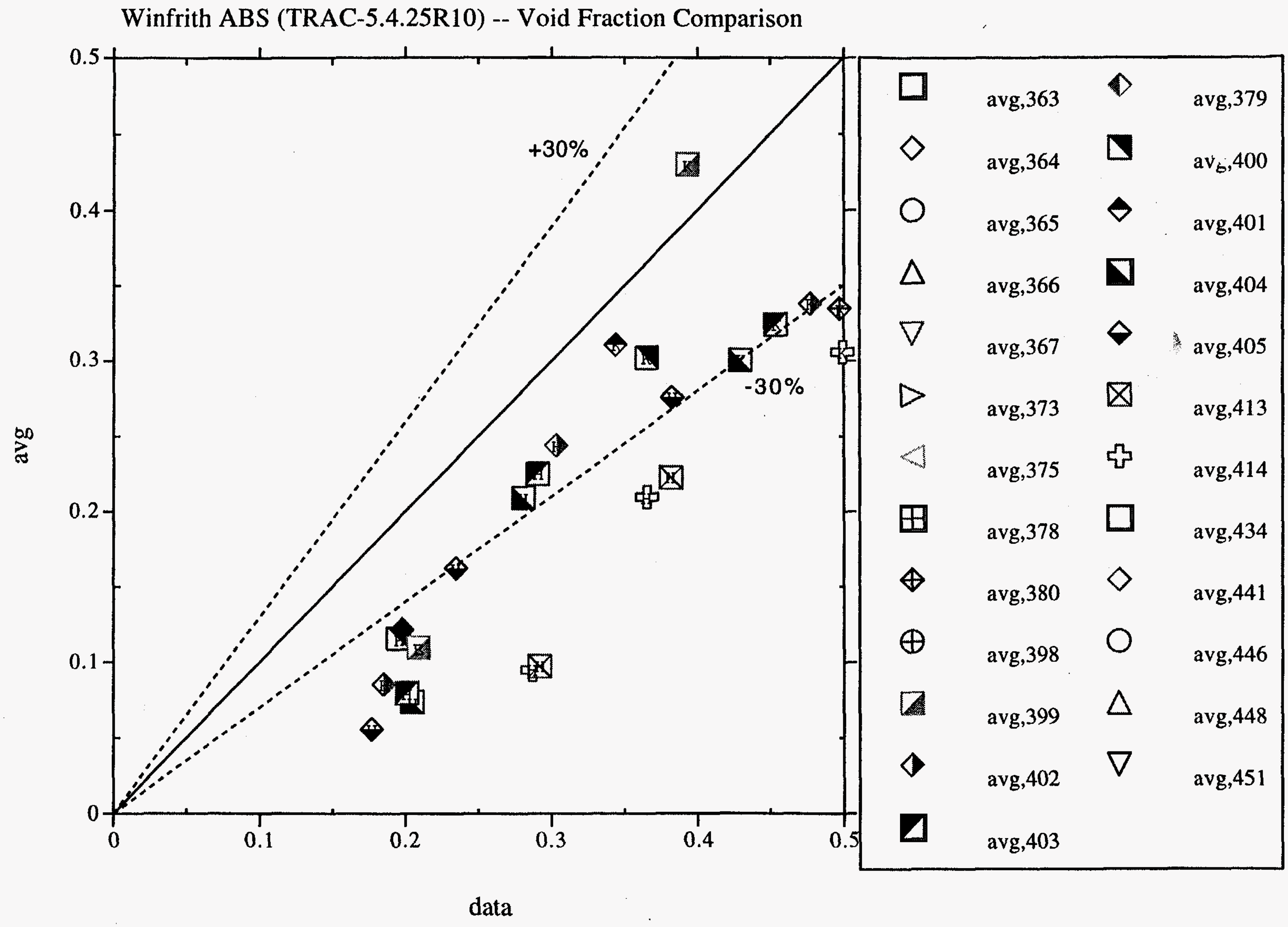

Fig. 21a. Time-averaged vapor void fraction calculated using the Absolute Pedigree coefficients vs Winfrith steady-state and quasi-steady-state post-CHF-up-flow data (modified range on axes).

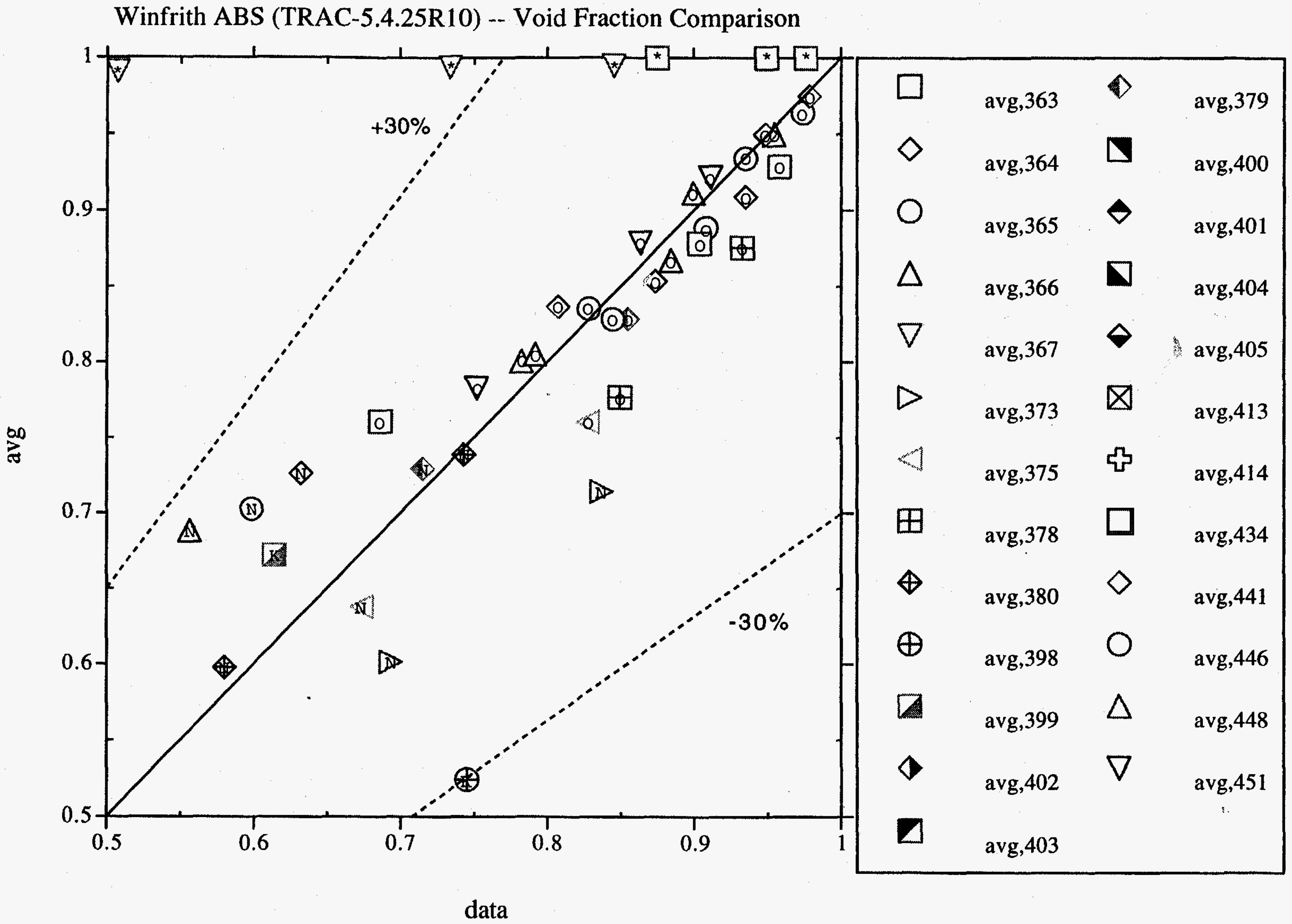

Fig. 21b. Time-averaged vapor void fraction calculated using the Absolute Pedigree coefficients vs Winfrith steady-state and quasi-steady-state post-CHF-up-flow data (modified range on axes).

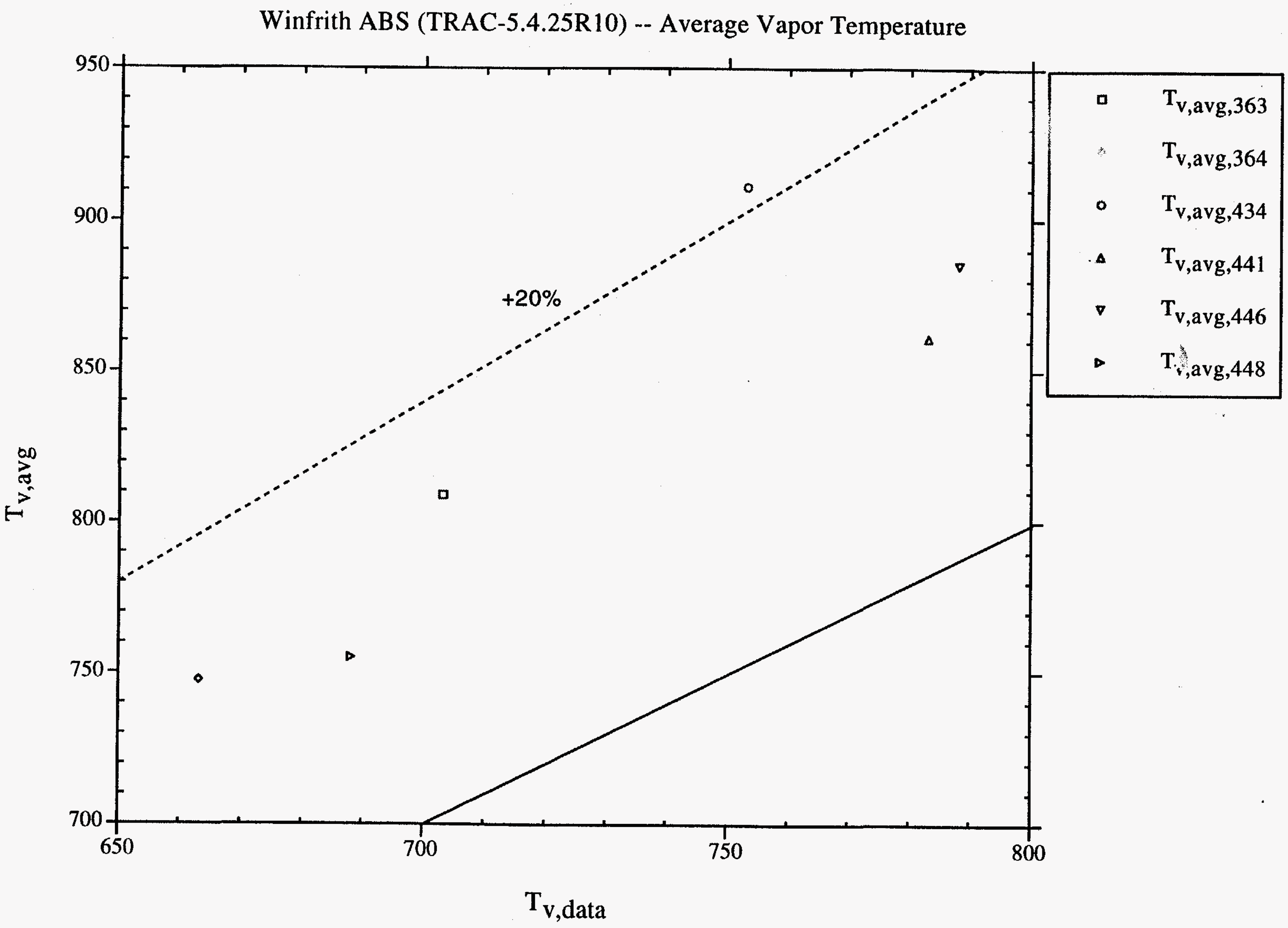

Fig. 22. Time-averaged vapor temperature calculated using the Absolute Pedigree coefficients vs Winfrith steady-state and quasi-steady-state post-CHF-up-flow data.

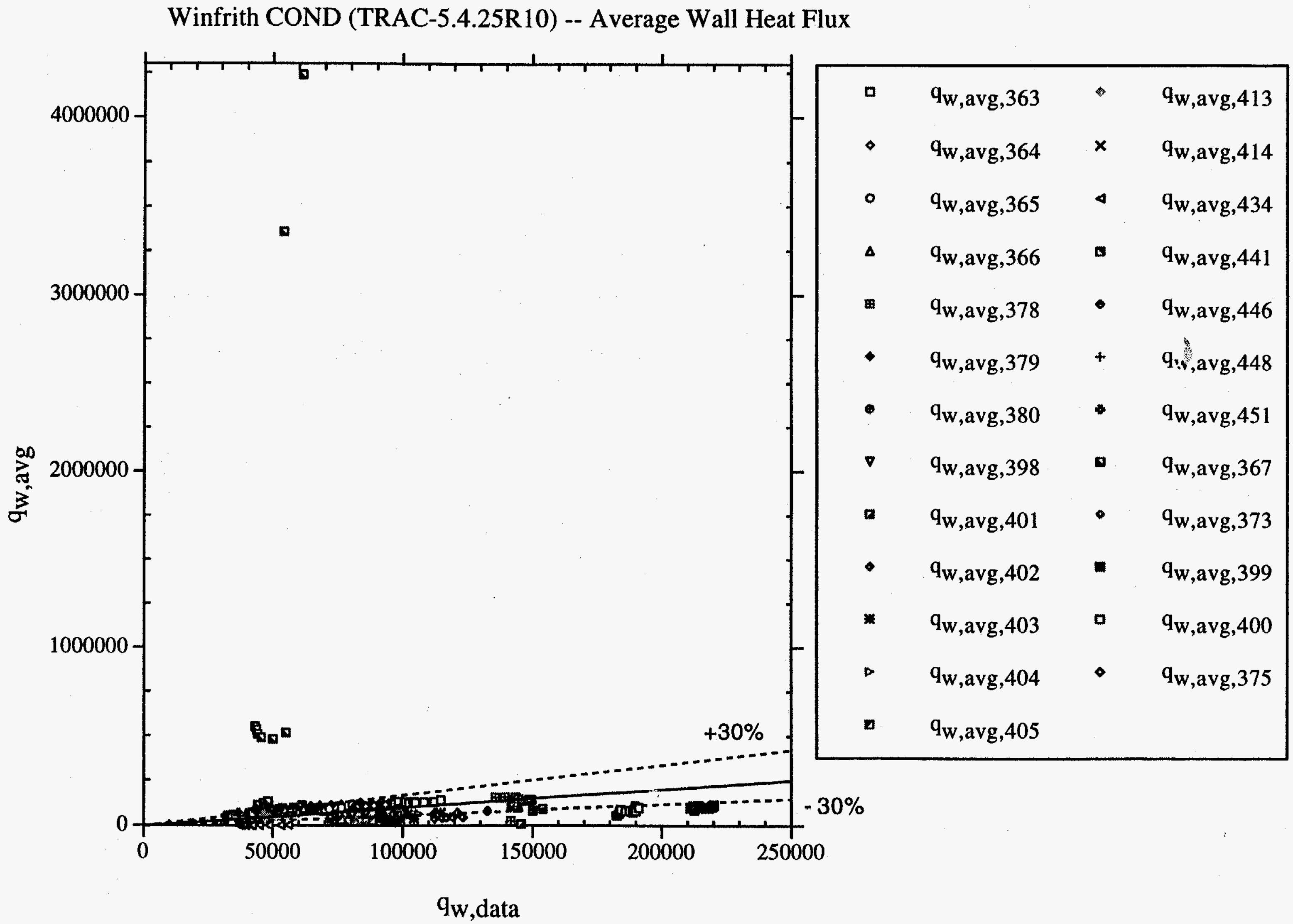

Fig. 23. Time-averaged wall heat flux calculated using the Conditional Pedigree coefficients vs Winfrith steady-state and quasi-steady-state post-CHF-up-flow data.

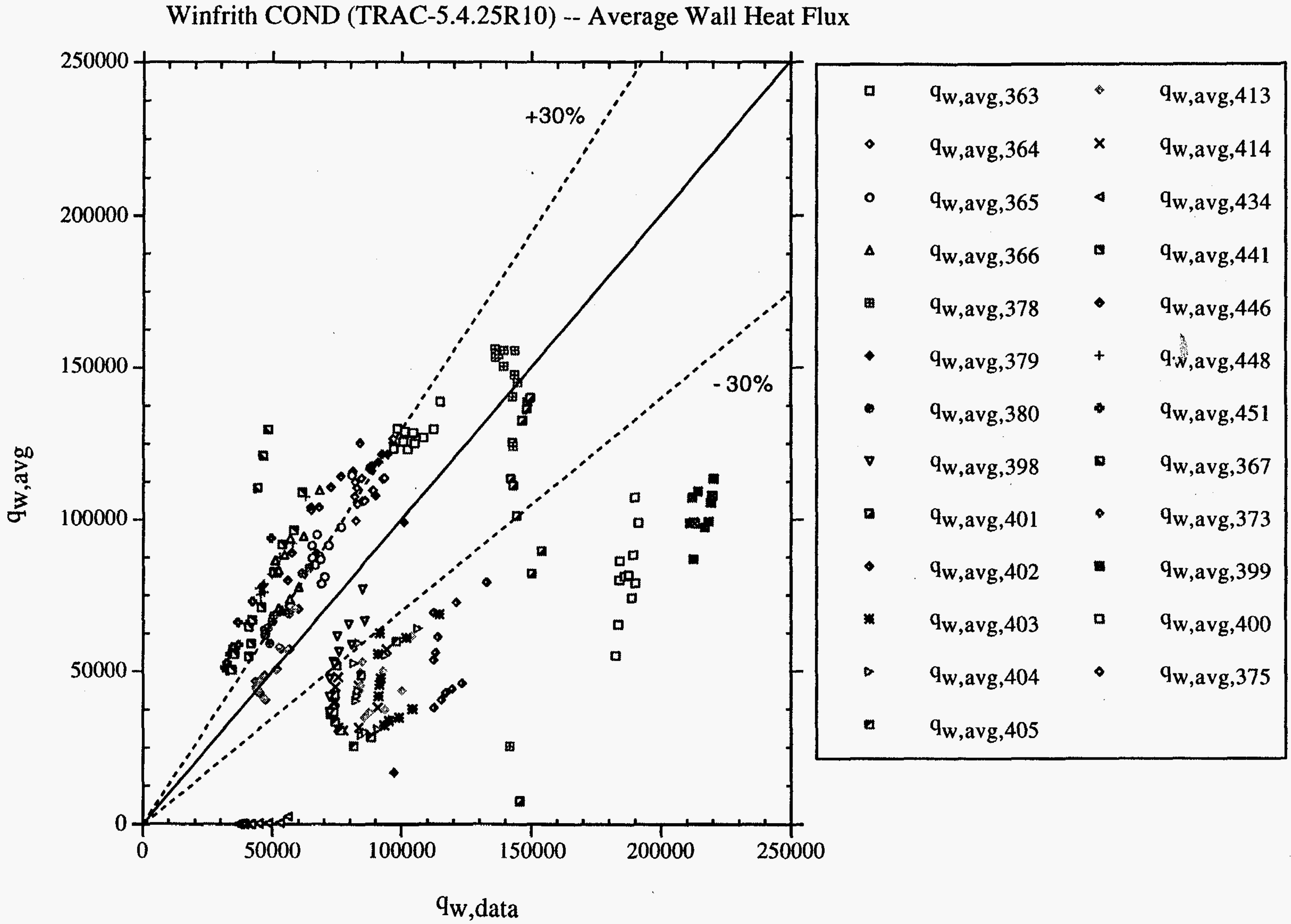

Fig. 23a. Time-averaged wall heat flux calculated using the Conditional Pedigree coefficients vs Winfrith steady-state and quasi-steady-state post-CHF-up-flow data (modified range on vertical axes).

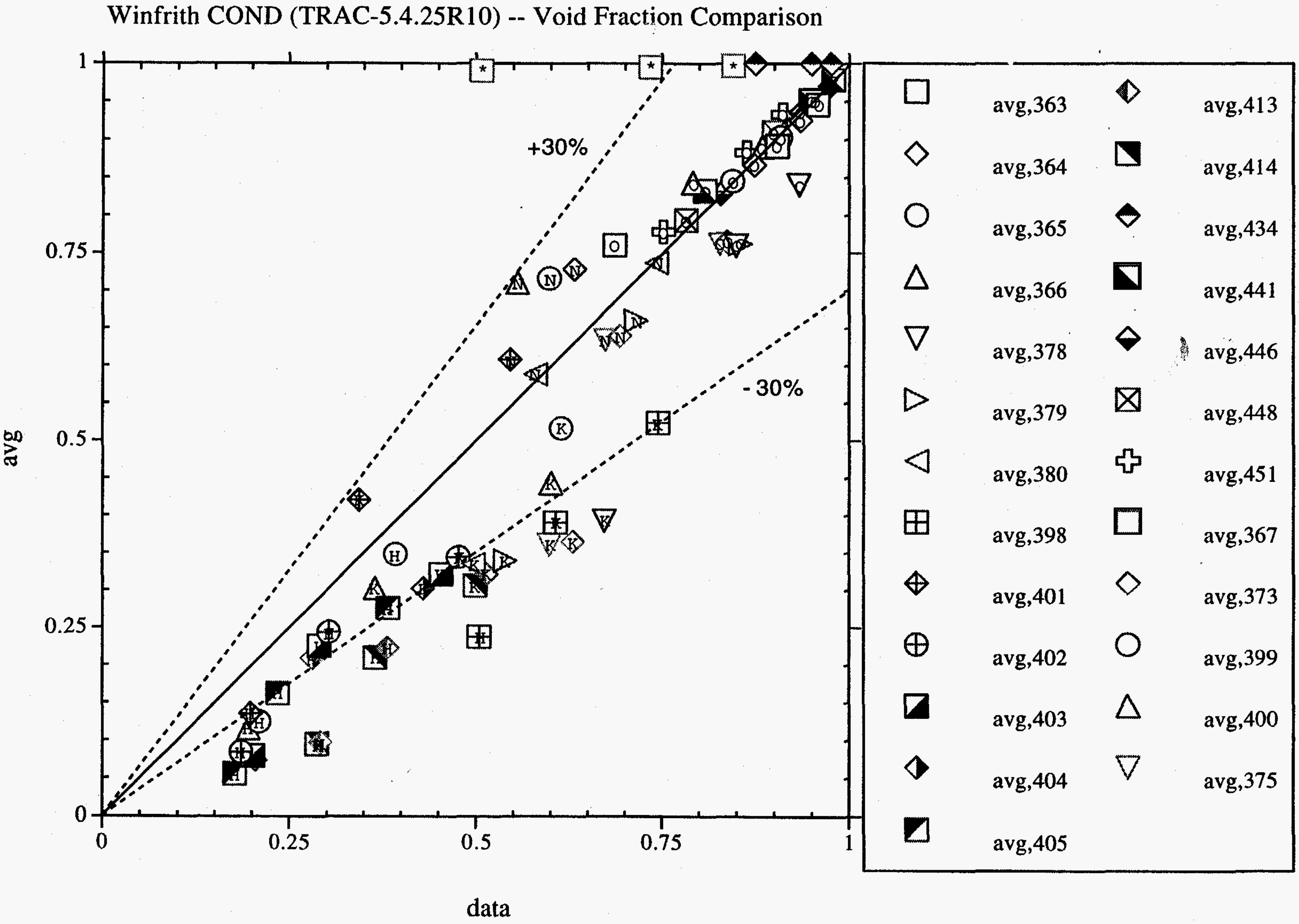

Fig. 24. Time-averaged vapor void fraction calculated using the Conditional Pedigree coefficients vs Winfrith steady-state and quasi-steady-state post-CHF-up-flow data.

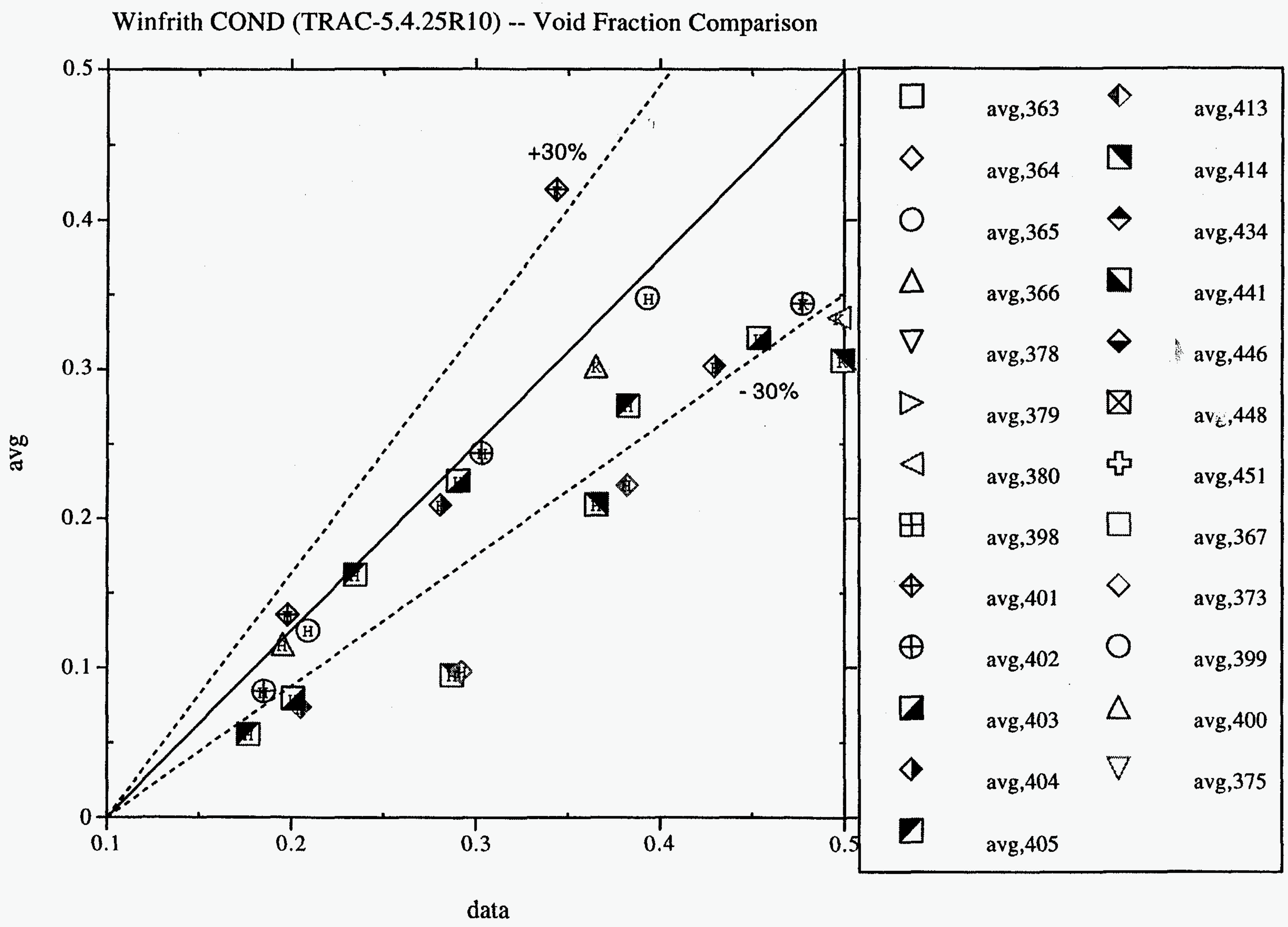

Fig. 24a. Time-averaged vapor void fraction calculated using the Conditional Pedigree coefficients vs Winfrith steady-state and quasi-steady-state post-CHF-up-flow data (modified range on axes).

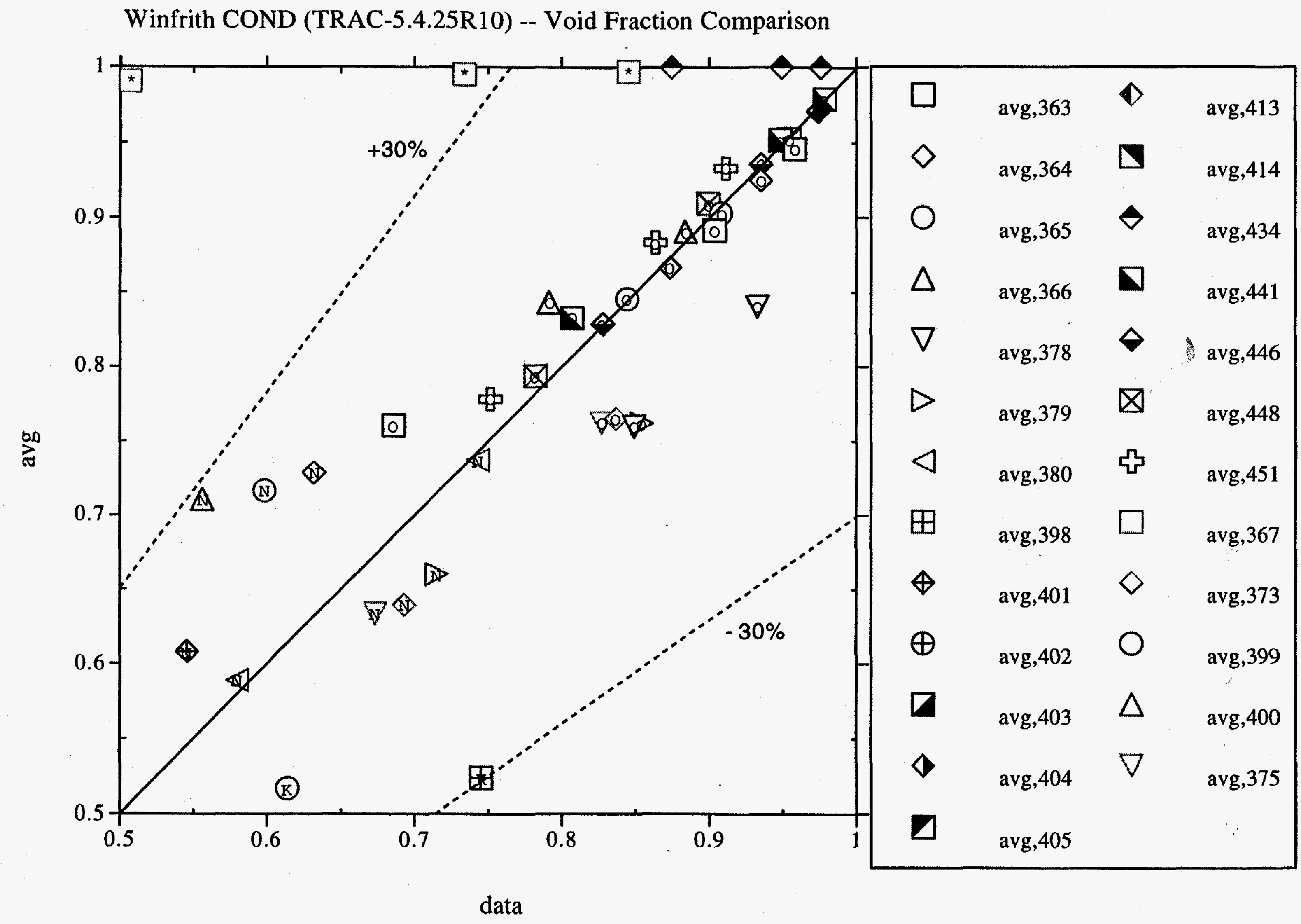

Fig. 24b. Time-averaged vapor void fraction calculated using the Conditional Pedigree coefficients vs Winfrith steady-state and quasi-steady-state post-CHF-up-flow data (modified range on axes).

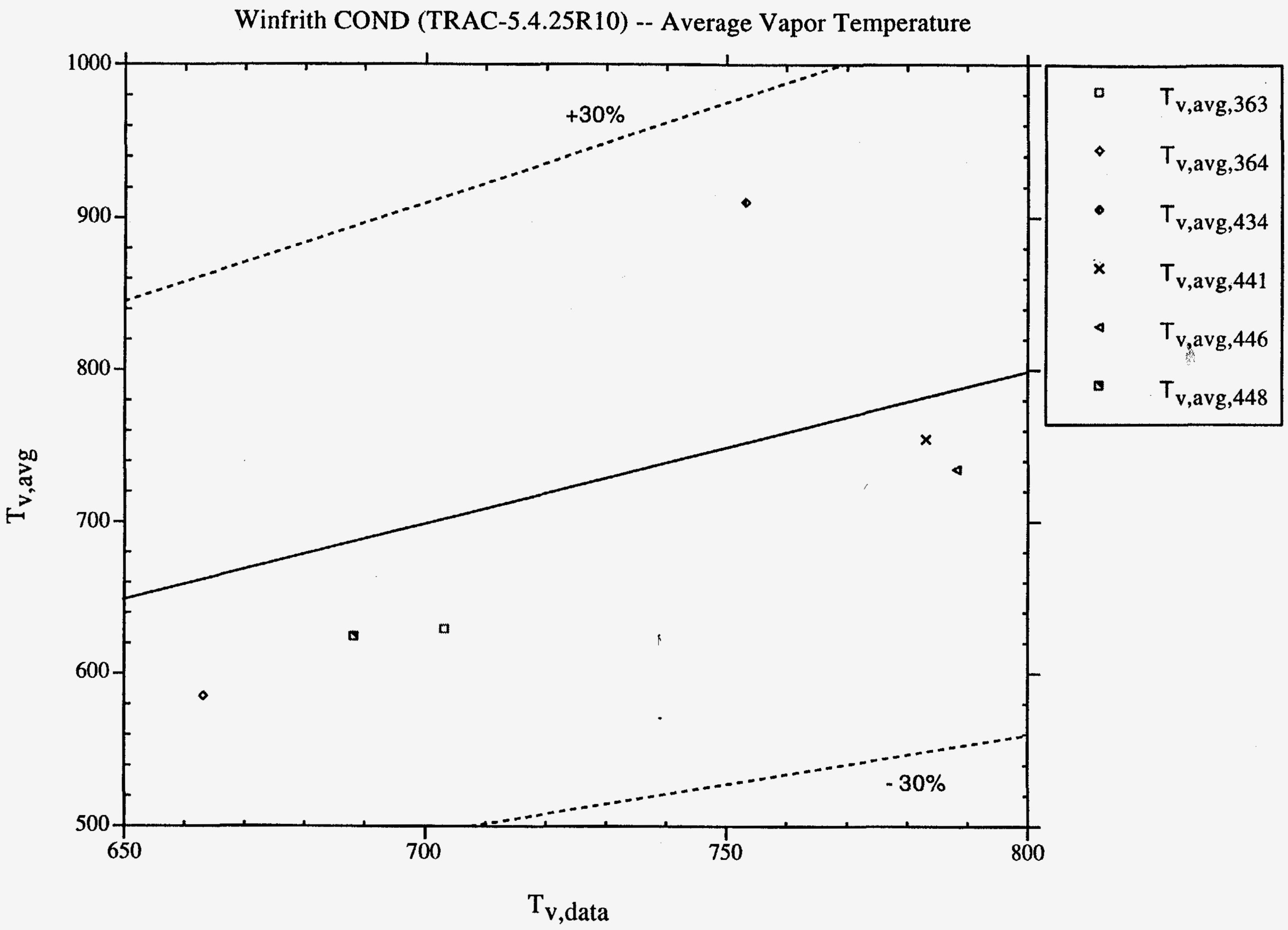

Fig. 25. Time-averaged vapor temperature calculated using the Conditional Pedigree coefficients vs Winfrith steady-state and quasi-steady-state post-CHF-up-flow data.

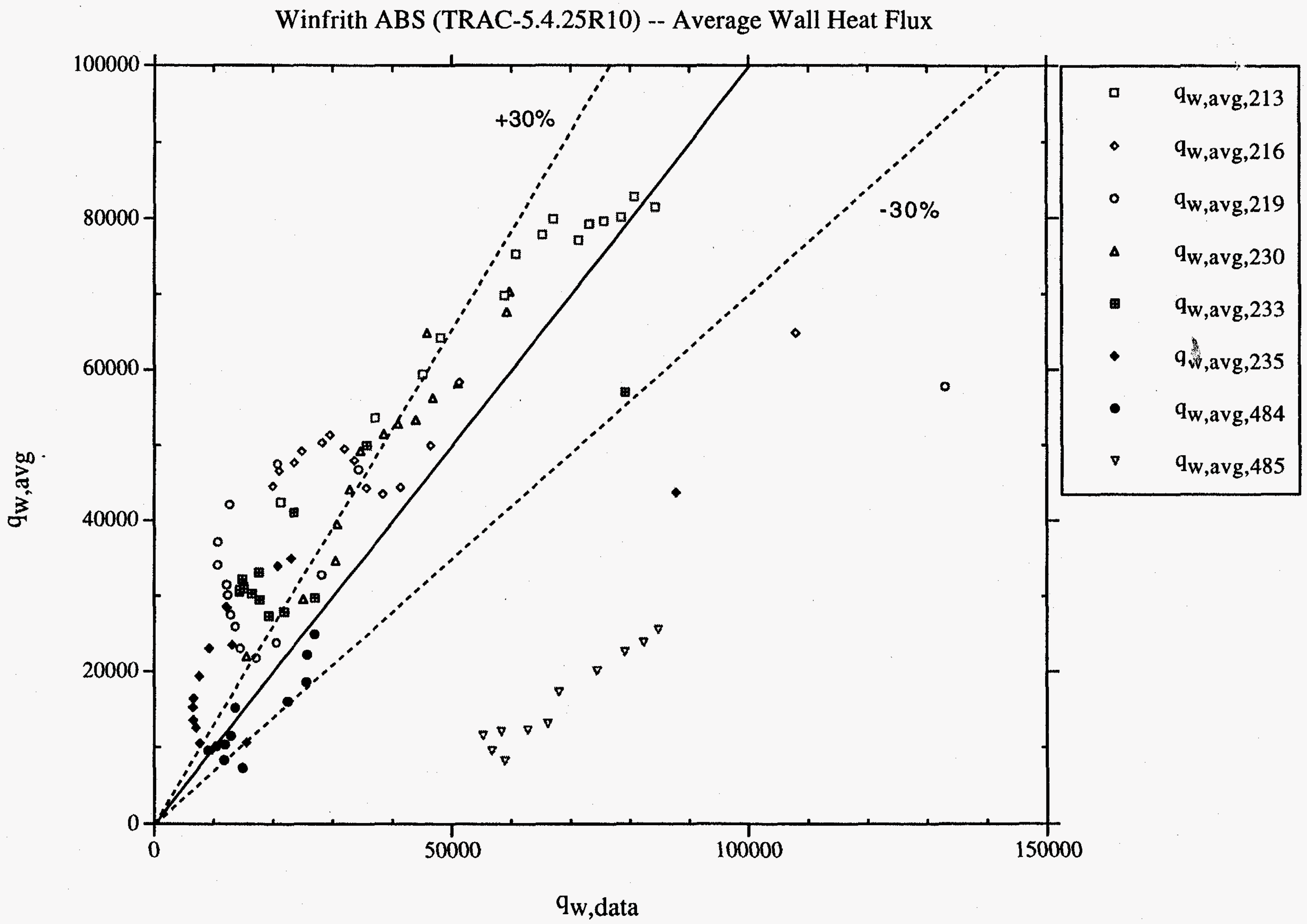

Fig. 26. Time-averaged wall heat flux calculated using the Absolute Pedigree coefficients vs Winfrith steady-state and quasi-steady-state post-CHF-down-flow data.

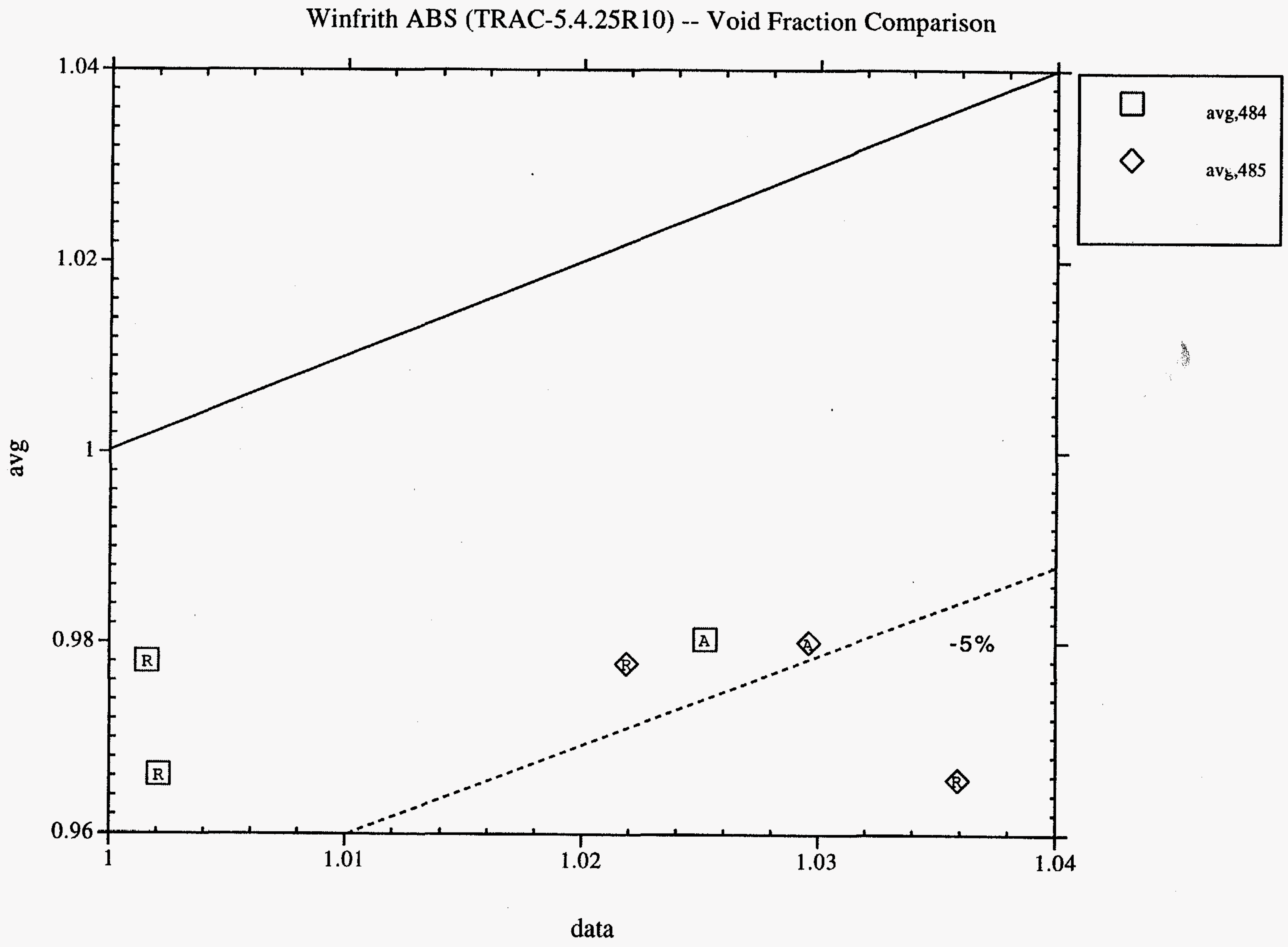

Fig. 27. Time-averaged vapor void fraction calculated using the Absolute Pedigree coefficients vs Winfrith steady-state and quasi-steady-state post-CHF down-flow data.

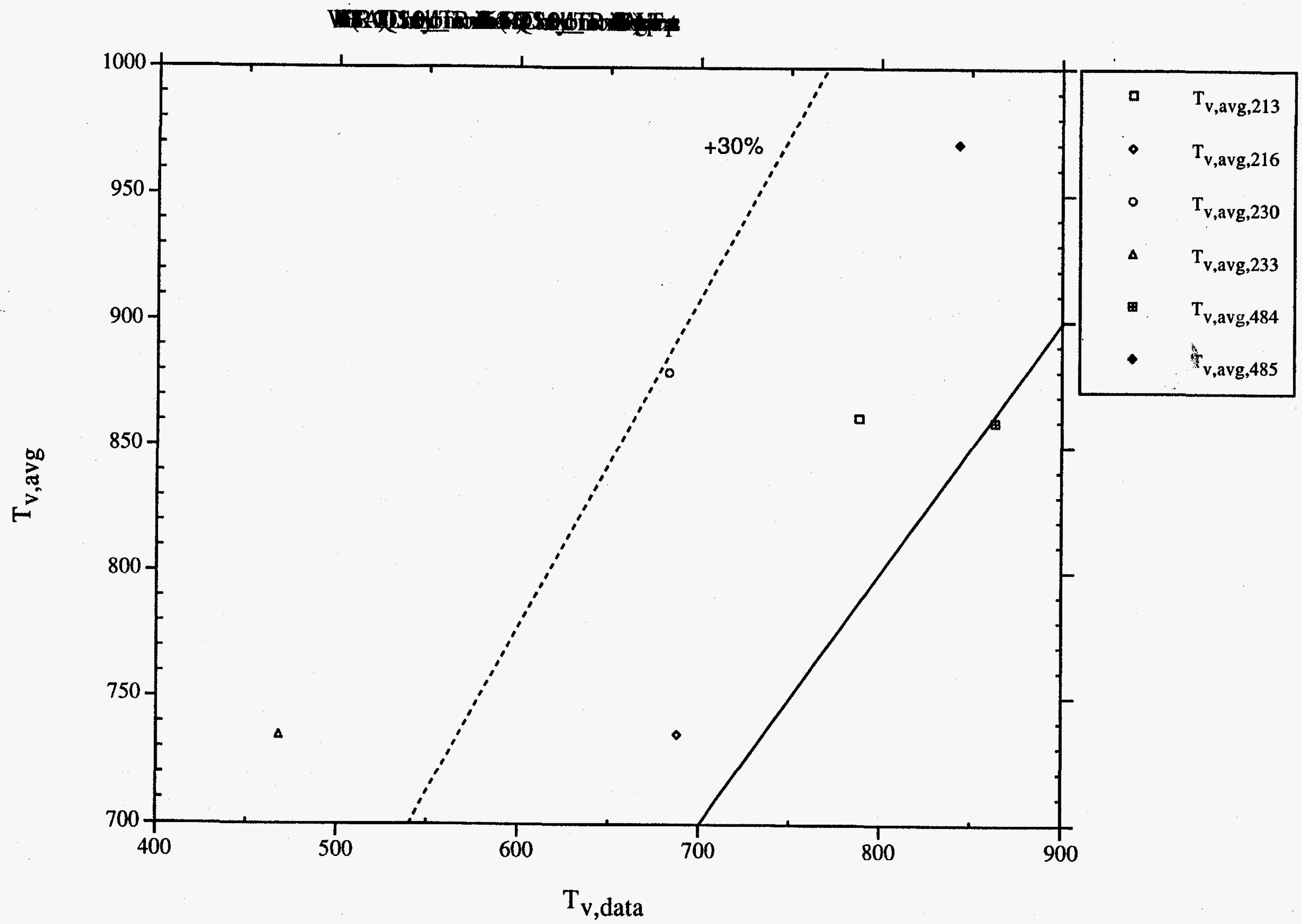

Fig. 28. Time-averaged vapor temperature calculated using the Absolute Pedigree coefficients vs Winfrith steady-state and quasi-steady-state post-CHF down-flow data.

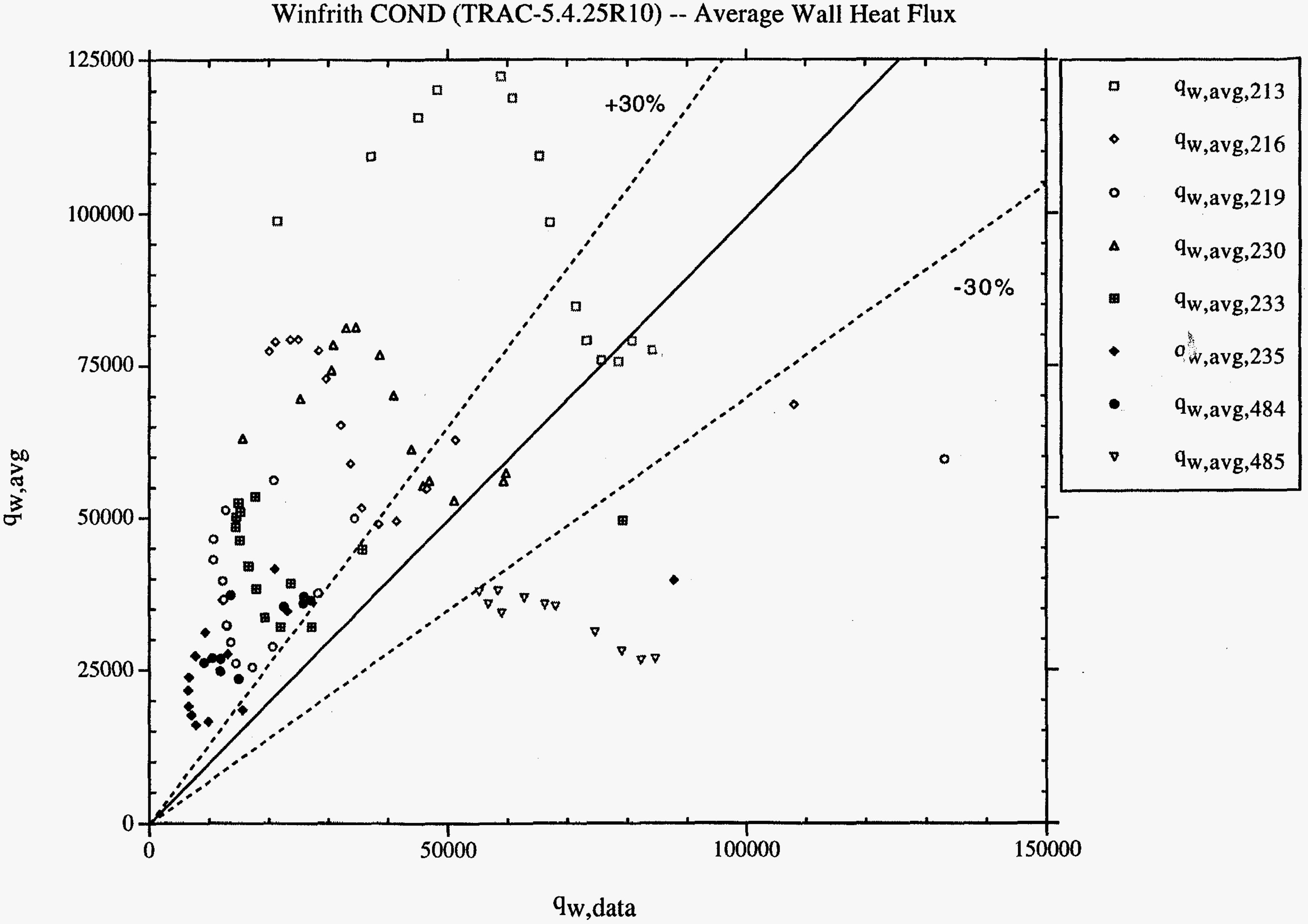

Fig. 29. Time-averaged wall heat flux calculated using the Conditional Pedigree coefficients vs Winfrith steady-state and quasi-steady-state post-CHF down-flow data.

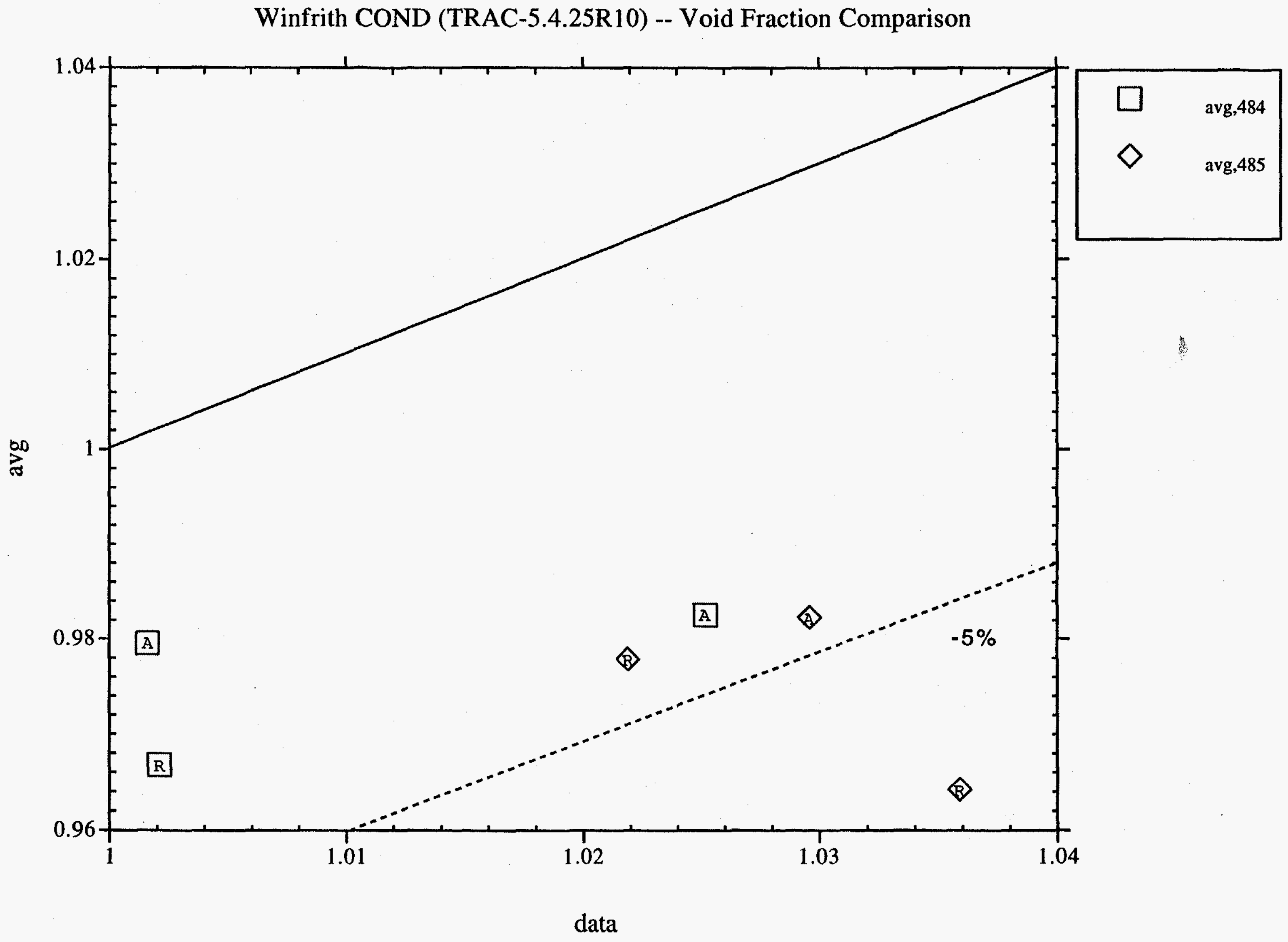

Fig. 30. Time-averaged vapor void fraction calculated using the Conditional Pedigree coefficients vs Winfrith steady-state and quasi-steady-state post-CHF-down-flow data.

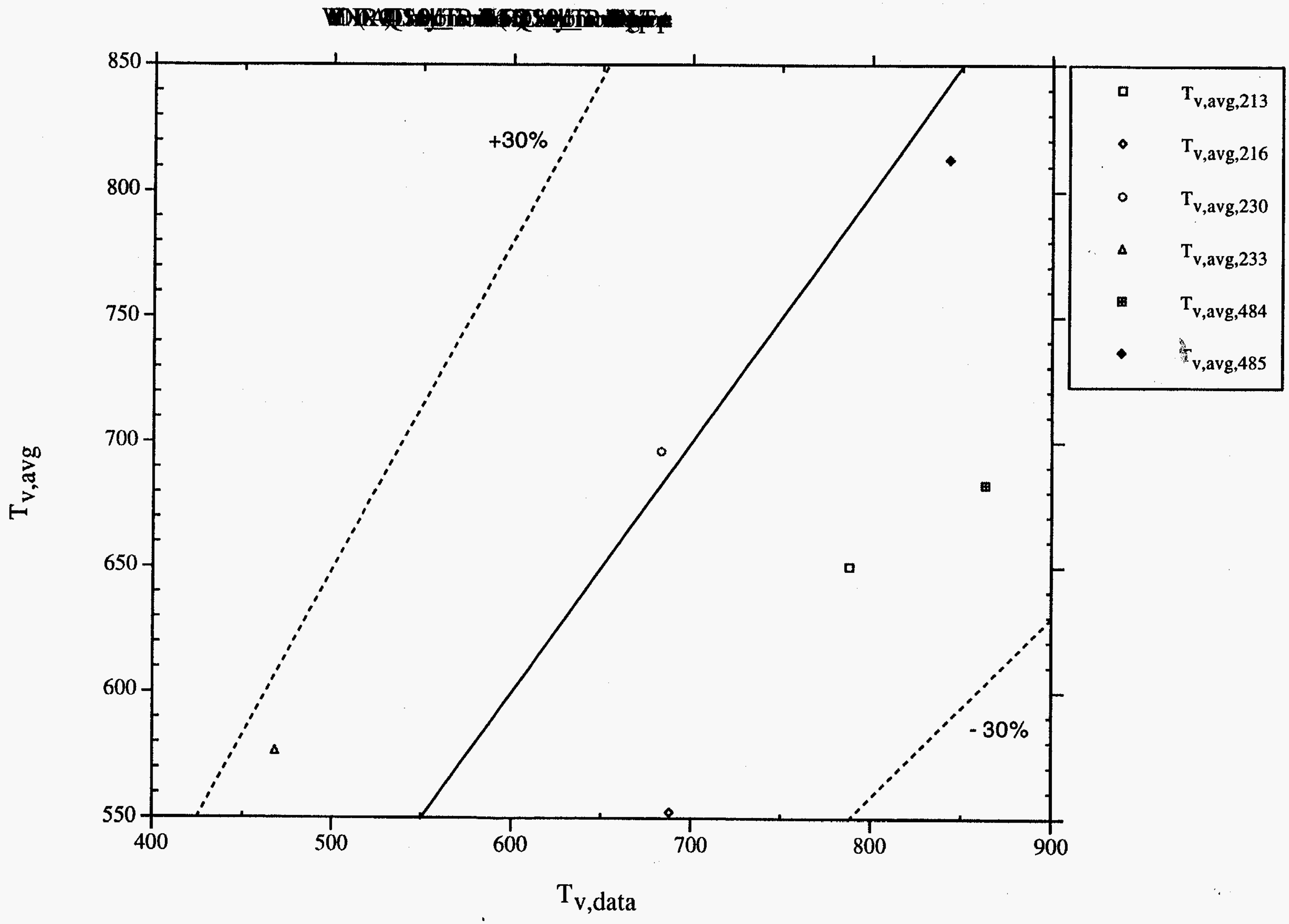

Fig. 31. Time-averaged vapor temperature calculated using the Conditional Pedigree coefficients vs Winfrith steady-state and quasi-steady-state post-CHF-down-flow data.

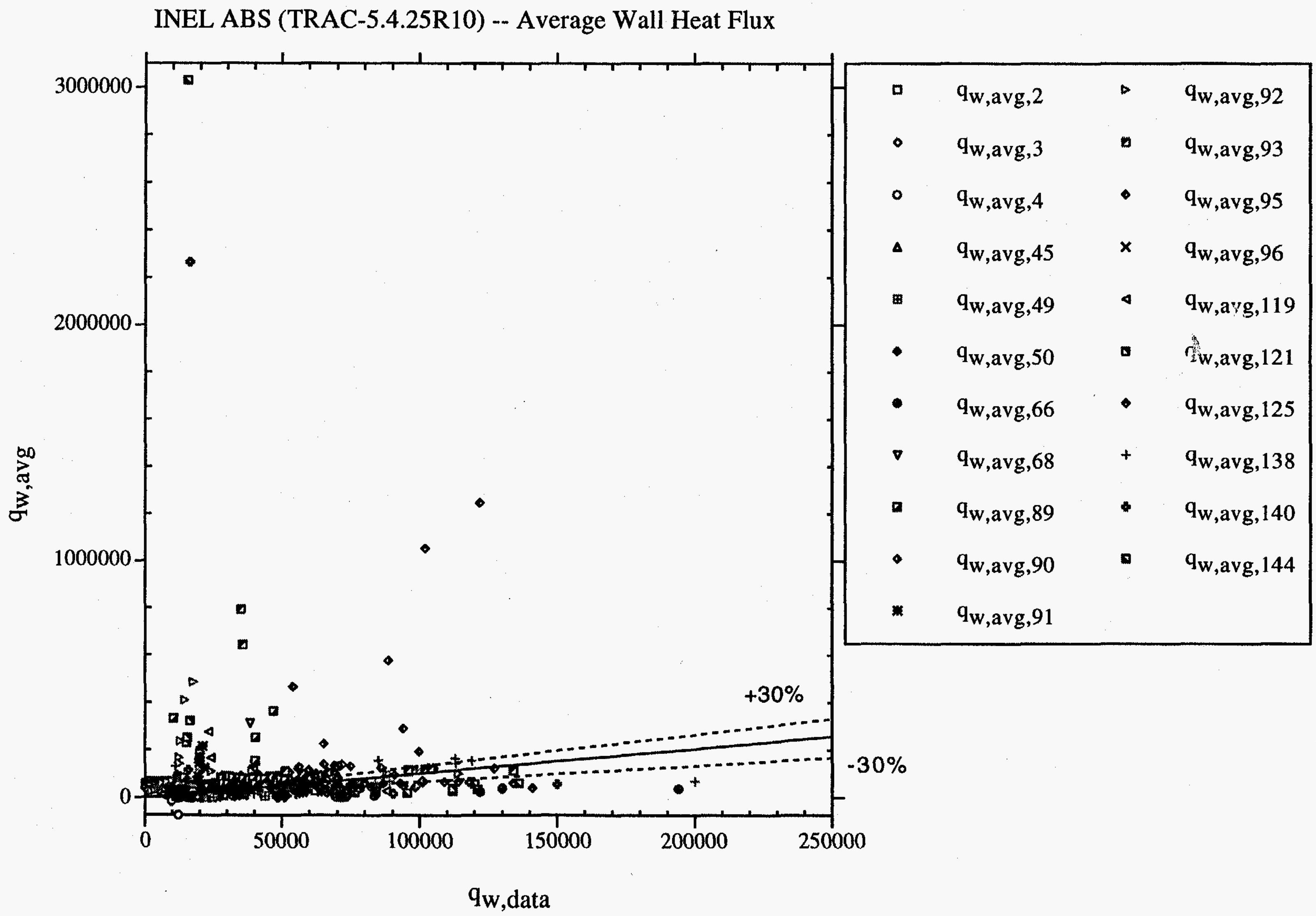

Fig. 32. Time-averaged wall heat flux calculated using the Absolute Pedigree coefficients vus INEL steady-state and quasi-steady-state post-CHF-up-flow data.

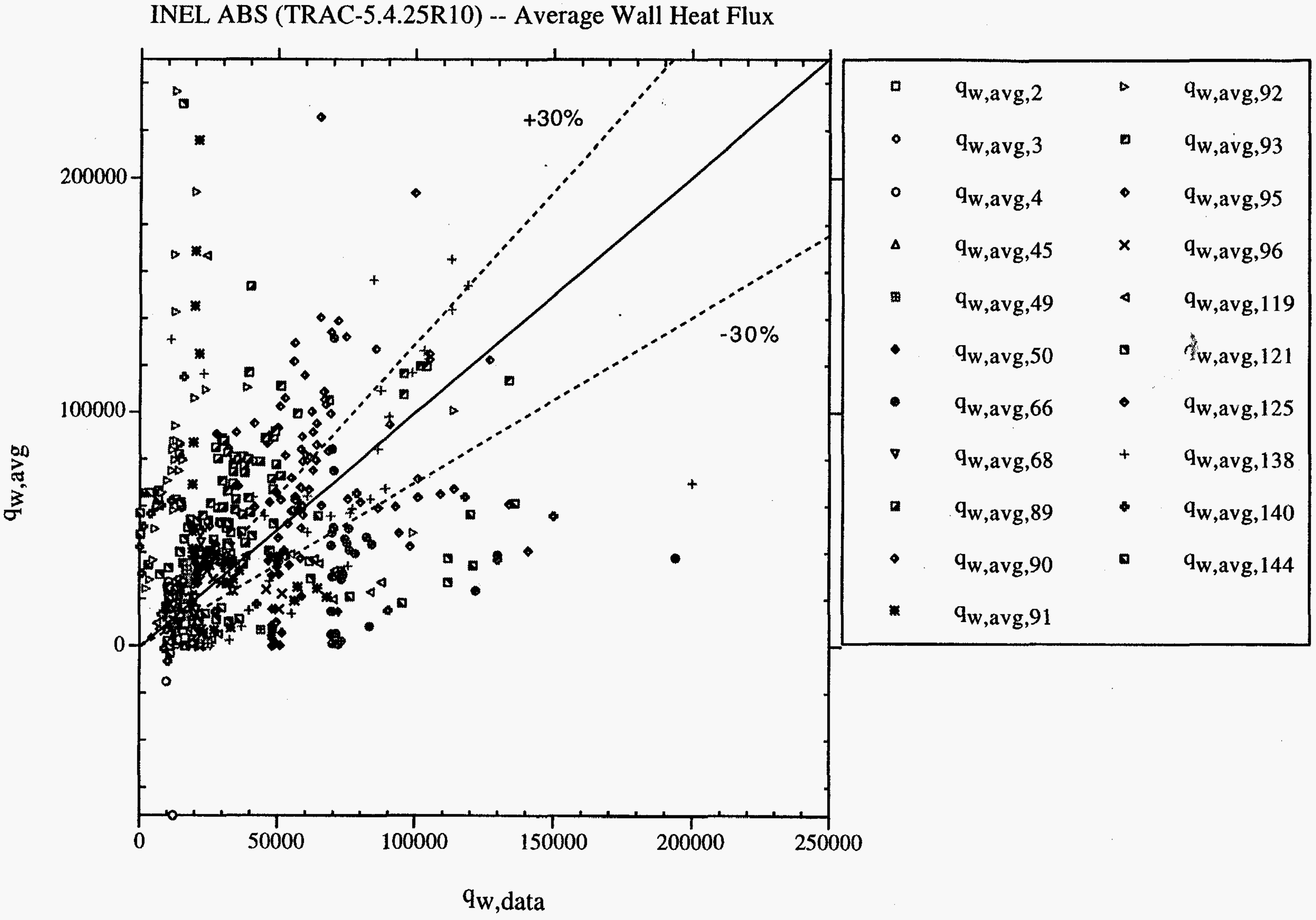

Fig. 33. Time-averaged wall heat flux calculated using the Absolute Pedigree coefficients vs INEL steady-state and quasi-steady-state post-CHF-up-flow data—same as Fig. 32 with adjusted ordinate scale.

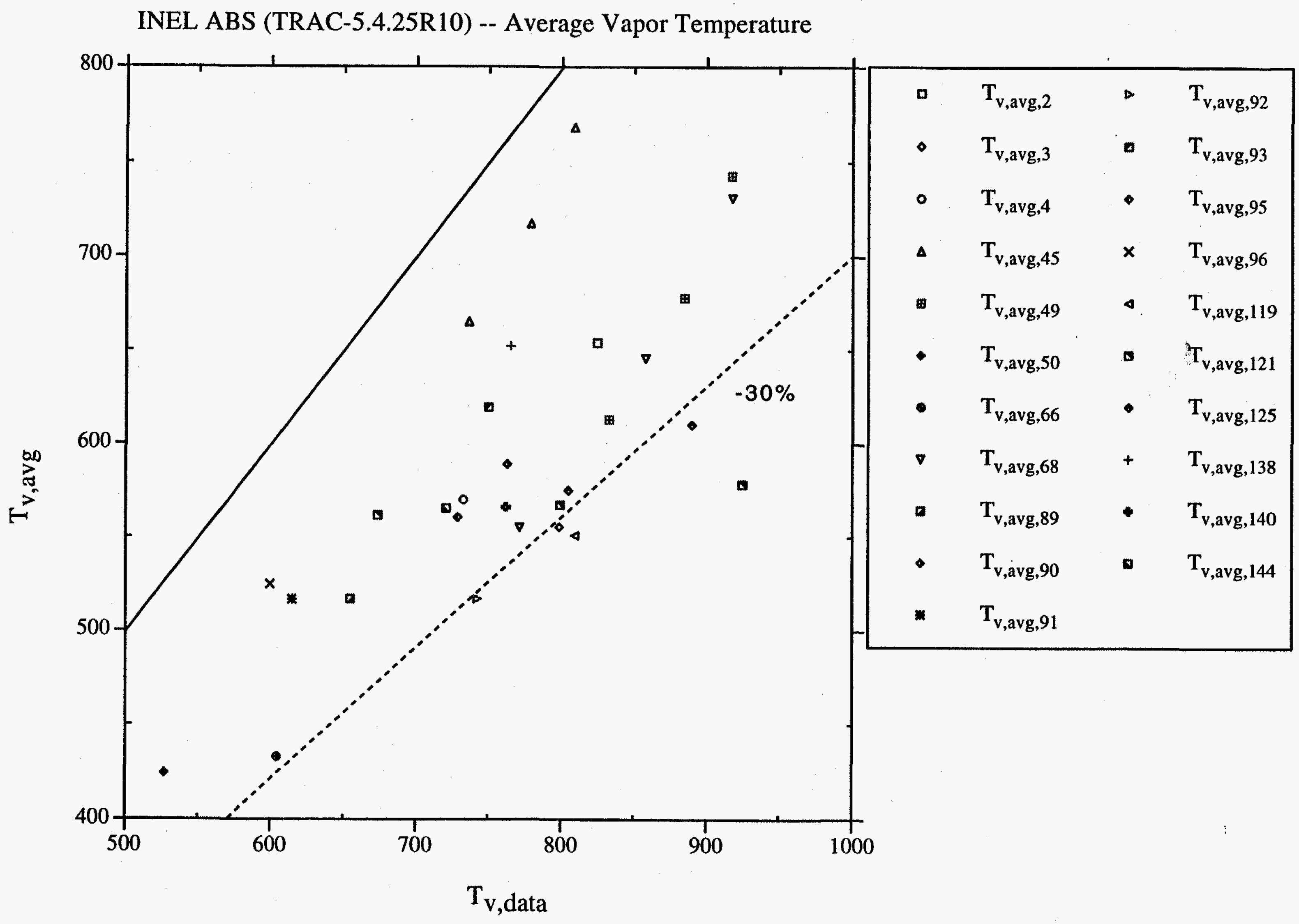

Fig. 34. Time-averaged vapor temperature calculated using the Absolute Pedigree coefficients vs INEL steady-state and quasi-steady-state post-CHF-up-flow data.

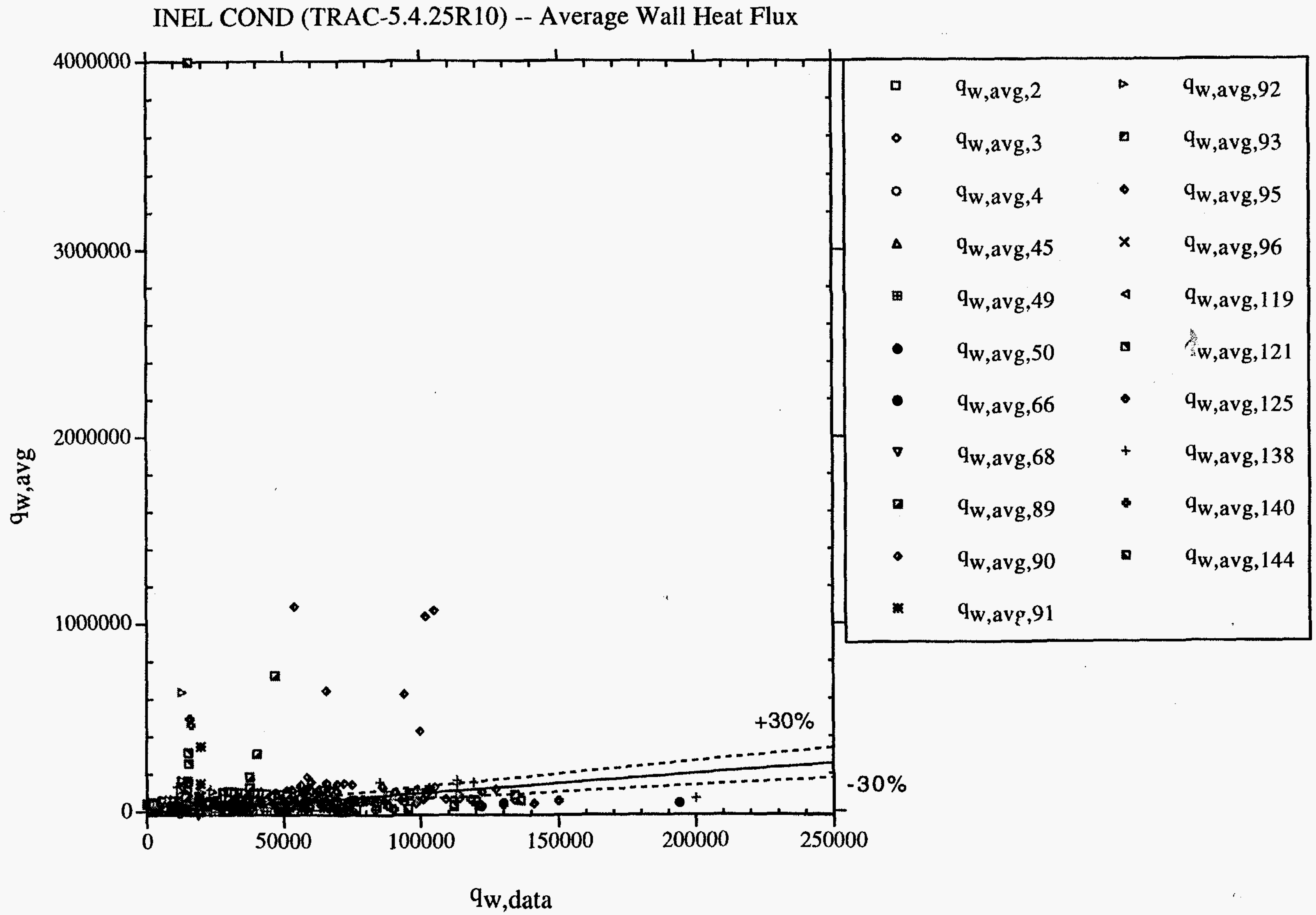

Fig. 35. Time-averaged wall heat flux calculated using the Conditional Pedigree coefficients vs INEL steady-state and quasi-steady-state post-CHF-up-flow data.

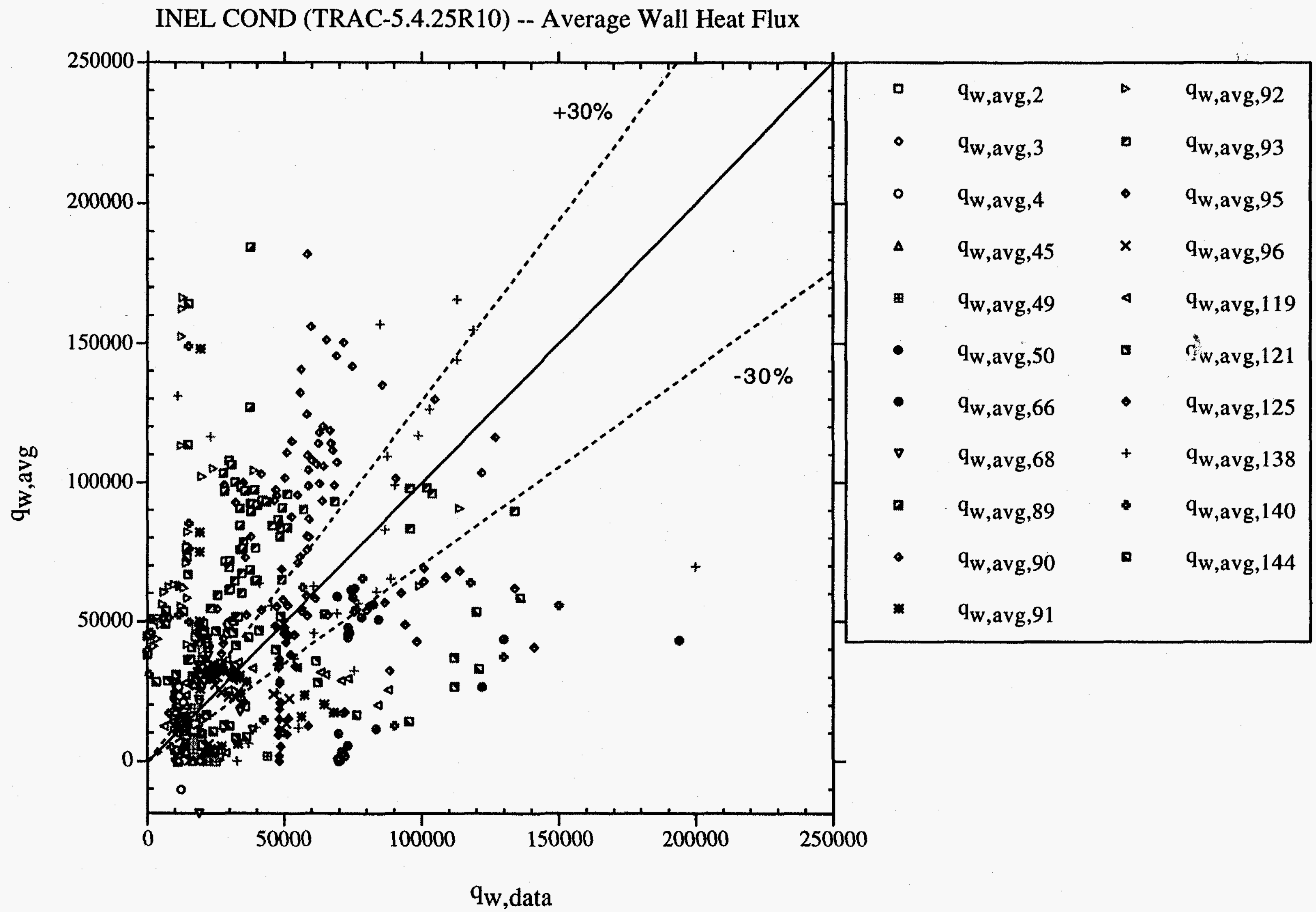

Fig. 36. Time-averaged wall heat flux calculated using the Conditional Pedigree coefficients vs INEL steady-state and quasi-steady-state post-CHF-up-flow data—same as Fig. 35 with adjusted ordinate scale.

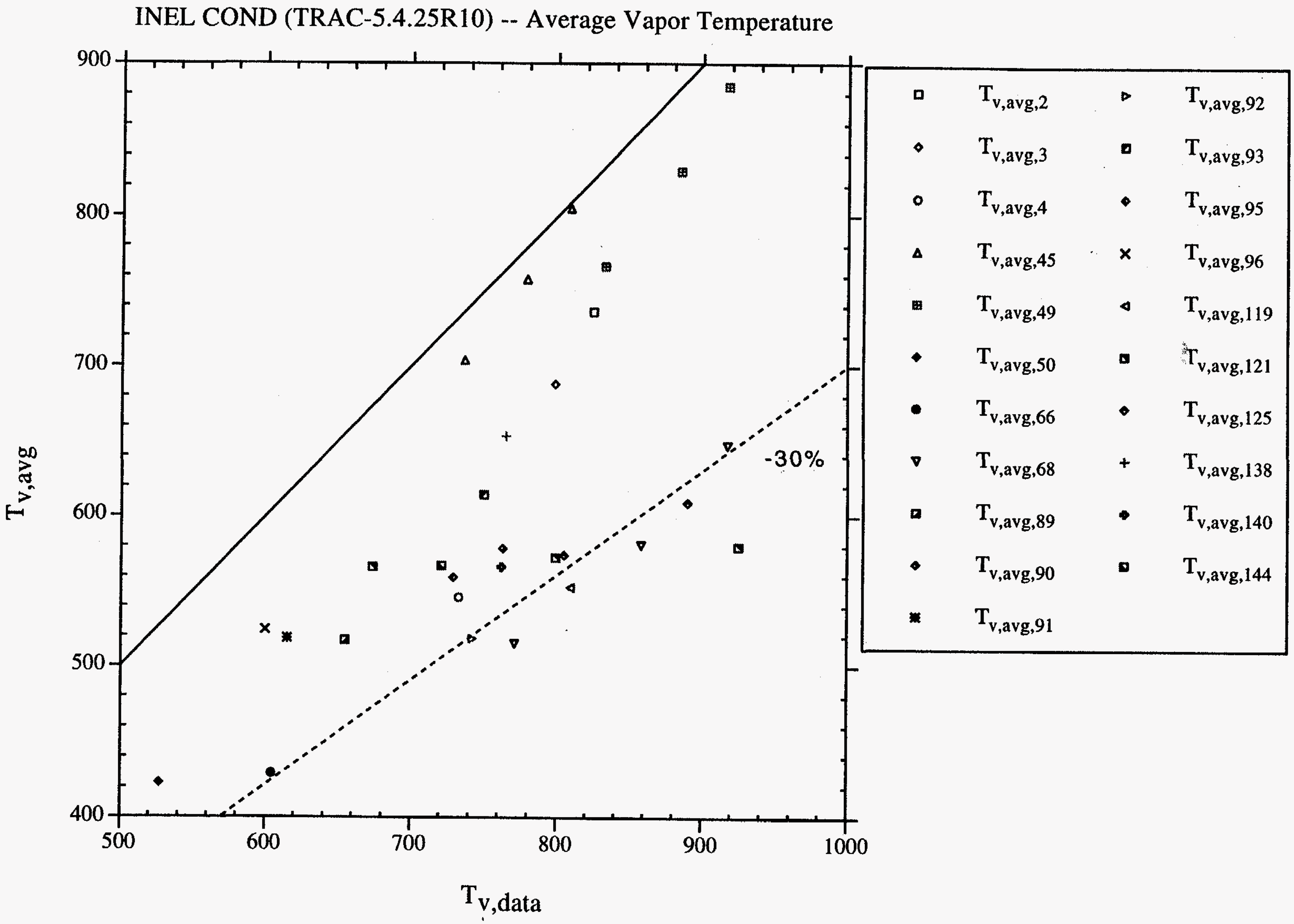

Fig. 37. Time-averaged vapor temperature calculated using the Conditional Pedigree coefficients vs INEL steady-state and quasi-steady-state post-CHF-up-flow data.

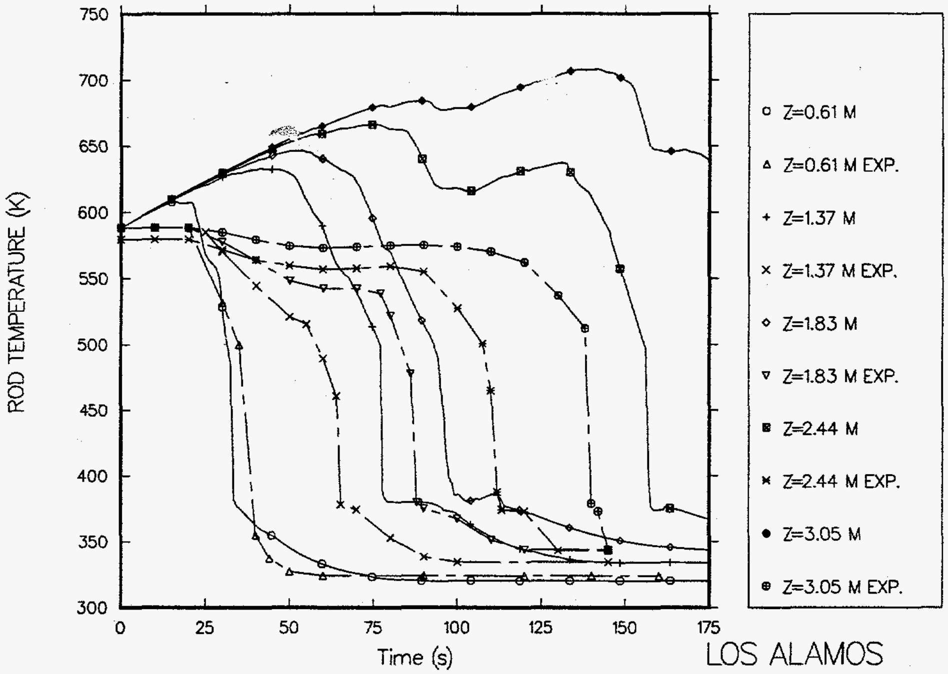

Fig. 38. Predicted and measured wall temperature histories for Berkeley Run-166 using the Absolute Pedigree coefficients.

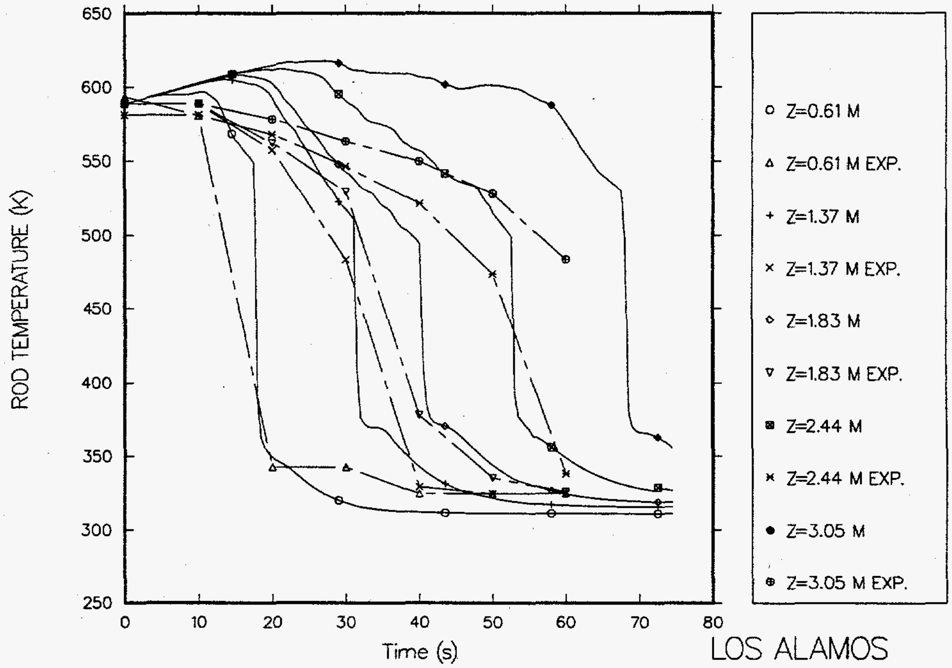

Fig. 39. Predicted and measured wall temperature histories for Berkeley Run-167 using the Absolute Pedigree coefficients.

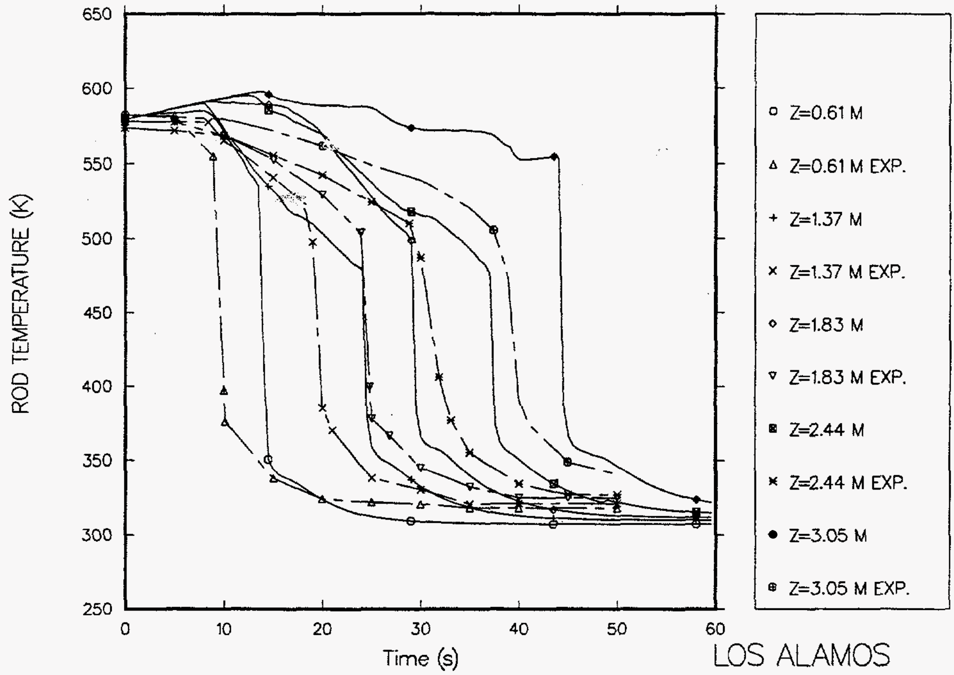

Fig. 40. Predicted and measured wall temperature histories for Berkeley Run-186 using the Absolute Pedigree coefficients.

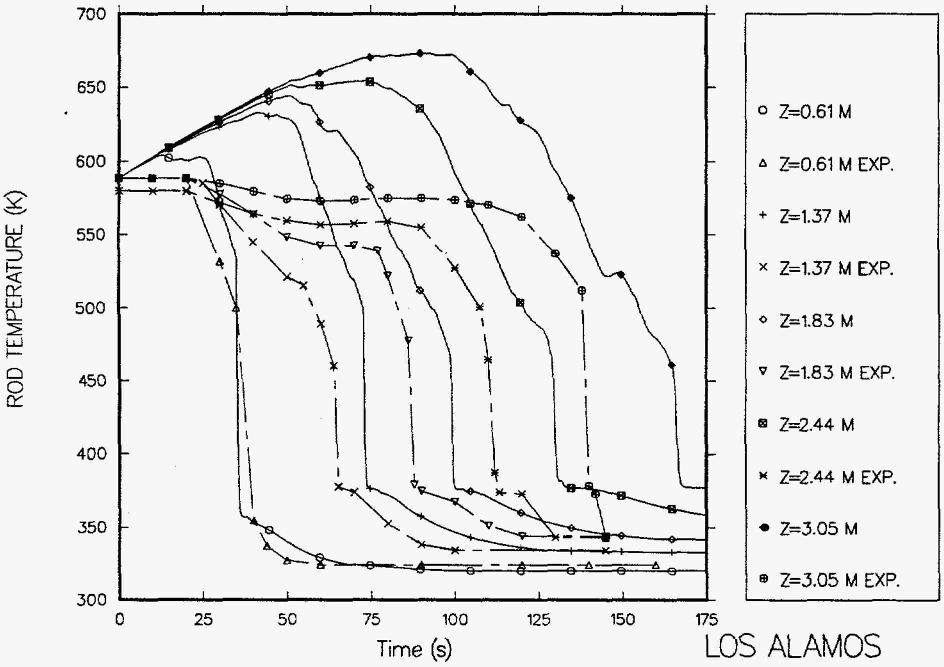

Fig. 41. Predicted and measured wall temperature histories for Berkeley Run-166 using the Conditional Pedigree coefficients.

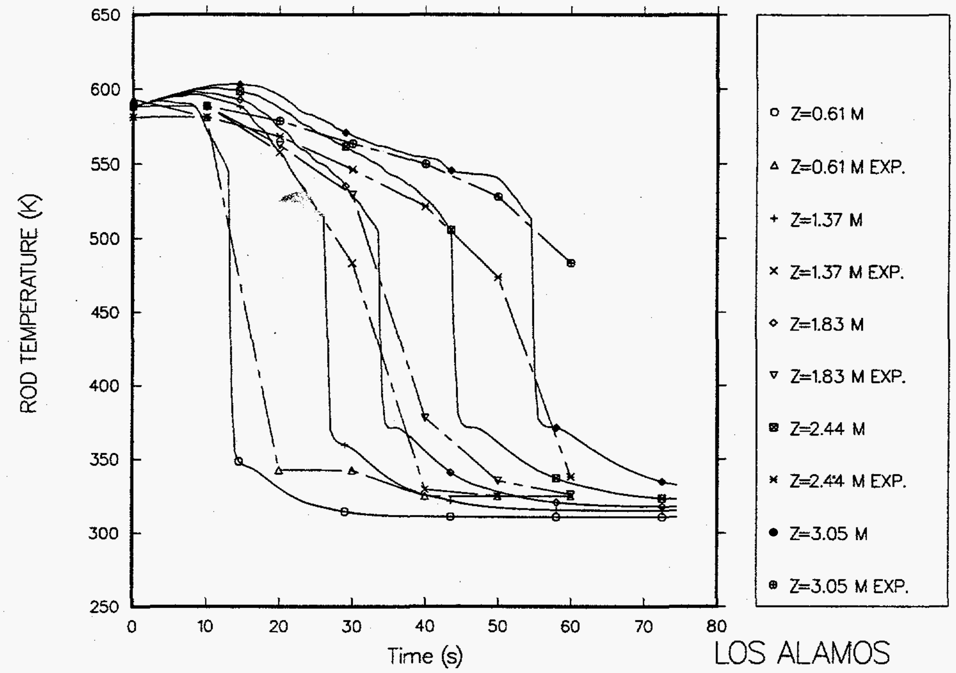

Fig. 42. Predicted and measured wall temperature histories for Berkeley Run-167 using the Conditional Pedigree coefficients.

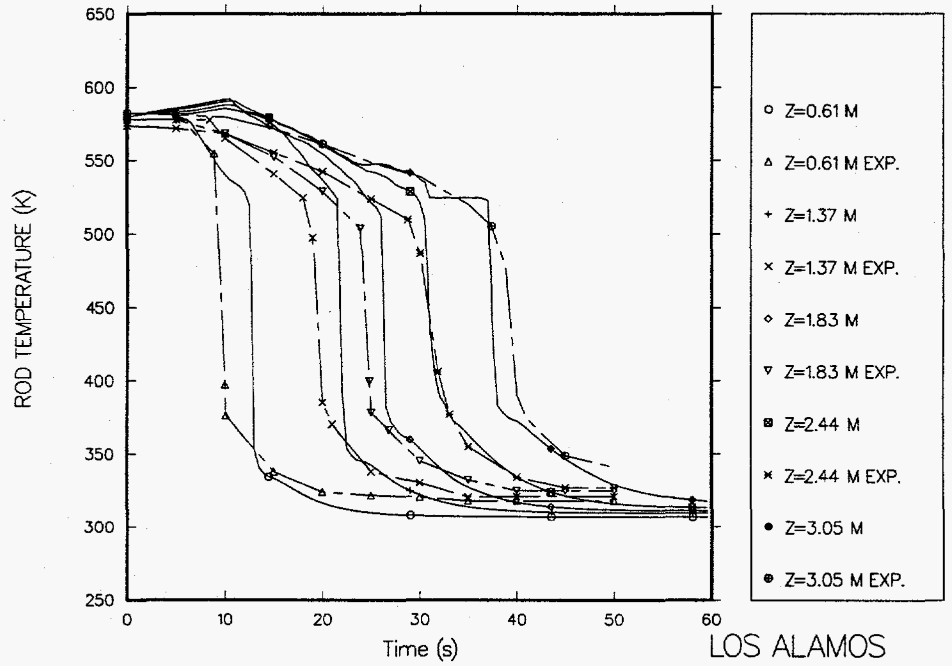

Fig. 43. Predicted and measured wall temperature histories for Berkeley Run-186 using the Conditional Pedigree coefficients.

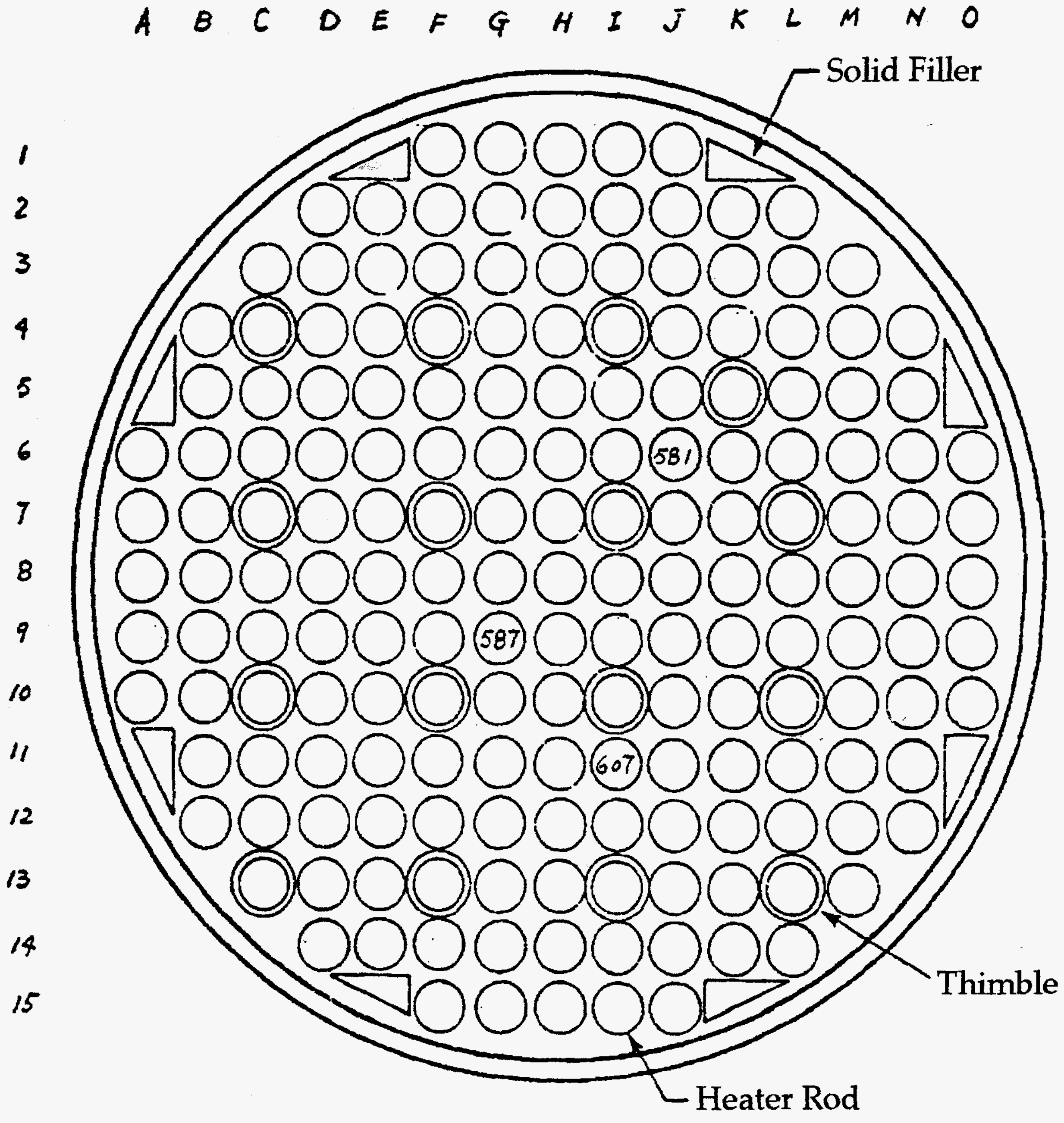

Fig. 44. Cross-section diagram of the FLECHT-SEASET heater-rod bundle.

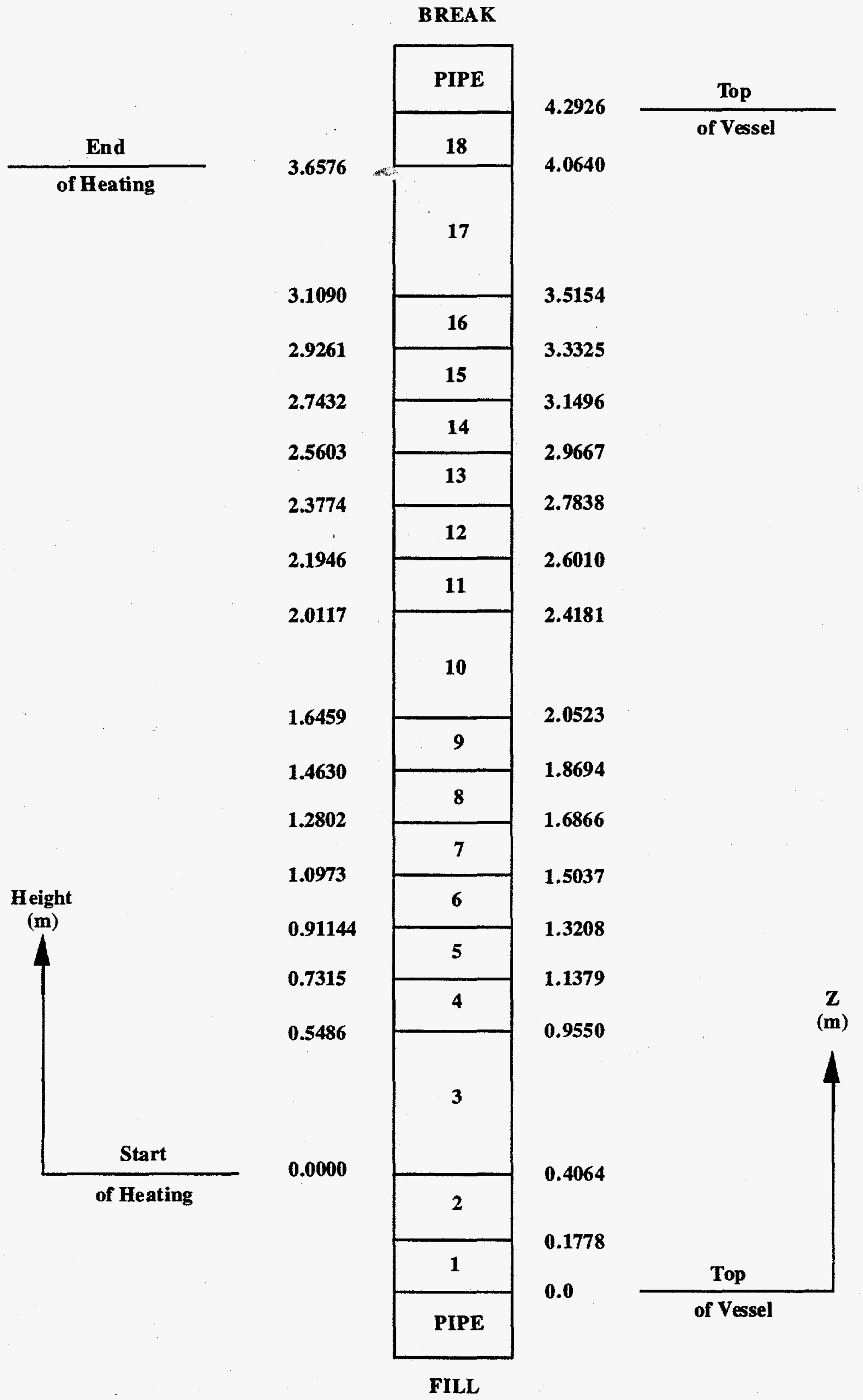

Fig. 45. TRAC model of the FLECHT-SEASET facility.

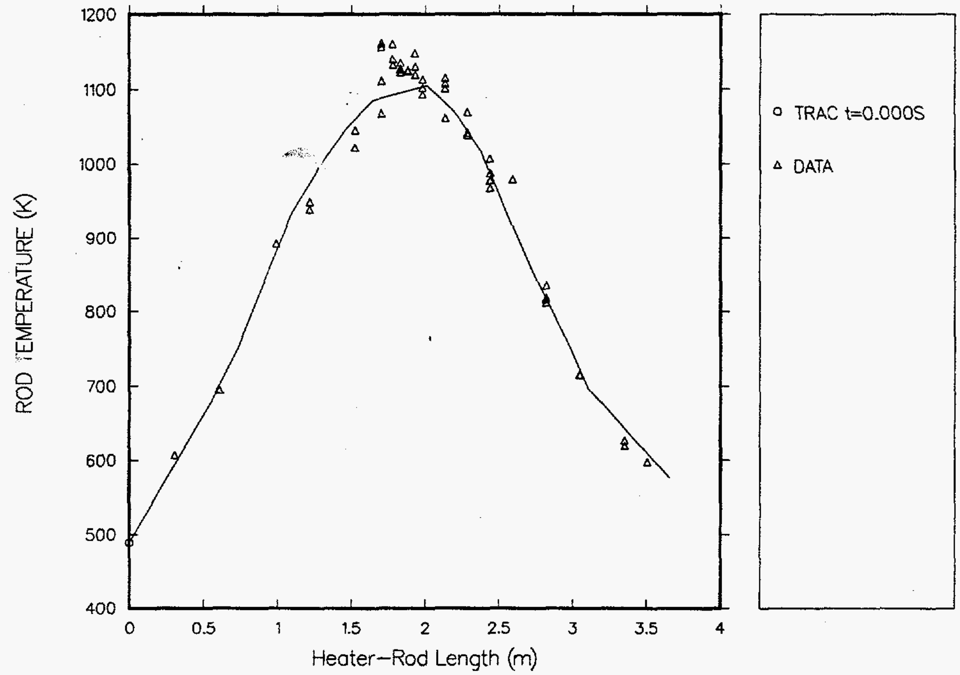

Figure 45a. Intial axially-dependent cladding temperature calculated using the Absolute Pedigree coefficients versus the FLECHT-SEASET Run 31504 experimental data.

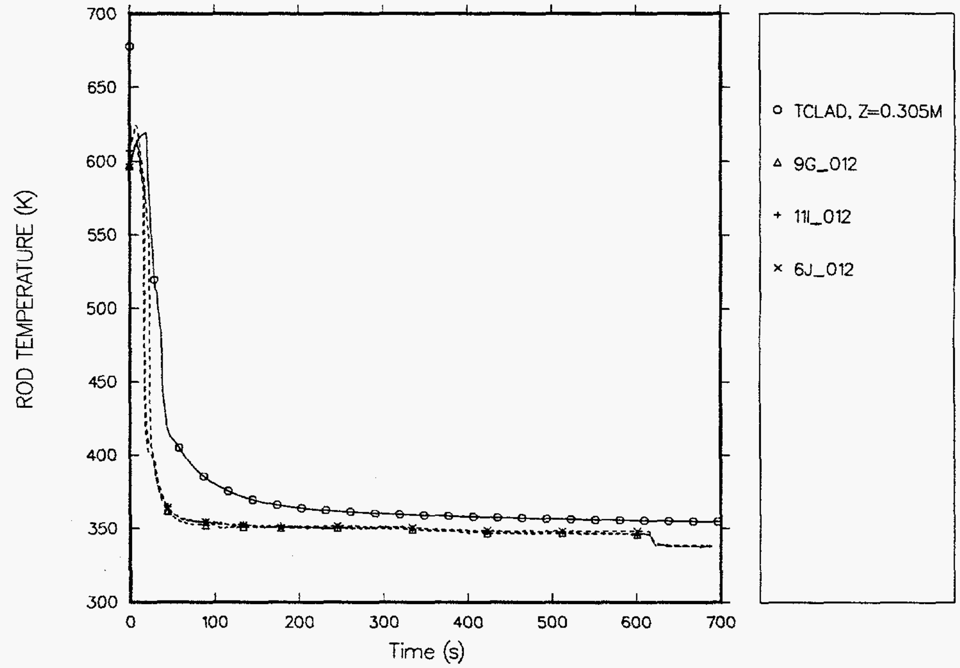

Figure 46. Time-dependent cladding temperature at 0.305 m (12 in.) calculated using the Absolute Pedigree coefficients the FLECHT-SEASET Run 31504 experimental data.

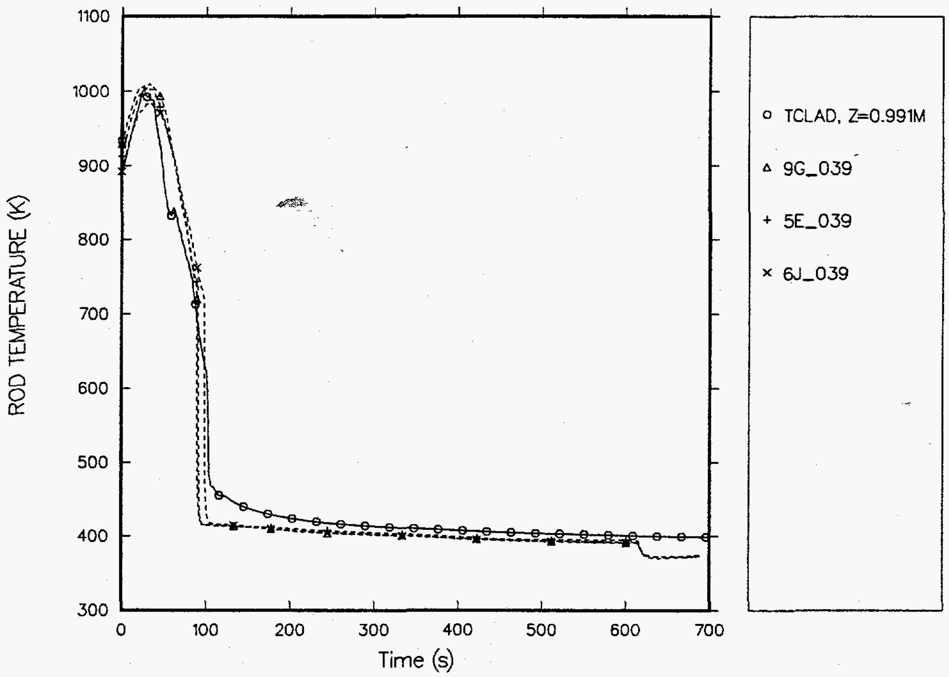

Figure 47. Time-dependent cladding temperature at 0.991 m (39 in.) calculated using the Absolute Pedigree coefficients versus the FLECHT-SEASET Run 31504 experimental data.

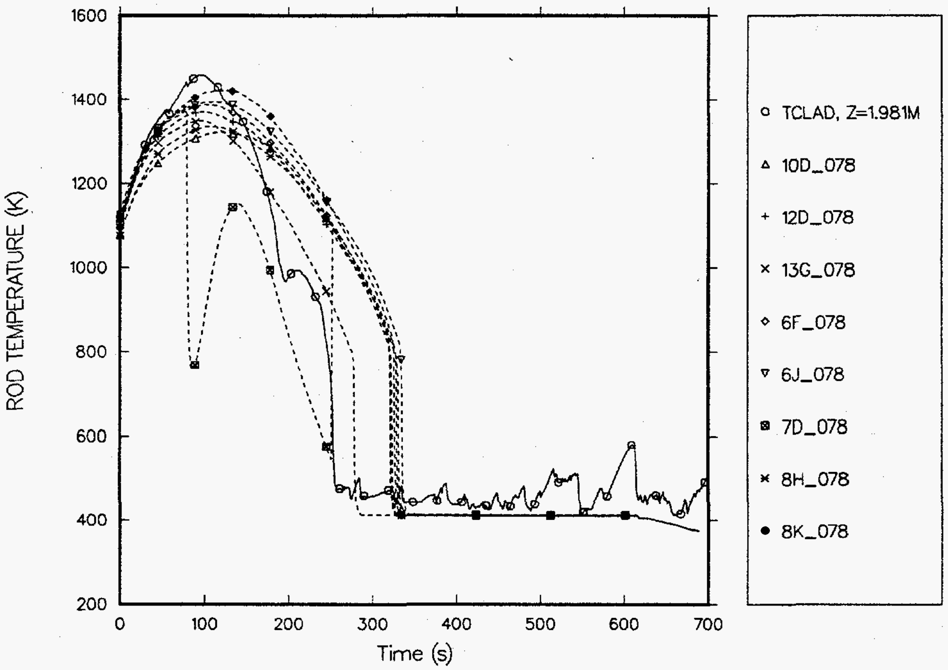

Figure 48. Time-dependent cladding temperature at 1.981 m (78 in.) calculated using the Absolute Pedigree coefficients versus the FLECHT-SEASET Run 31504 experimental data.

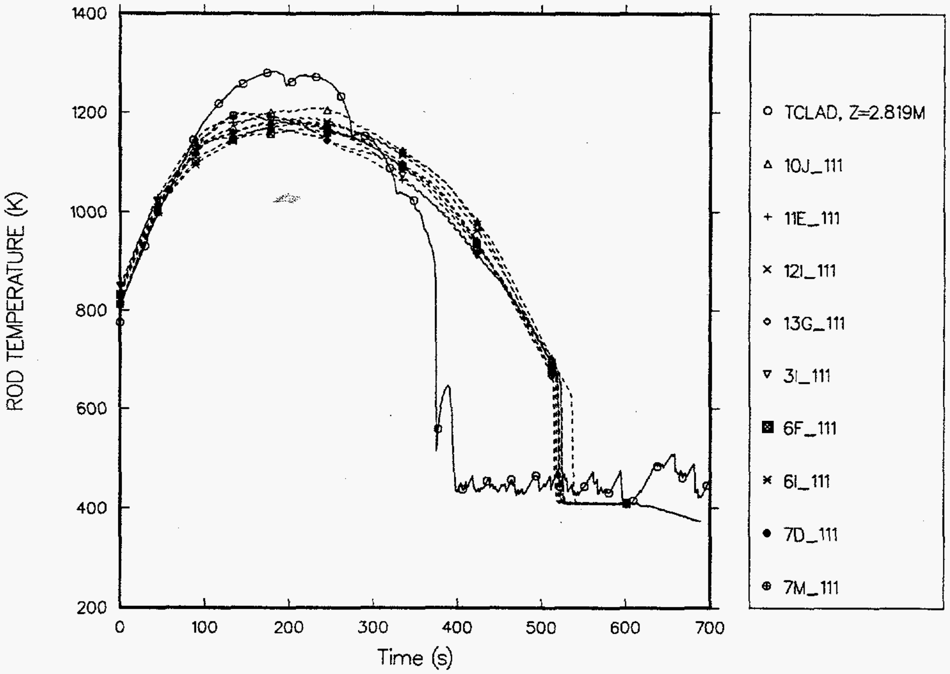

Figure 49. Time-dependent cladding temperature at 2.819 m (111 in.) calculated using the Absolute Pedigree coefficients versus the FLECHT-SEASET Run 31504 experimental data.

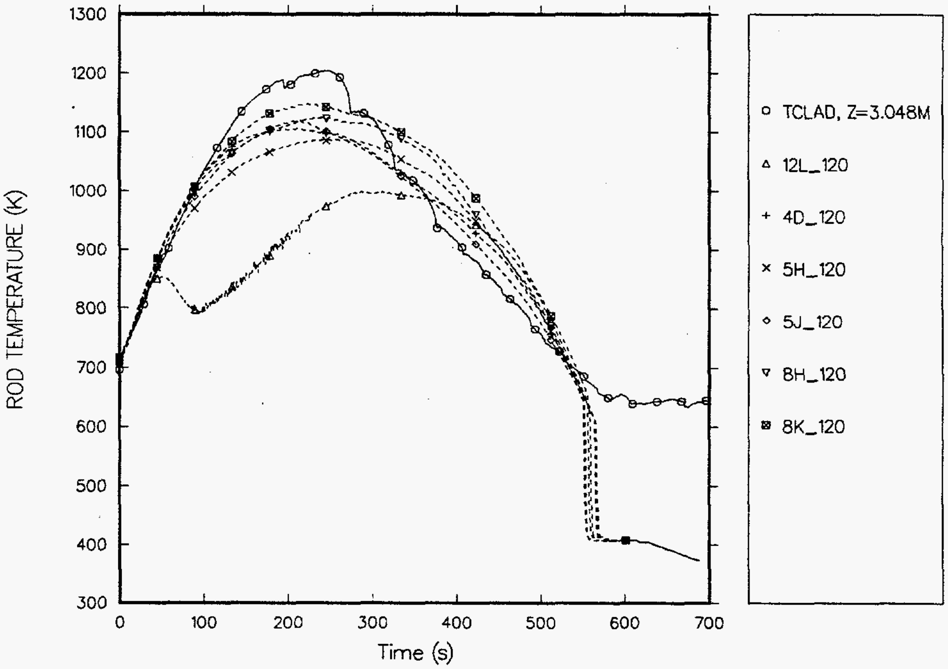

Figure 50. Time-dependent cladding temperature at 3.048 m (120 in.) calculated using the Absolute Pedigree coefficients versus the FLECHT-SEASET Run 31504 experimental data.

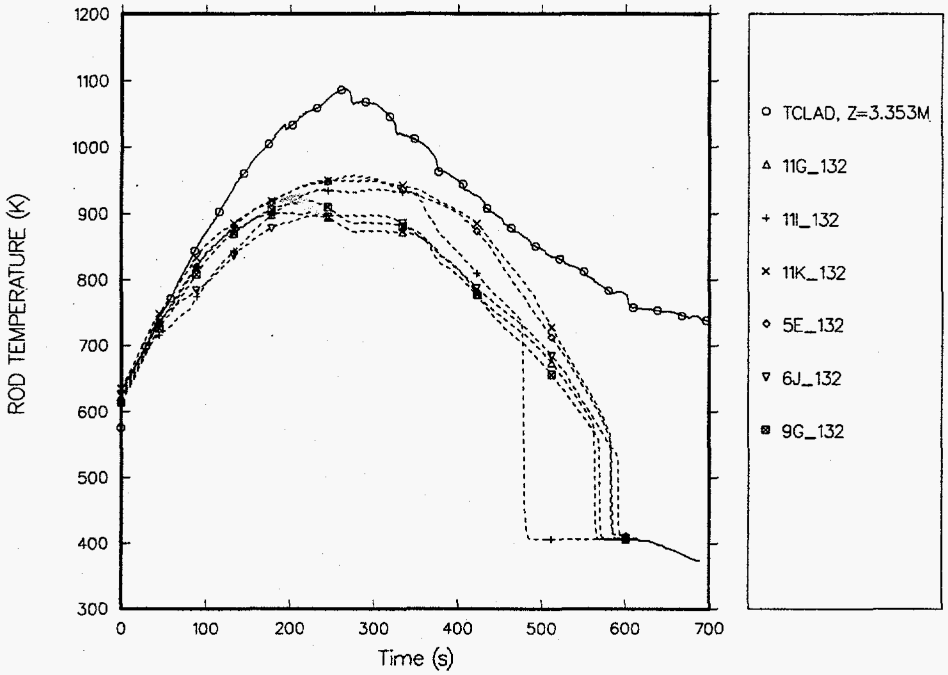

Figure 51. Time-dependent cladding temperature at 3.353 m (132 in.) calculated using the Absolute Pedigree coefficients versus the FLECHT-SEASET Run 31504 experimental data.

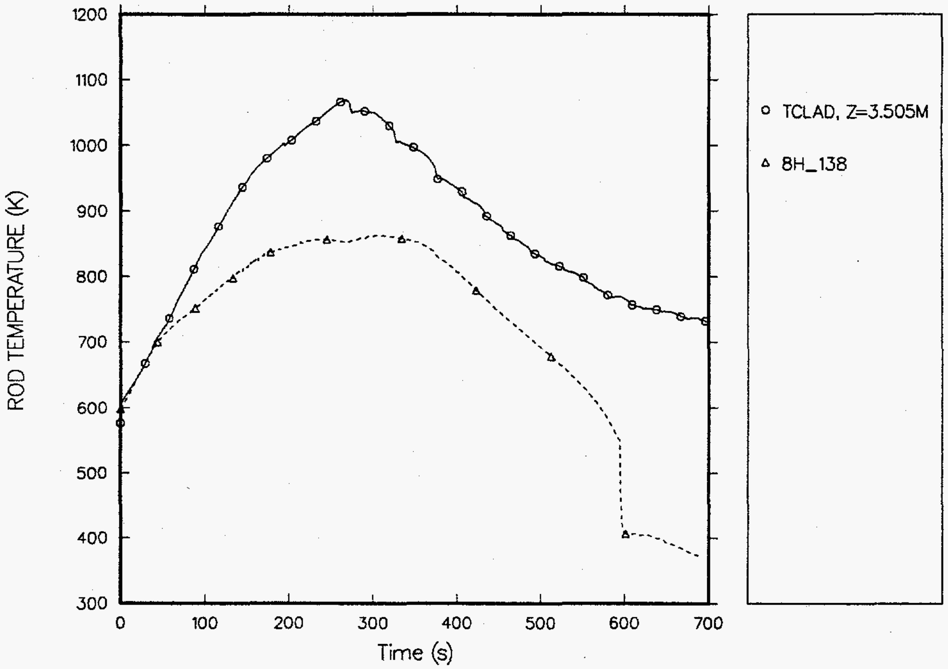

Figure 52. Time-dependent cladding temperature at 3.505 m (138 in.) calculated using the Absolute Pedigree coefficients versus the FLECHT-SEASET Run 31504 experimental data.

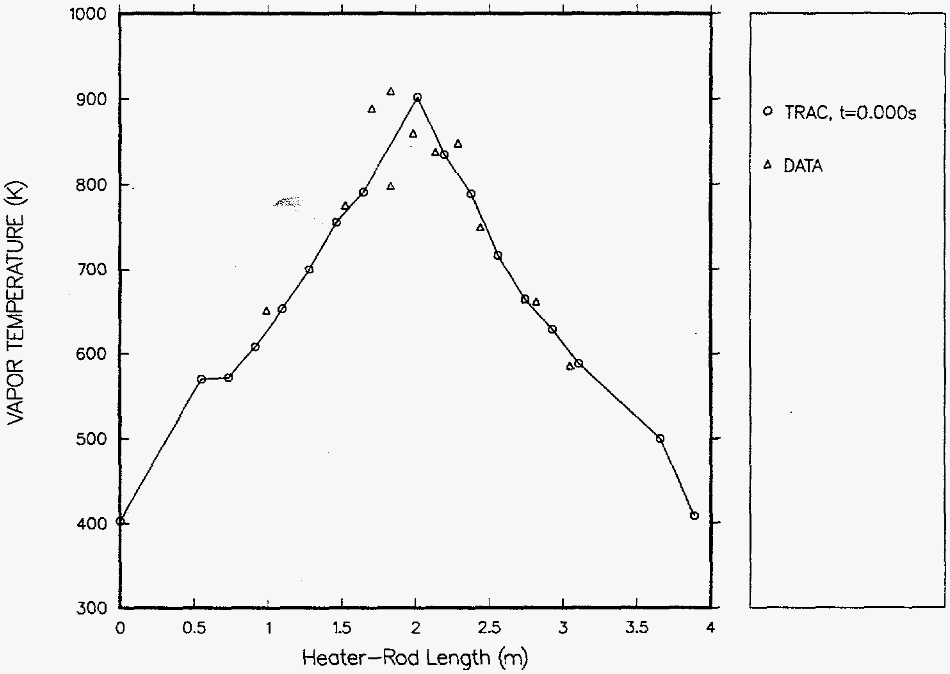

Figure 53. Intial axially-dependent vapor temperature calculated using the Absolute Pedigree coefficients versus the FLECHT-SEASET Run 31504 experimental data.

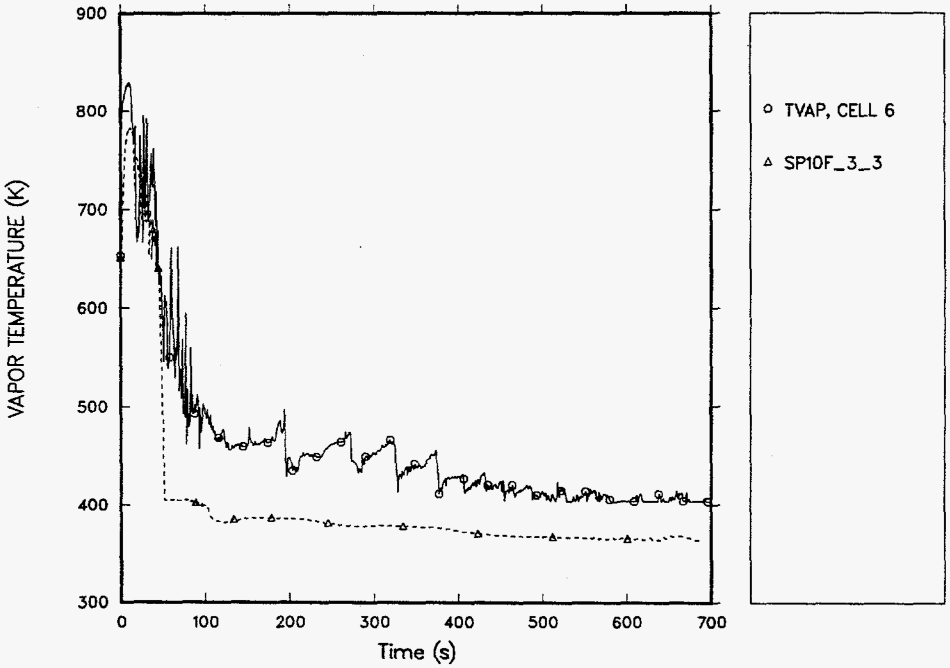

Figure 54. Time-dependent vapor temperature at 0.991 m (39 in.) calculated using the Absolute Pedigree coefficients versus the FLECHT-SEASET Run 31504 experimental data.

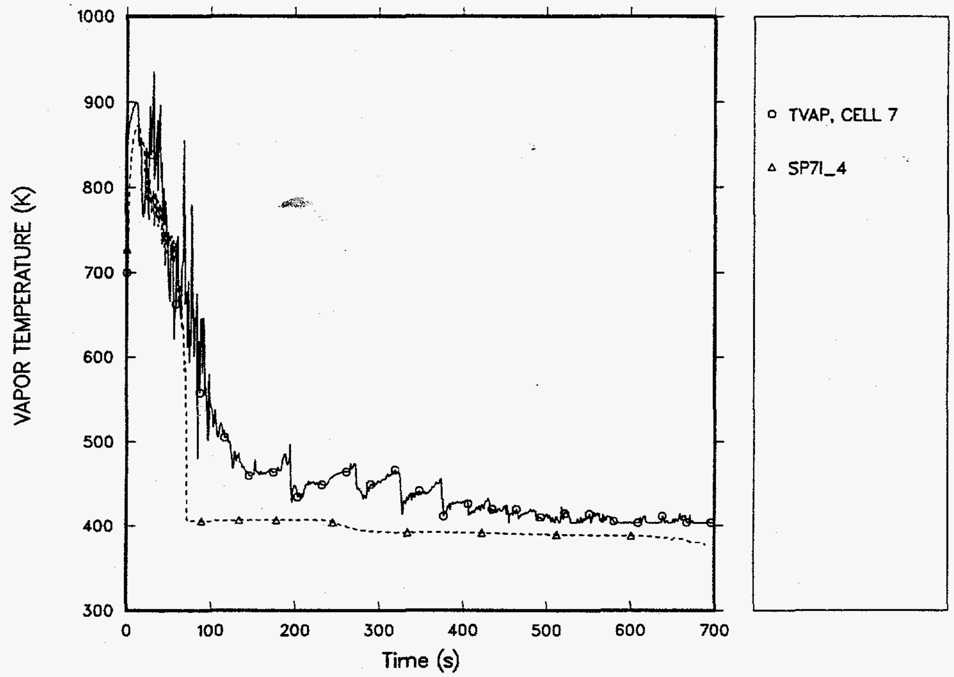

Figure 55. Time-dependent vapor temperature at 1.219 m (48 in.) calculated using the Absolute Pedigree coefficients versus the FLECHT-SEASET Run 31504 experimental data.

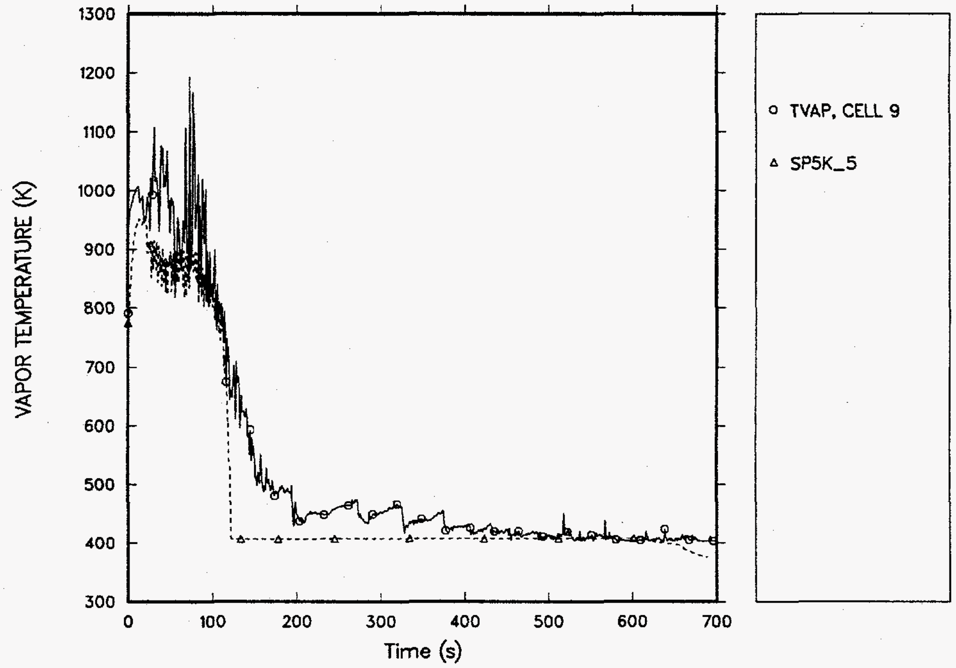

Figure 56. Time-dependent vapor temperature at 1.524 m (60 in.) calculated using the Absolute Pedigree coefficients versus the FLECHT-SEASET Run 31504 experimental data.

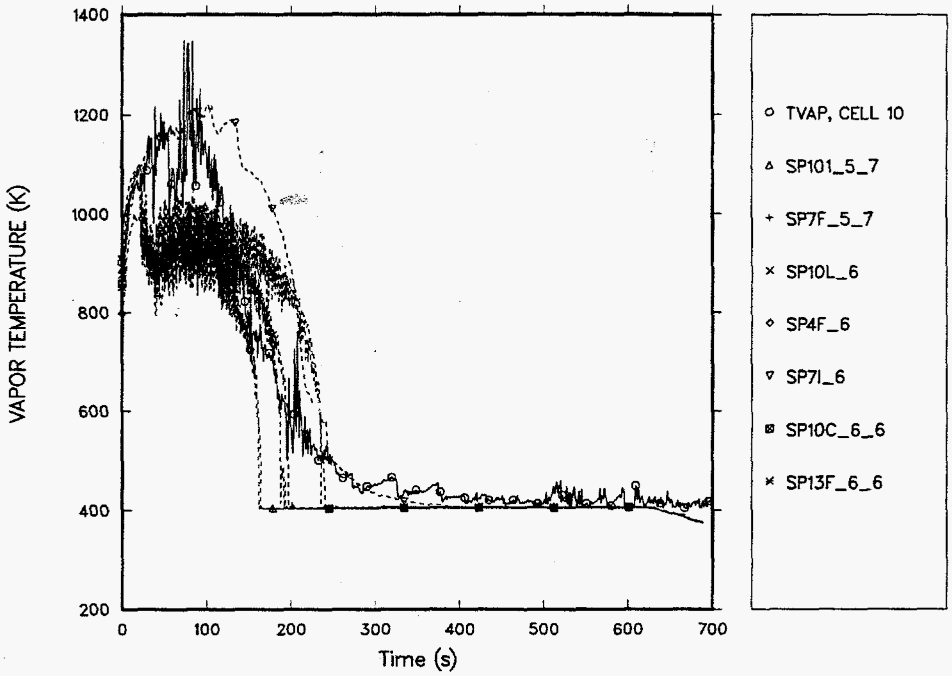

Figure 57. Time-dependent vapor temperature at 1.702 m (67 in.) calculated using the Absolute Pedigree coefficients versus the FLECHT-SEASET Run 31504 experimental data.

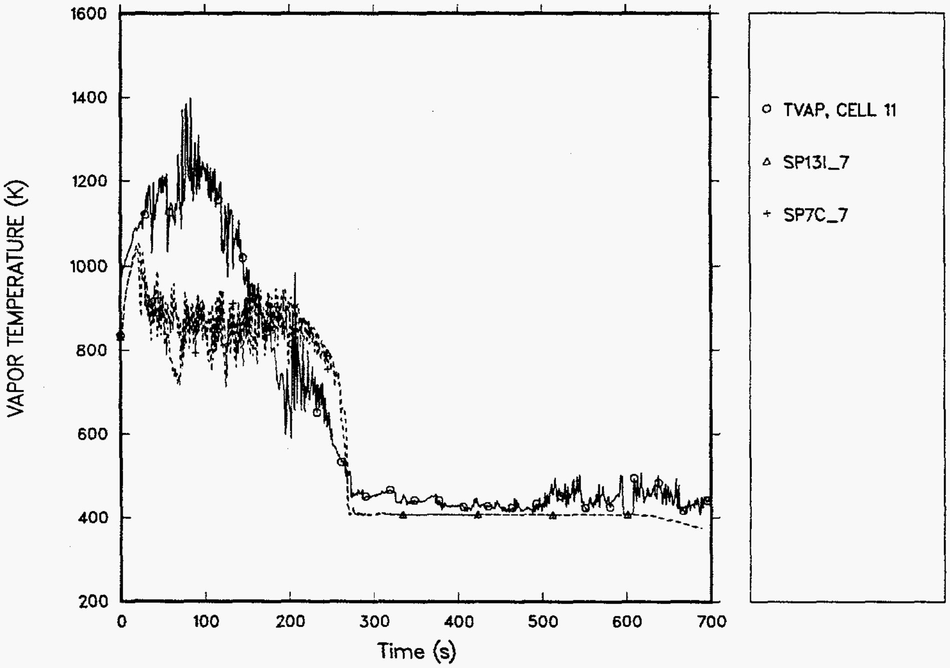

Figure 58. Time-dependent vapor temperature at 2.134 m (84 in.) calculated using the Absolute Pedigree coefficients versus the FLECHT-SEASET Run 31504 experimental data.

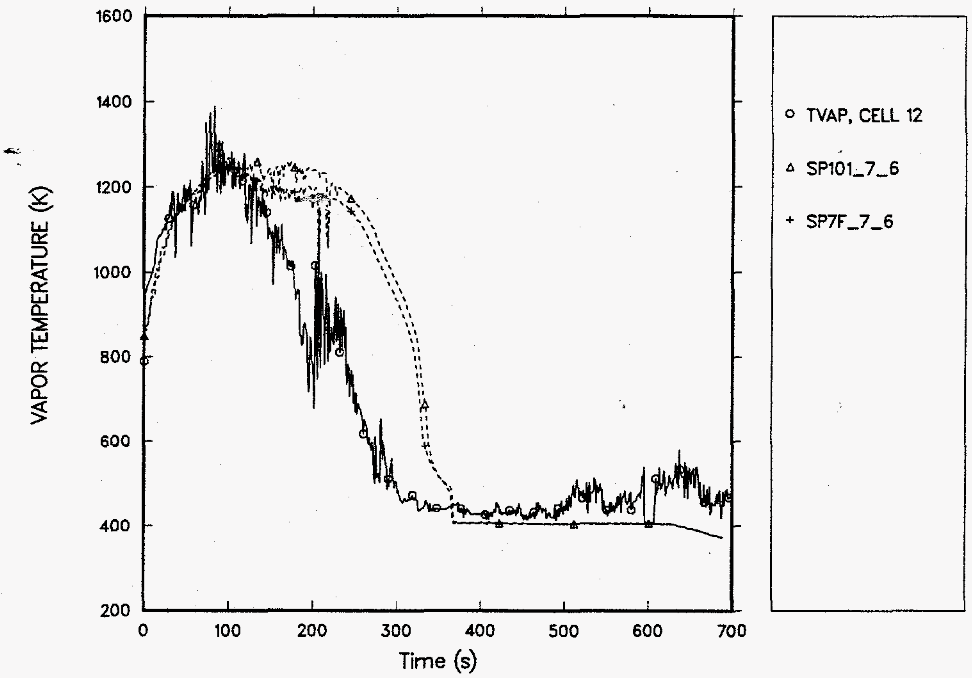

Figure 59. Time-dependent vapor temperature at 2.286 m (90 in.) calculated using the Absolute Pedigree coefficients versus the FLECHT-SEASET Run 31504 experimental data.

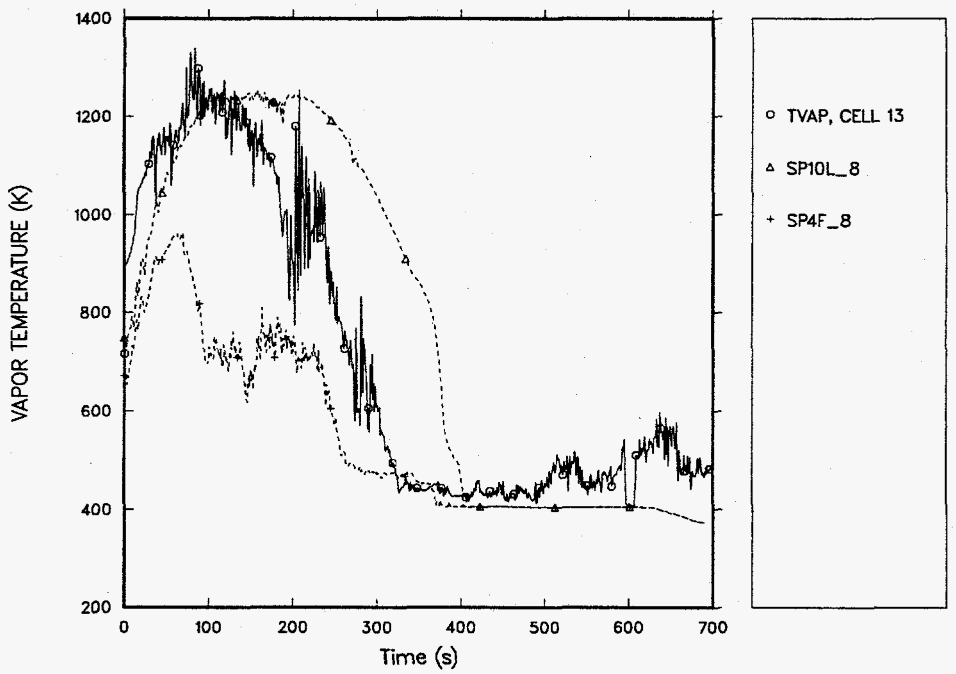

Figure 60. Time-dependent vapor temperature at 2.438 m (96 in.) calculated using the Absolute Pedigree coefficients versus the FLECHT-SEASET Run 31504 experimental data.

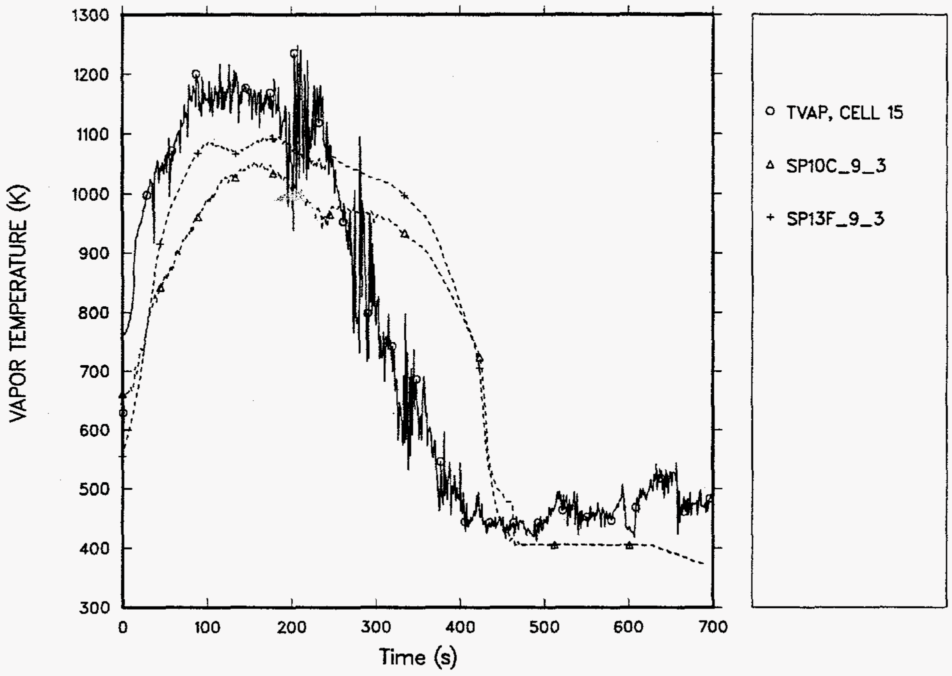

Figure 61. Time-dependent vapor temperature at 2.819 m (111 in.) calculated using the Absolute Pedigree coefficients versus the FLECHT-SEASET Run 31504 experimental data.

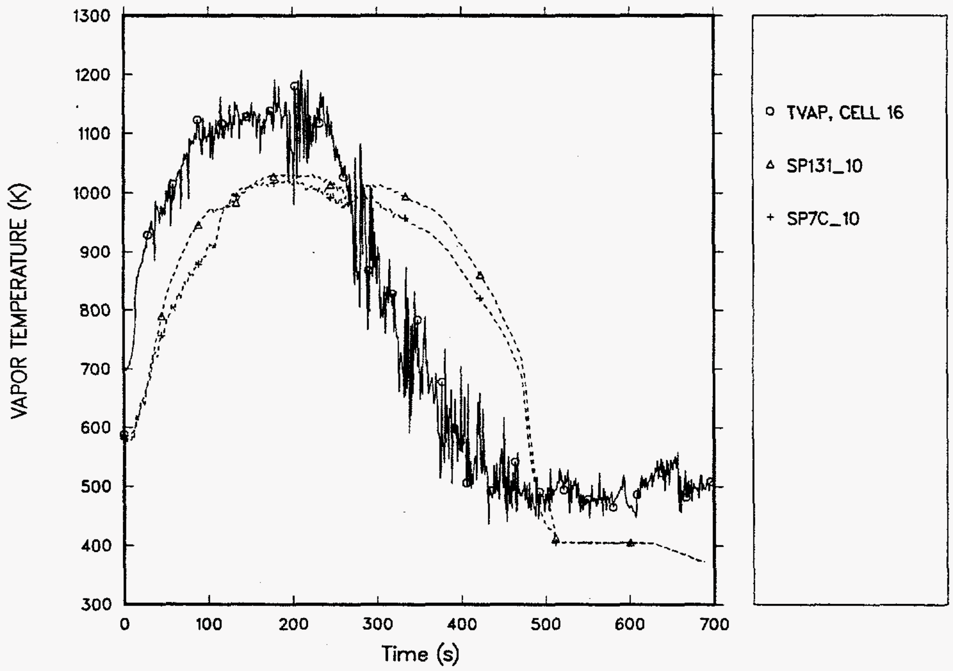

Figure 62. Time-dependent vapor temperature at 3.048 m (120 in.) calculated using the Absolute Pedigree coefficients versus the FLECHT-SEASET Run 31504 experimental data.

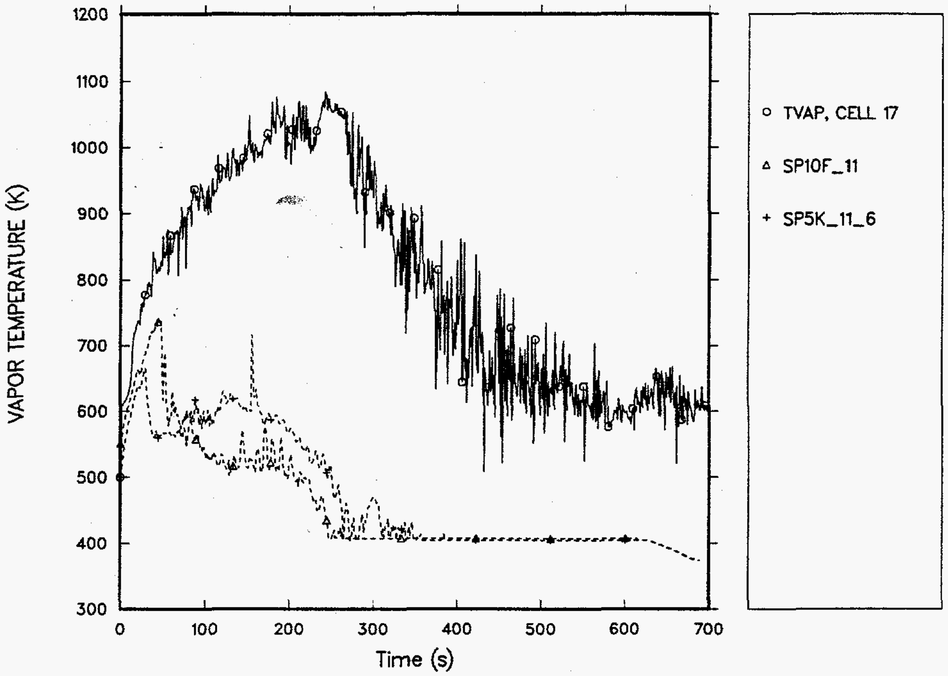

Figure 63. Time-dependent vapor temperature at 3.353 m (132 in.) calculated using the Absolute Pedigree coefficients versus the FLECHT-SEASET Run 31504 experimental data.

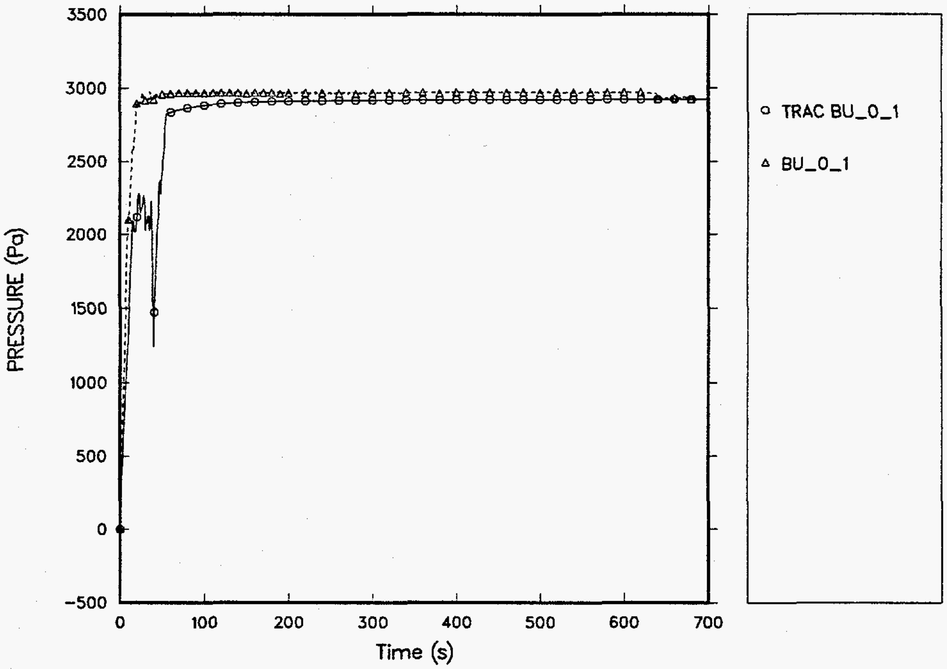

Figure 64. Time-dependent differential pressure from 0 to 0.3048 m (0 to 12 in.) calculated using the Absolute Pedigree coefficients versus the FLECHT-SEASET Run 31504 experimental data.

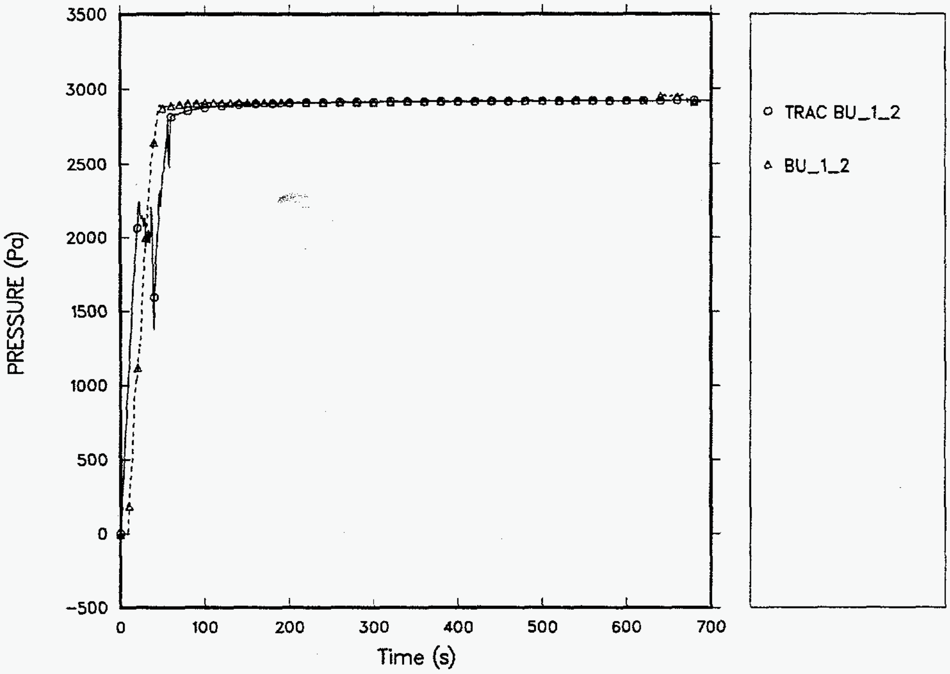

Figure 65. Time-dependent differential pressure from 0.3048 to 0.6096 m (12 to 24 in.) calculated using the Absolute Pedigree coefficients versus the FLECHT-SEASET Run 31504 experimental data.

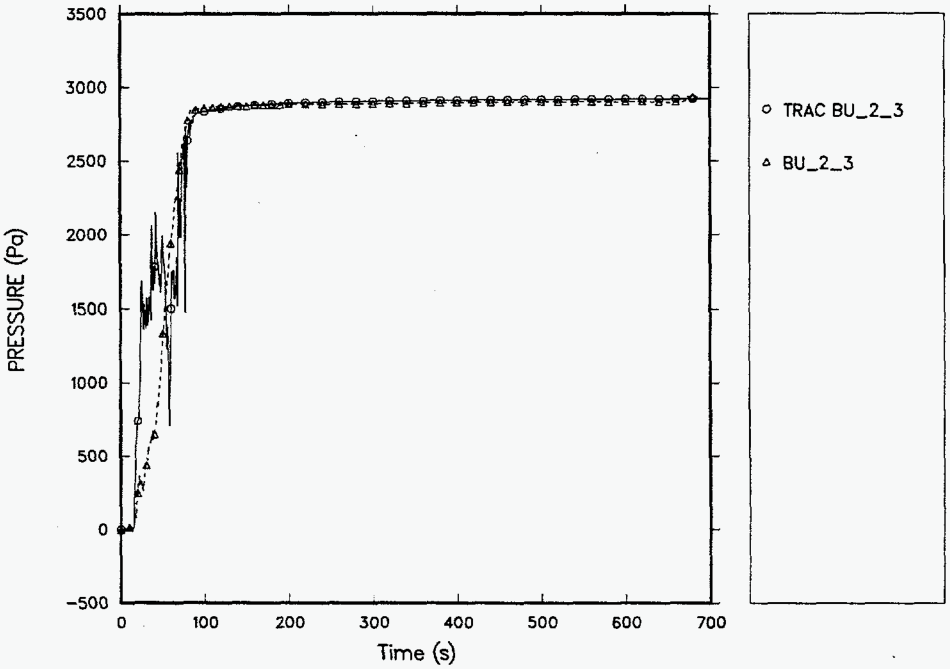

Figure 66. Time-dependent differential pressure from 0.6096 to 0.9144 m (24 to 36 in.) calculated using the Absolute Pedigree coefficients versus the FLECHT-SEASET Run 31504 experimental data.

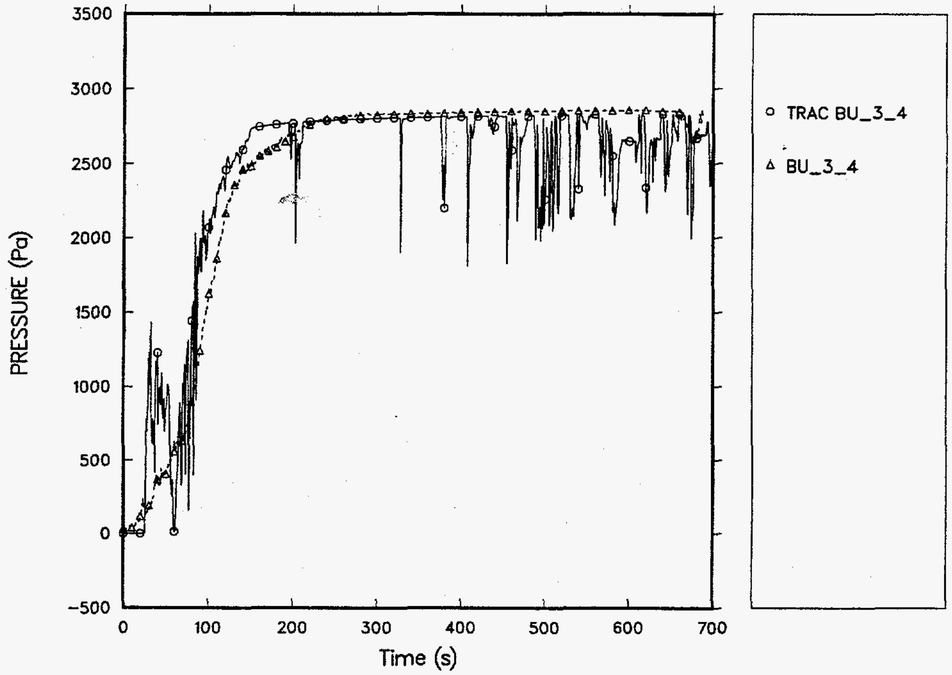

Figure 67. Time-dependent differential pressure from 0.9144 to 0.1.2192 m (36 to 48 in.) calculated using the Absolute Pedigree coefficients versus the FLECHT-SEASET Run 31504 experimental data.

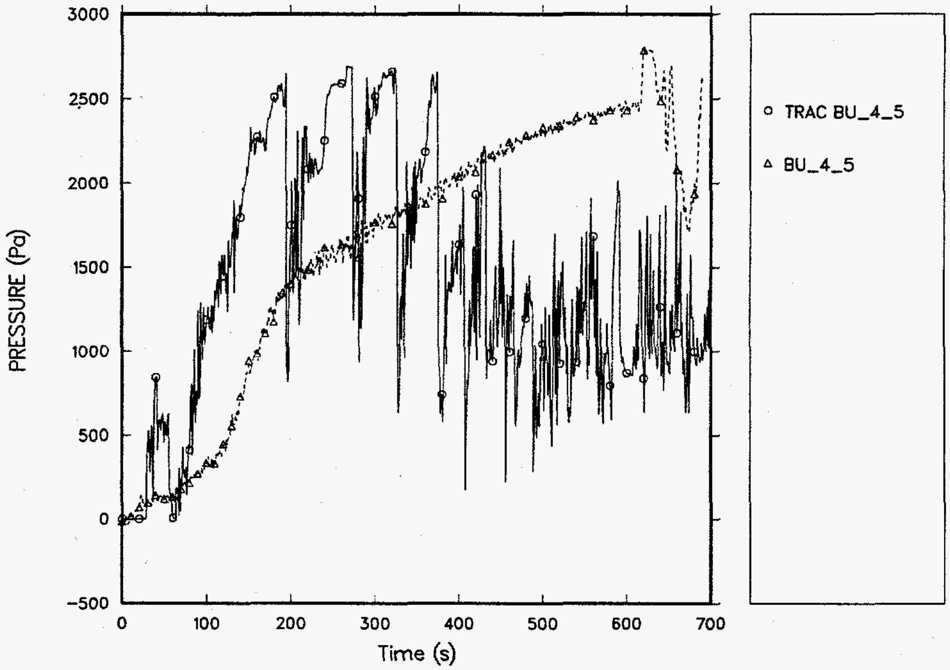

Figure 68. Time-dependent differential pressure from 1.2192 to 1.524 m (48 to 60 in.) calculated using the Absolute Pedigree coefficients versus the FLECHT-SEASET Run 31504 experimental data.

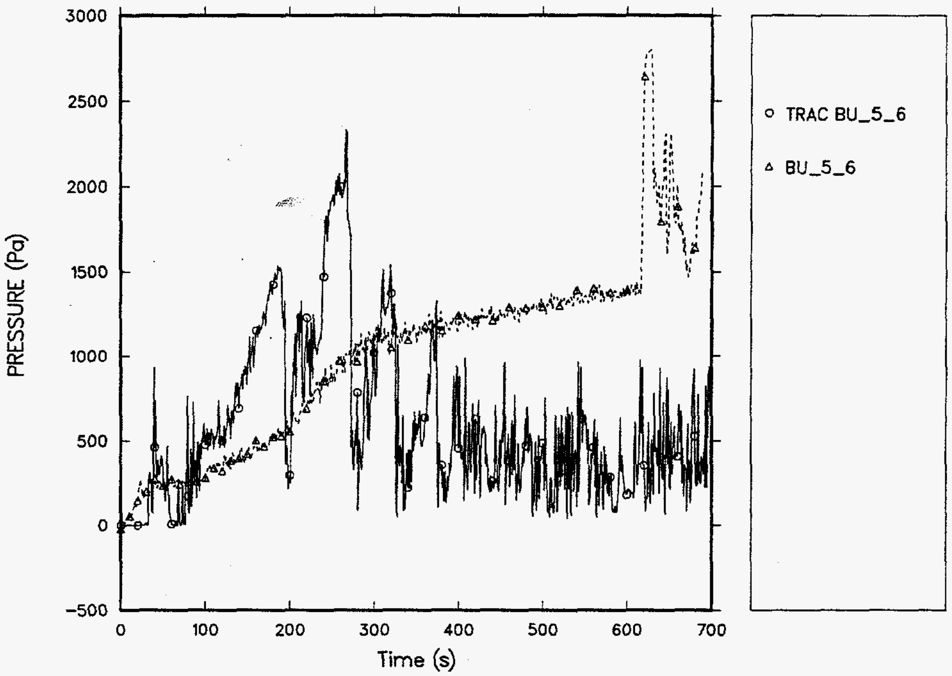

Figure 69. Time-dependent differential pressure from 1.524 to 1.8288 m (60 to 72 in.) calculated using the Absolute Pedigree coefficients versus the FLECHT-SEASET Run 31504 experimental data.

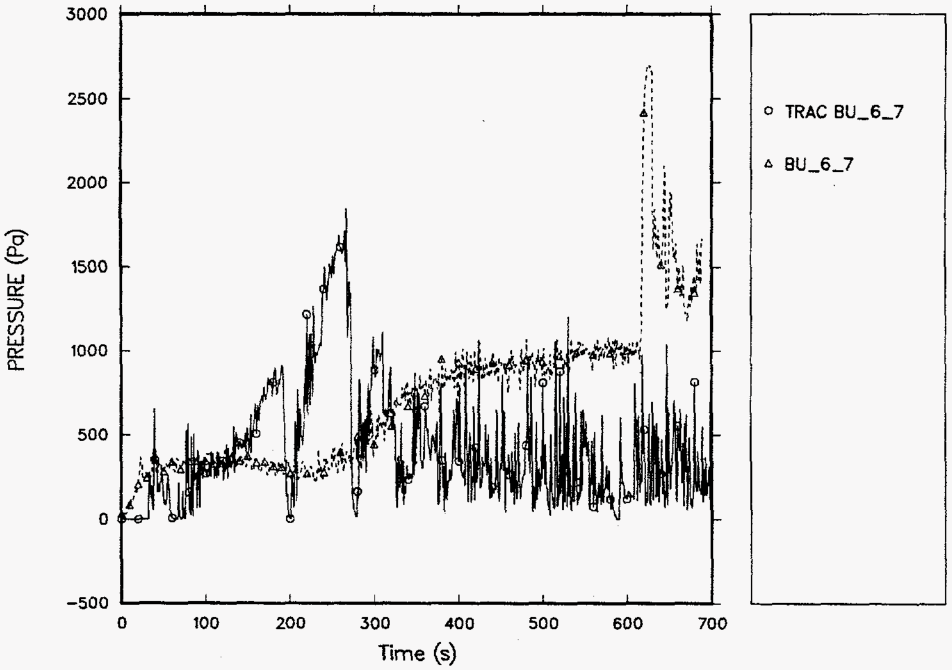

Figure 70. Time-dependent differential pressure from 1.8288 to 2.1336 m (72 to 84 in.) calculated using the Absolute Pedigree coefficients versus the FLECHT-SEASET Run 31504 experimental data.

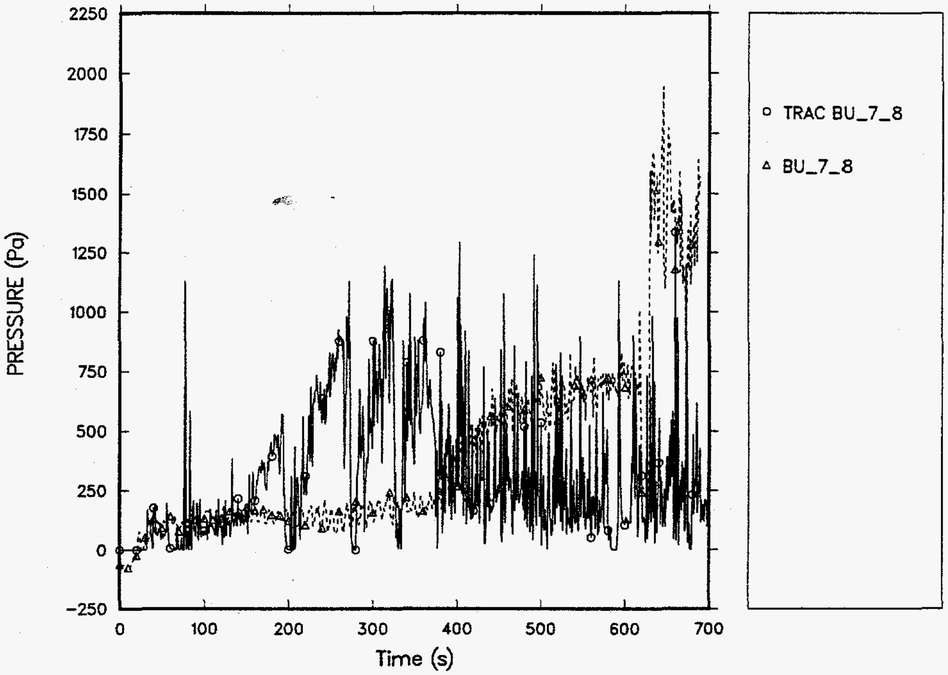

Figure 71. Time-dependent differential pressure from 2.1336 to 2.4384 m (84 to 96 in.) calculated using the Absolute Pedigree coefficients versus the FLECHT-SEASET Run 31504 experimental data.

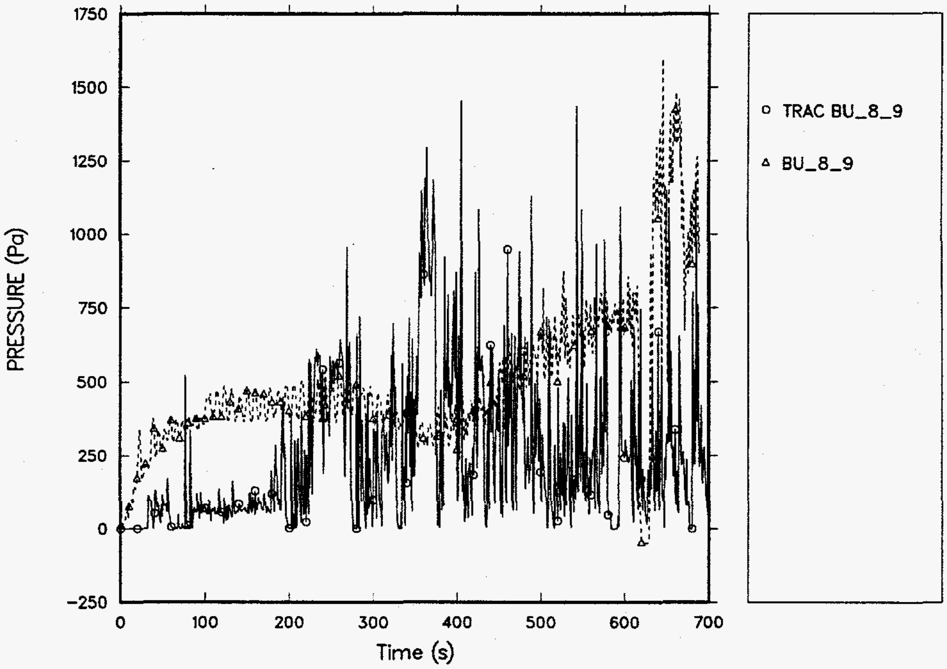

Figure 72. Time-dependent differential pressure from 2.4384 to 2.7432 m (96 to 108 in.) calculated using the Absolute Pedigree coefficients versus the FLECHT-SEASET Run 31504 experimental data.

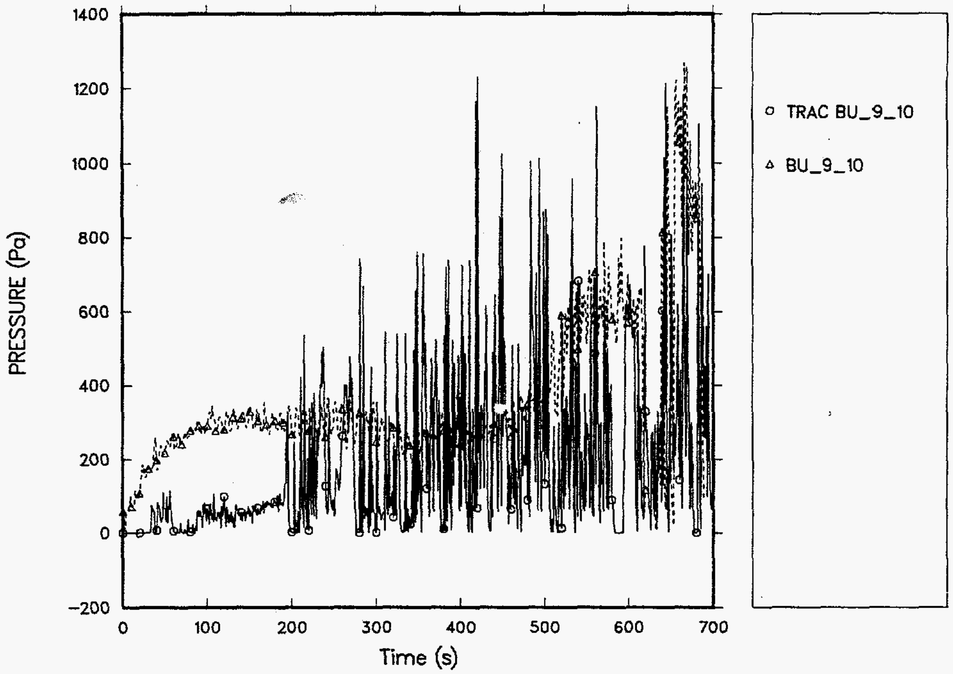

Figure 73. Time-dependent differential pressure from 2.7432 to 3.048 m (108 to 120 in.) calculated using the Absolute Pedigree coefficients versus the FLECHT-SEASET Run 31504 experimental data.

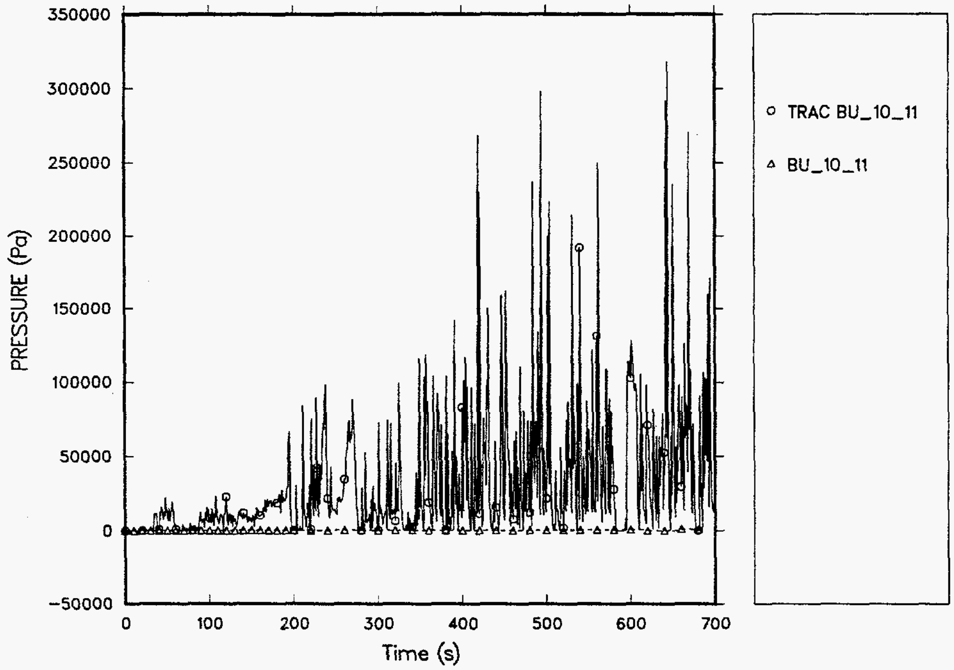

Figure 74. Time-dependent differential pressure from 3.048 to 3.3528 m (120 to 132 in.) calculated using the Absolute Pedigree coefficients versus the FLECHT-SEASET Run 31504 experimental data.

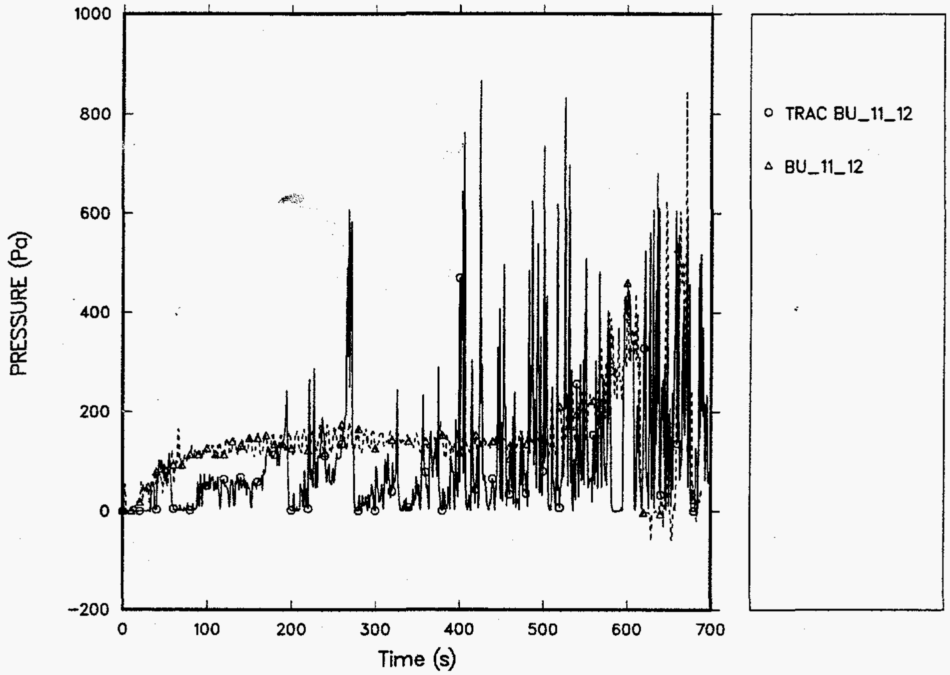

Figure 75. Time-dependent differential pressure from 3.3528 to 3.6576 m (132 to 144 in.) calculated using the Absolute Pedigree coefficients versus the FLECHT-SEASET Run 31504 experimental data.

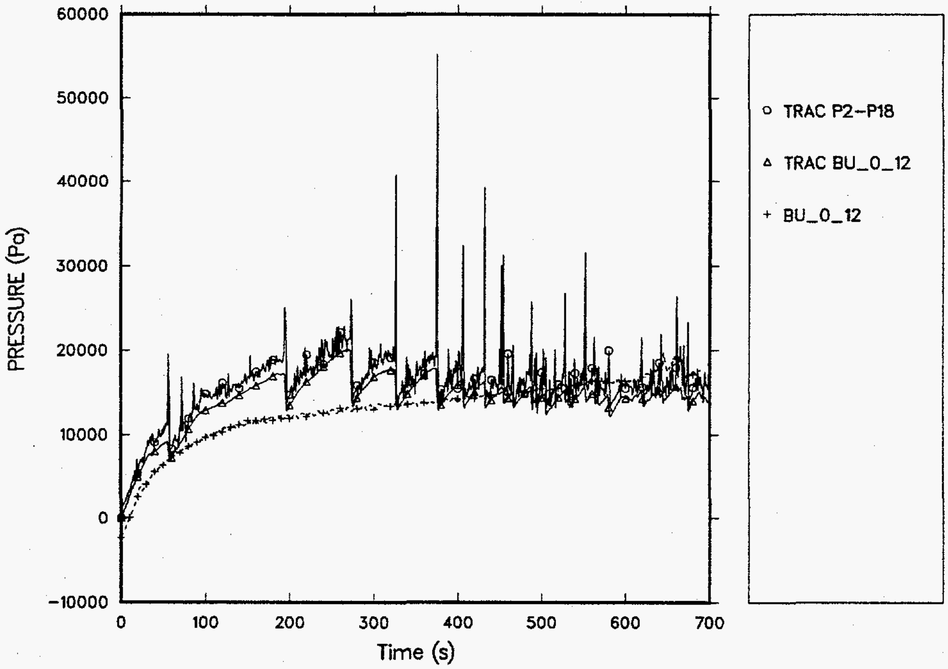

Figure 76. Time-dependent differential pressure from 0 to 3.3528 m (0 to 144 in.) calculated using the Absolute Pedigree coefficients versus the FLECHT-SEASET Run 31504 experimental data.

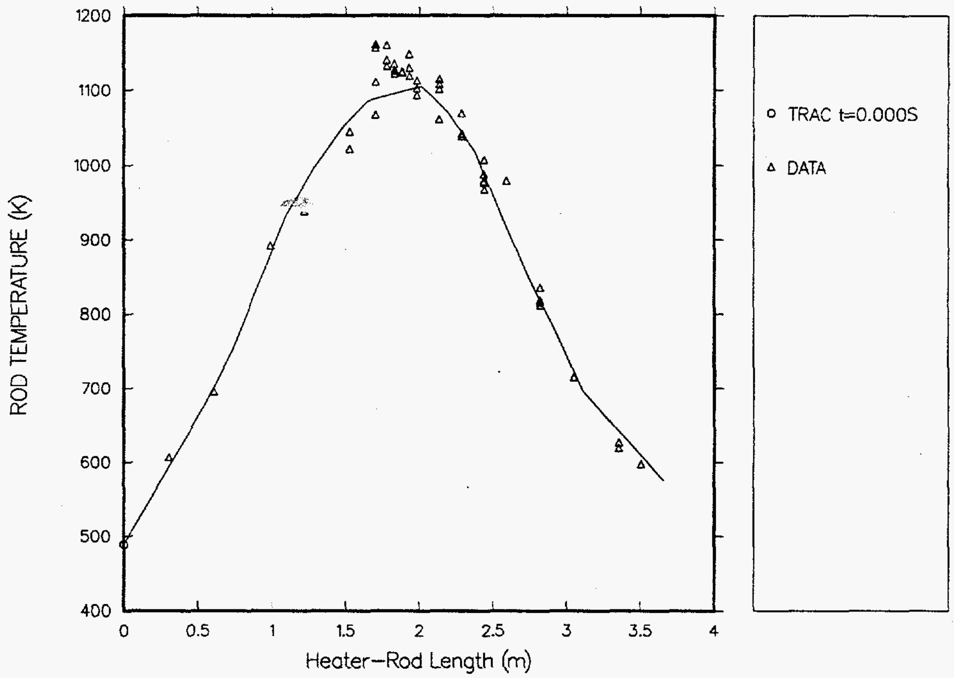

Figure 77. Intial axially-dependent cladding temperature calculated using the Conditional Pedigree coefficients versus the FLECHT-SEASET Run 31504 experimental data.

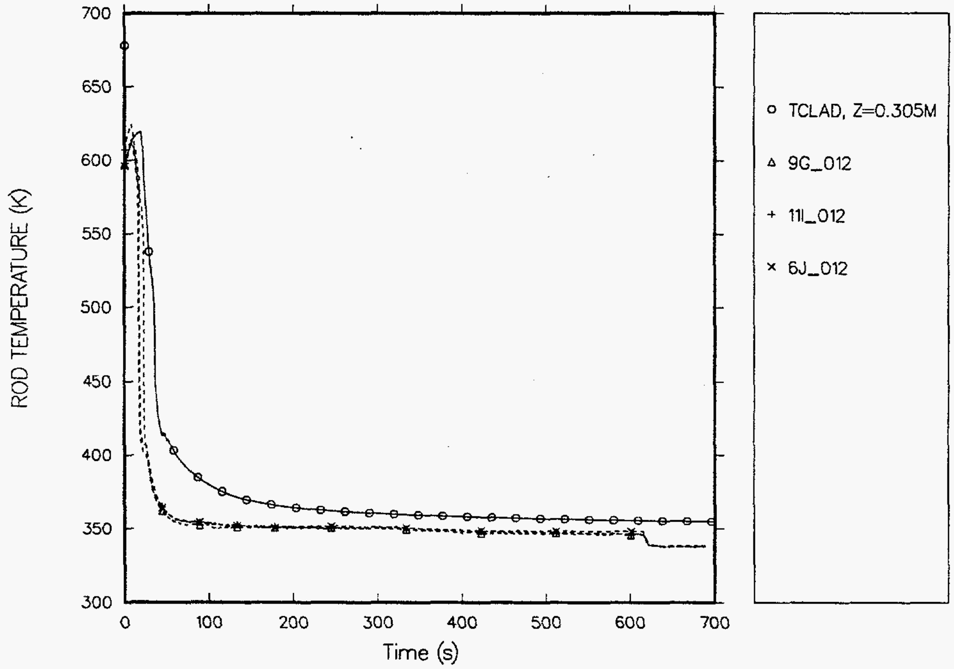

Figure 78. Time-dependent cladding temperature at 0.305 m (12 in.) calculated using the Conditional Pedigree coefficients versus the FLECHT-SEASET Run 31504 experimental data.

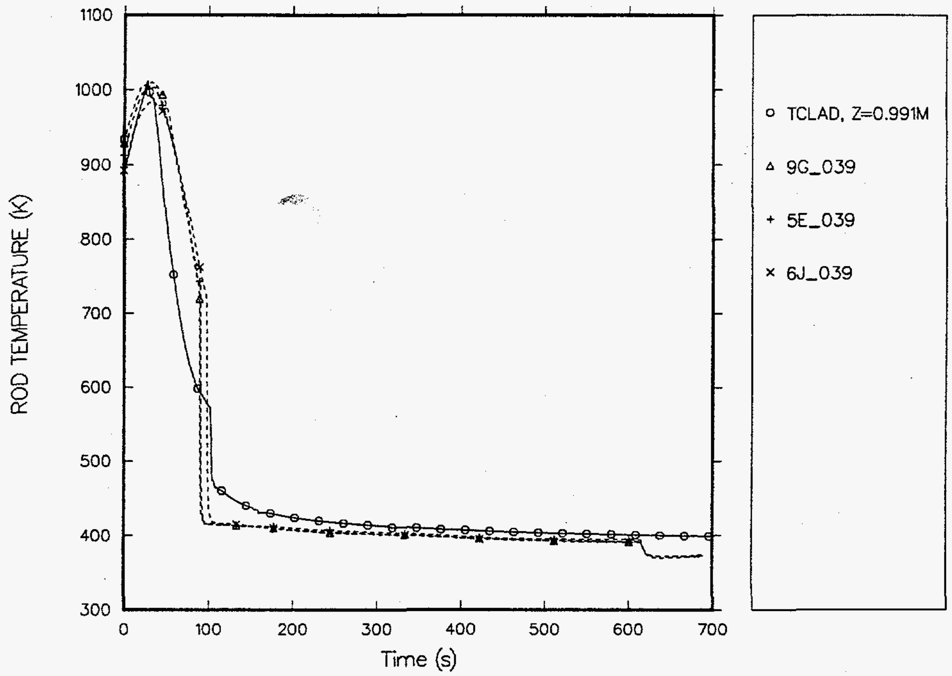

Figure 79. Time-dependent cladding temperature at 0.991 m (39 in.) calculated using the Conditional Pedigree coefficients versus the FLECHT-SEASET Run 31504 experimental data.

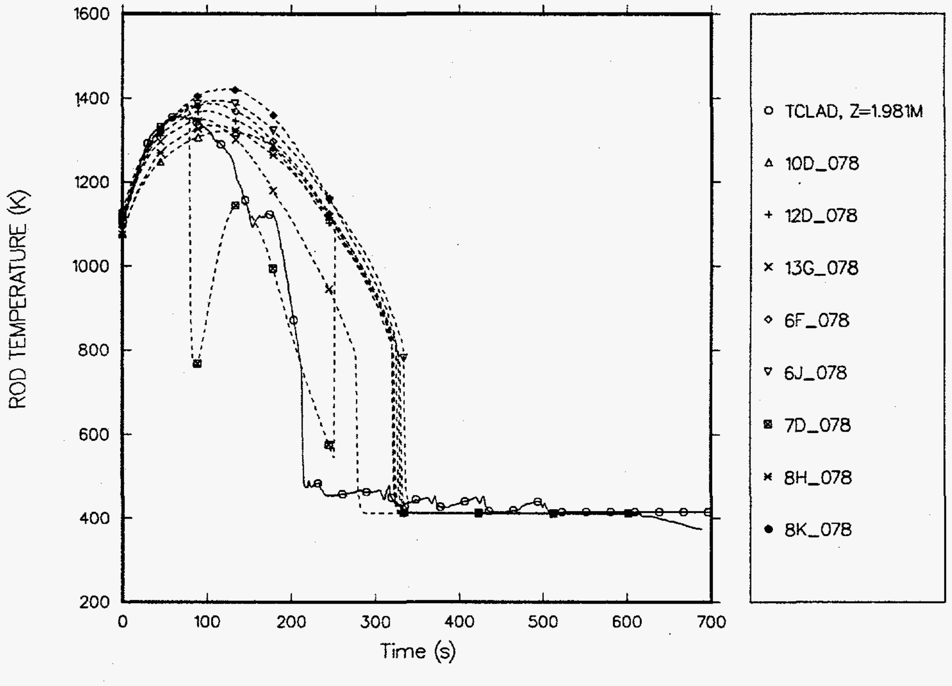

Figure 80. Time-dependent cladding temperature at 1.981 m (78 in.) calculated using the Conditional Pedigree coefficients versus the FLECHT-SEASET Run 31504 experimental data.

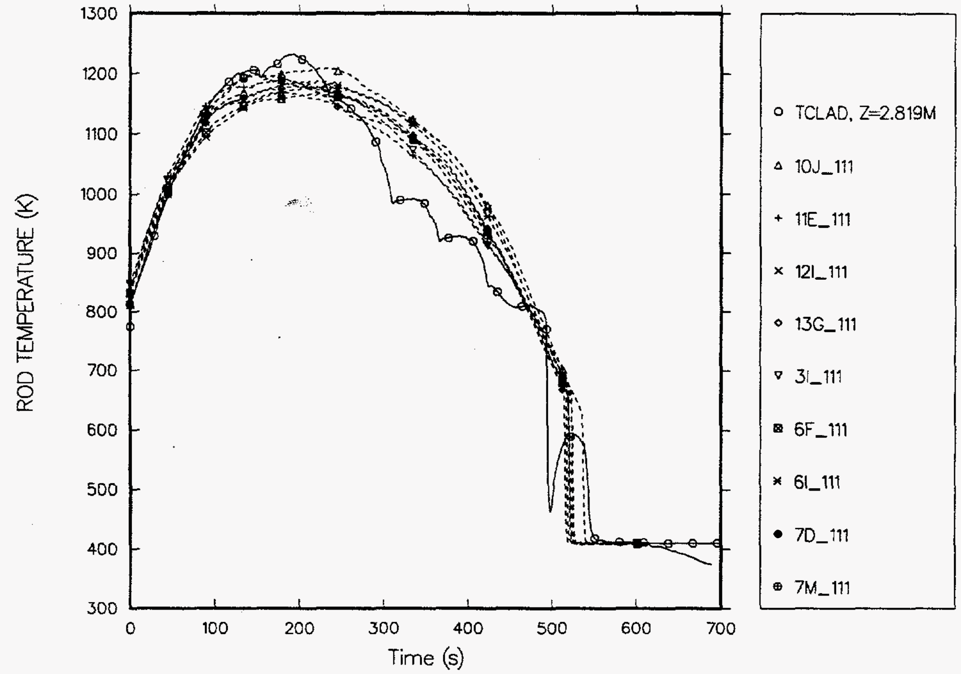

Figure 81. Time-dependent cladding temperature at 2.819 m (111 in.) calculated using the Conditional Pedigree coefficients versus the FLECHT-SEASET Run 31504 experimental data.

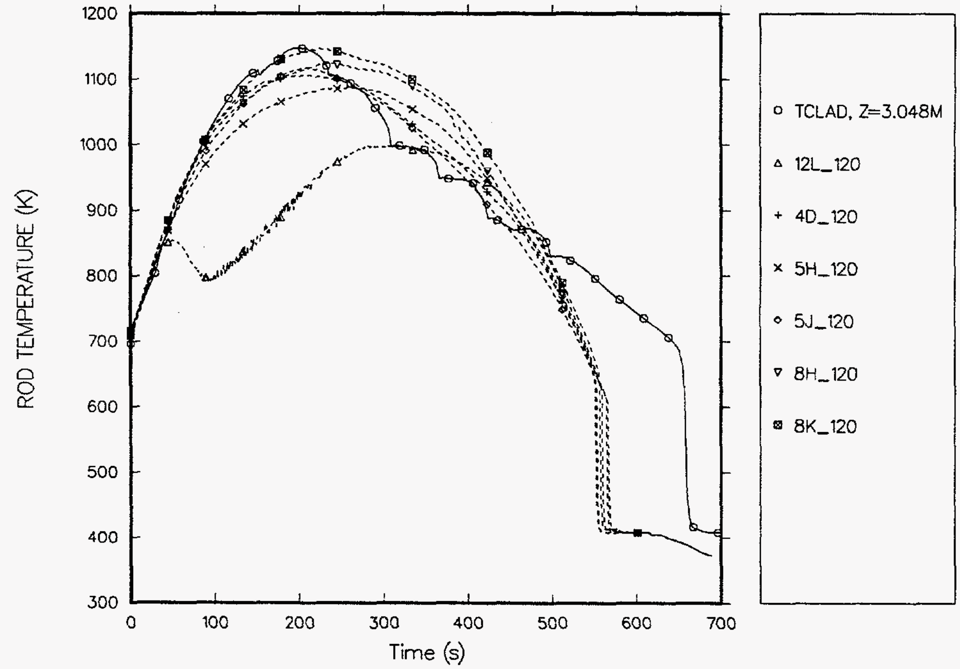

Figure 82. Time-dependent cladding temperature at 3.048 m (120 in.) calculated using the Conditional Pedigree coefficients versus the FLECHT-SEASET Run 31504 experimental data.

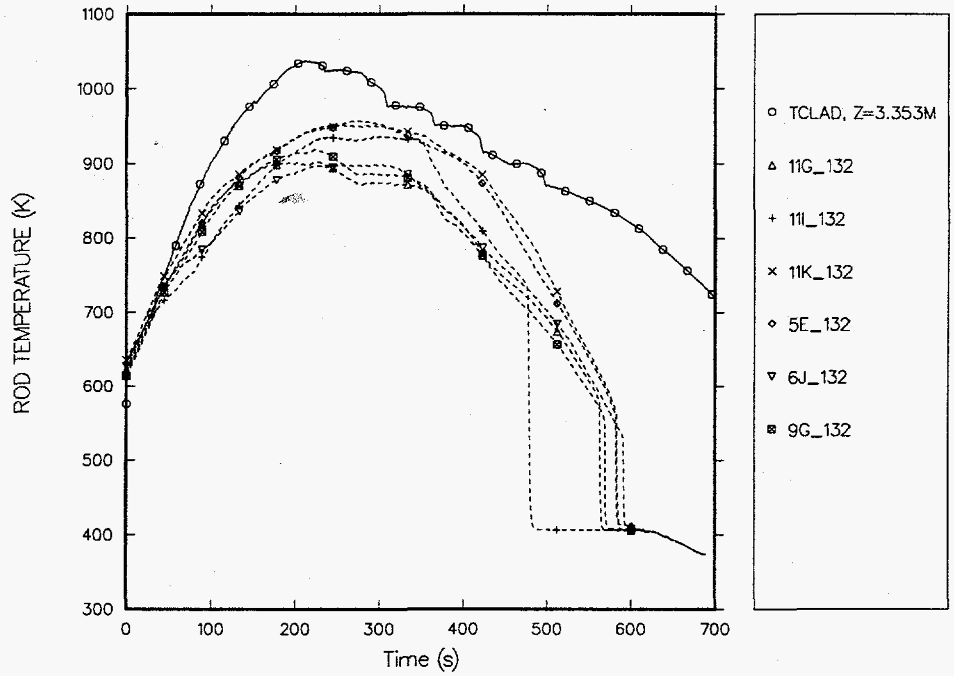

Figure 83. Time-dependent cladding temperature at 3.353 m (132 in.) calculated using the Conditional Pedigree coefficients versus the FLECHT-SEASET Run 31504 experimental data.

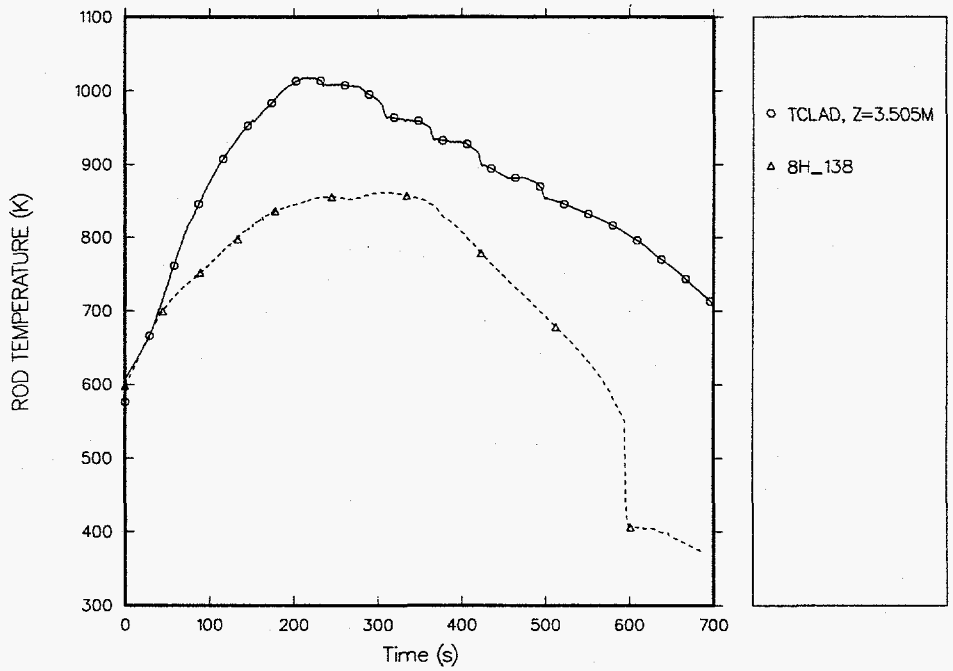

Figure 84. Time-dependent cladding temperature at 3.505 m (138 in.) calculated using the Conditional Pedigree coefficients versus the FLECHT-SEASET Run 31504 experimental data.

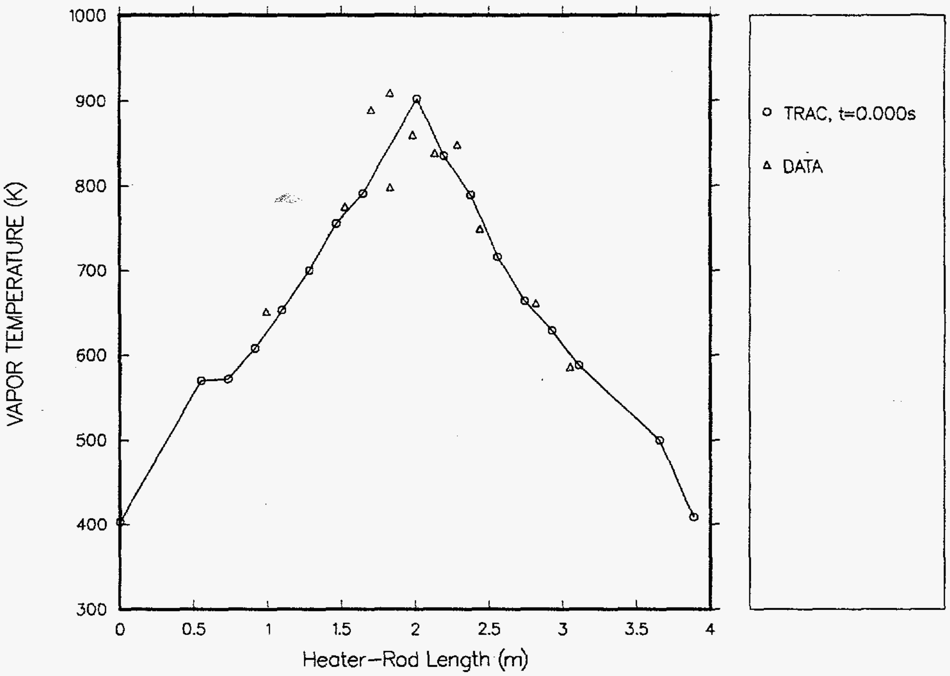

Figure 85. Intial axially-dependent vapor temperature calculated using the Conditional Pedigree coefficients versus the FLECHT-SEASET Run 31504 experimental data.

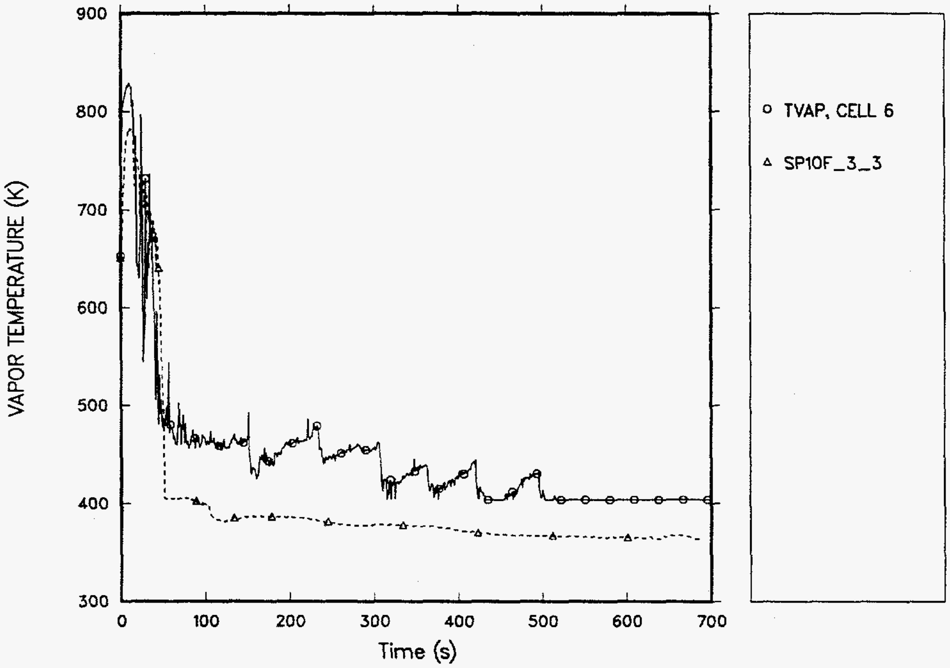

Figure 86. Time-dependent vapor temperature at 0.991 m (39 in.) calculated using the Conditional Pedigree coefficients versus the FLECHT-SEASET Run 31504 experimental data.

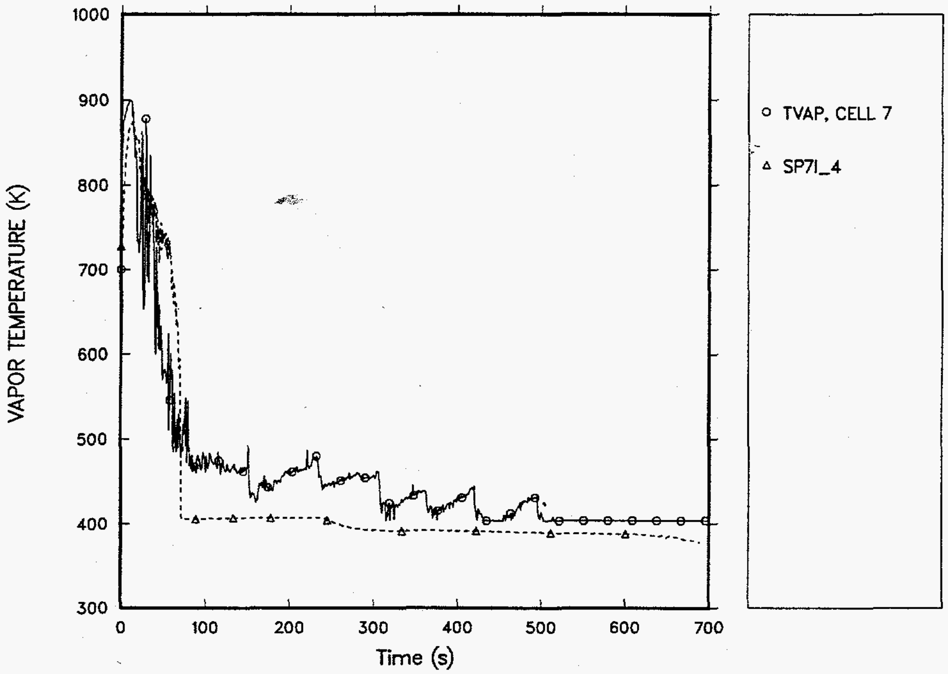

Figure 87. Time-dependent vapor temperature at 1.219 m (48 in.) calculated using the Conditional Pedigree coefficients versus the FLECHT-SEASET Run 31504 experimental data.

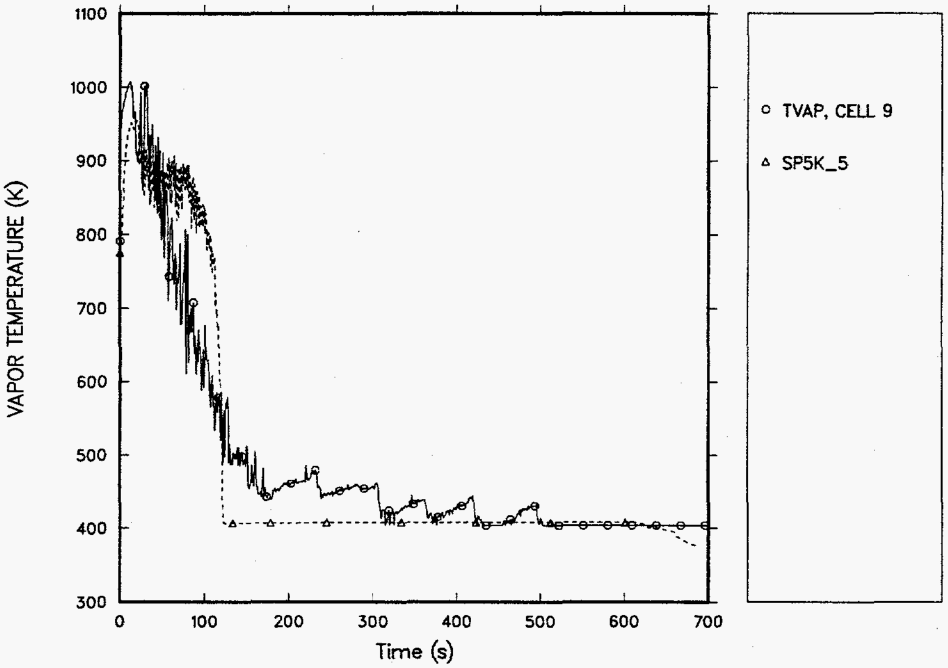

Figure 88. Time-dependent vapor temperature at 1.524 m (60 in.) calculated using the Conditional Pedigree coefficients versus the FLECHT-SEASET Run 31504 experimental data.

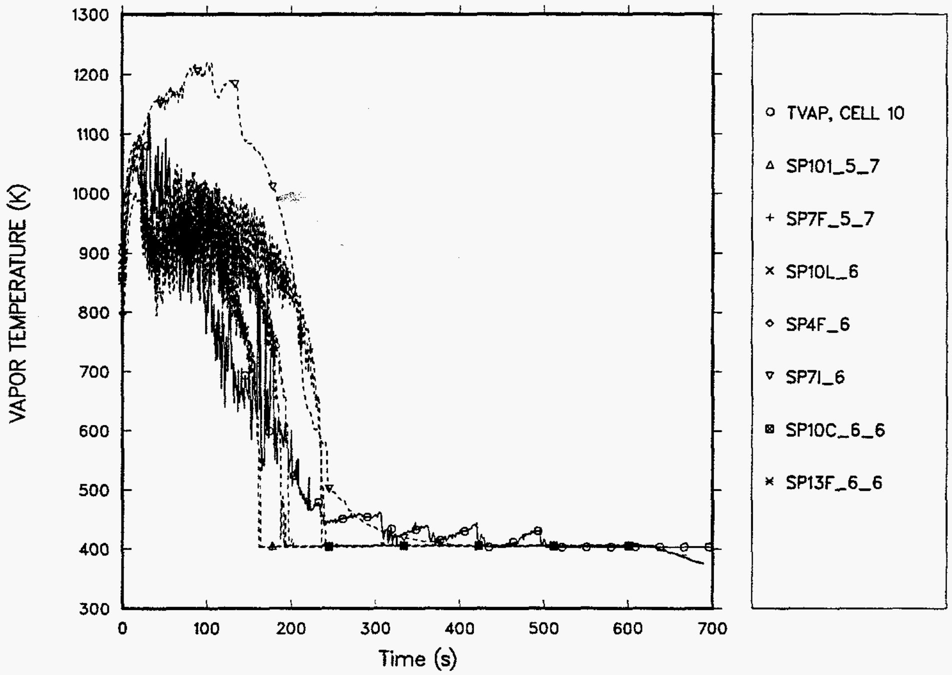

Figure 89. Time-dependent vapor temperature at 1.702 m (67 in.) calculated using the Conditional Pedigree coefficients versus the FLECHT-SEASET Run 31504 experimental data.

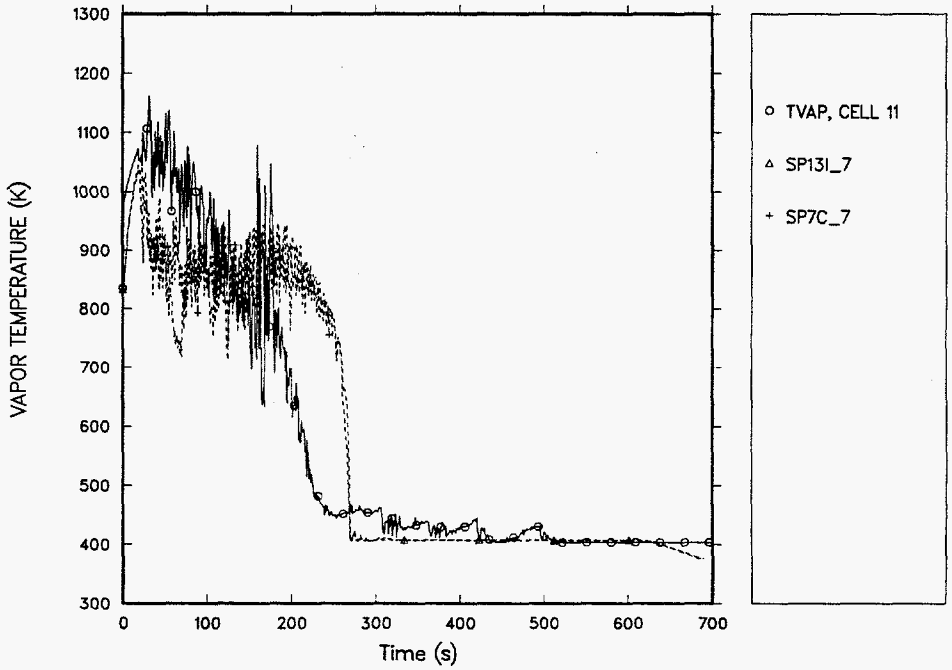

Figure 90. Time-dependent vapor temperature at 2.134 m (84 in.) calculated using the Conditional Pedigree coefficients versus the FLECHT-SEASET Run 31504 experimental data.

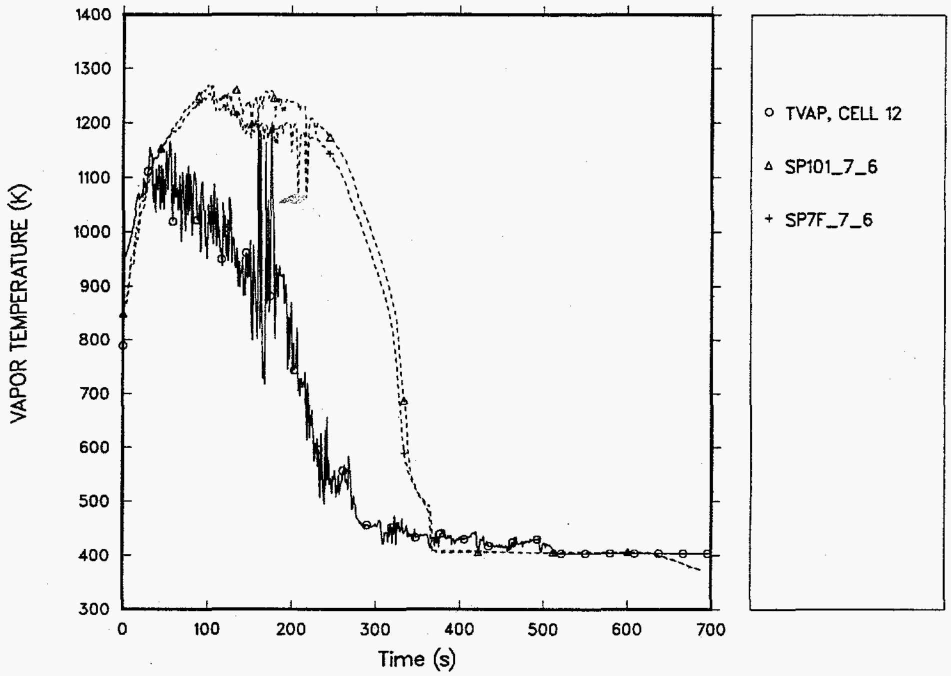

Figure 91. Time-dependent vapor temperature at 2.286 m (90 in.) calculated using the Conditional Pedigree coefficients versus the FLECHT-SEASET Run 31504 experimental data.

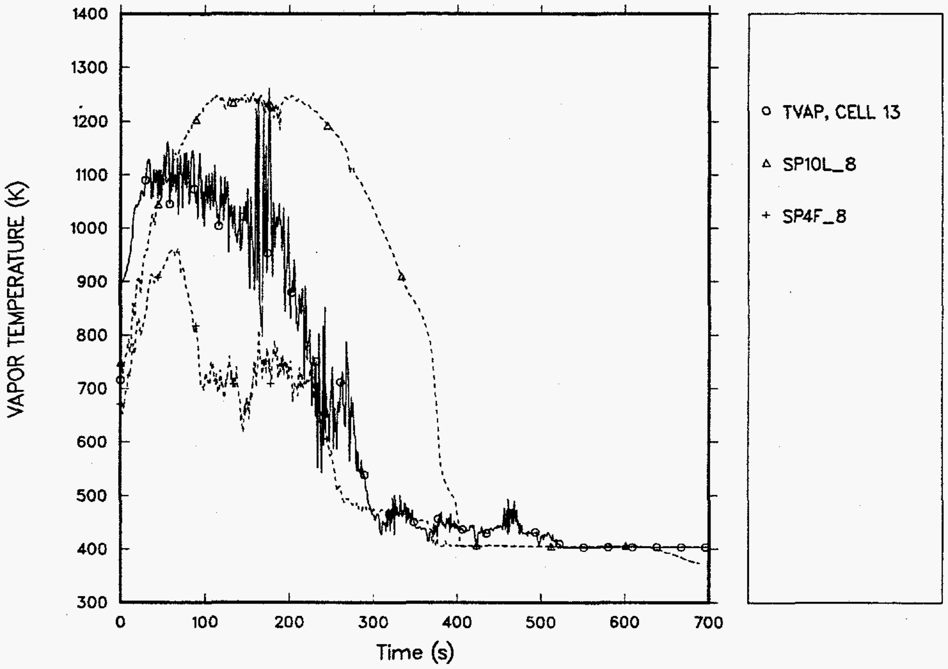

Figure 92. Time-dependent vapor temperature at 2.438 m (96 in.) calculated using the Conditional Pedigree coefficients versus the FLECHT-SEASET Run 31504 experimental data.

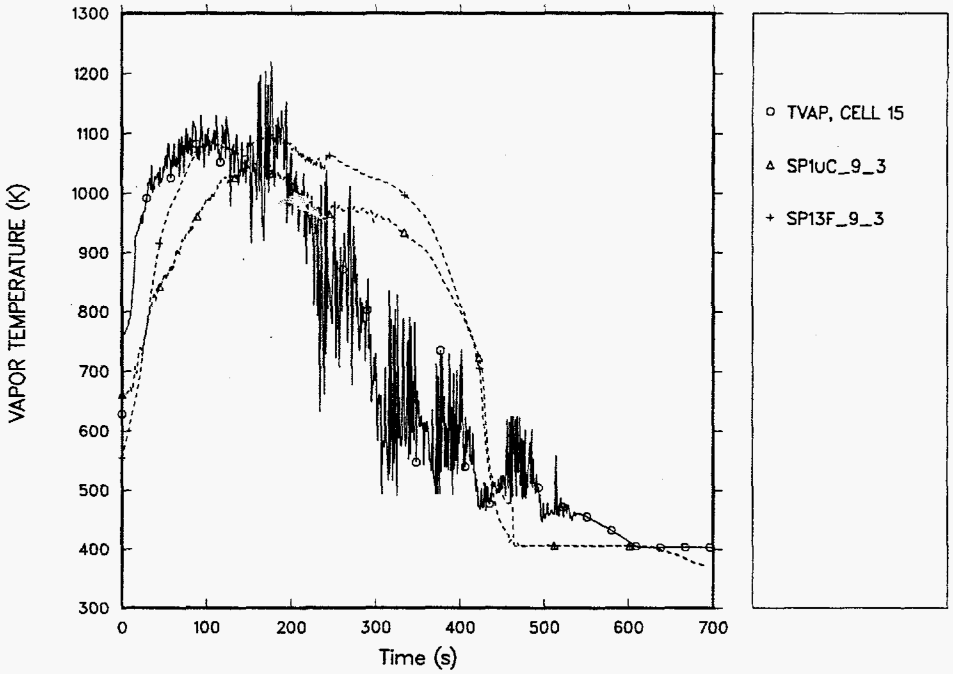

Figure 93. Time-dependent vapor temperature at 2.819 m (111 in.) calculated using the Conditional Pedigree coefficients versus the FLECHT-SEASET Run 31504 experimental data.

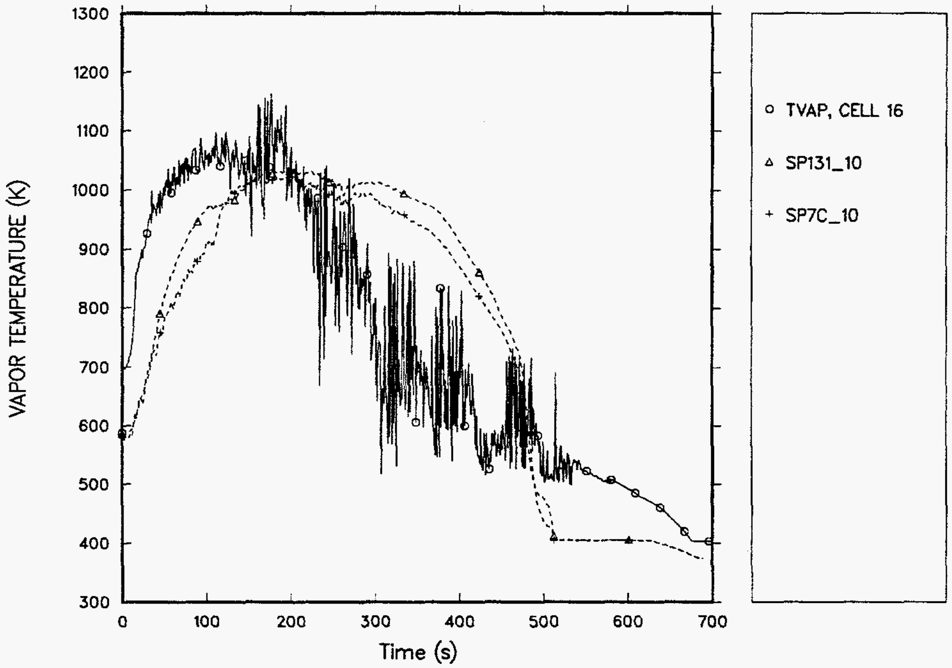

Figure 94. Time-dependent vapor temperature at 3.048 m (120 in.) calculated using the Conditional Pedigree coefficients versus the FLECHT-SEASET Run 31504 experimental data.

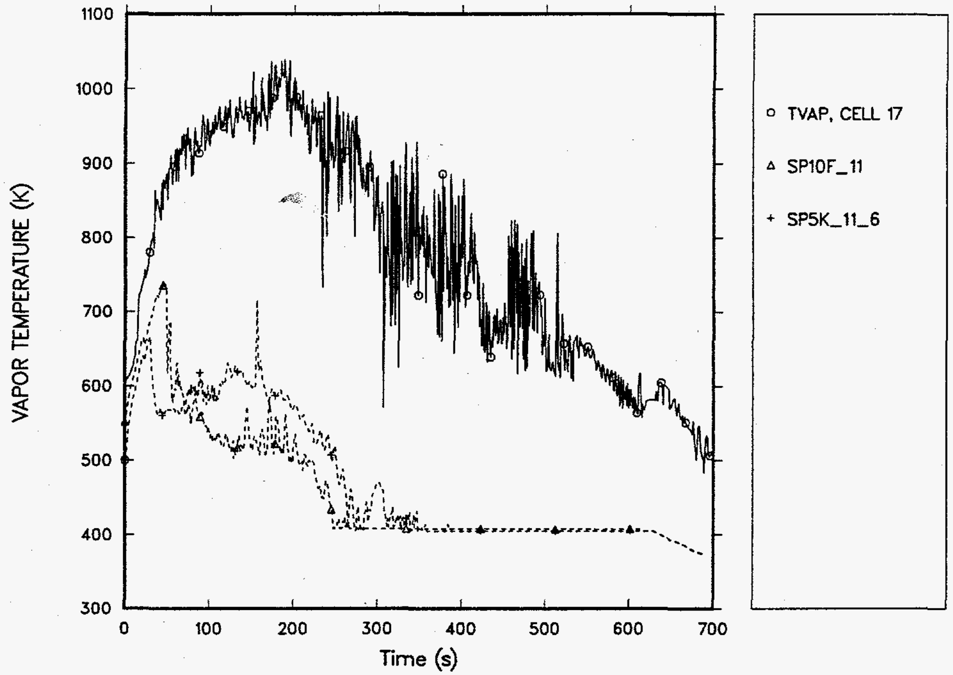

Figure 95. Time-dependent vapor temperature at 3.353 m (132 in.) calculated using the Conditional Pedigree coefficients versus the FLECHT-SEASET Run 31504 experimental data.

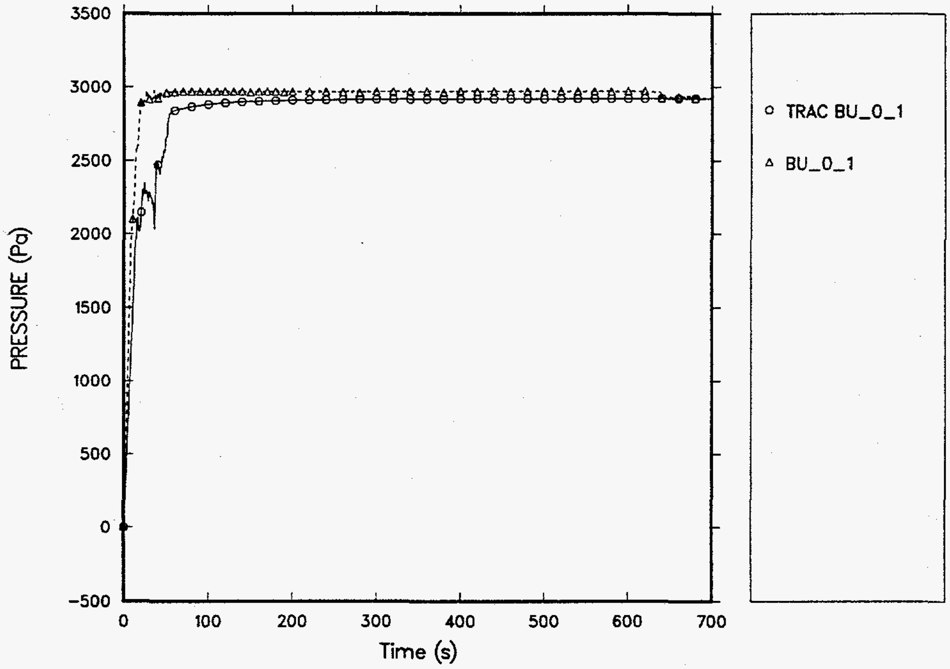

Figure 96. Time-dependent differential pressure from 0 to 0.3048 m (0 to 12 in.) calculated using the Conditional Pedigree coefficients versus the FLECHT-SEASET Run 31504 experimental data.

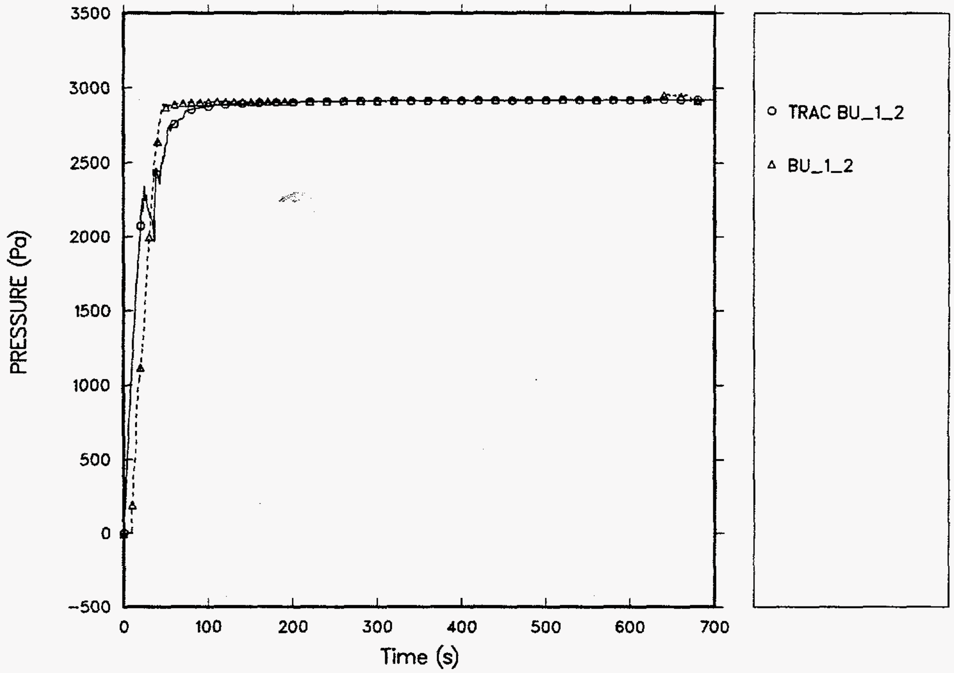

Figure 97. Time-dependent differential pressure from 0.3048 to 0.6096 m (12 to 24 in.) calculated using the Conditional Pedigree coefficients versus the FLECHT-SEASET Run 31504 experimental data.

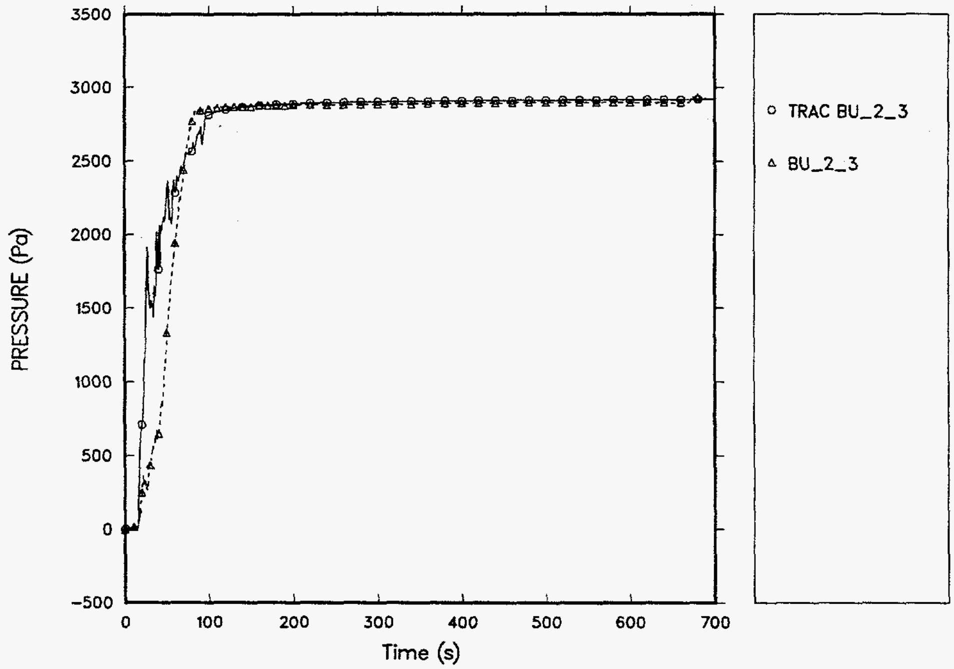

Figure 98. Time-dependent differential pressure from 0.6096 to 0.9144 m (24 to 36 in.) calculated using the Conditional Pedigree coefficients versus the FLECHT-SEASET Run 31504 experimental data.

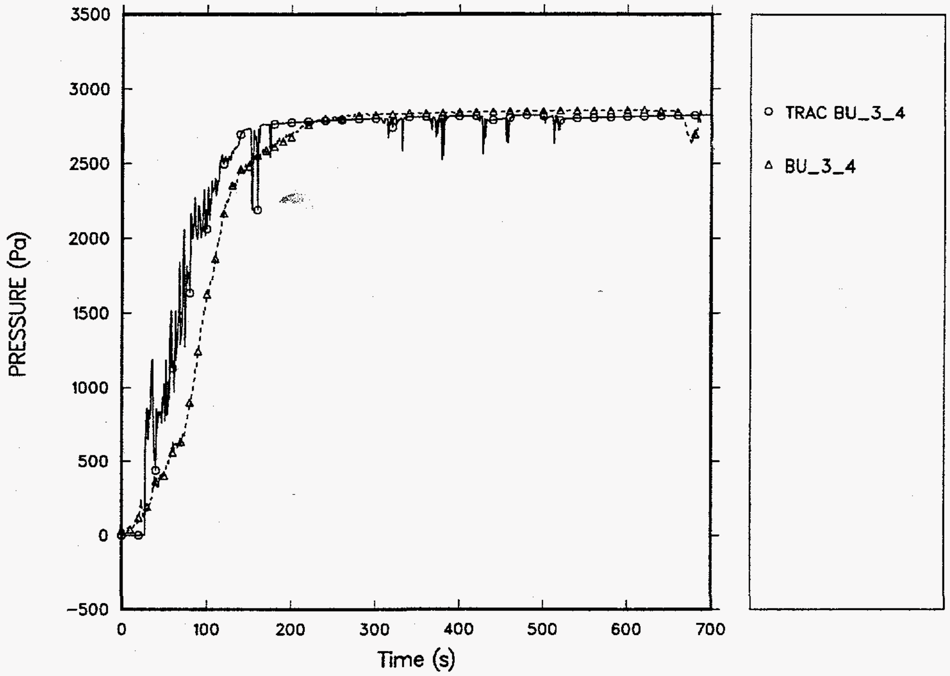

Figure 99. Time-dependent differential pressure from 0.9144 to 0.1.2192 m (36 to 48 in.) calculated using the Conditional Pedigree coefficients versus the FLECHT-SEASET Run 31504 experimental data.

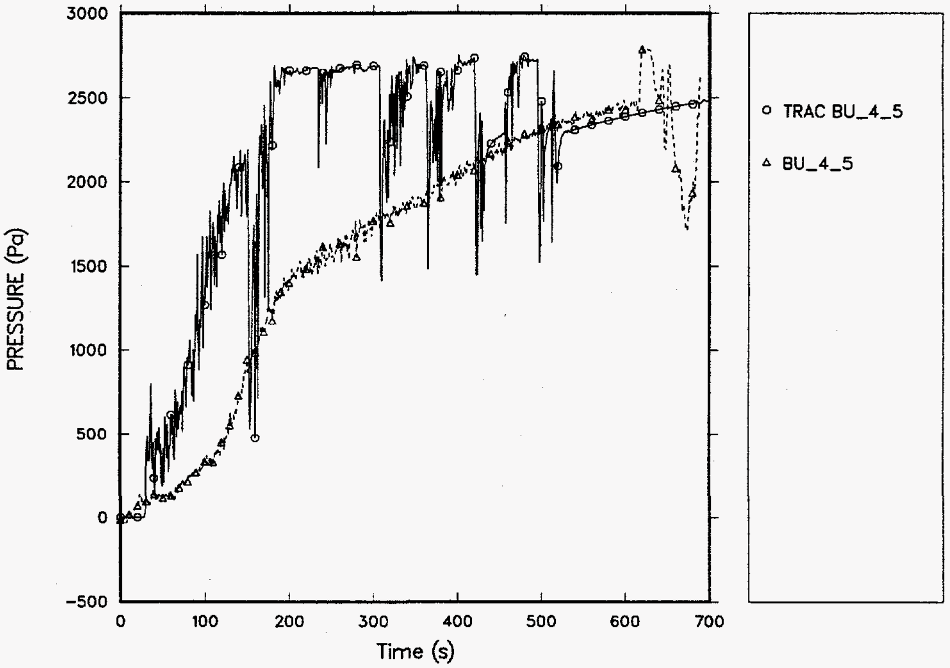

Figure 100. Time-dependent differential pressure from 1.2192 to 1.524 m (48 to 60 in.) calculated using the Conditional Pedigree coefficients versus the FLECHT-SEASET Run 31504 experimental data.

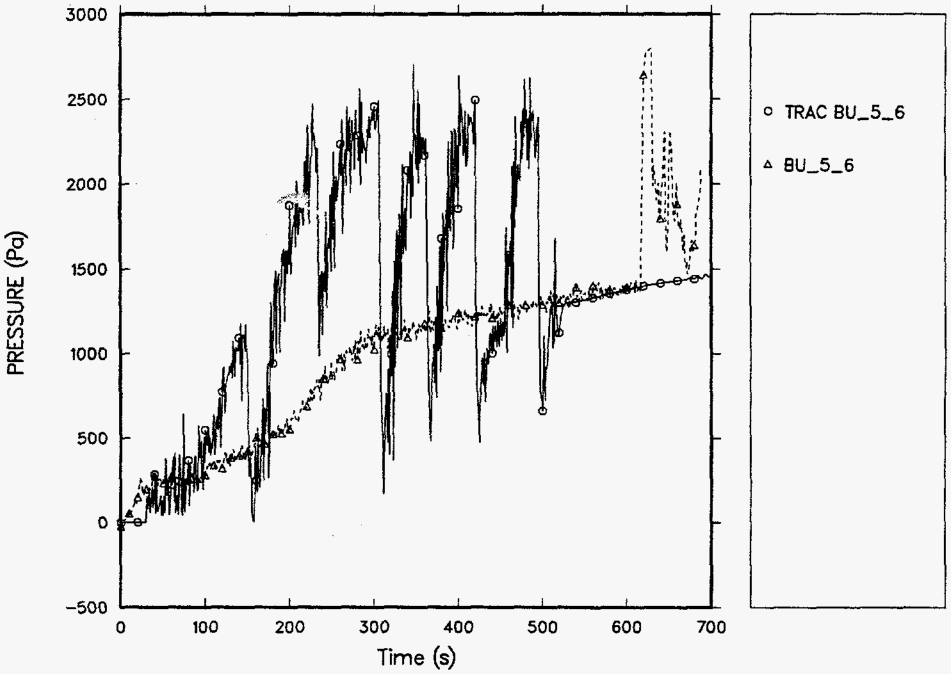

Figure 101. Time-dependent differential pressure from 1.524 to 1.8288 m (60 to 72 in.) calculated using the Conditional Pedigree coefficients versus the FLECHT-SEASET Run 31504 experimental data.

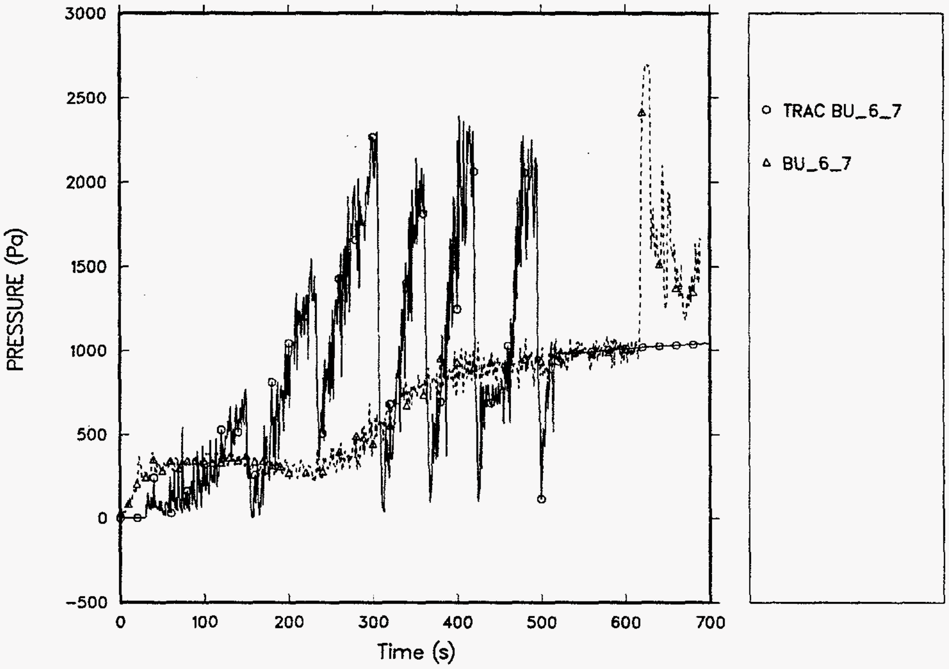

Figure 102. Time-dependent differential pressure from 1.8288 to 2.1336 m (72 to 84 in.) calculated using the Conditional Pedigree coefficients versus the FLECHT-SEASET Run 31504 experimental data.

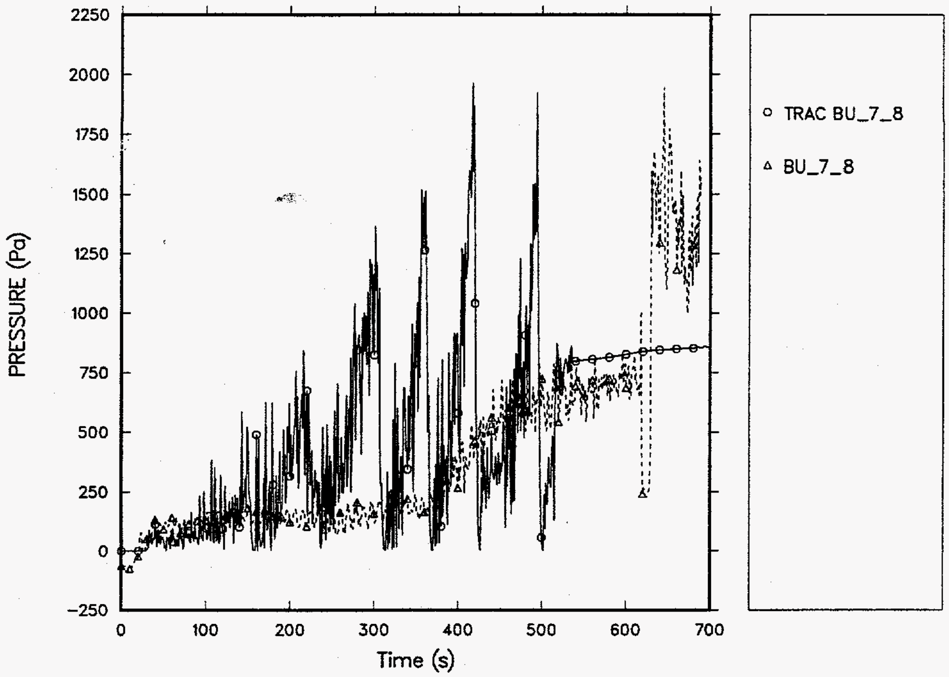

Figure 103. Time-dependent differential pressure from 2.1336 to 2.4384 m (84 to 96 in.) calculated using the Conditional Pedigree coefficients versus the FLECHT-SEASET Run 31504 experimental data.

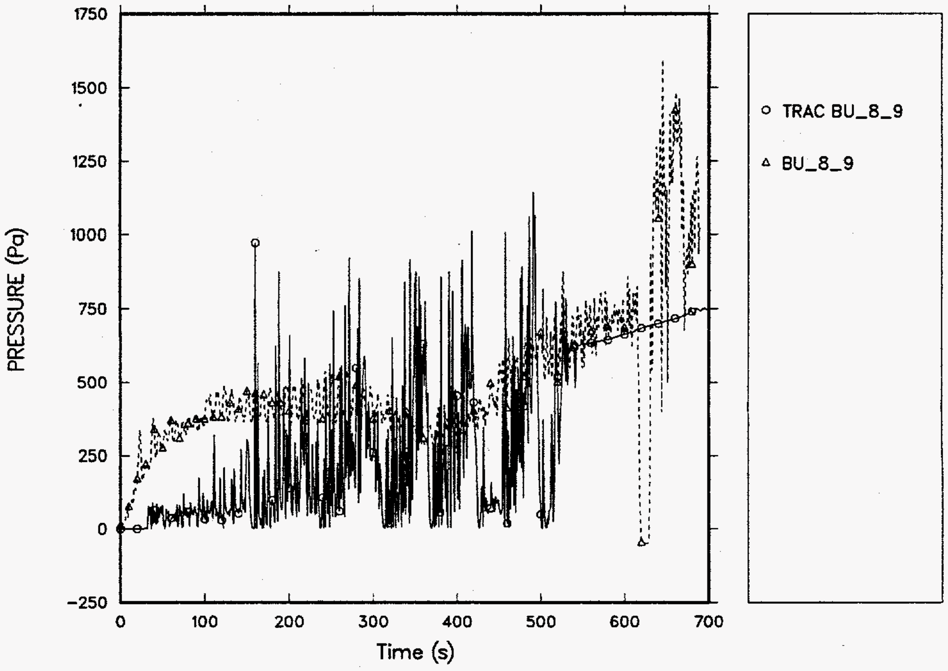

Figure 104. Time-dependent differential pressure from 2.4384 to 2.7432 m (96 to 108 in.) calculated using the Conditional Pedigree coefficients versus the FLECHT-SEASET Run 31504 experimental data.

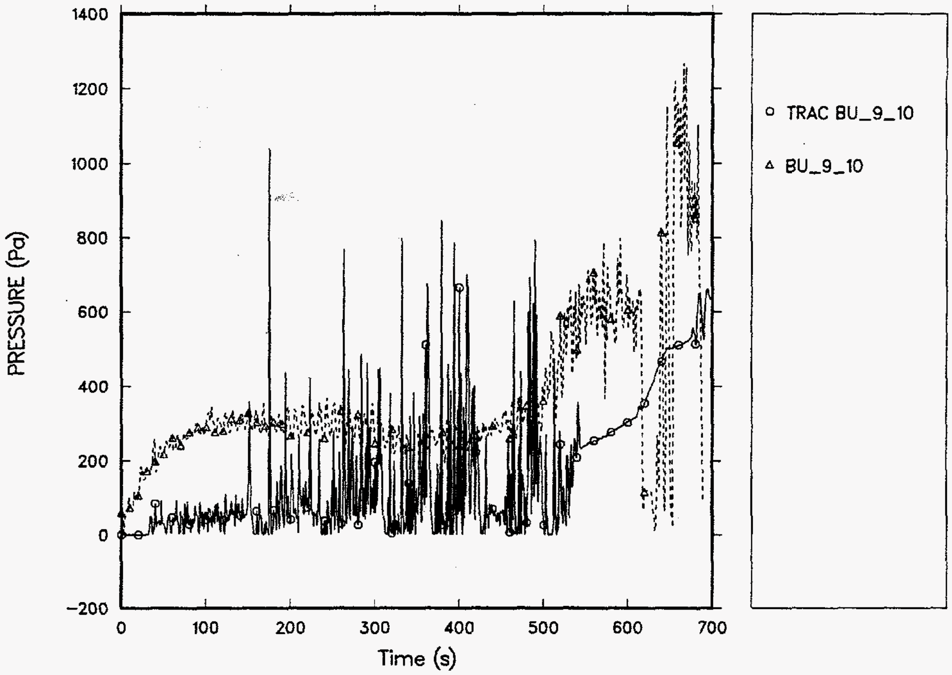

Figure 105. Time-dependent differential pressure from 2.7432 to 3.048 m (108 to 120 in.) calculated using the Conditional Pedigree coefficients versus the FLECHT-SEASET Run 31504 experimental data.

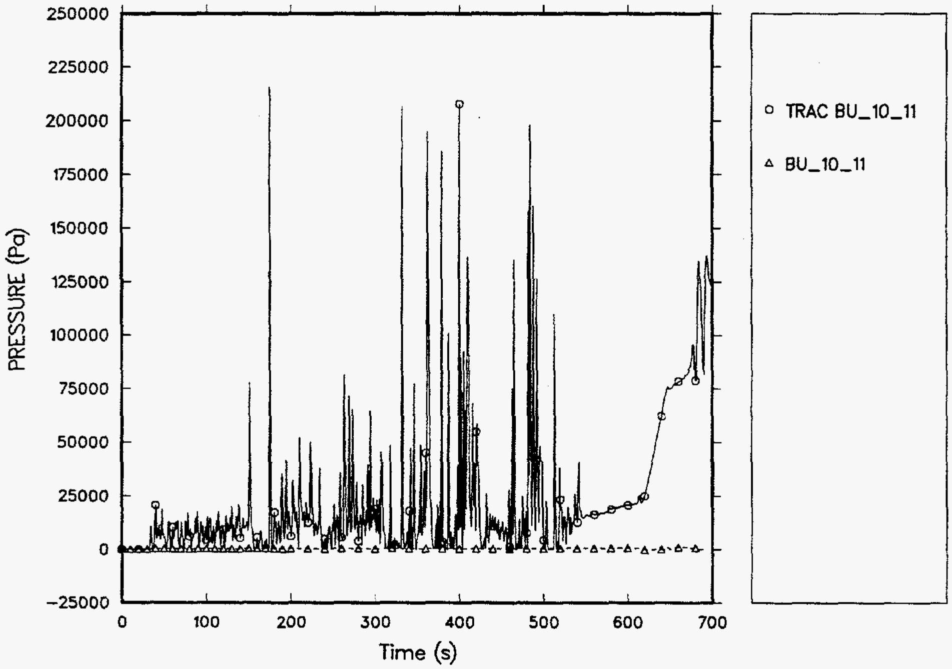

Figure 106. Time-dependent differential pressure from 3.048 to 3.3528 m (120 to 132 in.) calculated using the Conditional Pedigree coefficients versus the FLECHT-SEASET Run 31504 experimental data.

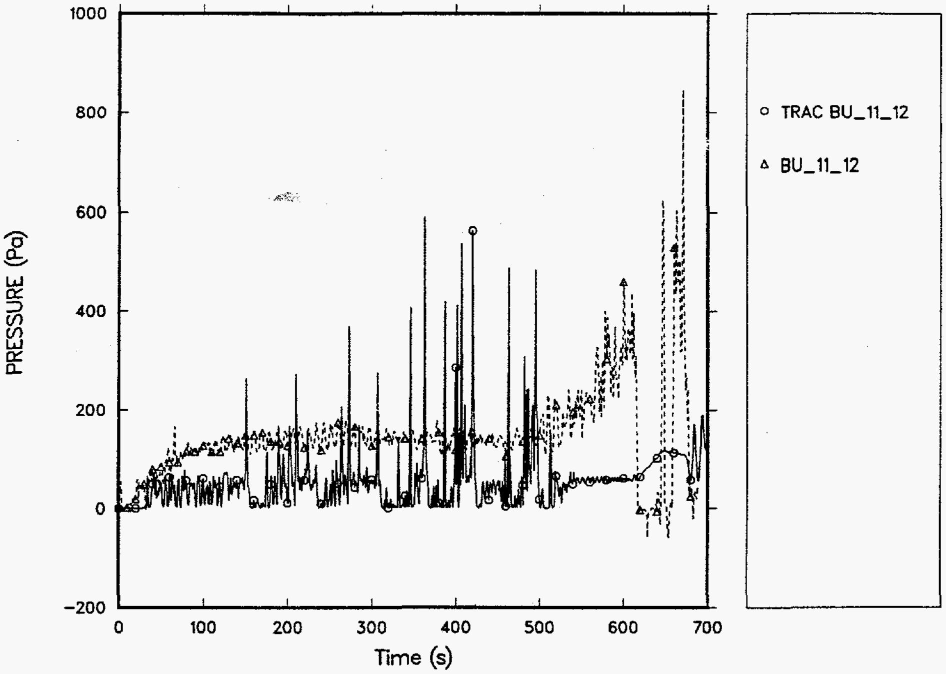

Figure 107. Time-dependent differential pressure from 3.3528 to 3.6576 m (132 to 144 in.) calculated using the Conditional Pedigree coefficients versus the FLECHT-SEASET Run 31504 experimental data.

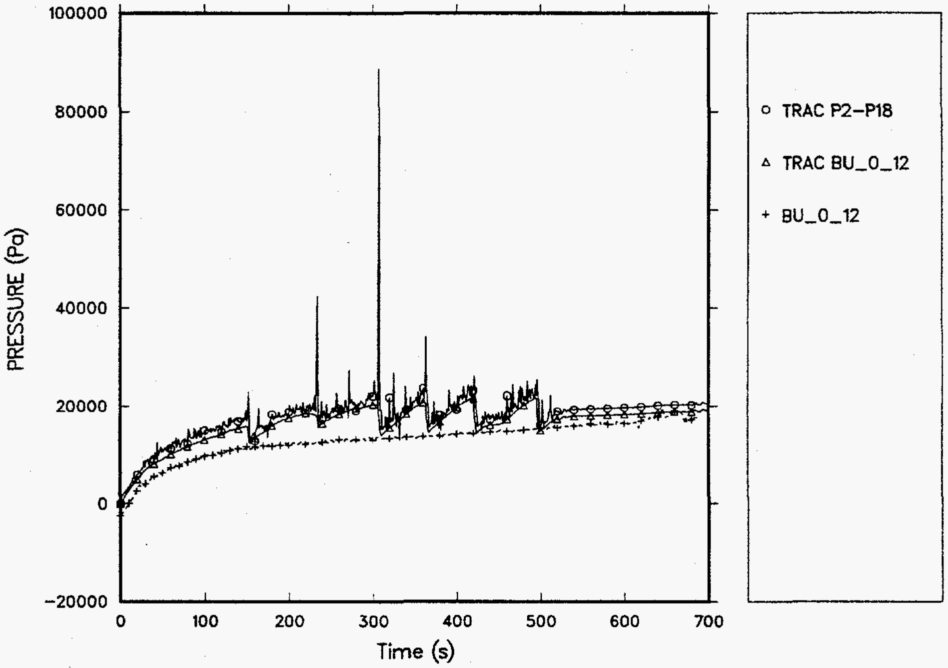

Figure 108. Time-dependent differential pressure from 0 to 3.3528 m (0 to 144 in.) calculated using the Conditional Pedigree coefficients versus the FLECHT-SEASET Run 31504 experimental data.

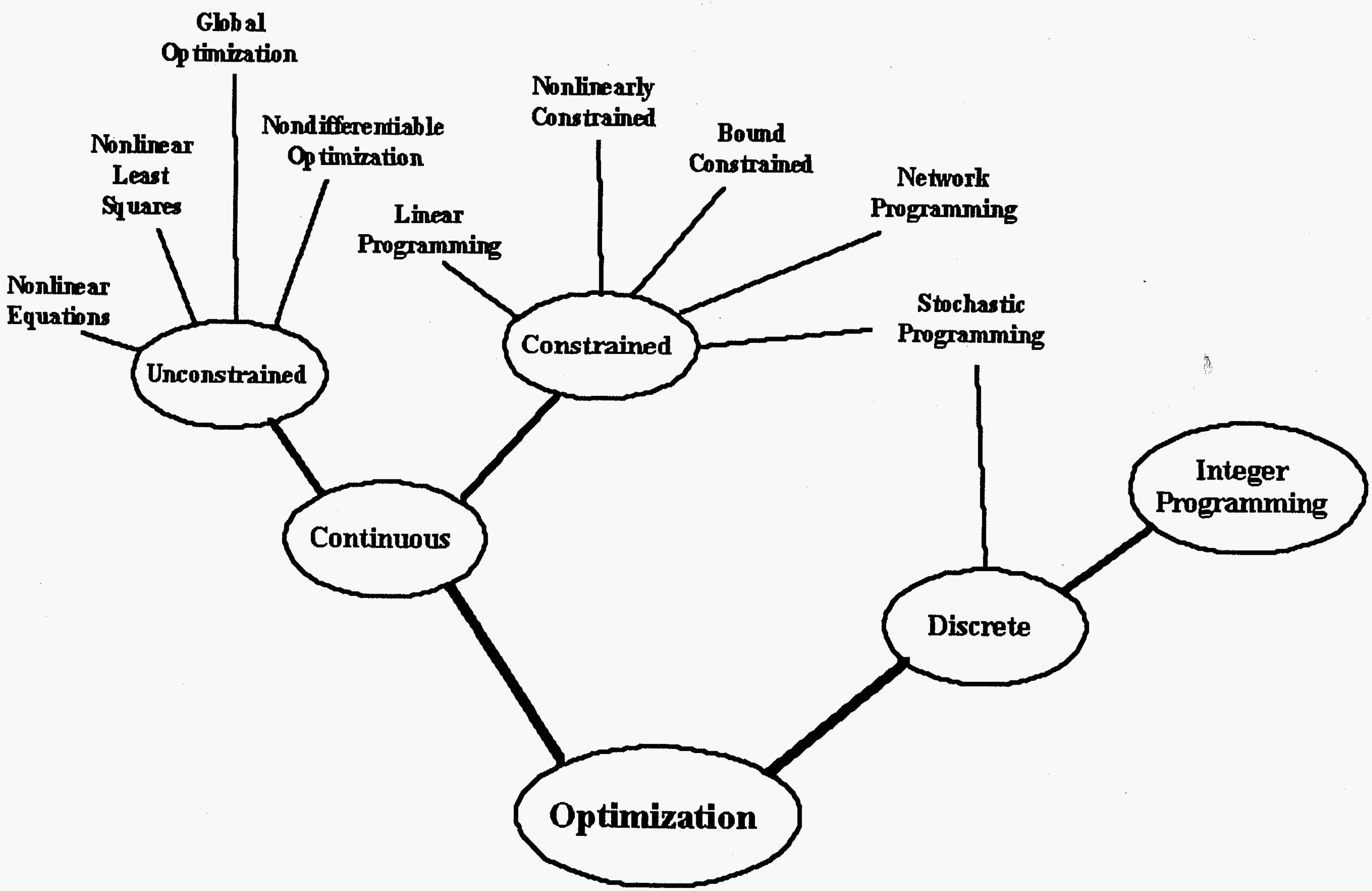

Fig. 109. The "Optimation Tree" showing various optimation techniques and their interrelationships.

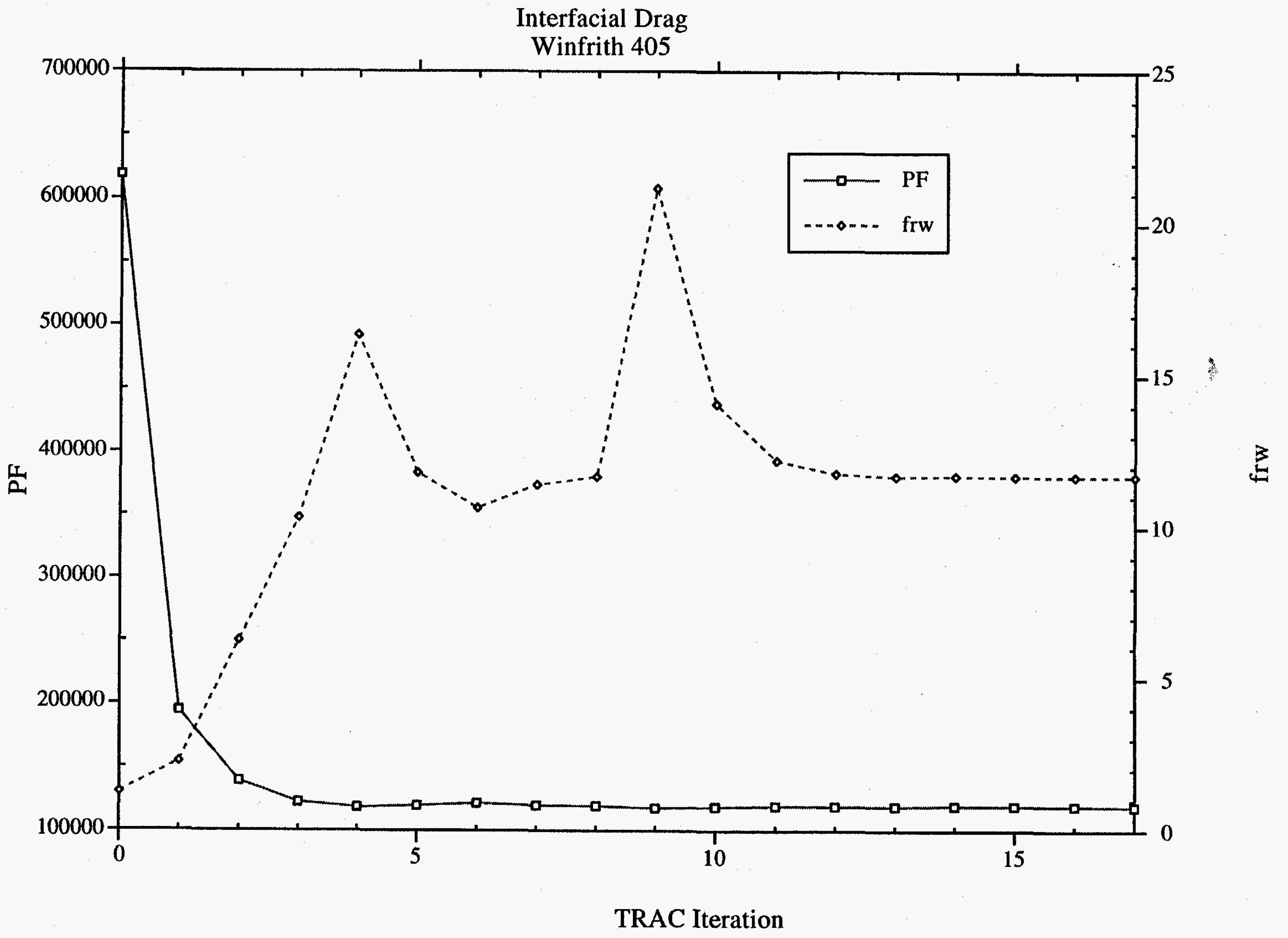

Fig. 110. The penalty function (PF) and coefficient **frw** (Section 4) are shown as functions of each iteration of TRAC using the post-CHF-up-flow data and TRAC input deck for Winfrith Experiment 405 and beginning with the Conditional Pedigree values.

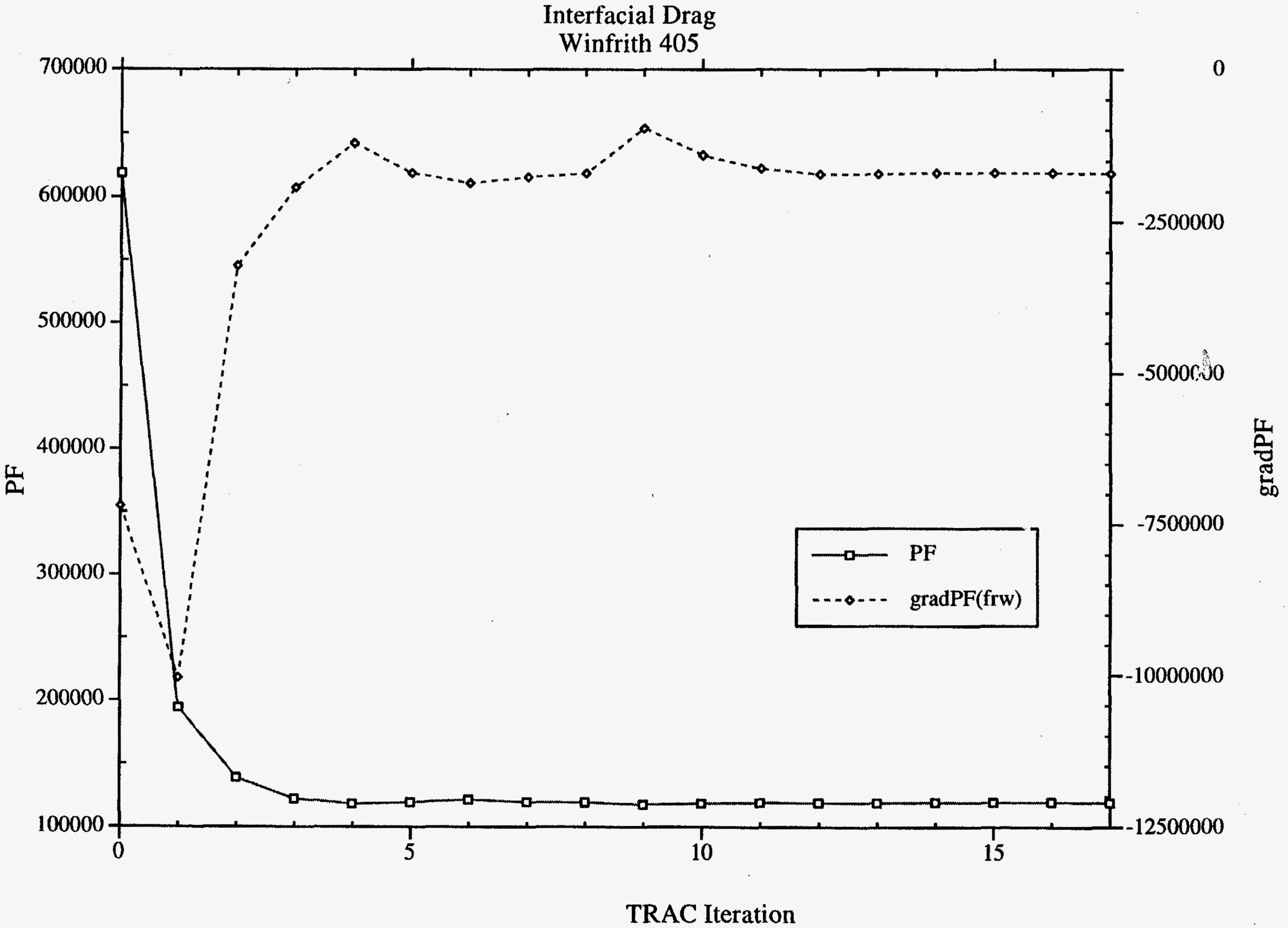

Fig. 111. The partial derivative (gradPF) of the penalty function (PF) with respect to the coefficient **frw** (Section 4) is shown as a function of each iteration of TRAC using the post-CHF-up-flow data and TRAC input deck for Winfrith Experiment 405 and beginning with the Conditional Pedigree values.

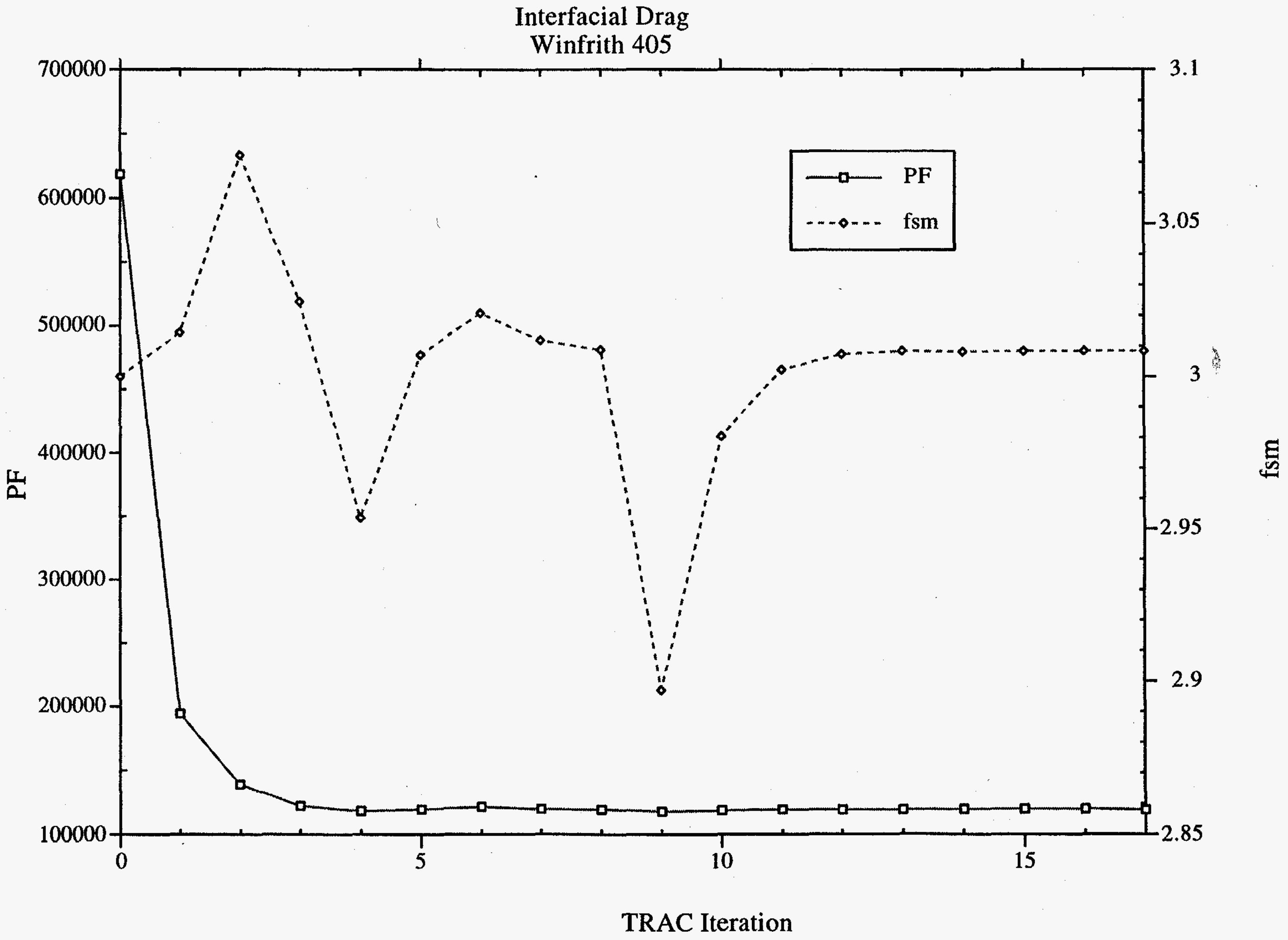

Fig. 112 The penalty function (PF) and coefficient **fsm** (Section 4) are shown as functions of each iteration of TRAC using the post-CHF-up-flow data and TRAC input deck for Winfrith Experiment 405 and beginning with the Conditional Pedigree values.

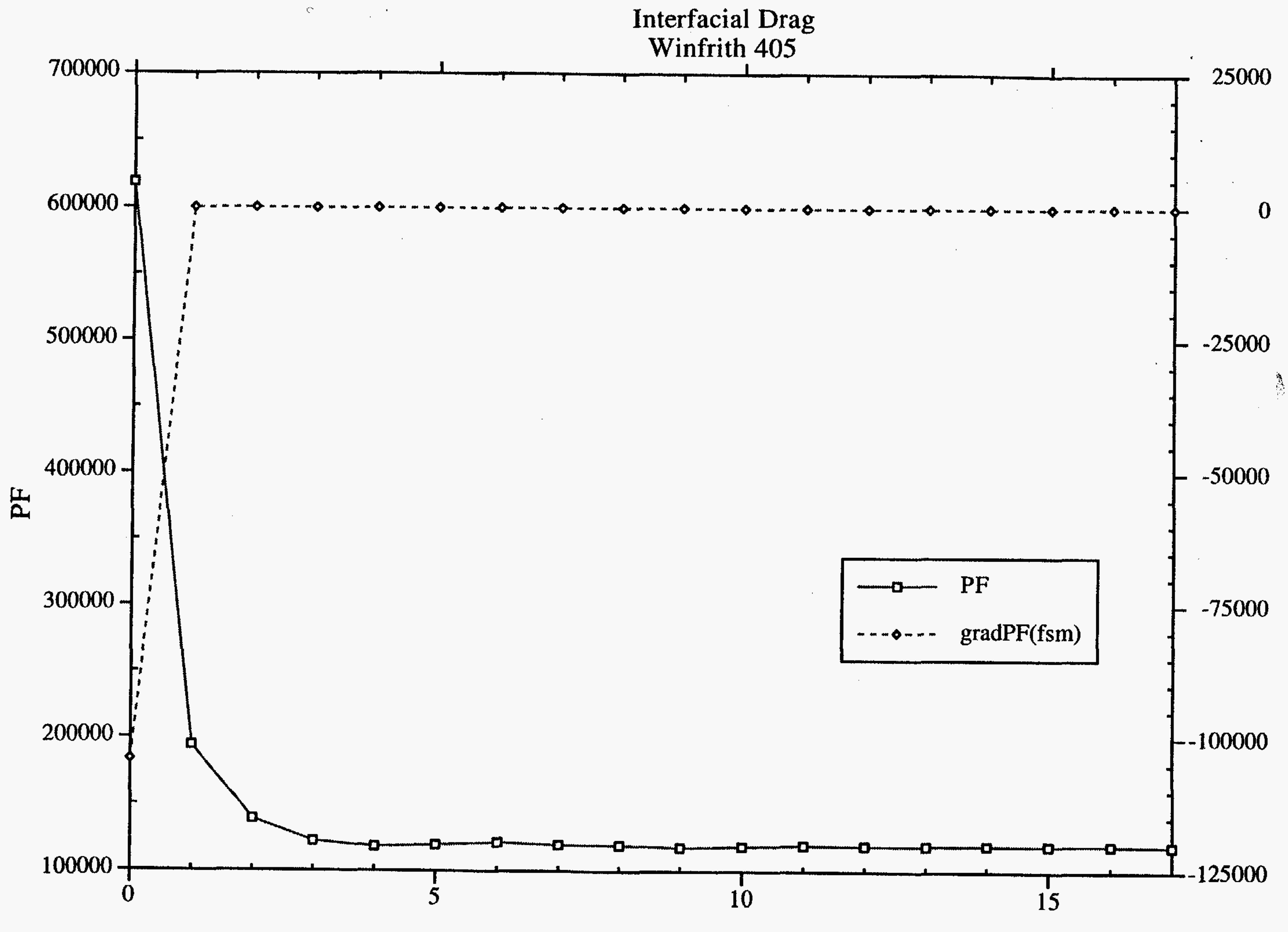

Fig. 113. The partial derivative (gradPF) of the penalty function (PF) with respect to the coefficient **fsm** (Section 4) is shown as a function of each iteration of TRAC using the post-CHF-up-flow data and TRAC input deck for Winfrith Experiment 405 and beginning with the Conditional Pedigree values.

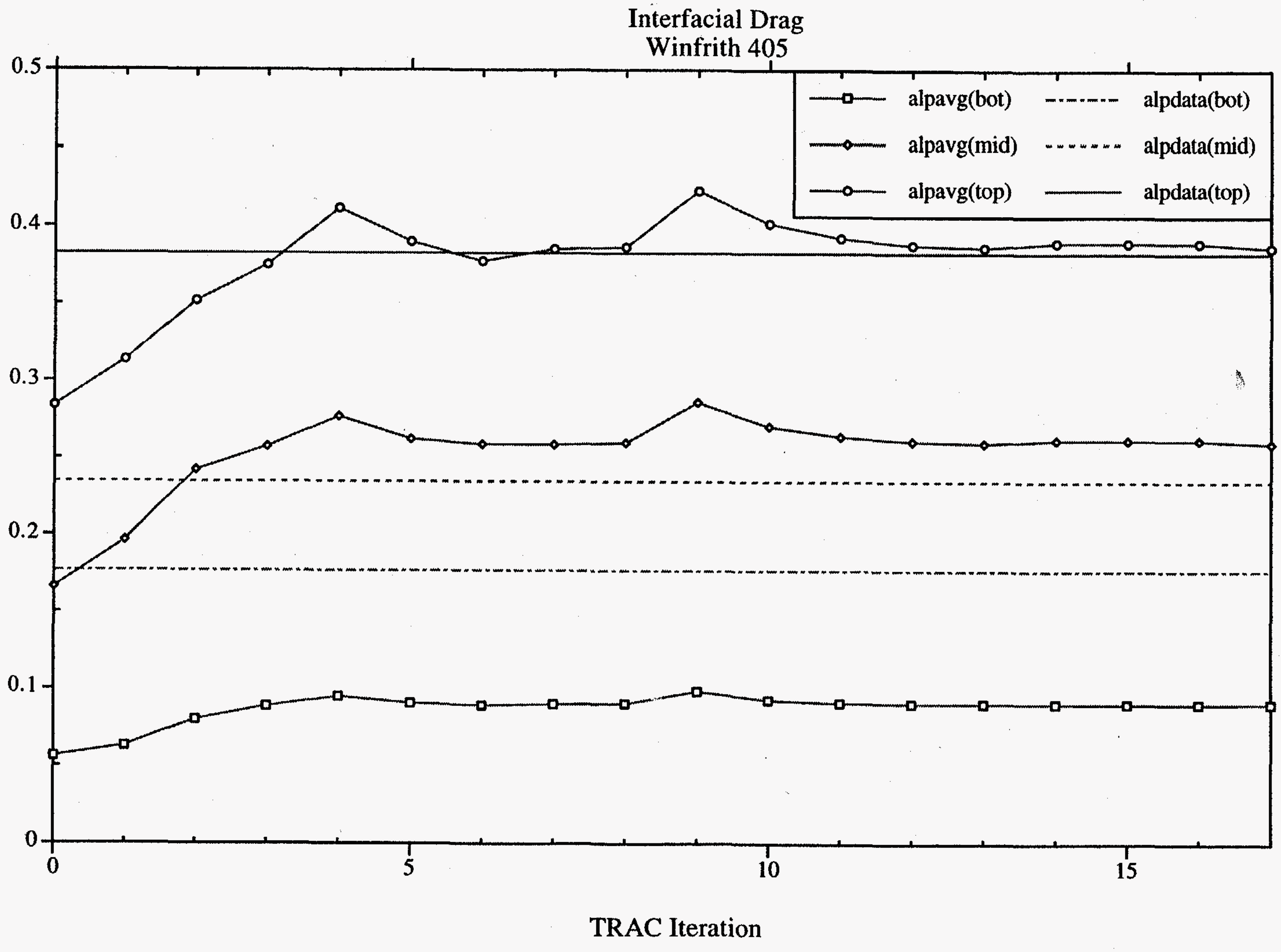

Fig. 114. The void fraction corresponding to the experimental measurement elevation(s) is shown as a function of each iteration of TRAC as the coefficients **frw** and **fsm** (Section 4) are tuned using the post-CHF-up-flow data and TRAC input deck for Winfrith Experiment 405 and beginning with the Conditional Pedigree values.

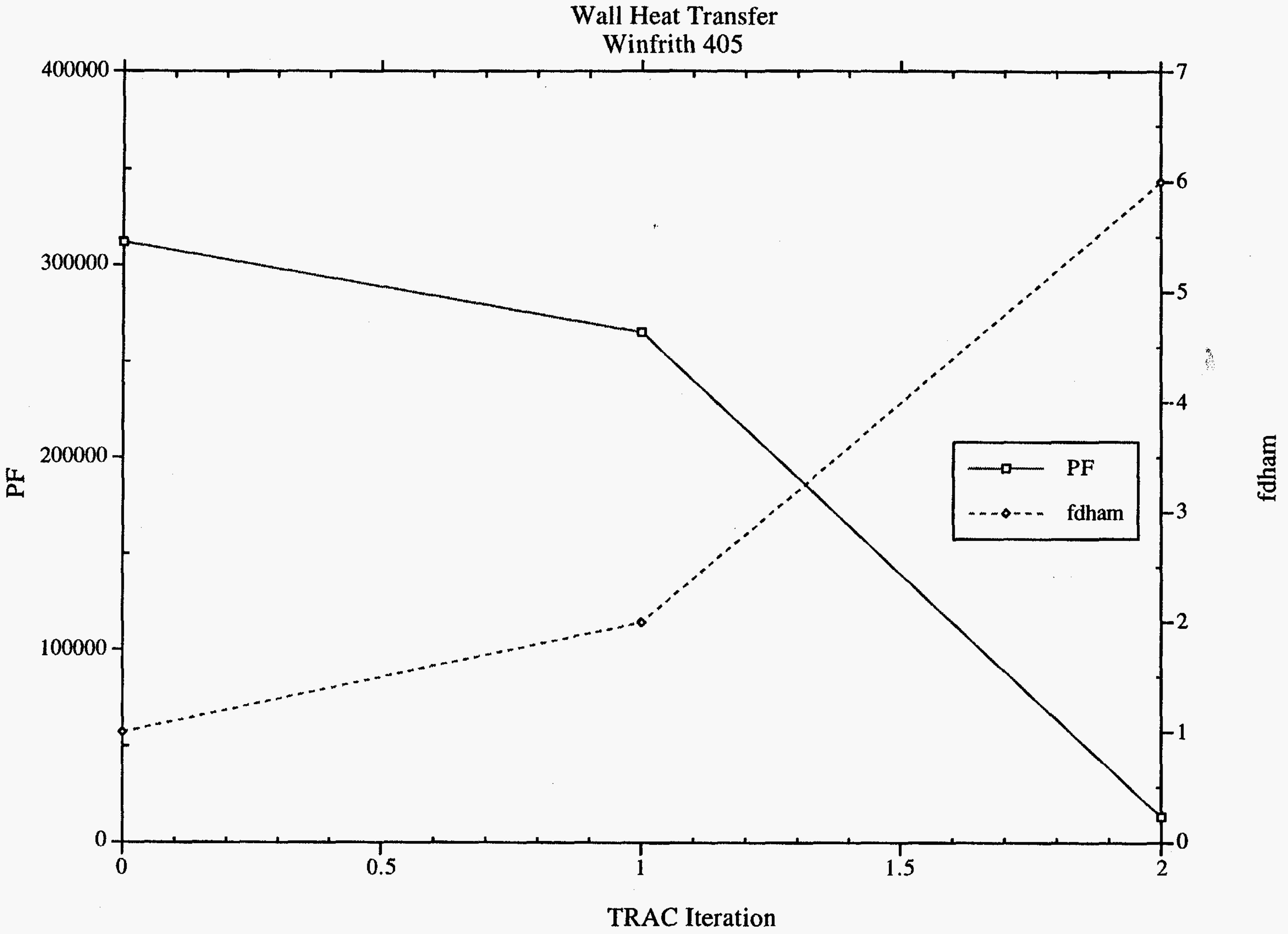

Fig. 115. The penalty function (PF) and coefficient **fdham** (Section 4) are shown as functions of each iteration of TRAC using the post-CHF-up-flow data and TRAC input deck for Winfrith Experiment 405 and beginning with the Conditional Pedigree values.

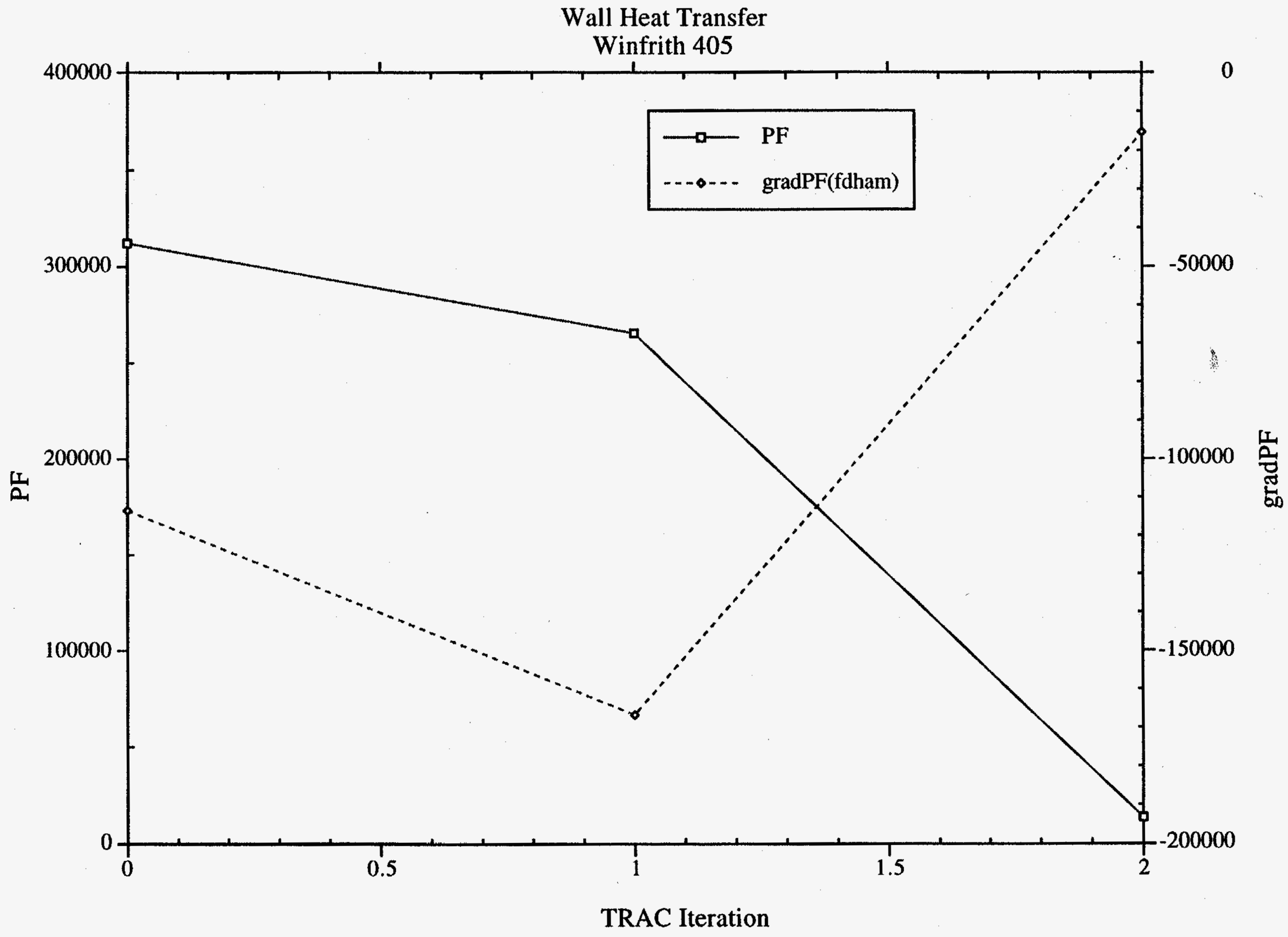

Fig. 116. The partial derivative (gradPF) of the penalty function (PF) with respect to the coefficient **fdham** (Section 4) is shown as a function of each iteration of TRAC using the post-CHF-up-flow data and TRAC input deck for Winfrith Experiment 405 and beginning with the Conditional Pedigree values.

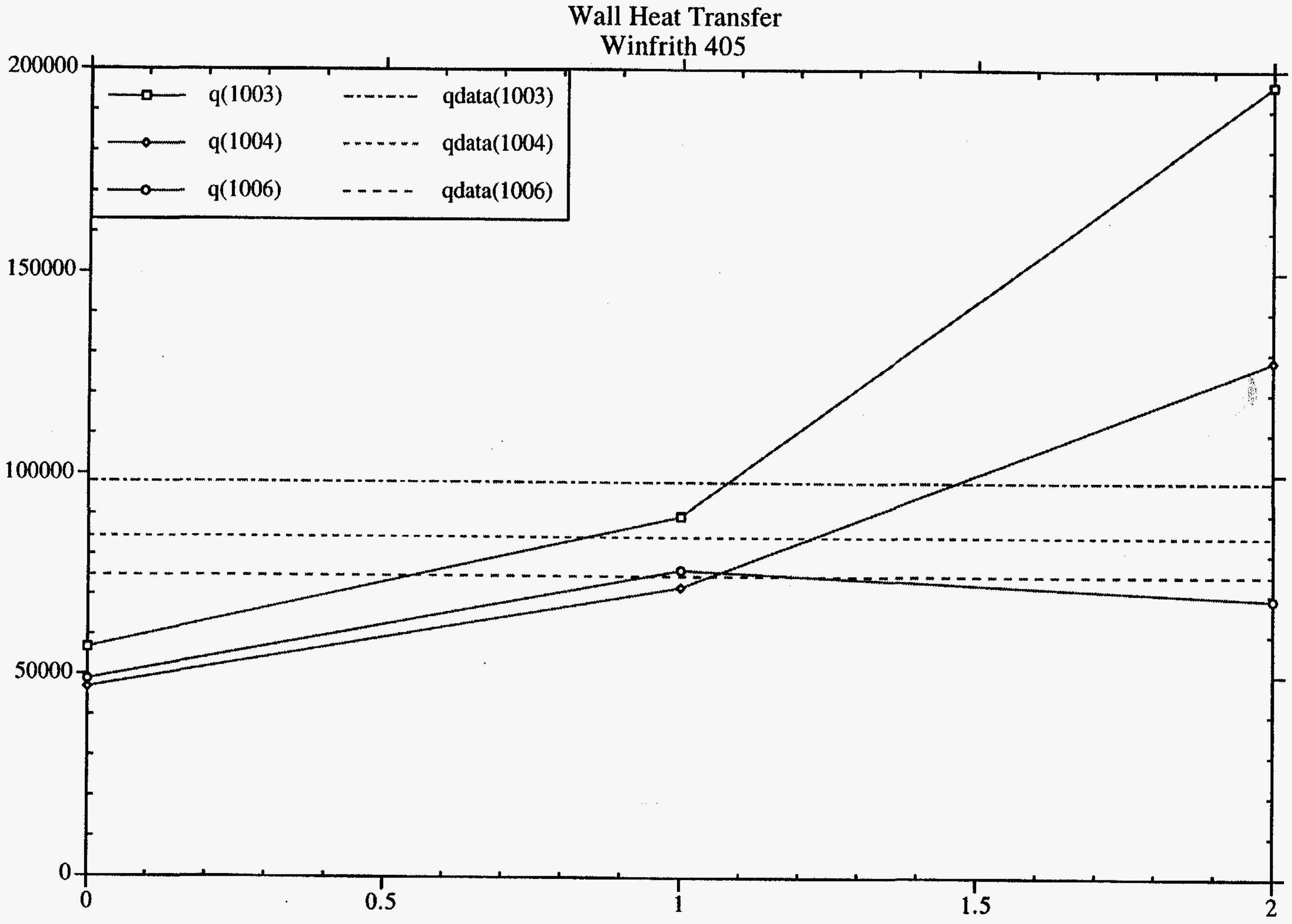

Fig. 117. The wall heat transfer corresponding to the experimental measurement elevation(s) is shown as a function of each iteration of TRAC as the coefficient **fdham** (Section 4) is tuned using the post-CHF-up-flow data and TRAC input deck for Winfrith Experiment 405 and beginning with the Conditional Pedigree values (plot 1 of 4).

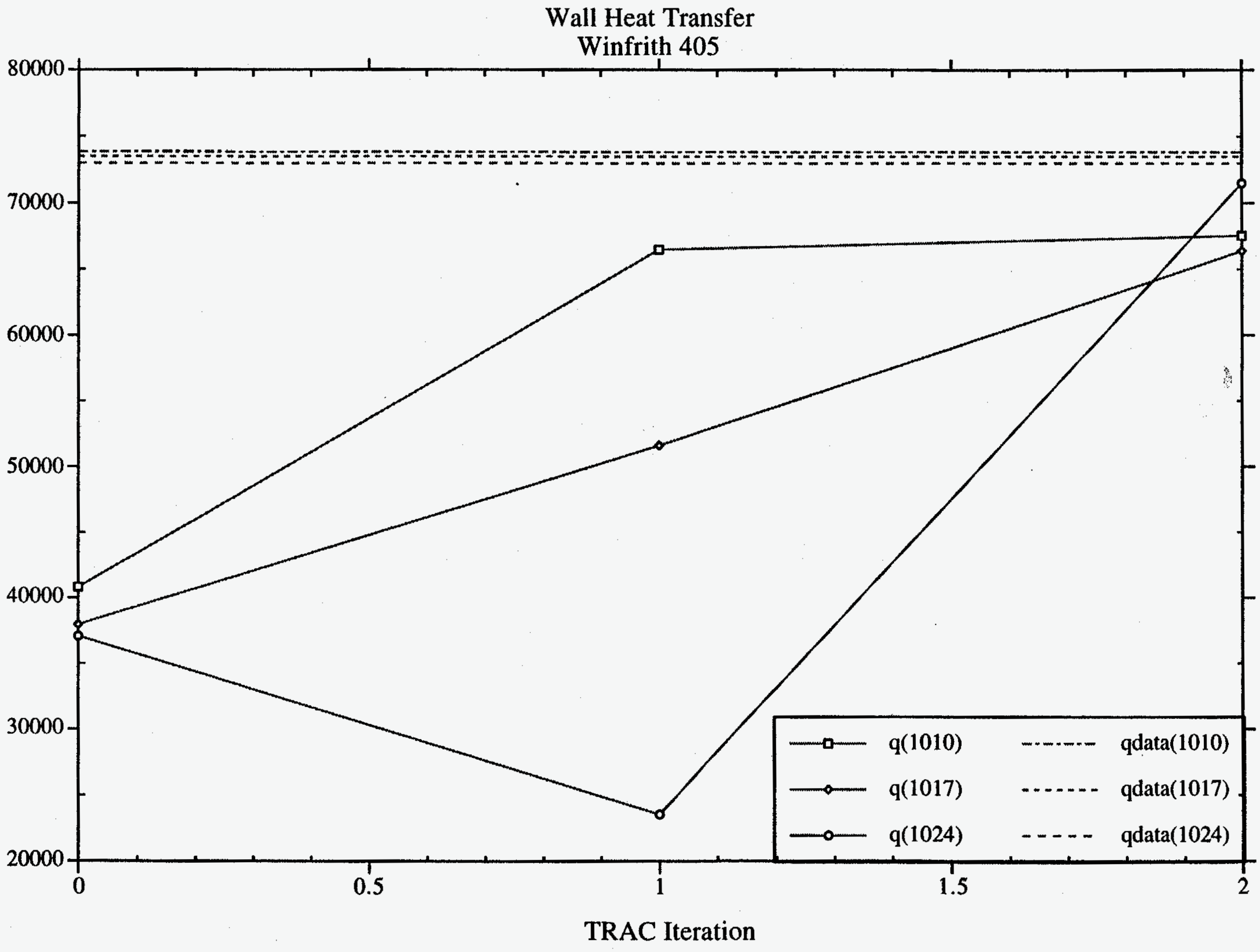

Fig. 118. The wall heat transfer corresponding to the experimental measurement elevation(s) is shown as a function of each iteration of TRAC as the coefficient **fdham** (Section 4) is tuned using the post-CHF-up-flow data and TRAC input deck for Winfrith Experiment 405 and beginning with the Conditional Pedigree values (plot 2 of 4).

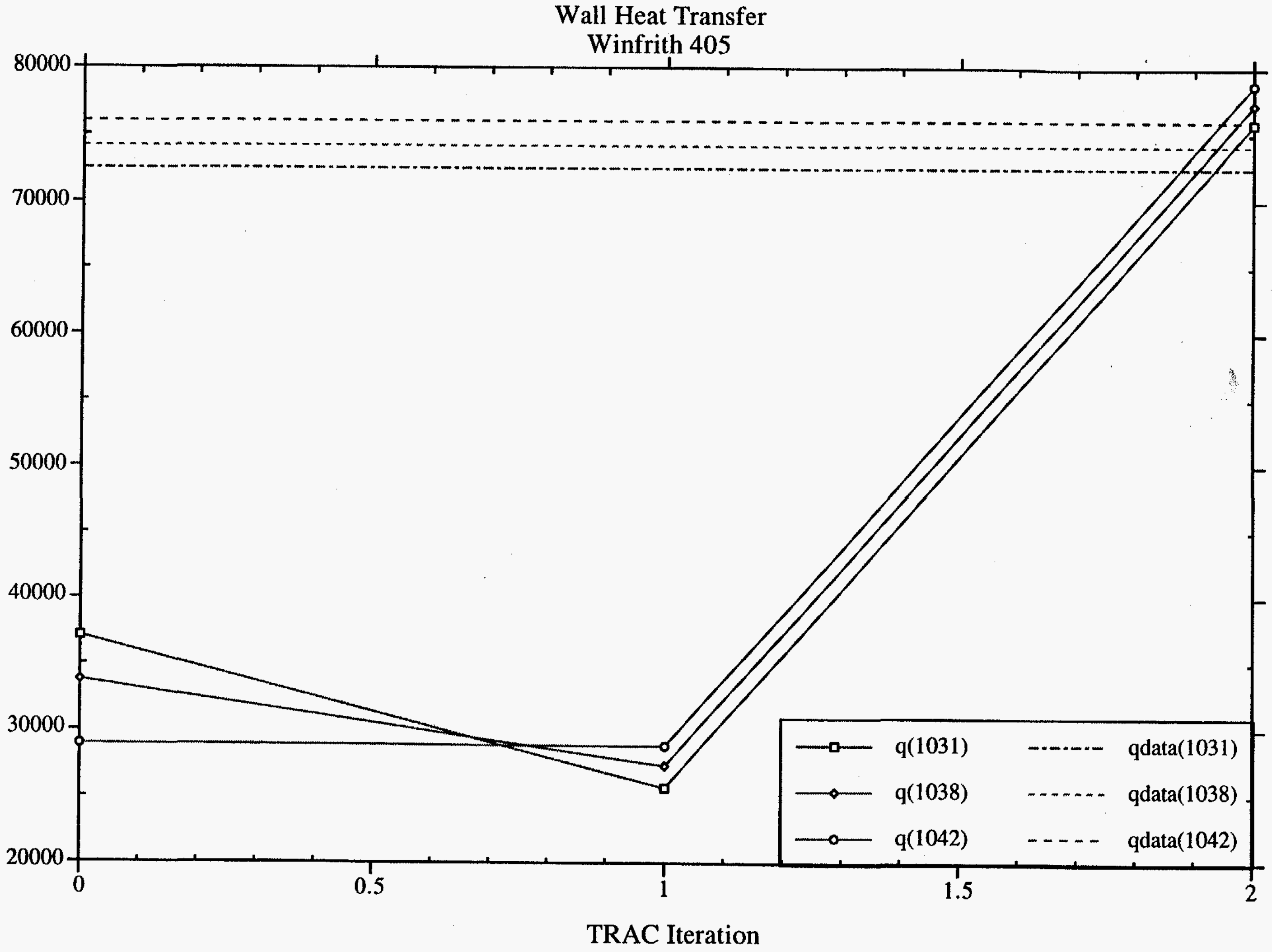

Fig. 119. The wall heat transfer corresponding to the experimental measurement elevation(s) is shown as a function of each iteration of TRAC as the coefficient **fdham** (Section 4) is tuned using the post-CHF-up-flow data and TRAC input deck for Winfrith Experiment 405 and beginning with the Conditional Pedigree values (plot 3 of 4).

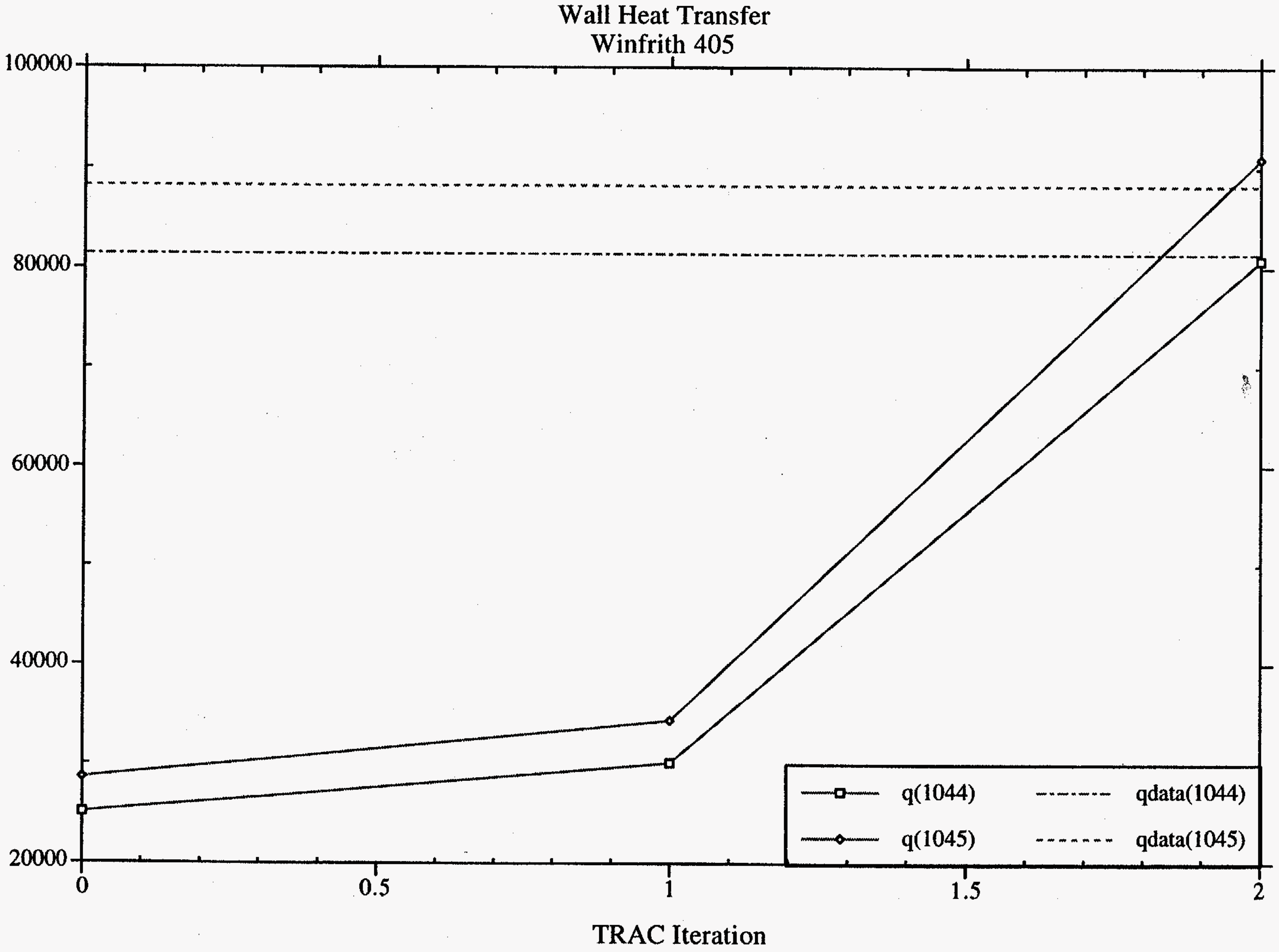

Fig. 120. The wall heat transfer corresponding to the experimental measurement elevation(s) is shown as a function of each iteration of TRAC as the coefficient **fdham** (Section 4) is tuned using the post-CHF-up-flow data and TRAC input deck for Winfrith Experiment 405 and beginning with the Conditional Pedigree values (plot 4 of 4).

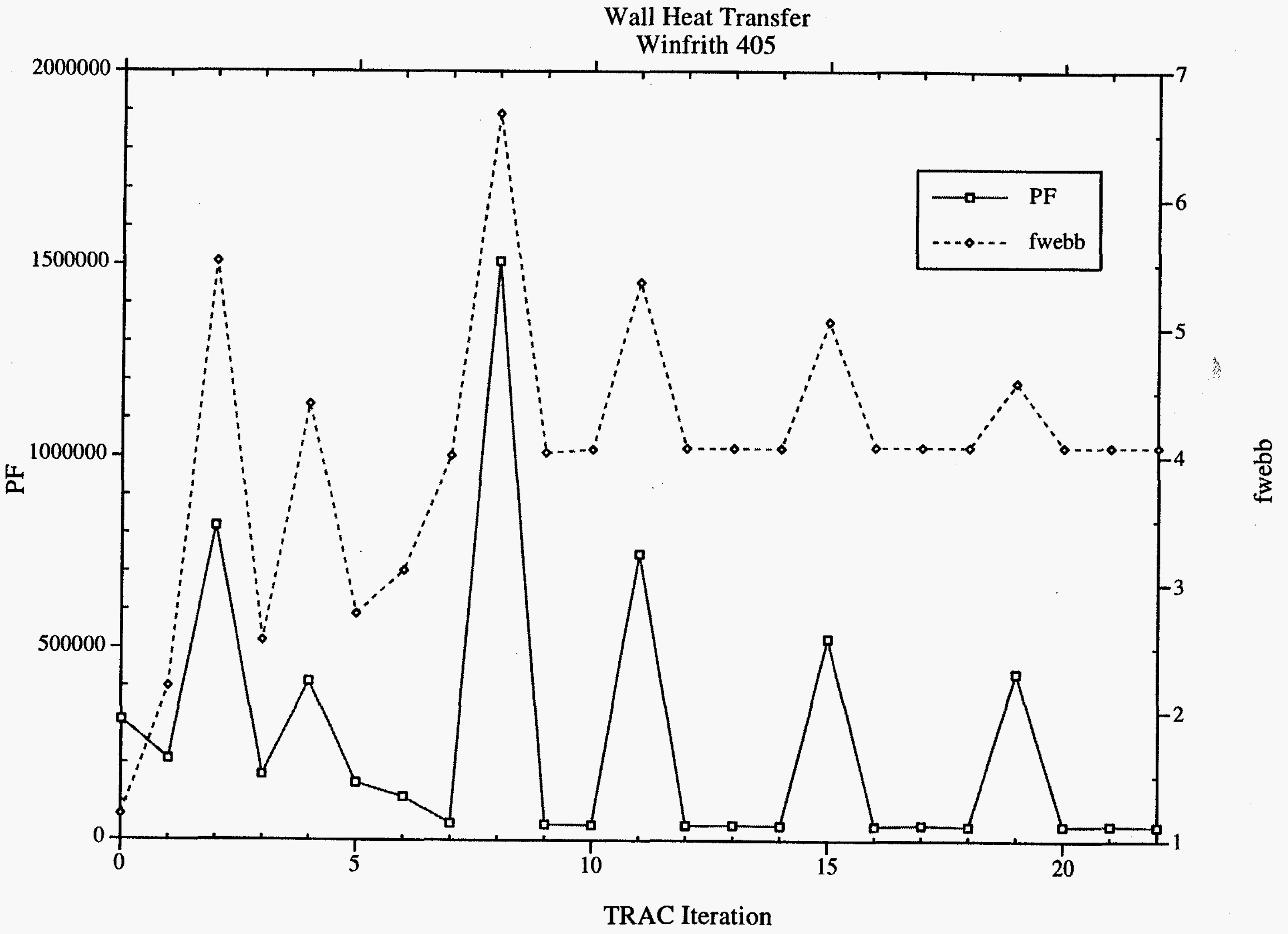

Fig. 121. The penalty function (PF) and coefficient **fwebb** (Section 4) are shown as functions of each iteration of TRAC using the post-CHF-up-flow data and TRAC input deck for Winfrith Experiment 405 and beginning with the Conditional Pedigree values.

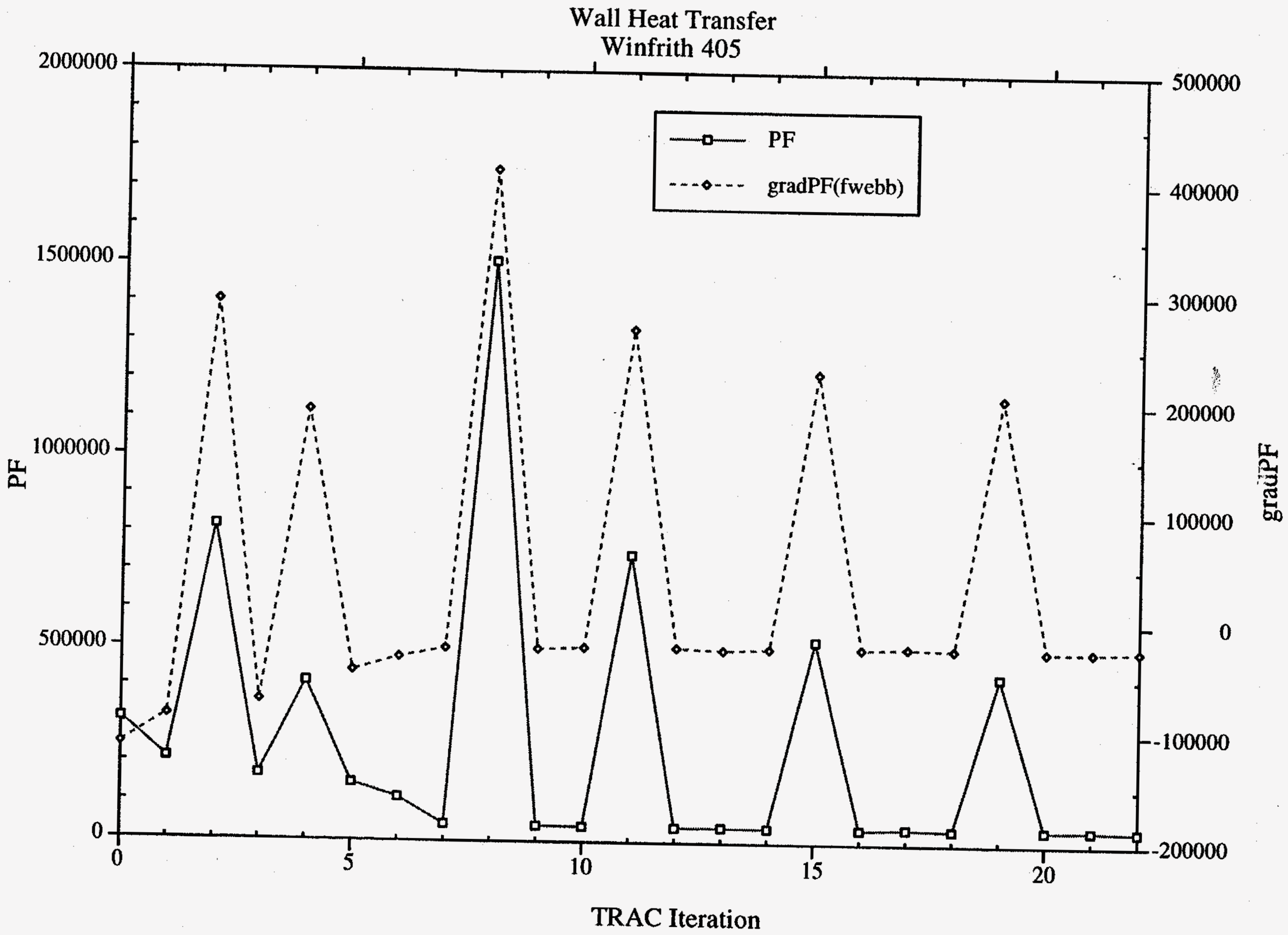

Fig. 122. The partial derivative (gradPF) of the penalty function (PF) with respect to the coefficient **fwebb** (Section 4) is shown as a function of each iteration of TRAC using the post-CHF-up-flow data and TRAC input deck for Winfrith Experiment 405 and beginning with the Conditional Pedigree values.

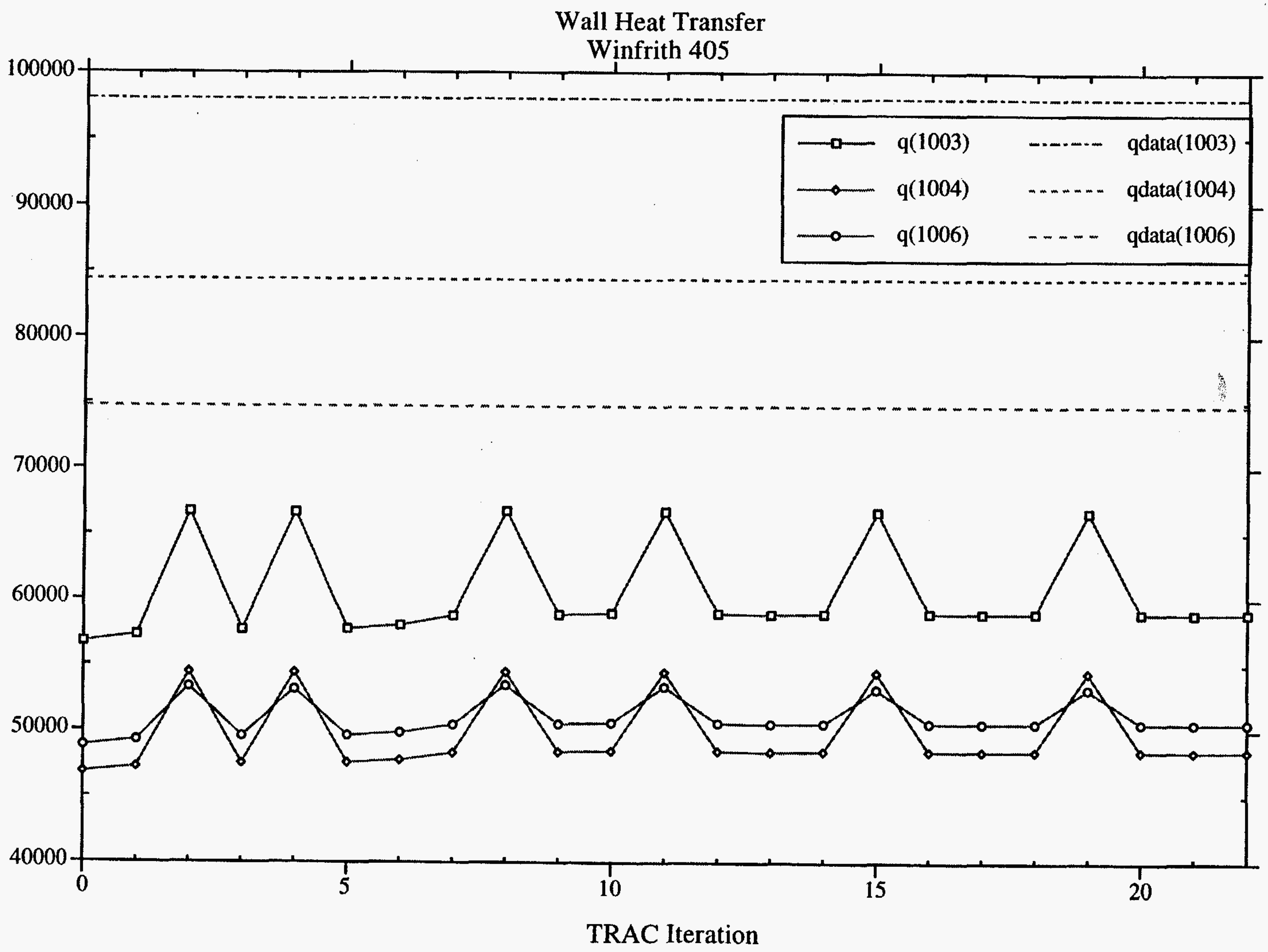

Fig. 123. The wall heat transfer corresponding to the experimental measurement elevation(s) is shown as a function of each iteration of TRAC as the coefficient **fwebb** (Section 4) is tuned using the post-CHF-up-flow data and TRAC input deck for Winfrith Experiment 405 and beginning with the Conditional Pedigree values (plot 1 of 4).

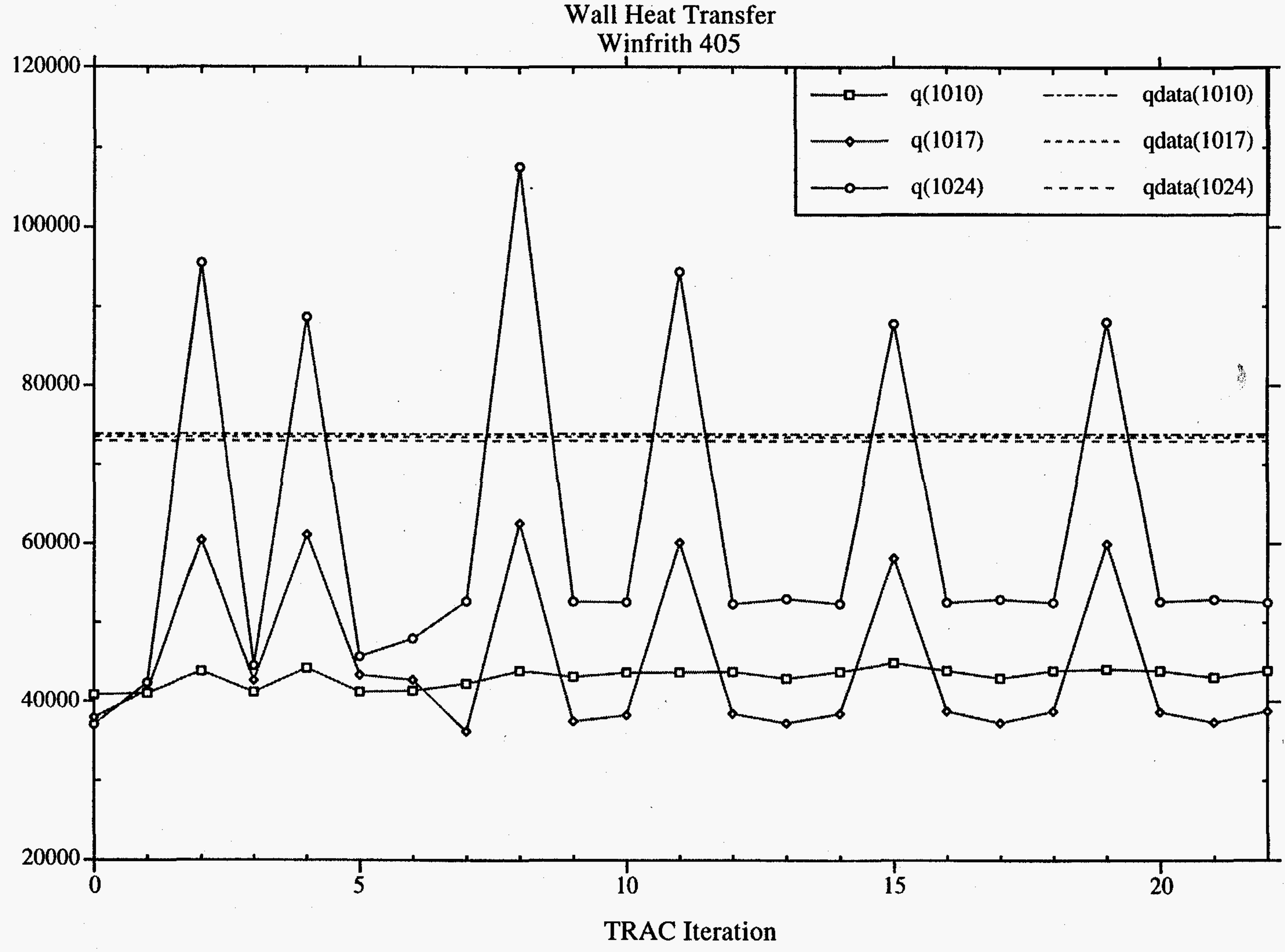

Fig. 124. The wall heat transfer corresponding to the experimental measurement elevation(s) is shown as a function of each iteration of TRAC as the coefficient **fwebb** (Section 4) is tuned using the post-CHF-up-flow data and TRAC input deck for Winfrith Experiment 405 and beginning with the Conditional Pedigree values (plot 2 of 4).

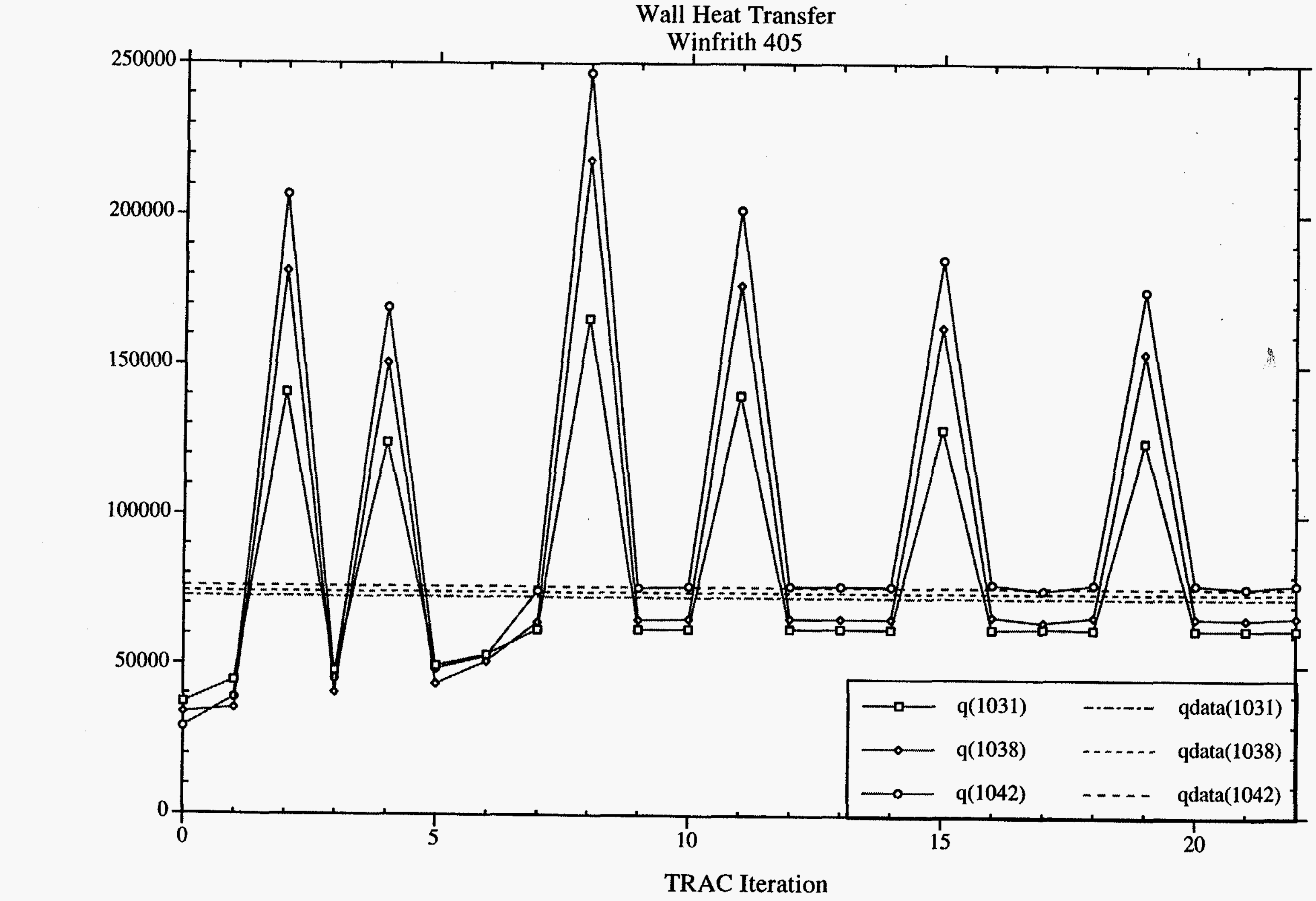

Fig. 125. The wall heat transfer corresponding to the experimental measurement elevation(s) is shown as a function of each iteration of TRAC as the coefficient **fwebb** (Section 4) is tuned using the post-CHF-up-flow data and TRAC input deck for Winfrith Experiment 405 and beginning with the Conditional Pedigree values (plot 3 of 4).

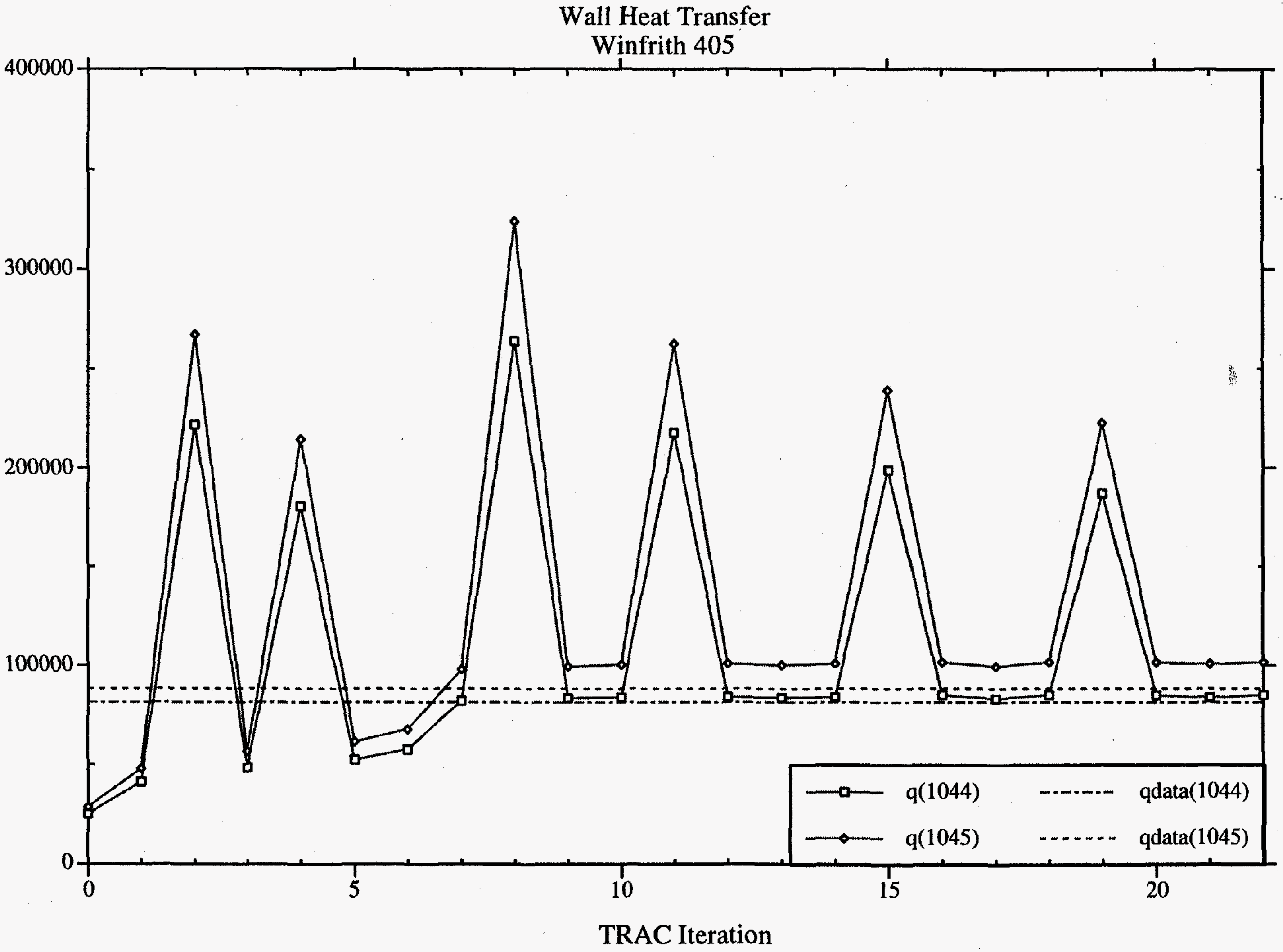

Fig. 126. The wall heat transfer corresponding to the experimental measurement elevation(s) is shown as a function of each iteration of TRAC as the coefficient **fwebb** (Section 4) is tuned using the post-CHF-up-flow data and TRAC input deck for Winfrith Experiment 405 and beginning with the Conditional Pedigree values (plot 4 of 4).

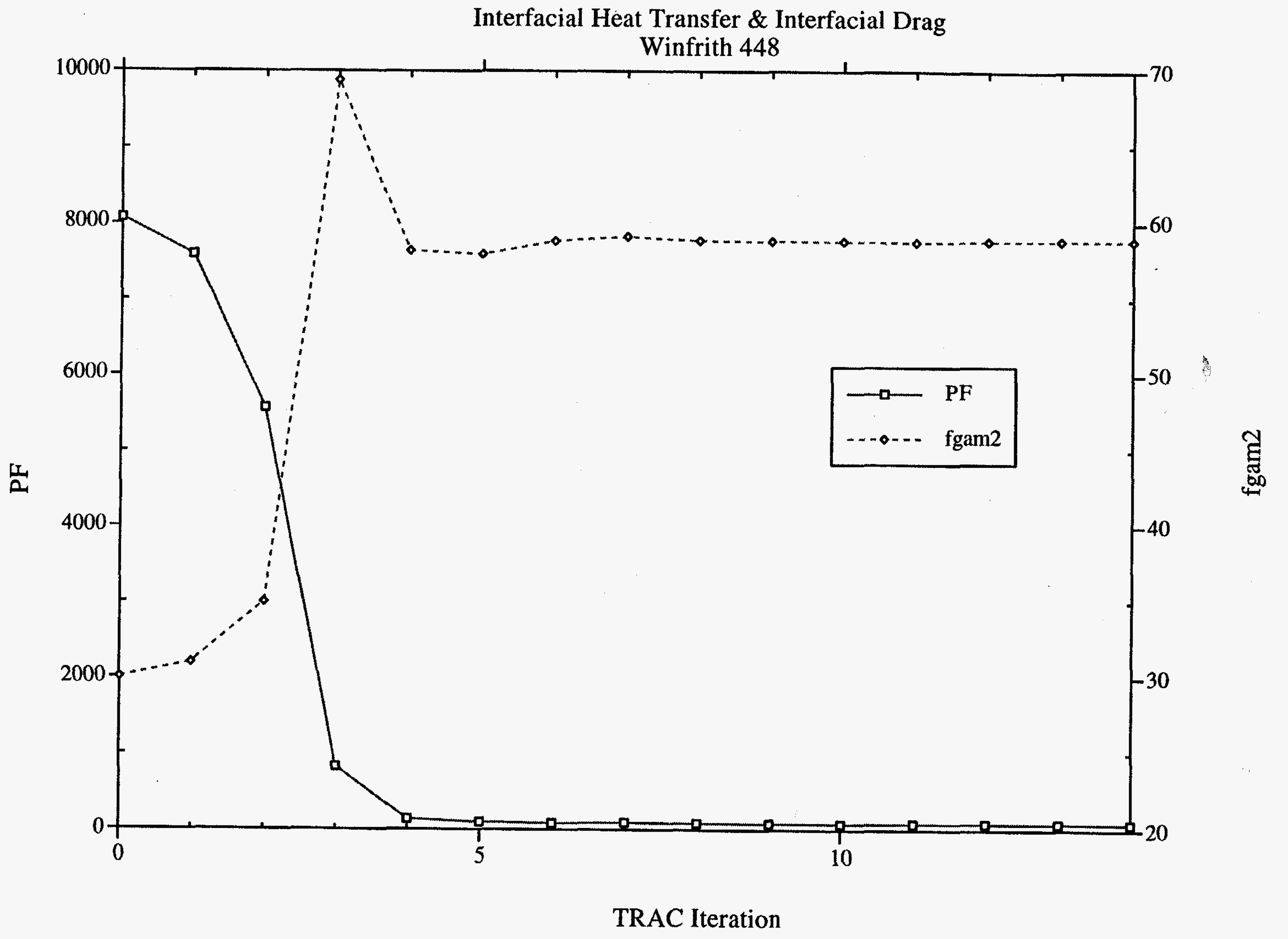

Fig. 127. The penalty function (PF) and coefficient **fgam2** (Section 4) are shown as functions of each iteration of TRAC using the post-CHF-up-flow data and TRAC input deck for Winfrith Experiment 448 and beginning with the Conditional Pedigree values.

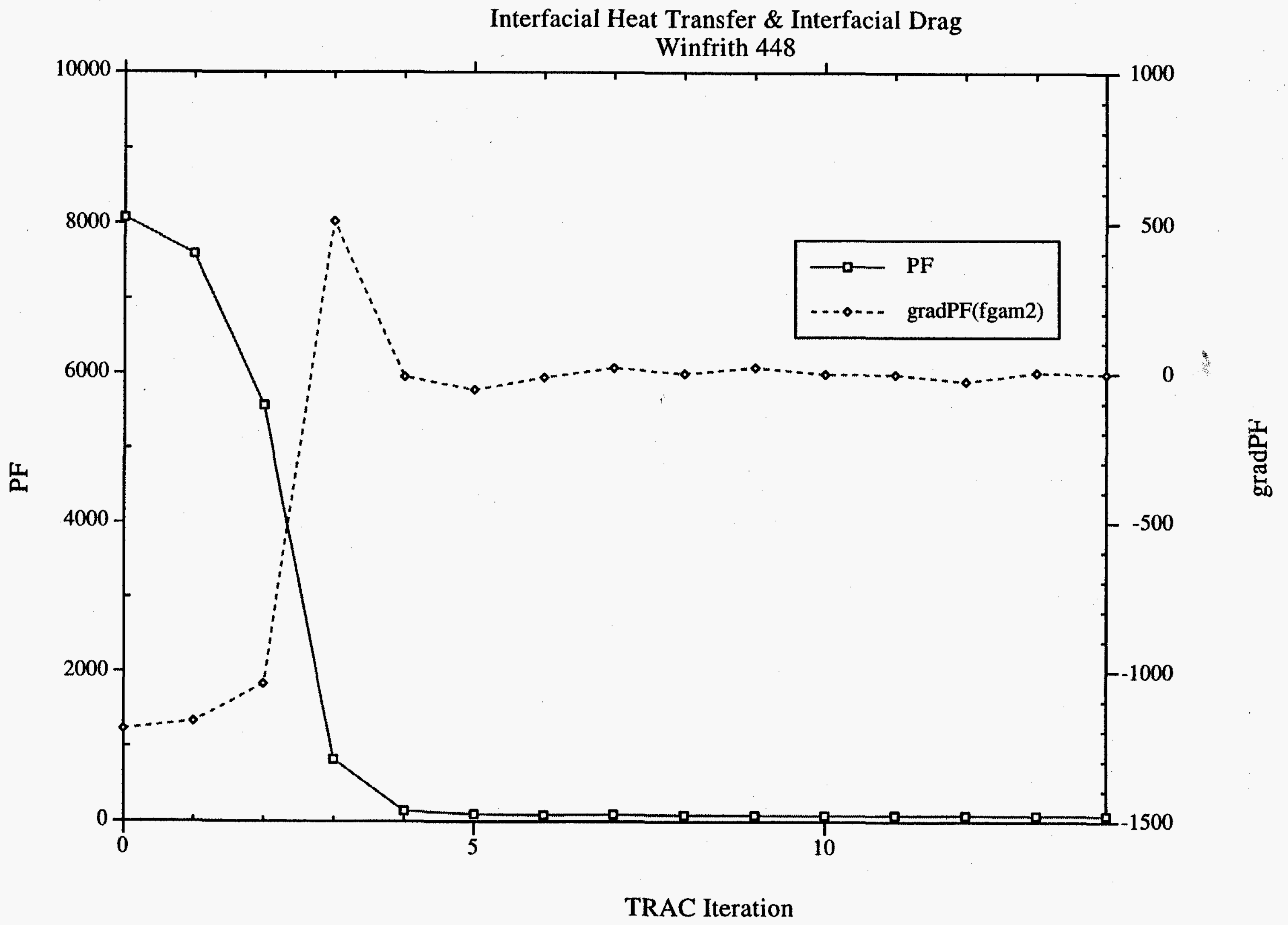

Fig. 128. The partial derivative (gradPF) of the penalty function (PF) with respect to the coefficient **fgam2** (Section 4) is shown as a function of each iteration of TRAC using the post-CHF-up-flow data and TRAC input deck for Winfrith Experiment 448 and beginning with the Conditional Pedigree values.

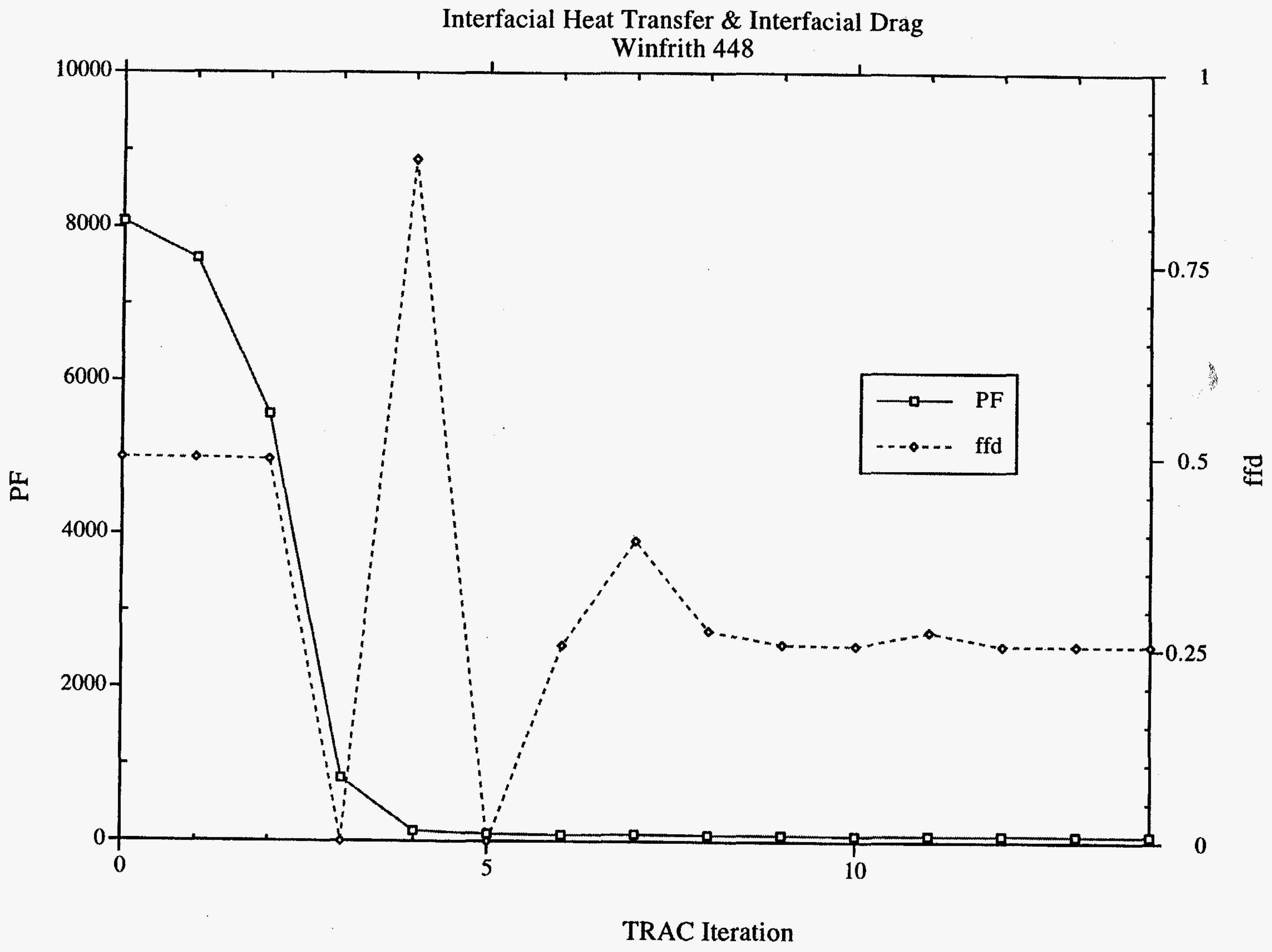

Fig. 129. The penalty function (PF) and coefficient **ffd** (Section 4) are shown as functions of each iteration of TRAC using the post-CHF-up-flow data and TRAC input deck for Winfrith Experiment 448 and beginning with the Conditional Pedigree values.

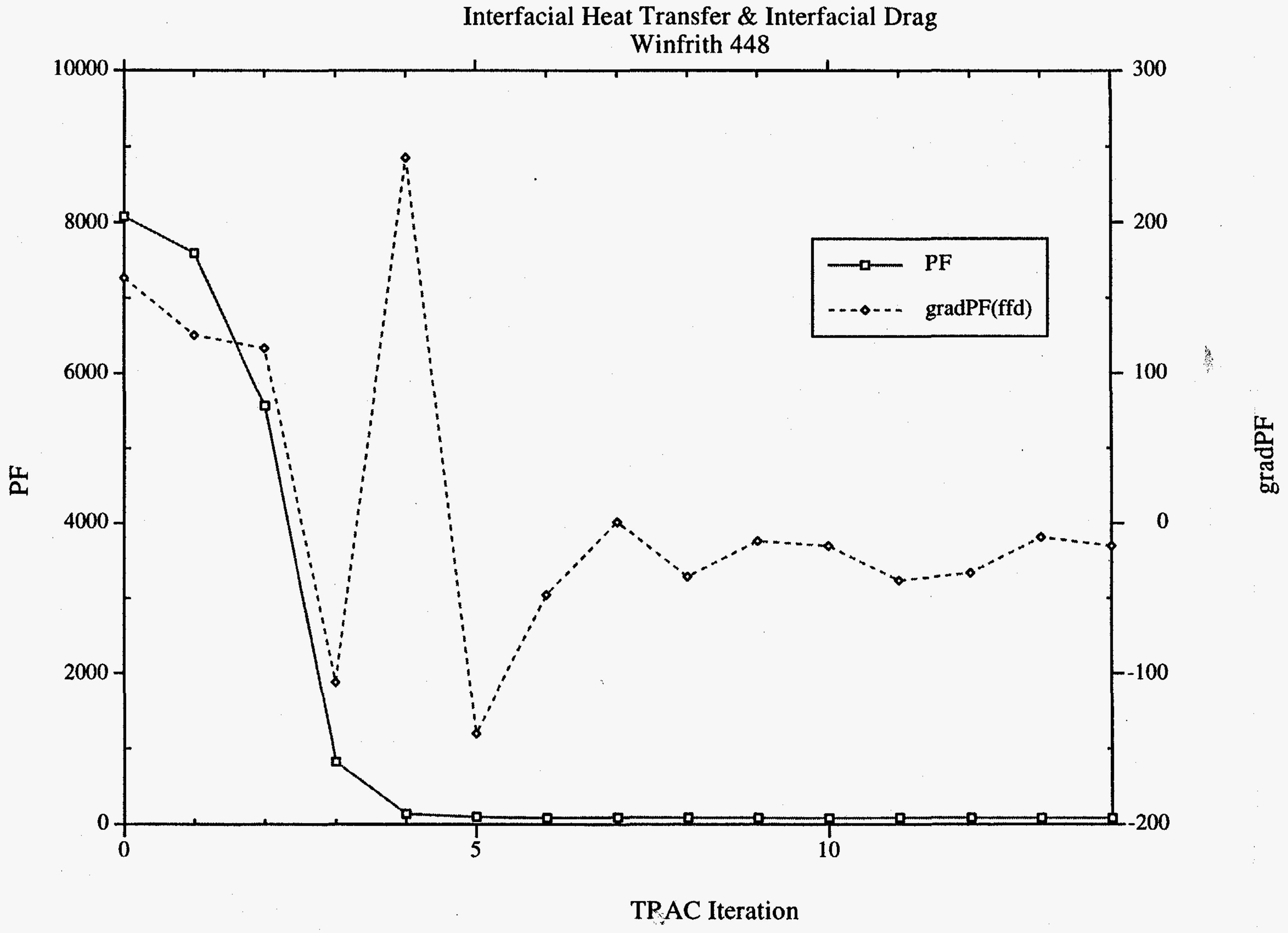

Fig. 130. The partial derivative (gradPF) of the penalty function (PF) with respect to the coefficient **ffd** (Section 4) is shown as a function of each iteration of TRAC using the post-CHF-up-flow data and TRAC input deck for Winfrith Experiment 448 and beginning with the Conditional Pedigree values.

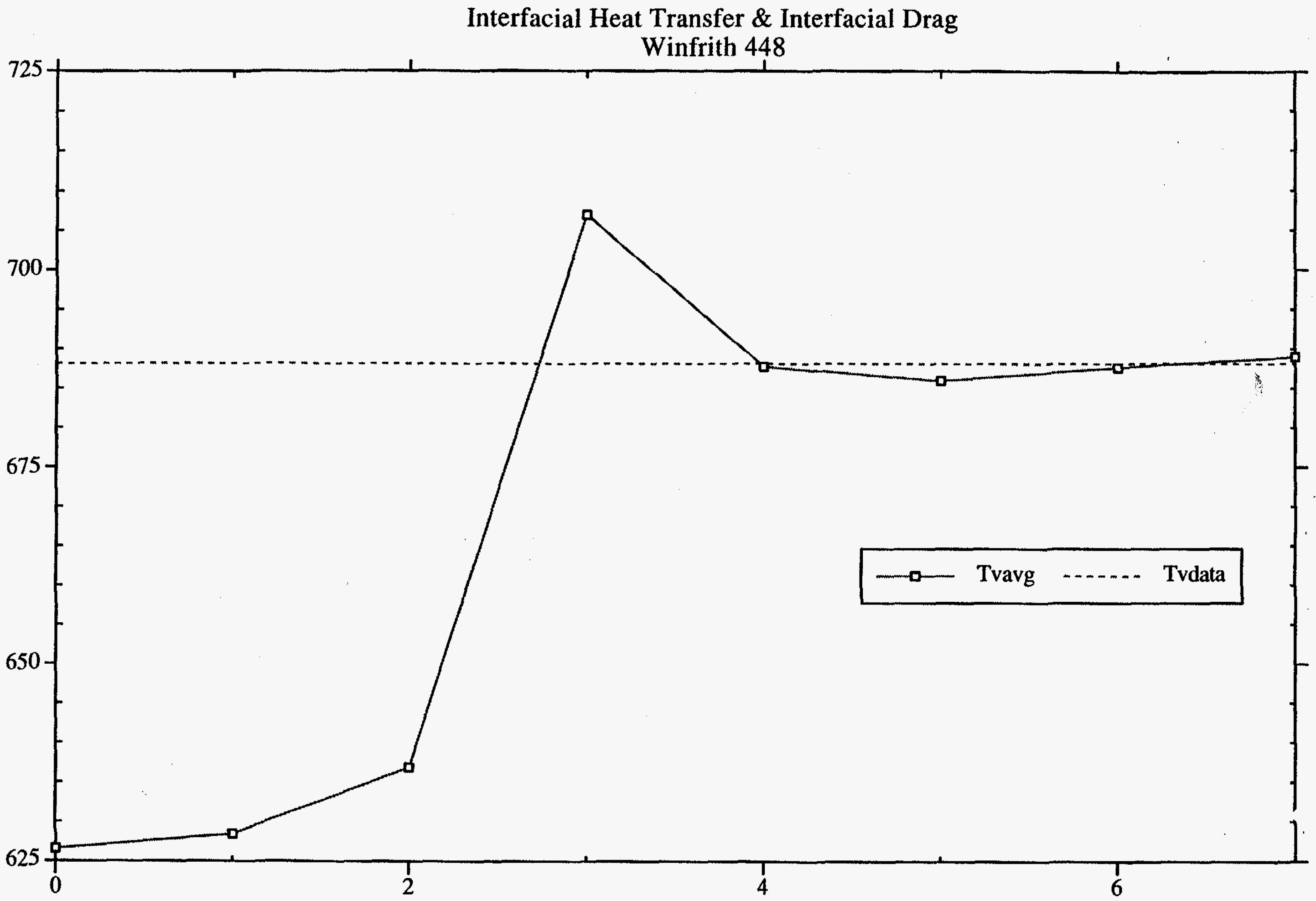

Fig. 131. The vapor temperature corresponding to the experimental measurement elevation(s) is shown as a function of each iteration of TRAC as the coefficients **fgam2** and **ffd** (Section 4) are tuned using the post-CHF-up-flow data and TRAC input deck for Winfrith Experiment 448 and beginning with the Conditional Pedigree values.

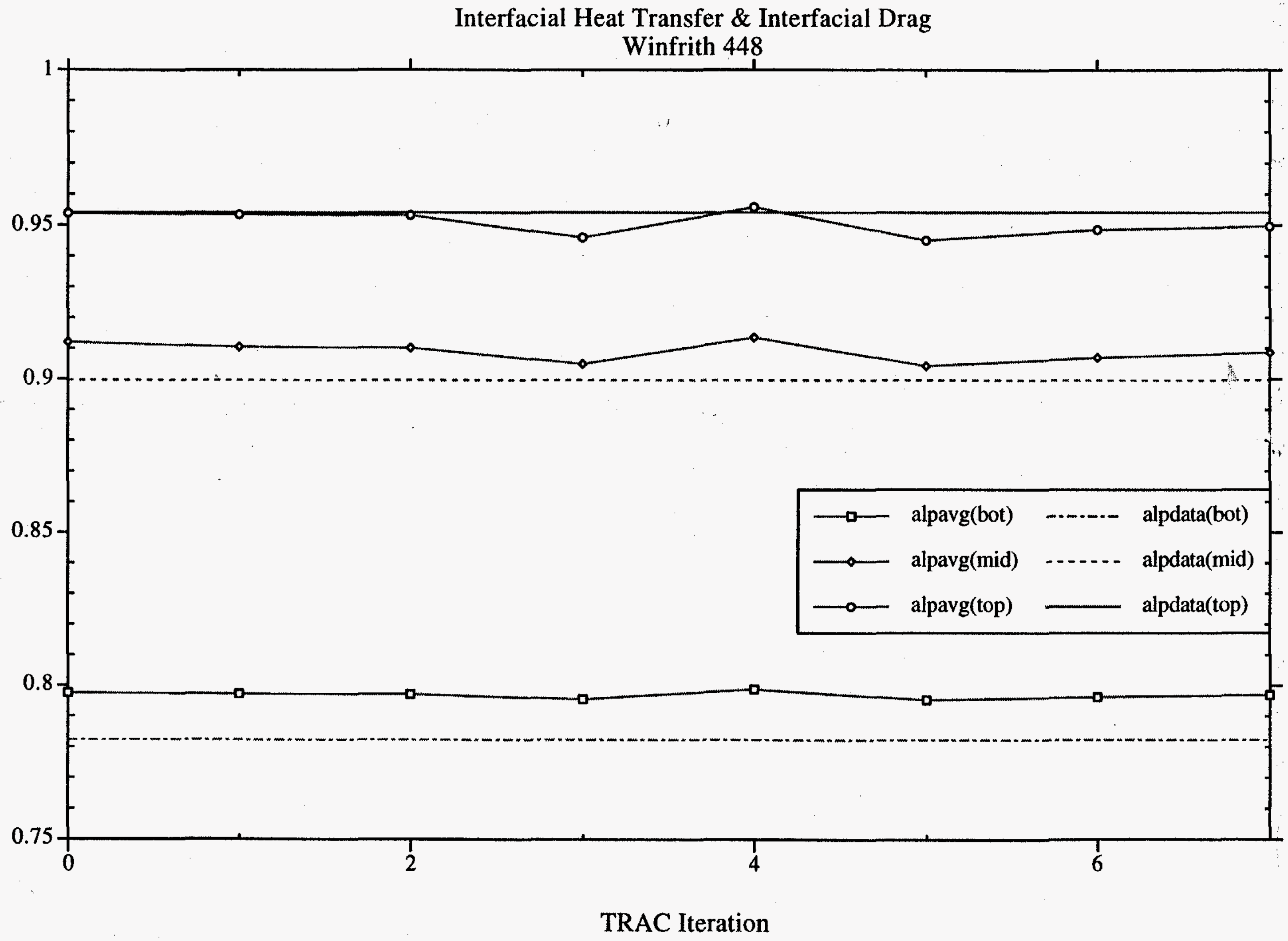

Fig. 132. The void fraction corresponding to the experimental measurement elevation(s) is shown as a function of each iteration of TRAC as the coefficients **fgam2** and **ffd** (Section 4) are tuned using the post-CHF-up-flow data and TRAC input deck for Winfrith Experiment 448 and beginning with the Conditional Pedigree values.